DEVELOPMENT OF INTERMETALLIC-HARDENED

ABRASION-RESISTANT WELD HARDFACING ALLOYS

Milton R. Scholl
B.S., Cal. Poly. State University, San Luis Obispo, California, 1979
M.S., Oregon Graduate Center, Beaverton, Oregon, 1982

A dissertation submitted to the faculty
of the Oregon Graduate Center
in partial fulfillment of the
requirements for the degree
Doctor of Philosophy
in
Materials Science and Engineering

1986

The dissertation "Development of Intermetallic-Hardened Abrasion-Resistant Weld Hardfacing Alloys" by Milton R. Scholl has been examined and approved by the following Examination Committee:

William E. Wood, Thesis Advisor
Department Chairman and Professor

Paul Clayton
Associate Professor

Jack H. Devletian
Associate Professor

Paul Davis
Associate Professor

Robert Blickensderfer
Metallurgist, U.S. Bureau of Mines

Acknowledgements

I would like to thank the staff and faculty of the Oregon Graduate Center for their help and useful discussions. In particular I would like to thank Bob Turpin for his welding expertise which I hoped would rub off on me; Bill Wood for many useful discussions and overall guidance in keeping the project to a manageable size; John Johnsen and Dan Danks for their input; and Barbara Ryall for drawing all those impressive figures. I would also like to thank the staff of the U.S. Bureau of Mines, especially Rob Blickensderfer for his assistance, guidance, and many useful discussions about abrasive wear. Finally I would like to thank my wife, Hazel, for putting up with me while I wrote this.

INDEX

List of Figures and Captions

List of Tables

Abstract

Chromium and cobalt are strategic materials in the U.S. and both are major constituents in many weld hardfacing alloys. Substitution for these materials or alternatives to their use was a primary direction of this investigation which was conducted in conjunction with the U.S. Bureau of Mines. Minimization of the use of strategic materials was the criteria guiding the development of intermetallic-hardened abrasion resistant weld hardfacing materials. Other criteria were that the new alloy contain a hard intermetallic compound in an FCC matrix, and that these intermetallic compounds be stable at room temperature.

A survey of ternary systems was made and the Fe-Mo-Ni system was selected to provide a basis for alloy development. Powder metallurgical techniques and arc-melting provided samples for initial examination. Further development was performed using the submerged-arc welding process with alloyed metal powder additions. Specimens were examined and wear resistance tested using the pin-on-drum abrasive wear test. Final compositions were also subjected to heat treatment and melting point analysis.

Fe-Mo-Ni alloys synthesized by arc-melting and similar alloys made by welding possessed similar microstructures, a $(Fe,Ni)_7Mo_6$ intermetallic plus austenite eutectic in an austenitic matrix. These materials exhibited poor abrasive resistance. Silicon additions to the alloy promoted formation of a Laves phase FeMoSi intermetallic which helped increase the abrasive wear resistance. Through a series of alloy chemistry iterations a final composition of Fe-20Mo-15Ni-5Si was selected. Heat treatment of this alloy

at 550 to 650°C caused second phase precipitation in the matrix and raised the hardness about 14 points HRC to 50 HRC. The alloy's wear rate, measured with the pin-on-drum abrasive wear test, was 6.3 to 6.5 mg/m. However this was twice the wear rate observed in commercial high-carbon high-chromium alloys. Based on examination of the alloy microstructures, their chemistry, and an analysis of the Fe-Mo-Si phase system; directions for further research are to increase the molybdenum and silicon content to produce a Fe-20Mo-10Ni-15Si composition. Based on the phase diagram analysis this alloy promises better abrasive wear resistance through a larger volume fraction of hard phases formed and the formation of a harder ternary intermetallic compound, Fe_2MoSi_2.

Objective

Weld hardfacing alloys typically contain large amounts of chromium as chromium-based carbides or cobalt as a base material or both. Chromium and cobalt are considered strategically important materials in the U.S. since more than 90% of that used is imported. Finding and developing substitutes or alternatives to strategic materials such as chromium and cobalt is one of the missions of the U.S. Bureau of Mines. The scope of this investigation was bounded by this mission since the research was conducted in conjunction with the U.S. Bureau of Mines.

The search for alternatives to hardfacings containing chromium and cobalt was approached by recognizing two available directions. One was to adapt current hardfacing alloys to minimize cobalt and chromium contents while maintaining adequate wear resistance. The other was to explore the use of hard phases other than carbides. The research conducted followed the latter approach and further narrowed the scope of investigation by limiting the work to alloys containing intermetallic compounds. Thus, research was conducted with two goals: to develop a weld hardfacing alloy hardened with intermetallic compounds and to minimize the use of strategic materials in the alloy.

1.0 Introduction

1.1 Strategic Materials

The purpose behind this investigation was to develop alternatives to the use of the strategic materials, particularly cobalt and chromium, in weld hardfacing alloys. The following section presents background information on strategic and critical materials. It is divided into two parts; the first providing a historical background of strategic materials and the second a description of materials now considered strategically critical.

1.1.1 Historical Background

Until the last 60 or 70 years, the U.S. has been able to freely exploit its natural resources and those elsewhere in the world without regard to possible depletion of the resource. By the end of the first world war it became evident that resources were not boundless, and that there were additional factors involved in their procurement, though this last acknowledgement took thirty years to solidify [1].

Wars were the principle reason that importance of materials availability came to the forefront. Each war added new materials to a list of those materials considered important and vital to the war effort. At the end of World War I the list of materials which experienced supply shortages numbered 28. After World War II an incomplete list numbered 298 items. As technology changed, the list grew with new materials that became vital [1].

The Strategic and Critical Materials Stock Piling Act of 1946 was

the first government action taken. Its goal was to stockpile materials for a three year war. This Act has seen many changes in goals and philosophy since its inception. The Stock Piling Act of 1946 stated that the stock pile was for "national defense only and not for economic or budgetary reasons" [2]. In the 1950's the stock pile was enlarged to help a depressed U.S. mining industry by enlarging the stockpile to support a five year war effort plus a year of normal use. In 1963 the plan was criticized for not meeting its objectives. Between 1963 and the early 1970s, the nation was involved in the Vietnam War which relied extensively on new technology in electronics, weapons, and aircraft. At this time sales of 'excess' material were made from the stockpile. By the mid-sixties the public was becoming increasingly environmentally aware and the suitability of a resource for exploitation took on a new importance.

In 1970 a bill concerning strategic materials was attached as an amendment to the Resource Recovery Act. This bill convened a commission to examine the state of strategic materials in the U.S. Its findings were essentially the same as those of a similar commission convened in the 1950s, but in the recent report scarcely a mention was made of defense issues or of national security [1]. This was a far cry from the Stock Piling Act of 1946 which stated that the stock pile was for military uses only.

During the 1970's a number of changes took place in the stockpile. During this decade, the General Services Administration, which administered the stockpile, sold seven to nine million pounds of cobalt. The amount sold constituted about 50% of annual U.S. usage of cobalt and about 25%

of world usage. Sales ceased in 1976 and primary cobalt producers, mainly those in South Africa, experienced a 25% increase in demand. By this time stockpiles of nickel, aluminum, and copper had been almost totally liquidated. Stockpiles of tantalum, molybdenum, columbium, and tungsten were sold as well. After sales of cobalt ceased in 1976, policy was reversed and the stockpile goal doubled over its previous size, though this time with an emphasis on aerospace grade cobalt [2]. At this same time Katanese rebels invaded the Shaba province in Zaire and mine production was curtailed for two weeks [3]. A result was that for a short period of time the price of cobalt rose from 6$/lb to 50$/lb.

1980 saw passage of the National Materials Policy which set goals and called for combined integrated action by different segments of the government to implement those goals. In 1981 the Critical Materials Act which focused responsibility and authority for establishing and implementing policy within the executive branch of the government [2] was introduced. In 1981, there were yet more changes in the cobalt stockpile. At a time when there was a decline in demand and price of cobalt, the General Services Administration wanted to add another 5.2 million pounds to a stockpile which some said was too large to begin with [2]. The stockpile size was going to increase to almost 85 million pounds while cobalt usage in 1981 was only 10 million pounds.

From this synopsis of the history of U.S. Strategic materials policy, it is evident that many changes have occurred since the stockpile was created in 1946. It is also clear that policy decisions regarding the stockpile have far reaching effects.

1.1.2 Material Distribution

Even with accessibility to large portions of the earth's surface, man has only substantially explored only a small fraction of one percent of the area. Only about 35% of the U.S.'s land mass has been geologically mapped. The earth's crust is from 25 to 40 miles thick yet most mines only penetrate a few hundreds of feet. Therefore tables of mineral reserves and resources must be examined with knowledge that these tables depict only what is known.

Some elements like titanium and aluminum abound in the earth's crust. Other elements are not as common. Table 1 lists the crustal abundance of various elements and their cut-off grade for feasible extraction. Common igneous rock contains many elements that are extractable, though not economically or technically. 100 tons of igneous rock contains 8 tons of aluminum, 5 tons of iron, 1200 pounds of titanium, 180 pounds of manganese, 30 pounds of vanadium, 20 pounds of copper, and 10 pounds of tungsten [4]. It would, however take a tremendous amount of energy and effort to extract these metals. Table 2 shows the concentration of other elements in igneous rock.

A number of factors limit exploitation of a resource, besides net energy costs. The limits of exploitation could be defined as [5]:

1) The limit of net energy profit and/or work savings; e.g. processing igneous rock.

2) The limit of comparable utility; meaning that a mineral is a resource only as long as it serves a function for man.

3) The unwillingness of society to exploit or to pay

> the costs of exploitation. This is increasingly true for social and political reasons such as environmentalism and an increasing sense of the importance of livability.

Other considerations that determine the strategic importance of a mineral are [6]:

1) The nature of the source of the material.
2) The degree to which the material is used.
3) The number of substitutes available.

Most materials are considered strategic or critical because of their source. Table 3 is a list of some strategic materials, their import origin, and quantities. As is evident from an examination of this table there are materials which the U.S. imports in totality, with large fractions of imports from Soviet Bloc nations and South Africa. Principle among these metals and of paramount interest to this investigation, are chromium and cobalt, and to a lesser extent tungsten.

Cobalt is almost 100% imported and there are essentially no known reserves in the U.S. other than deep sea manganese nodules. Table 4 shows the distribution of import sources of cobalt. In 1977 U.S. demand was 37% of total world usage and was growing at a rate of 2.7% per year [7]. About 40% of U.S. annual usage of cobalt is used in superalloys, and about 10% in wear resistant alloys [6]. The magnetics industry has been a primary user of cobalt in the past, but with substitutions and new alloys, the industry has decreased its portion of the U.S. demand from 25% in 1977 to 15% in 1980. It would appear that this would substantially decrease cobalt usage in the U.S. except that in two years, 1978

to 1980, superalloy demand for cobalt increased 80% [8].

The magnetics industry found substitutes for cobalt and was able decrease their dependence. Lack of suitable substitutes is one reason a material becomes strategic. Research into substitutes for metals like cobalt and chromium which are important strategic materials has been increasing as awareness of the situation grows. Actions by the U.S. government are becoming increasingly frequent as discussed in the previous section discussed. Finally, a search for suitable substitutes in wear resistant alloys and hardfacings provided the direction of this investigation. The next section deals with theoretical aspects of abrasive wear, the type of wear most hardfacings are designed to combat.

Table 1

Table of Elemental Crustal Abundance and Cut-Off Grade for Extraction. Arranged in order of Cut-Off Grade to Abundance [5].

Element	Crustal Abundance (ppm)	Cut-off Grade (ppm)	Ratio
Mercury	0.089	1,000	11,200
Tungsten	1.1	4,500	4,000
Chromium	110	230,000	2,100
Silver	0.075	100	1,330
Gold	0.0035	3.5	1,000
Molybdenum	1.3	1,000	770
Zinc	94	35,000	370
Uranium	1.7	700	350
Carbon	320	100,000	310
Manganese	1,300	250,000	190
Nickel	89	9,000	100
Cobalt	25	2,000	80
Copper	63	3,500	56
Titanium	6,400	100,000	16
Iron	58,000	200,000	3.4
Aluminum	83,000	185,000	2.2

Table 2

Elemental Concentrations in Basaltic Igneous Rock [9]
(in ppm by wieght)

Aluminum	78,000	Mercury	0.007
Antimony	0.2	Molybdenum	1.5
Arsenic	2.0	Neodymium	20
Barium	330	Nickel	130
Beryllium	1.0	Niobium	190
Bismuth	0.007	Nitrogen	20
Boron	5.0	Oxygen	440,000
Bromine	3.6	Palladium	0.002
Cadmium	0.22	Phosphorus	1,100
Calcium	76,000	Potassium	8,300
Cerium	48	Praseodymium	4.6
Cesium	1.1	Rubidium	30
Chlorine	60	Samarium	5.3
Chromium	170	Scandium	30
Cobalt	48	Selenium	0.05
Copper	87	Silicon	230,000
Dysprosium	3.8	Silver	0.11
Erbium	2.1	Sodium	18,000
Europium	0.81	Strontium	465
Fluorine	400	Sulfur	300
Gadolinium	5.3	Tantalum	1.1
Gallium	17	Terbium	0.8
Germanium	1.3	Thallium	0.21
Gold	0.004	Thorium	4
Hafnium	2.0	Thulium	0.2
Holmium	1.1	Tin	1.5
Indium	0.22	Titanium	13,800
Iodine	0.5	Tungsten	0.7
Iron	86,500	Uranium	1.0
Lanthanum	15	Vanadium	250
Lead	6.0	Ytterbium	2.1
Lithium	17	Yttrium	21
Lutetium	0.6	Zinc	105
Magnesium	46,000	Zirconium	140
Manganese	1,500		

Table 3
U.S. Annual Import Reliance and Import Sources [10]

CHROMIUM	92% Imported
Import Sources:	
(Chromite)	
	35% South Africa, 18% U.S.S.R., 16% Philippines, 31% Other
(Ferroalloy)	
	38% South Africa, 23% Southern Rhodesia, 39% Other
COBALT	97% Imported
Import Sources:	
	42% Zaire, 23% Belgium-Luxembourg, 7% Zambia, 28% Other
COLUMBIUM	100% Imported
Import Sources:	
	73% Brazil, 8% Thailand, 8% Canada, 11% Other
MANGANESE	98% Imported
Import Sources:	
(Ore)	
	36% Gabon, 33% Brazil, 13% Australia, 18% Other
(Ferroalloy)	
	32% France, 30% South Africa, 14% Japan, 24% Other
MOLYBDENUM	1% Imported, Net Exporter
Import Sources:	
	89% Canada, 9% Chili, 9% Other
NICKEL	77% Imported
Import Sources:	
	58% Canada, 42% Other
PLATINUM GROUP	91% Imported
Import Sources:	
	42% South Africa, 26% U.S.S.R., 17% U.K., 15% Other
TANTALUM	97% Imported
Import Sources:	
	36% Thailand, 16% Canada, 9% Malaysia, 4% Brazil, 35% Other
TUNGSTEN	50% Imported
Import Sources:	
	22% Canada, 16% Bolivia, 12% Peru, 50% Other
VANADIUM	27% Imported
Import Sources:	
	56% South Africa, 25% Chili, 9% U.S.S.R., 10% Other

Table 4

Estimated World Mine Production, Reserves, and Resources for Cobalt in 1979 [4]. (in millions of pounds)

	Mine Production	Reserves	Resources
North America			
United States	0	0	1,700
Canada	2.0	66	546
Cuba	3.6	240	2,340
Europe			
USSR	4.4	460	500
Finland	3.0	40	50
Africa			
Zaire	29.0	1000	1,500
Zambia	6.0	250	770
Morocco	4.0	28	30
Botswana	0.4	50	70
Oceania			
New Caledonia	9.2	600	850
Australia	7.6	110	650
Philipines	2.4	420	450
World Total =	71.6	3,272	9,456
Seabed Nodules	-	-	500,000

1.2 Abrasive Wear

1.2.1 General Classification of Wear

A simple precise definition of 'wear' does not exist and loose terminology in the wear research field exaggerates differences between various accepted definitions. The OECD (Organization for Economic Cooperation and Development) has defined 'wear' as 'the progressive loss of substances from the operating surface of a body, occurring as a result of relative motion of the surface'. Most other definitions of wear are conceptually similar, stating that material is being removed or a surface is being destroyed in some manner. Other definitions of wear are:

1) 'Removal of material from solid surfaces as a result of mechanical action' [11].

2) 'Destruction of material as a result of repeated disturbances of the frictional bonds' [12].

3) 'Removal of material from surfaces in a tribosystem' [13].

Definitions of 'wear' tend to be all-encompassing, making no reference to the manner in which material is removed or destroyed except perhaps by specifying that the removal and/or destruction is by mechanical means.

Classifications of different wear types, processes, and mechanisms are almost as catch-all as the definition of 'wear'. Classifications can be made by wear mechanism, the fundamental manner in which surface degradation occurs; by type of wear, a collection of wear phenomena, processes, and other ancillary properties that are related; and by wear process, which varies and depends on the types and the mechanisms. Classifications can also be made using damage observed or by the mechanical

systems involved.

There are many types, mechanisms, and processes of wear that are recognized in the terminology of the wear field. Unfortunately, terms one investigator uses to describe a wear type or mechanism may not be the same as another worker's. Some common terms are:

> Adhesive Wear, occurring between two surfaces A and B where material lost on surface A may momentarily or even permanently become part of surface B. Surface A exhibits material loss and surface B may show material gain. The adhesive 'process' is microscopic in scale.
>
> Abrasive Wear , occurring between a surface and other body or bodies such that the latter acts on the surface to mechanically remove material. Actions which occur are macroscopic.
>
> Erosive Wear, acting much like abrasive wear but generally with a large size difference between the eroding media and the surface being eroded. The process tends to between microscopic and macroscopic in scale.

Of interest to this investigation is abrasive wear. The processes and mechanisms involved in abrasive wear and other phenomenological observations will be examined further in the next section.

1.2.2 Classification of Abrasive Wear

About half of the material degradation in the world has been attributed to abrasive wear. Almost half of that occurs in metallurgical and related

industries. The OECD definition of abrasive wear is 'wear by the displacement of material caused by hard particles or protuberances'. This can be attributed to several situations:

- hard particles trapped between two surfaces, classically called three-body abrasive wear.
- hard particles embedded in one surface, classically called two-body abrasive wear.
- hard asperities or protuberances on one surface.
- abrasive material rolling or sliding along a surface.

Abrasive wear has also been classified as to whether it is two-body or three-body. The former is the case of an abrasive medium moving freely over a surface, the latter deals with an abrasive medium between two surfaces. Misra and Finnie [14] have shown that many variables affecting abrasive wear resistance are the same for two-body and three-body abrasion. Abrasive wear can be classified by the type of action which occurs, such as low-stress, high-stress, or impact. It can be classified by the observable aspects of the damage, like gouging, grooving, or scratching. For purposes of this investigation, terms used will be low-stress or low-load abrasion, high-stress or high-load abrasion, and impact abrasion where material removal occurs in very short amounts of time.

Vingsbo [13] suggested three mechanisms for abrasive wear: gouging, cutting, and deformation; but lumps them all under the term 'ploughing'. Vingsbo stated that ploughing is the principle process in abrasive wear. Energy involved in abrasive wear either goes into plastic deformation and cutting in most metals, or into fracture processes with brittle materials. Murray, Mutton, and Watson [17] in their review of abrasive wear kept the

three mechanisms separate. They used the term 'ploughing' for large scale plastic deformation in the wear groove; 'cutting' for grooves exhibiting only a small amount of plastic deformation and material cut or sheared from groove faces; and fragmentation' or fracture of groove edges. They plotted these mechanisms schematically versus wear resistance and hardness (Figure 1) of ductile and brittle materials. In between the predominantly ploughing region and that of cutting they defined a transistion region which they suggested was responsible for the deviation of wear behaviour of alloys from that of pure metals.

The simplest model of abrasive wear involves only two bodies, one a geometrically shaped particle and the other a free surface. Two extreme actions can be contemplated in this system. In both the particle penetrates the material. In one case material is displaced and removed from the surface by cutting or fracture as the particle moves across the surface. In the other case material is not removed from the surface, but is pushed aside. The latter is referred to as ploughing or gouging. Figure 2 illustrates these. Both cases are assumed equivalent in a simple mathematical model in which the manner of material displacement is not regarded.

Rabinowitz [11] was among the first to develop the following model. It has since been derived by other methods, yet all the various added complexities yield the same result. A derivation of the model follows.

Consider a particle as shown in Figure 3. The diameter of the particle at the surface is 'D'. It is under a vertical loading 'W' and penetrates the surface to a depth 'H' while moving at a velocity 'v'. 'ß' is the angle the leading edge of the particle makes with the surface. The change in volume of the groove, 'dV', can be equated to the cross-sectional

area of the particle, 'A', and the distance slid, 'L', by:

$$dV = (A)(L). \qquad \text{(Equation 1)}$$

Pure cutting (micromachining) would mean that all material removed from the groove would be removed from the surface. Since this model is not considering that one specific case, a constant 'C_1' is introduced:

$$dV = (C_1)(A)(L). \qquad \text{(Equation 2)}$$

Several assumptions are now made and equations derived based on this model vary with these assumptions. The first assumption is that the cross-sectional area that the particle presents in the groove is proportional to p . This is an assumption on the particle shape. The second assumption is that the projected area is proportional to p which infers that the hardness 'H' is proportional to W/p since p is proportional to W/A. Addition of these assumptions to equation 2 lead to:

$$dV \text{ prop. to } (C_1)(W/H)(L). \qquad \text{(Equation 3)}$$

This applies to a single particle. Extending the equation to multiple particles necessitates a third assumption that the number of particles 'N' contacting the surface per unit surface area is proportional to 1/D . Since W = P/N where 'P' is the load per unit area, when the preceding assumption is considered 'W' is then proportional to PD . A fourth assumption is that only a portion of the particles contacting the surface produce a groove. This introduces a constant 'C_2' which is independent of particle size and loading. Combining these with equation 3 yields:

$$dV \text{ prop. to } (C_1)(W/H)(L) \text{ prop. to } (C_1)(PD/H)(L). \qquad \text{(Equation 4)}$$

for a single particle and:

$$dV \text{ prop. to } (C_1)(C_2)(N)(Pd/H)(L). \qquad \text{(Equation 5)}$$

for all particles. Adding a constant of proportionality yields:

$$V = (C_1)(C_2)(C_3)(N)(Pd/H)(L). \qquad \text{(Equation 6)}$$

where C_1 => percentage of groove volume removed,

C_2 => percentage of contacting particles, their shape and orientation,

C_3 => depends on the particle shape and dispersion.

Combining all this into a simplified form:

$$V = (K_1)(PL/H) \qquad \text{(Equation 7)}$$

where V = the total wear volume

P = the load

L = the length of contact

H = the surface hardness

K_1 = all the previous constants.

The equation shows, mathematically at least, that the amount of wear is directly proportional to the load/area and the sliding distance and inversely proportional to the hardness. Many studies have been under taken to experimentally verify this model's predictions, as well as predictions when other constraints are used. Principle among constraints are corrections for particle shape and for the degree of pure cutting involved.

When compared to experimental data, trends predicted by this model, or its more complicated variations, have been verified with some deviations. The model works well when considering pure metals or within a single class of materials in a particular testing regimen. This can be seen in Figure 4 which compares the wear resistance of a material with the bulk hardness, where the materials tested are pure metals, plain carbon steels, and Cr-Mo steels. Beckmann and Westermeier [15], on the otherhans,

developed a model combining delamination theory [16] and statistical descriptions of the surfaces and contact geometries suggested that mean compressive strength rather than hardness would be a better variable to predict the effects of material properties on the abrasive wear resistance.

Most abrasive wear systems defy accurate modeling of their behaviour due to complexity of the mechanical system, as just mentioned, and due to the influence of other factors, as can be seen in Figure 5. This data was obtained from Dry-Sand-Rubber-Wheel (DSRW) tests on pure metals and reveals a dependence between crystal structure and wear resistance. This introduces a new factor to the topic of abrasive wear: the metallurgical considerations necessary when examining relationships between the abrasive wear process, abrading media, and the abraded surface. This will be the topic of the next section.

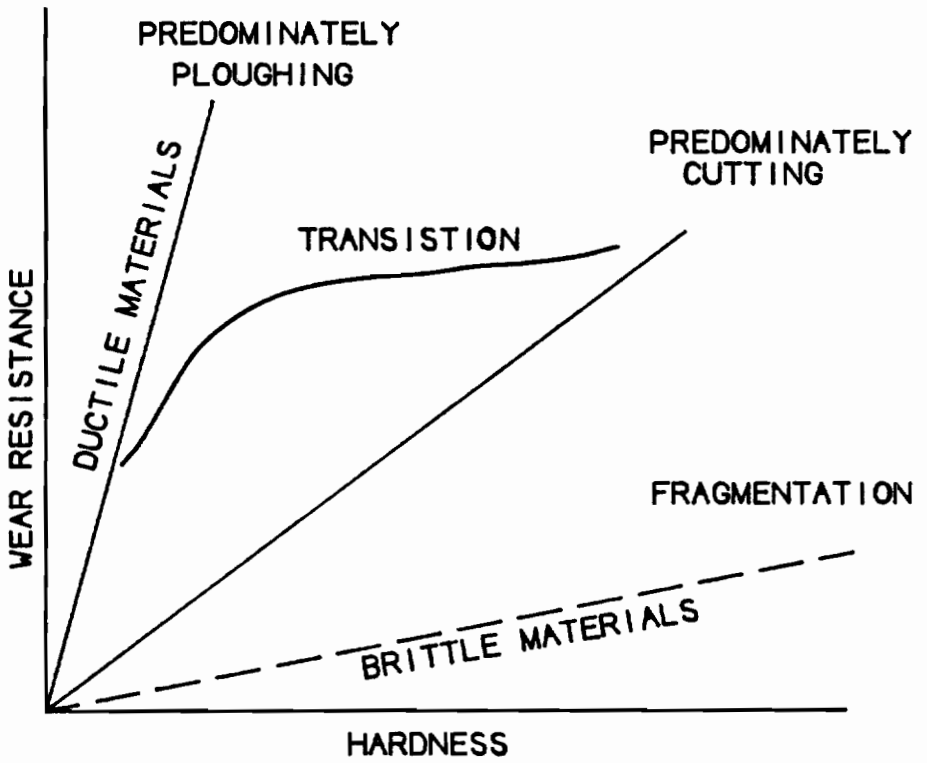

Figure 1. Wear resistance versus abrasive wear mechanism, after Murray et al [17].

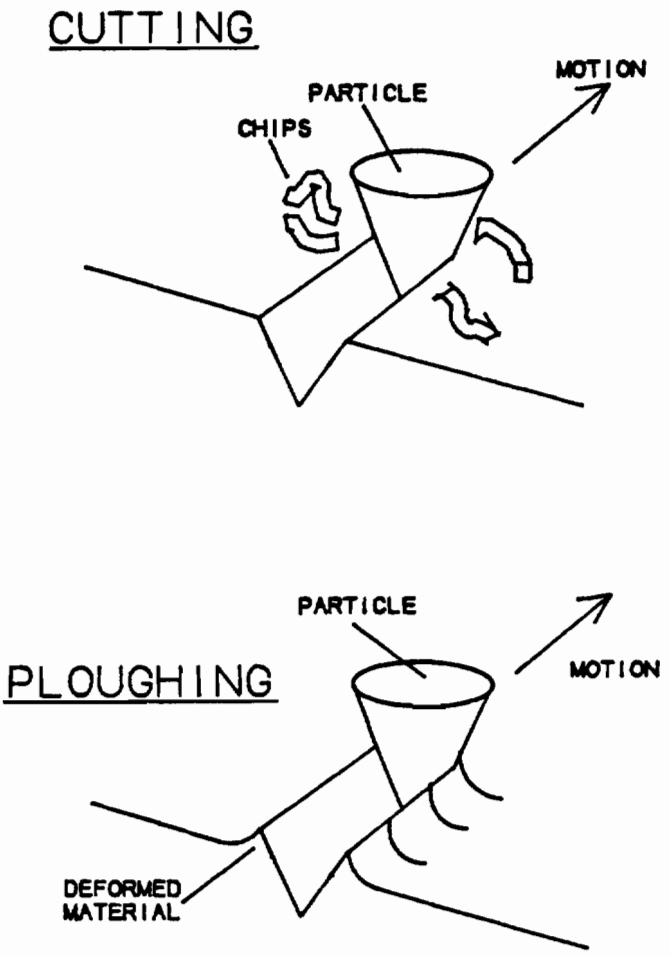

Figure 2. Schematic of ploughing versus cutting abrasive wear.

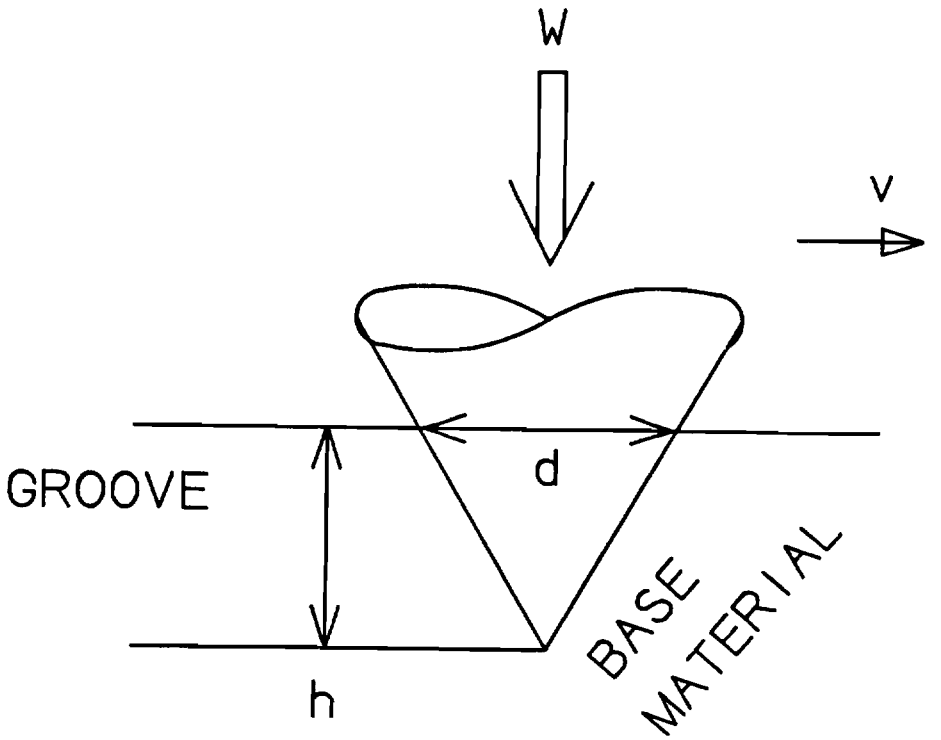

Figure 3. Schematic of an abrasive particle in a groove.

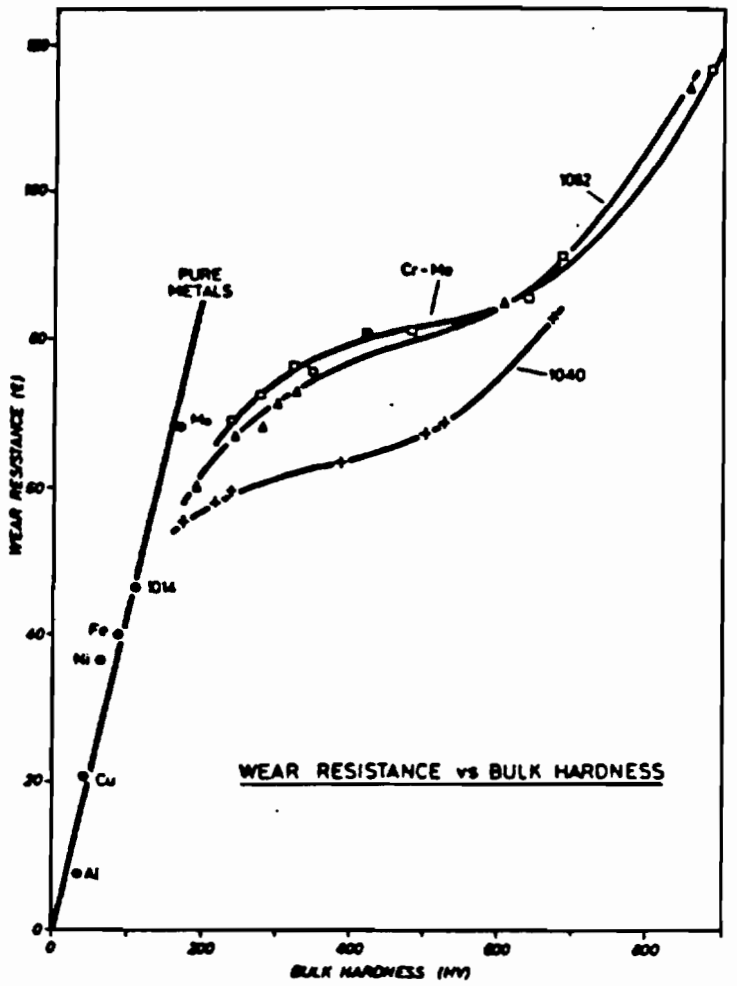

Figure 4. Wear resistance versus hardness for three steels and for pure metals [17].

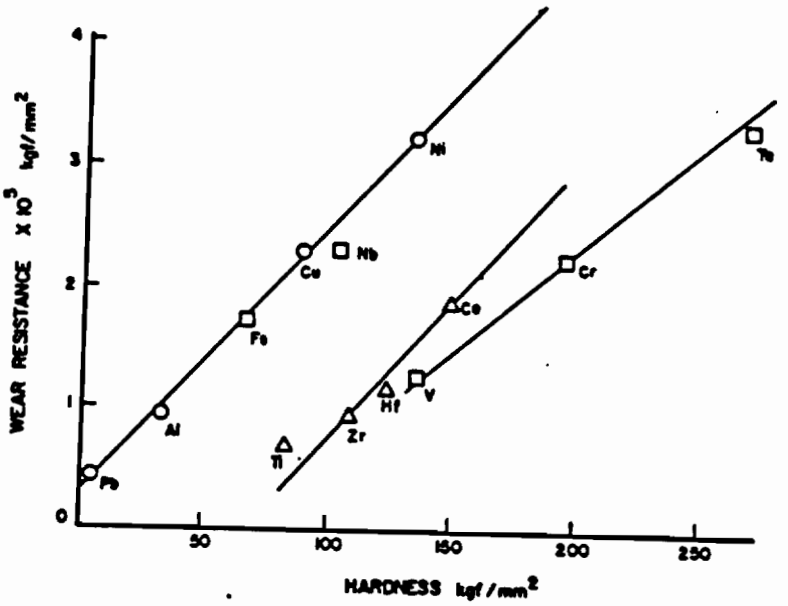

Figure 5. Wear resistance versus hardness and crystal structure for pure metals [18].

1.2.3 Metallurgical Factors in Abrasive Wear

Models and theories regarding abrasive wear generally regard both the damaging body and the worn surface to be homogeneous material. Real world materials are notably not homogeneous, and in fact the most abrasion resistant materials are very inhomogeneous. Confining discussion to metals and alloys, very few metals are used in their homogeneous elemental form since metallurgical factors such as crystal structure and bulk hardness can only be varied little in pure metals.

There are a number of metallurgical factors to consider when looking at alloys to resist abrasive wear. Zum Gahr [19] identified several microstructural parameters which influence an alloy's wear resistance and mechanical properties. These are matrix structure, presence of internal notches, anisotropy, grain boundaries, presence of second phases, and inclusions. Two factors were considered as being of prime importance in this investigation. One is matrix or substrate crystal structure, as shown previously in Figure 5, and matrix mechanical properties and hardness. The other is the type and amount of second phases present.

Numerous studies have been made on the effect of metallurgical factors on abrasive wear resistance. Kruschchov and Babichev [20] did some of the earliest work relating abrasive wear resistance to the structure of inhomogenous materials. They used macroscopically composite specimens of mechanically joined hard and soft metals. They also examined the behaviour of a hypereutectic aluminum-silicon alloy. Samples were tested on a rotating disc covered with abrasive cloth or paper. Their results showed a linear relationship between the wear resistance and the volume fraction

of hard phase present. They examined carbon steels and found that as the carbon content increased, the hardness and wear resistance increased. Kruschchov's conclusion from the bulk of this work was that abrasive wear resistance of inhomogeneous materials was the sum of a phase's volume fraction multiplied by that phase's abrasive wear resistance. The results are shown in Figure 6. This has become known as Kruschchov's Rule. As recently as 1982 this observation has been readdressed. Garrison [21] affirmed Kruschchov's results and applied the additional stipulation that for the rule to be valid the volume wear rate of each constituent phase must be proportional to the load.

In the time between these two investigations, and continuing today, there have been a number of investigations of the relationship between volume fraction of hard phase and a metal's abrasive wear resistance. Much work has been done on carbide-containing materials such as cobalt-based alloys and high-chromium white irons. In RubberWheel-Abrasion-Tests (RWAT), Fulcher et al [22] showed that as carbide volume fraction increases, wear resistance increases in hypoeutectiod chromium-molybdenum white irons. In hypereutectiod white irons the wear resistance decreased with increasing carbide volume fraction as shown in Figure 7. Their explanation for the decrease in wear resistance was that more massive carbides in hypereutectiod alloys protruded from the matrix a greater distance during the abrasive wear process and were prone to fracture, especially with hard abrasives such as quartz. Similar results showing an increase in wear resistance with increasing volume fraction of carbides was found in cobalt-based powder metallurgy alloys tested with Al_2O_3 abrasives [23] and with increasing volume fraction of pearlite in pearlitic steels [24].

Another metallurgical factor which greatly influences the abrasive wear resistance of an alloy is the matrix and its properties. Besides cohesivity between matrix and hard phase, the degree of matrix work hardening is an important factor. Kruschchov and Babichev [20] were among the first to investigate this effect. Richardson investigated the matrix work hardening as well [25]. Similar results to Richardson's work have been reported by Larson-Badse and Matthews [26] in a 1040 steel. The importance of matrix toughness and work-hardening has also been noted by Hurricks [27] and Zum Gahr [28,29].

Work-hardening is important in an abrasion resistance alloy because work-hardening at the surface during abrasion raises surface hardness while sub-surface structure remains unchanged. The harder surface in matrix regions allows the matrix to be more wear resistance. It also allows carbides or other hard phases to be held more firmly. The work-hardened matrix at the surface raises overall surface wear resistance in accordance with Kruschchov's Rule, since there is more area with a higher wear resistance.

The amount of work-hardening is dependent to some degree on matrix crystal structure. Bhansali [18] in work with pure annealed metals showed that face-centered-cubic metals were more wear resistant than hexagonal--close-packed or body-centered-cubic metals. De Gee [30] suggested that these results can be explained by the higher strain hardening exponent for FCC metals. In an abrasive wear environment, the wear process would consequently work-harden the surface to a higher hardness in FCC metals than in BCC or HCP metals, which would in turn increase the wear resistance.

As mentioned previously, abrasive particle properties play an important

role in influencing wear resistance. Abrasive properties are particle shape and size, and its hardness. Fulcher et al [22] showed a change in wear resistance with abrasive particle size where a decrease in wear was seen when particle sizes were below 100μ. Misra and Finnie [31] investigated this and noted several possible explanations for the 100μ cutoff. Their results are shown in Figures 8 and 9. The 100μ cutoff was seen when wear rate was examined as a function of erosion, two- or three-body abrasion, or as a function of the material, for both pure metals and alloys. Some explanations for the 100μ cutoff were clogging of the abrasive, abrasive grit damage, and elastic contacts between abrasive particle and surface. Misra and Finnie contended that the only possible explanation for the effect of abrasive size was that the abraded surface exhibits a higher flow stress than the bulk; so that as particle size diminished, interactions at the surface decreased.

Kosel et al [32] studied abrasive size effects with two materials, a 1020 steel and cobalt-based Stellite 19, using the Rubber-Wheel Abrasion--Test (RWAT). They reported that the plain carbon steel wear rate increased with increasing abrasive particle size. A cobalt-based alloy's wear rate increased with increasing particle size when tested with quartz abrasive. Kosel concluded that micromachining was the primary wear mechanism in plain carbon steels while in Stellite 19 wear was governed by carbide microfracture.

The hardness of the abrasive and its angularity influence abrasive wear processes, and consequentially the abrasive wear resistance of a metal. Shetty et al [33] compared single and multiple scratch tests using Al_2O_3 and diamond pyramid abraders on Stellite alloys. The Al_2O_3

hardness is near that of the chromium carbides in Stellite alloys while the diamond is much harder. Shetty et al attributed the differences in test results with the two abrasive materials to differences in the abrading particle shape and sharpness, and particularly to particle angularity. The diamond presented a constant angularity while the Al_2O_3 did not. Carbides were worn by microcutting with both abraders if the carbide was large enough. Small carbides were removed in micromachined chips.

Prasad and Kosel [34] using single scratch tests in an electron microscope found that quartz abrasives did not cut carbides in high-chromium white irons. Carbide wear was caused by microfracture of protruding edges of a carbide particle. Gross failure of a carbide particle was thought to be caused by a series of micro-fracture events rather than a single event.

In practice there is no control over abrasive size, shape, or hardness and there is considerable variability between each environment. The size and shape of abrasive particles are primarily of interest for academic reasons to establish the abrasive wear process and its mechanisms. While in practice control of the abrasive environment is generally unattainable, control of metallurgical factors influencing abrasive wear resistance of a material are feasible. Through alloy design, alloys can be developed to minimize abrasive wear.

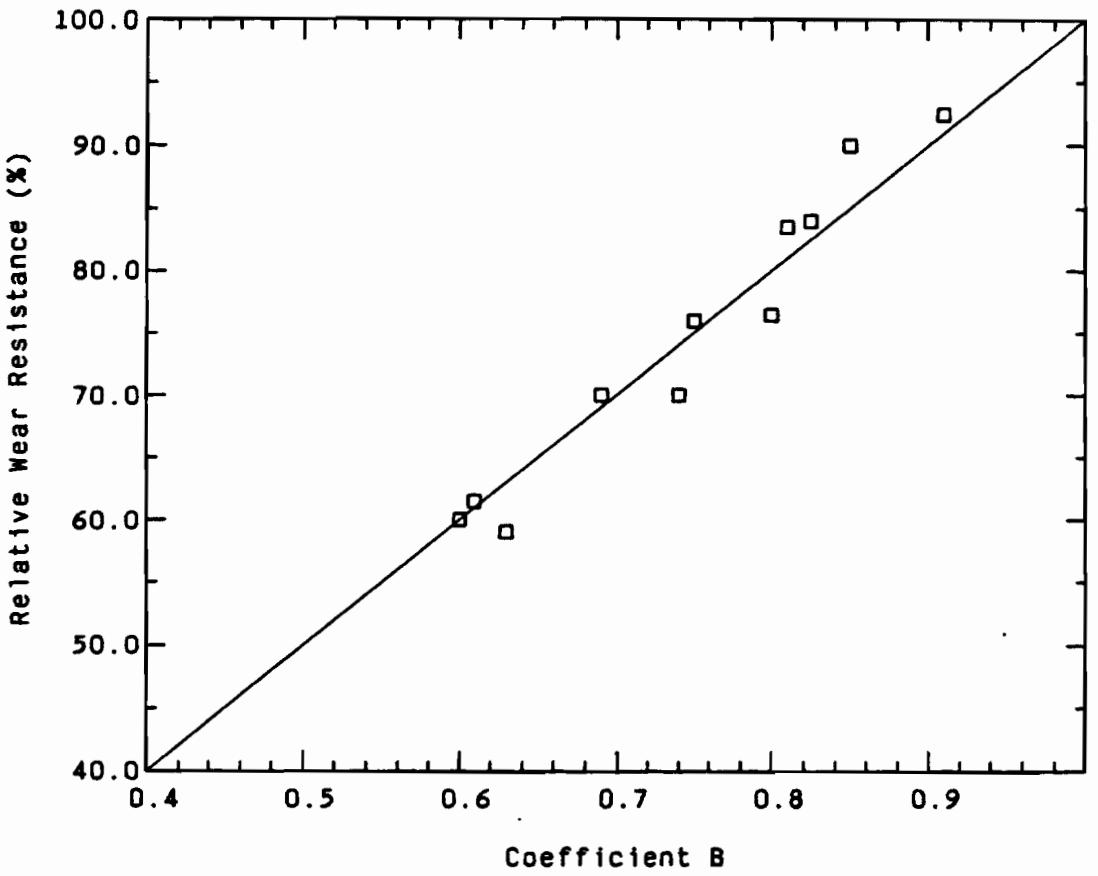

Figure 6. Wear resistance versus volume fraction of second phase for composite metal samples [20].

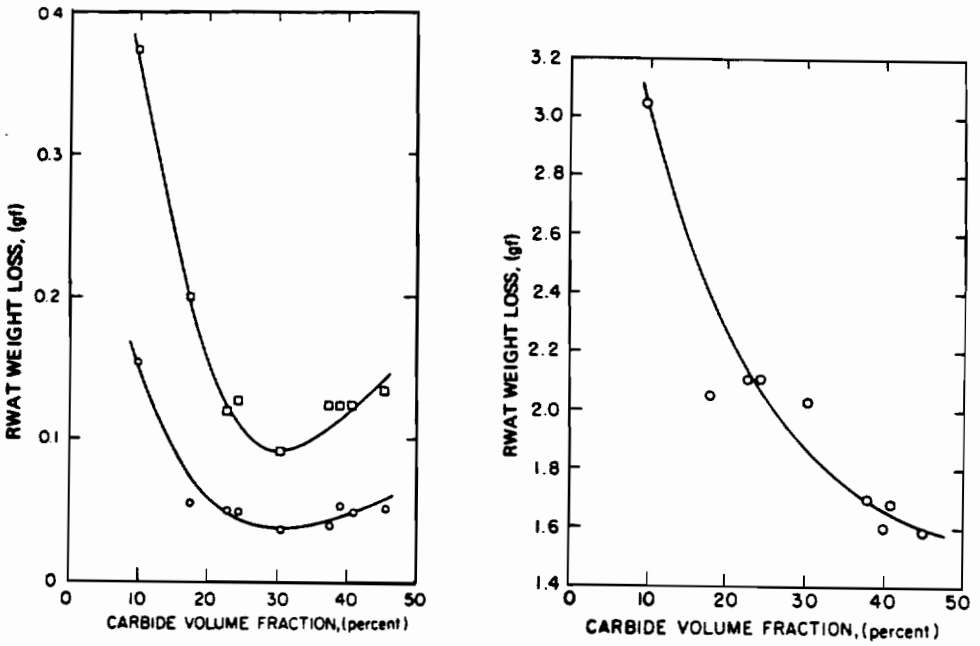

(a) (b)

Figure 7. Rubber wheel abrasion test weight losses for Cr-Mo white iron versus carbide volume fraction [22].

a) SiO_2 Abrasive b) Al_2O_3 Abrasive

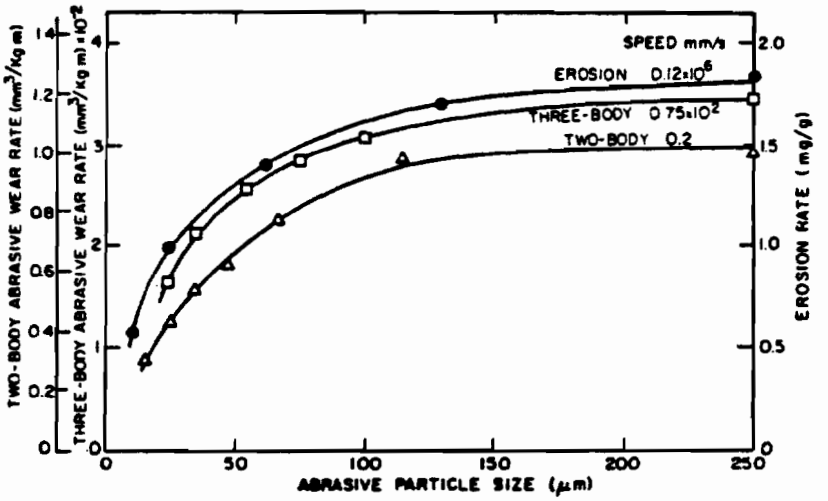

Figure 8. Wear rate versus SiC particle size for different abrasive wear types [31].

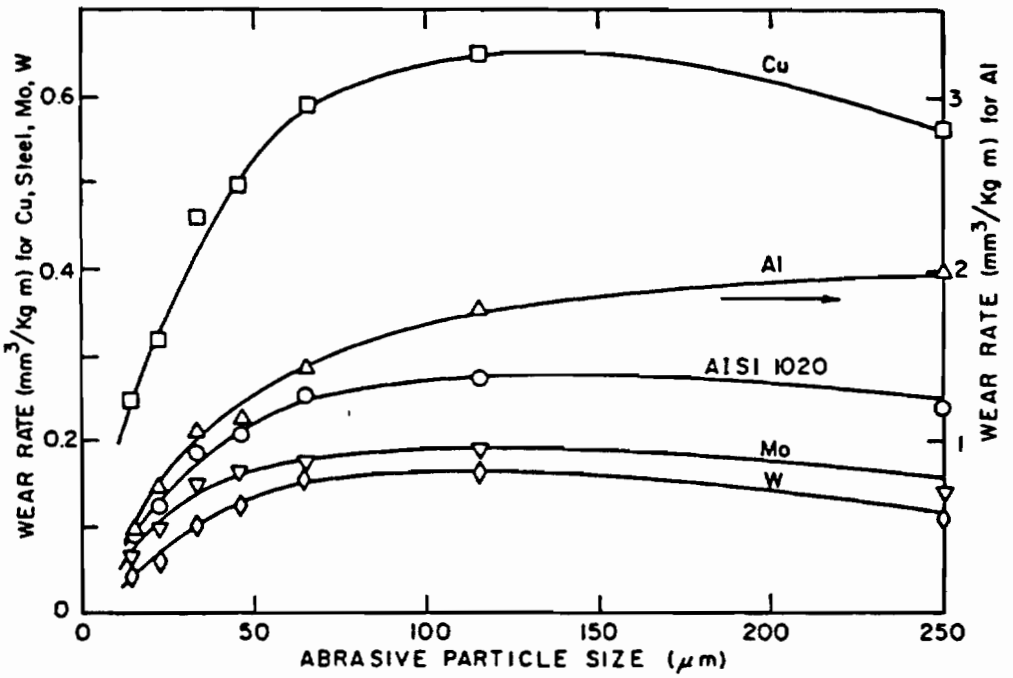

Figure 9. Wear rate versus abrasive particle size for different materials [31].

1.3 Hardfacing Methods

In many abrasive wear environments the base metal of the component experiencing interaction with an abrasive medium is protected with a metal whose sole purpose is to resist wear. For the purposes of this investigation this material will be known as a 'hardfacing', since generally it is of high hardness to resist wear. The term 'hardfacing' is also used to describe the processes used to apply a hard, wear resistant coating to a surface. Another term which is similar to hardfacing is 'surfacing'. 'Surfacing' is a generalized expression taken to mean application of any layer to a metal surface. Hardfacing is specialized, denoting only those materials which are hard and wear resistant.

The principal users of hardfacing alloys are the mining and metallurgical industries. Ore extraction and handling, metal extraction from the ore in smelting, and even final fabrication processes involve an abrasive wear environment. Parts such as shovel digger teeth, earthmover blade lips, bucket liners, and crusher rolls are all hardfaced to reduce abrasive wear. Other applications are in the wearing edges of plow shares, in valve seats, and in dredge pumps.

Hardfacing alloys can be applied to a substrate by two methods; one by mechanically attaching it to the part by means of bolts or rivets. This is commonly done with ball mill liners, pulp mill refiner plates, and with replaceable shovel teeth. Hardfacing alloys can also be applied by using one of a number of welding processes. Of the many welding processes used to apply hardfacing alloys, a number stand out because of their high usage. Oxy-fuel welding, Tungsten-Inert-Gas (TIG) welding,

Gas-Metal-Arc-Welding (GMAW), Shielded-Metal-Arc-Welding (SMAW), and Submerged-Arc Welding (SAW) are among the most commonly used processes [36-40].

Among the factors which determine the suitability of a welding process for hardfacing are the percent dilution of the weld deposit by the base metal and deposition rate. The deposition rate is simply the amount of weld deposit that can be applied per unit time. A process with a low deposition rate would not be economically feasible for hardfacing a large component. High deposition rates tend to have higher heat inputs relative to low deposition rate processes. The percentage dilution is the amount of melted base metal that is mixed or diluted into the weld deposit. Dilution must be considered when selecting hardfacing alloy filler materials in order that the weld deposit chemistry meet requirements.

Most welding processes can deposit a variety of hardfacing alloys but most are limited by the availability of the alloy in suitable sheet, rod, wire, or powder form. Submerged-arc welding, on the other hand, can be used with solid or tubular wire or strip electrodes as well as with metal powder additions, giving the SAW process a versatility beyond other processes.

1.3.1 Submerged Arc Welding

The SAW process uses a consumable wire electrode to produce the arc. There is no gas shielding. A strip electrode can also be used in the SAW process, yielding high deposition rates with wide deposits and only moderate dilution. In the SAW process shielding of the molten metal pool is done by a molten slag layer (Figure 10). The slag layer is formed

by the arc melting a flux blanket. The flux composition is formulated to protect molten metal and the cooling weld deposit, as well as to produce a certain amount of refining action in the molten metal pool [45]. Alloying elements can be added to the flux to change weld deposit chemistry. Additional filler materials can be added by means of extra wires or rods fed into the weld pool or as additions of powder to the weld line [46-48]. Powder additions can be used easily to vary the chemistry of a weld deposit, or to produce a weld deposit of a chemistry that could not be produced by using a solid or tubular wire or a strip electrode. Deposition rates can reach 150 lbs/hr with the use of powder additions, though typically they range up to 35 lbs/hr. Weld metal dilution, however, is moderate (15 to 25%) to high (30 to 60%). Dilution can be controlled to a great extent by welding parameter selection and the means by which filler metals are added. Powder additions and strip electrodes can lower weld metal dilution by the base metal. The SAW process can be used with a variety of electrode materials. The SAW process affords more versatility than other processes because of the variety of ways the alloying elements can be added to the weld deposit. It is, however, limited to the horizontal welding position because of the loose flux blanket required.

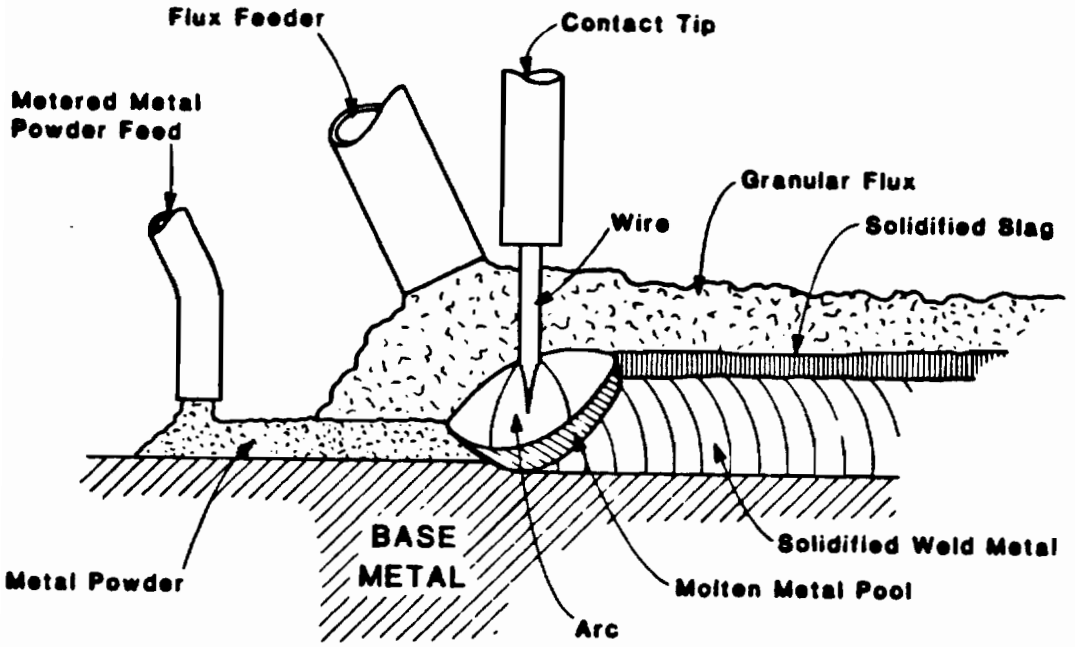

Figure 10. Diagram of submerged-arc welding with powder metal additions.

1.4 Commercial Hardfacing Alloys

Most abrasion resistant hardfacing alloys are cobalt-base, nickel-base, or iron-base alloys [58-61]. The latter covers all iron alloys from plain carbon steels to high-chromium white irons.

High-Chromium white irons and nickel-base alloys both contain up to 30 wt.% chromium. Typical cobalt-base alloys contain as much chromium as well as 50 to 60 wt.% cobalt [62]. Some manganese steels and high alloy steels contain up to 5 and 9 wt.% chromium respectively [63]. Both chromium and cobalt are among the most important of the strategic materials in use in the U.S.

1.4.1 Nickel-Base Alloys

Abrasion resistant nickel-base hardfacing alloys typically contain 15 to 30 wt.% chromium and several wt.% cobalt. Their use is not as prevalent as cobalt-base or iron-base alloys. Compositions of common nickel-based hardfacing alloys are shown in Table 5. Whelan [64,65] investigated several Ni-Mo-Cr-Fe-C alloys and reported that these alloys possessed greater hardness and abrasive wear resistance than Cobalt Alloy No. 6. Silence [66] compared a nickel-base alloy, several cobalt-base alloys, and an several iron-base alloys and found that a cast 30Ni-10Co--25Cr-10Fe alloy faired as well as cobalt-base alloys in abrasive wear tests. It also performed very well in metal-to-metal wear testing.

Nickel-base alloy microstructures contain primary carbides in a face-centered-cubic matrix. Whelan reported that in the alloys he investigated, the structure was a M_7C_3 acicular carbide eutectic in a FCC

matrix in lower carbon alloys (1.6 to 2.0 wt.% C) and a M_7C_3/FCC phase eutectic with primary idiomorphic M_7C_3 carbides in hypereutectic alloys (greater than 2.6 wt% carbon).

While most alloys rely on a dispersion of carbides in a tough matrix for their wear resistance, there are new nickel-base alloys which rely on a dispersion of intermetallic compounds in a tough matrix for wear resistance. One of these is the Tribaloy alloy number T-700 which contains 32 wt.% Mo, 8 wt.% Cr, and 2 wt.% Si. The microstructure is 60% Laves phase intermetallic by volume fraction, in a matrix of nickel [67].

1.4.2 Cobalt-Base Alloys

A good deal of research has been done with cobalt-base wear-resistant alloys. These alloys demonstrate superior abrasive and adhesive wear resistance compared to other hardfacing alloys [68]. They are commonly considered standards of wear resistance in wear testing. With the exception of a few alloys containing intermetallic compounds, the cobalt-base alloys consist of some distribution of discrete carbide particles in a tough cobalt-based face-centered-cubic matrix.

Cobalt-base alloys contain up to 60 wt.% cobalt as well as up to 30 wt.% chromium with 1 to 2½ wt.% carbon. Compositions of common cobalt-based alloys are shown in Figure 6. Other alloying elements commonly used in commercial cobalt-based alloys are iron, nickel, molybdenum, and tungsten. Modifications of the basic composition of Co-Cr-C-X have been done by several investigators [66,69,70] where additional alloying elements such as molybdenum, copper, nickel, and/or titanium were added in efforts to increase the abrasive wear resistance or the adhesive wear resistance.

Drapier [69] in particular reported that additions of 8 to 10 wt.% Mo and 18 wt.% nickel increased the abrasive wear resistance.

The cobalt-base alloy microstructure consists of carbides, typically chromium carbides, in a matrix of cobalt solid solution. The carbides are usually found in interdendritic regions as idiomorphic particles or as a eutectic. Silence [66] showed carbides forming in the interdendritic regions of both sand-cast alloys and those deposited by a welding process. Silence observed that carbides in alloys containing a moderate amount of tungsten (4 to 5 wt.%) were of type M_7C_3 while carbides of type M_6C were seen in alloys containing 10 wt.% tungsten. He also observed that abrasive wear resistance increased as particle size increased and that as the matrix wore the carbides stood proud. Smaller carbides were pulled out of the matrix sooner than larger carbides which required several passes of abrasive particles before being pulled out. Other investigators have observed the same phenomenon. Shetty et al [71] observed this behavior in an investigation using single and multiple scratch tests with diamond and quartz abraders on powder metallurgy cobalt-base alloys. Powder metallurgy techniques were used to produce a range of carbide sizes in the same overall alloy composition. Shetty et al observed coarse slip activity at the edge of the wear groove in the matrix as well as cracking of groove edges in subsequent passes in multi-pass tests. They reported evidence of carbide plastic deformation and cutting with the shaped diamond abrader making deeper scratches in the carbide. They also observed that carbides protruded from the surface as wear of the matrix increased.

Protrusion of carbides from the surface and the possible mechanism where they are bodily removed from the matrix serves to point out an

important factor; namely the nature of the carbide/matrix interface. The stronger this interface, the less the importance of the role of carbide removal will play in abrasive wear of carbide-matrix structure.

The preceding has focused on carbide-strengthened cobalt-based hardfacing alloys. Cobalt-base alloys strengthened by intermetallic compounds have also been produced, typically using a Laves phase intermetallic as the hard phase. Most of these alloys are based on the Co-Cr-Mo-Si system and are known by the name "Tribaloys". Table 6 shows the compositions of the 'Tribaloy' alloys. These alloys still contain a large amount of chromium, 8 to 18 wt.%. The wear properties of the intermetallic alloys are at least as good as the carbide containing alloys [72]. Halstead and Rawlings [73] have published research on Co-Cr-Mo-Si alloys containing 40 to 60% by volume fraction of CoMoSi and Co_3Mo_2Si Laves phase intermetallics. The alloys had a eutectic of the Laves phase plus a cobalt solid-solution matrix. In comparison with carbide-containing alloys, the 'Tribaloys' are similar only in that they have a microstructure of a hard phase in a cobalt matrix. Halstead and Rawlings found that both hexagonal-close-packed and face-centered-cubic allotrophs of cobalt exist in the matrix of the Co-Cr-Mo-Si alloys. With heat treatment they found that the amount of the cobalt face-centered-cubic allotroph decreased with a corresponding increase in the hexagonal-close-packed allotroph. The chromium in these alloys does not contribute to the formation of the Laves phase but is partitioned one-third to sites in the intermetallic compound and two-thirds to the matrix. The partitioning is beneficial since it enables chromium to impart some measure of corrosion resistance to the entire structure.

1.4.3 Iron-Base Alloys

Of the various types of hardfacing alloys, the iron-base alloys are most widely used and include a broad selection of compositions, all used for abrasive wear resistance. These include simple heat treated plain carbon steels, low alloy steels, chromium steels, semi- and fully austenitic manganese steels and high-chromium white irons. Except for manganese steels, all rely on carbides to raise alloy bulk hardness. Figure 11 depicts the relative relationship between hardness, abrasion resistance, and type of iron-base alloy.

The iron-base alloys can be divided into three groups: the carbon and low-alloy steels, stainless steels and high chromium steels; the manganese steels with over 8 wt%. Mn, semi- or fully austenitic; and white cast irons. The last is the most abrasion resistance of the iron-base alloys while the steels are the least although the steels can be heat treated to the same level of hardness.

Hardness is only one parameter for evaluating the ironbase alloys. Since iron can possess two allotrophs at room temperature: austenite, a tough face-centered-cubic crystal structure and ferrite, a body-centered--cubic crystal structure; the toughness of the alloys can be varied to suit the abrasive environment by changes in microstructure. Diesburg and Borik [63] in an extensive investigation of iron-base hardfacing alloys, categorized their laboratory test results with the type of abrasive environment. They found that in high-stress or high-load abrasion, gouging, and impact environments austenitic manganese steels afforded the best combination of toughness and abrasion resistance while white irons

provided excellent abrasion resistance in low-stress or low-load abrasive environments. Microstructures of iron-base alloys range from fully austenitic, ferritic, or martensitic with or without the presence of carbides to mixtures of these phases. The three basic groups of iron-base alloys will be discussed in the following sections.

1.4.3.1 Low-Alloy and Chromium Steels

Steels contain less than two wt.% carbon. Plain carbon steels and low-alloy steels are used infrequently in abrasive environments compared with other iron-base alloys. Many abrasion resistant steels contain 3 to 12 wt.% chromium and 0.3 to 0.5 wt.% carbon. Other alloying elements commonly used are vanadium and molybdenum. Typical compositions are shown in Table 7.

Besides increasing hardenability and the amount of stable retained austenite [74,75], high chromium contents increase corrosion resistance of abrasion resistant chromium steels [74,76]. El-Koussy et al [76] used a laboratory ball mill as a wear test with various combinations of sand and water and sand and sea water as the milling media. They reported that the difference in percent weight loss between milling with sand/water media and sand/sea water media was almost the same as the difference in the corrosion weight loss between water and sea water. They emphasized the importance of chemical composition and microstructure when considering an abrasive environment which is corrosive as well as abrasive.

Salesky and Thomas [75] while extensively examining the microstructural aspects of a series of chromium steels, tested abrasion resistance of their alloys in a dry pin-on-disc environment. They did not therefore

look at any aspect of the abrasive/corrosive wear with the chromium steels. They did however report that the martensite/retained austenite microstructures of the chromium steels were found to be the most desirable of the microstructures developed in steels for abrasive wear resistance.

1.4.3.2 Manganese Steels

Before the advent of high-chromium white cast irons, austenitic manganese steels were the principle iron-based alloy used in abrasive environments. Even today, with cobalt and nickel-base alloys, austenitic manganese steels are still used where the abrasive environment includes a large amount of high impact or gouging.

Austenitic manganese steels are produced in two common grades; a lean grade with 6 to 8 wt.% manganese [77-79] and a standard grade with 12 to 20 wt.% manganese. Carbon contents range from 1 to 1½ wt.%. Other alloying elements such as molybdenum (½ to 2¼ wt.%), nickel (2 to 4 wt.%), and vanadium (½ to 1 wt.%) are also added to some of the the austenitic manganese steels. Table 8 shows compositions of common manganese steels.

The semi-austenitic and fully austenitic microstructure of manganese steels is unequaled in its ability to work-harden. A 1 to 1.4 wt.% carbon, 10 to 14 wt.% manganese (standard grade) steel can be work-hardened from 220 HV to over 900HV [79]! In a railway application, such as the frogs in switches, surface hardnesses of 530 to 580 HV (495-535 Brinell) are commonly reached. Because of low hardness in the un-work hardened state, manganese steels exhibit low wear resistance in low-load abrasive environments, such as handling loose sand. They do, however, possess moderately good wear resistance in environments where impact or gouging occurs in the abrasive

wear process, such as in the handling, crushing, and milling of rock. The impact and gouging of the wear process workhardens the initially soft surface to a hardness where wear resistance is greater. In many applications where gouging and impact are part of the abrasive environment, manganese steels offer a range of toughness and wear resistance. There is a trade-off between toughness and wear resistance as shown in Table 9. As hard constituents in the microstructure increase, toughness decreases while wear resistance increases. Heat-treated steels and white irons can offer better wear resistance than the manganese steels, but not equivalent wear resistances at the same toughness levels (Figure 12).

1.4.3.3 High-Chromium White Cast Irons

Chromium rich white cast irons are perhaps today's most prevalent hardfacing alloys, Table 10. The bulk of applications are in grinding and milling [88-95] of such diverse materials as sugar cane and wood pulp as well as rock and ore. White cast irons are also among the most intensely studied of the hardfacing alloys. The microstructure of white irons contains eutectic carbides in a matrix of austenite or martensite. An austenitic matrix is preferred in many applications because of its work--hardening characteristics. Since carbides formed in white irons are solidification products, variations in carbide volume fraction and carbide size and shape (eutectic and/or primary) can be made by changing the alloy composition and when cast, the cooling rate.

De Mello et al [80] investigated the solidification properties of two series of white irons containing molybdenum and found a close correlation between the Cr/C ratio and the type of chromium carbide

formed. In high chromium alloys M_6C type carbides are formed while in low chromium alloys Mo_2C carbides are formed. While De Mello et al investigated solidification of white irons at typical 'production' cooling rates, Rivlin [81] in his review of Fe-Cr-C alloys published only equilibrium data as well as a detailed reaction sequence for the Fe-Cr-C ternary system solidification and solid state reactions.

Most research on high-chromium white cast irons has been on wear resistance versus heat treatment and/or composition and on applications of white irons in industry. The consensus of these studies was that as carbide volume fraction increased, wear resistance increased [63,66,82-85]. Studies have also been made relating wear resistance to fracture toughness [28,29,87], and have shown that as carbide volume fraction increased, hardness increased and both static and dynamic fracture toughness decreased. Fracture toughness was dependent on the resistance of the matrix to crack propagation in low to medium carbide volume fraction alloys [28,29,87] and on the nature of the carbide/matrix interface in high carbide volume fraction alloys. Particular importance was placed on the ability of the matrix to retard crack extension from carbide to carbide.

Table 5

Composition of Nickel-based Hardfacing Alloys (in wt.%).

	C	Cr	Fe	Mn	Mo	Si	Other
Tribaloy T-700[a]	-	15	-	-	32	3	
XN-930-C[b]	2	30	3	0.5	9	1	
Deloro 45[c]	0.3	7.5	1.5	-	-	4	
Amdry 754[d]	0.45	10	5	-	-	3.25	
Amdry 769[e]	0.6	15	5	-	2.25	4.25	2.25Cu

[a][67] [b][65] [c][36] [d][96] [e][97]

Table 6

Composition of Cobalt-based Hardfacing Alloys (in wt.%).

	C	Cr	Mo	Si	W	Other
Tribaloy T-100[a]	-	-	35	10	-	
Tribaloy T-400[a]	-	8	28	2	-	
Tribaloy T-800[a]	-	17	28	3	-	
AWS RCoCr-A[b] (Alloy 6)	1.1	28	-	1	4	
AWS RCoCr-B (Alloy 12)	1.4	29	-	1	8	
AWS RCoCr-C[b] (Alloy 1)	2.5	30	-	1	12	
Alloy 21[b]	0.4	27	5	1	-	
Deloro A83[c]	5.5	25	-	-	-	7 Nb, 1.5Ti, 6Fe
Amdry 850[d]	0.7	19	-	3.25	10	3.25 B, 2-5 Fe

[a][67] [b][62] [c][70] [d][98]

Table 7

Chemical Composition of Chromium Steels (in wt.%).

	C	Si	Mn	Cr	Mo	Ni
Cr-Steel[a]	0.80	0.32	0.7	1.04		0.40
Cr-Steel[a]	0.50	0.80	0.71	1.40		0.43
Cr-Steel[a]	1.25	0.35	0.55	5.02		0.71
Cr-Steel[a]	1.94	0.22	0.47	12.8		---
3CR12[b]	0.03	---	0.81	16.4		1.80
ARSteel[b]	0.30	---	0.50	0.72		0.20
Experimental Cr-Steel[c]	0.30	0.01	1.86	2.94	0.52	0.03

[a][76] [b][74] [c][75]

Table 8

Composition Ranges of Manganese Steels (in wt.%).

Cast Lean Alloys

	C	Mn	Si	Cr	Ni	Mo	Other
6Mn-5Cr-1Mo	0.7	6.0	0.5	5.0	--	1.0	
6Mn-5Cr-1Mo	1.2	6.0	0.5	5.0	--	1.0	
9Mn-1Mo-¼Ti	1.3	8.5	0.5	--	--	1.0	0.25 Ti

Cast Rich Alloys

	C	Mn	Si	Cr	Ni	Mo	Other
12Mn	1.0	13.0	0.5	--	--	--	
12Mn	1.2	12.5	0.5	--	--	0.05	
12Mn-1Mo	0.7	12.0	0.5	--	--	1.0	
12Mn-1Mo	1.0	12.0	0.5	--	--	1.0	
12Mn-1Mo-¼Ti	1.2	12.5	0.5	--	--	1.0	0.25 Ti
13Mn	1.2	13.0	0.5	--	--	--	
14Mn	1.6	14.0	0.75	--	--	2.0	

Table 9

Toughness and Wear Properties of Manganese Steels [78].

	wt.% C	Wt. Loss[a] (gm)	Toughness CVN (ft.lb)
Heat-Treated			
Std. Mn	1.05-1.20	0.082	50-100
12Mn-1Mo	1.10-1.40	0.077	10-50
6Mn-1Mo	1.20-1.35	0.058	10-40
Cast			
12Mn-1Mo	0.85-1.0	0.087	20-60
8Mn-1Mo	0.70-0.85	0.064	10-40
6-7Mn-1Mo	0.80-0.95	0.054	4-10

[a]Pin type abrasive wear test

Table 10

Composition of Some White Irons (in wt.%) [63].

	C	Cr	Mn	Mo	Ni	Si	Other
2Cr-4Ni	3.19	2.20	0.64	-	3.94	0.57	
15Cr-3Mo	3.60	15.0	0.80	2.6	-	0.4	
17Cr-1½Mo-1Cu	2.87	17.1	0.75	1.60	-	0.44	1.06 Cu
18Cr-1Cu	3.01	18.1	0.78	0.04	-	0.59	0.99 Cu
18Cr-2Mo-1Cu	3.11	27.0	0.8	-	-	0.4	

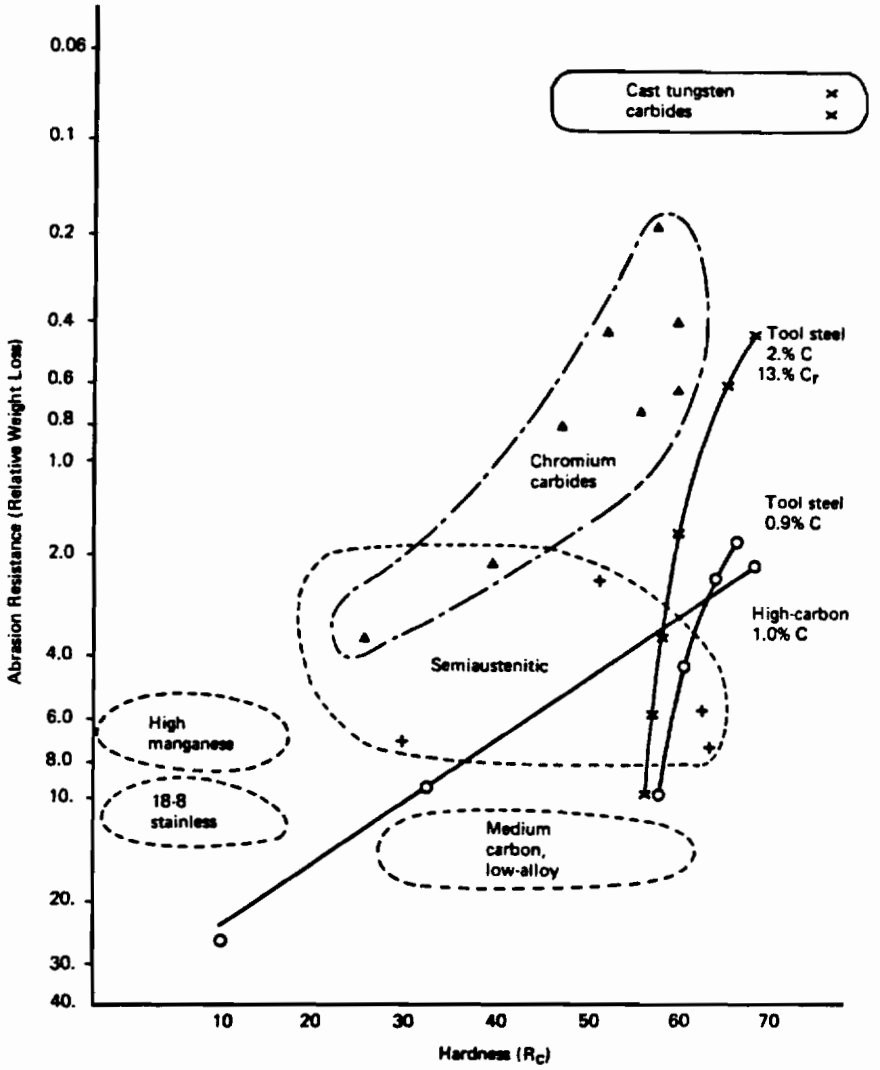

Figure 11. Hardness and abrasion resistance of common hardfacing alloys [40].

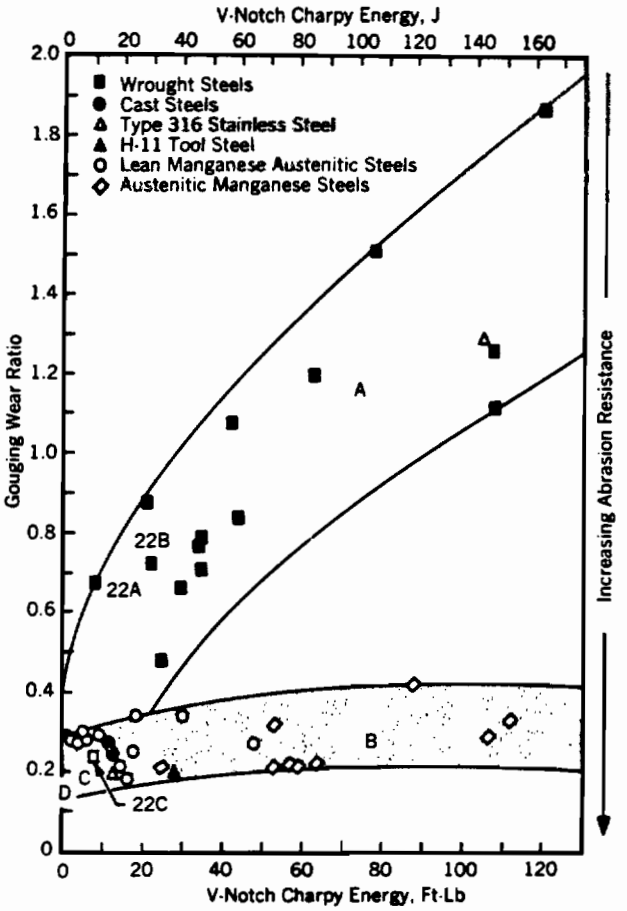

Area A = wrought and cast low-alloy steels.
Area B = austenitic manganese steels.
Area C = variety of heat-treated steels.
Area D = high-chromium irons.

Figure 12. Relationship between resistance to gouging wear and impact toughness [63].

1.5 Hardfacing Alloy Design

Perhaps one of the earliest attempts to rationalize the relationship between microstructure and abrasive wear resistance was the work done by Khruschov in the late 1950's [20]. Khruschov proposed a rule which stated that the overall wear resistance of a composite material is the sum of the wear resistances of each constituent phase multiplied by that phase's volume fraction. This rule, with exceptions to it, has been the focus of much refinement and debate, yet it has not really been disproved. A survey of commercial hardfacing alloys that are used in abrasive environments reveals that many alloys have microstructures of hard particles distributed in a softer, tougher matrix.

Some classes of material, like high-strength-low-alloy (HSLA) steels and manganese steels, do not appear to follow Khruschov's rule at a first glance, however on closer examination of the microstructure and at actions during the abrasive wear process, they do in fact follow Khruschov's rule. On a microscopic level HSLA steels are composed of carbides in a matrix of ferrite or retained austenite, the latter being of importance in high load abrasive environments [24,99]. Manganese steels on the other hand have a small volume fraction or carbides and the matrix, austenite, is relatively soft. However, upon work hardening in an abrasive environment, the surface hardness increases and overall wear resistance increases, which is in accordance with Khruschov's rule.

Work hardening is an important feature in successful abrasion resistance alloys [25,27,100,101]. The matrix phase in commercial hardfacing alloys typically has a face-centered-cubic crystal structure

based on cobalt, nickel, or an iron solid solution. Work hardening of the surface contributes to overall surface hardness along with the harder second phase in the microstructure. The hard phase in most alloys is a carbide, though some alloys using intermetallic compounds have been developed.

1.5.1 Alloys with Carbides

Carbides in commercial hardfacing alloys are typically based on chromium, and to a lesser extent tungsten carbides and titanium carbides are used. Carbides range in hardness from 1600 to 2900 Hardness Knoop. Some of the common abrasives used in abrasive wear testing range in hardness from about 5500 Knoop for diamond to 1860-2200 Knoop for alpha-Al_2O_3 to 1240-1400 Knoop for garnet [42]. Table 11 lists hardness for various carbides, matrix structures, and abrasives.

For optimum wear resistance, the carbide should be harder than the abrasive particle in order to resist cutting by the abrasive [33,34,71] and must be tough enough to resist fracture by loads imposed by the abrasive particle passing over it. The carbide particle must also be large enough such that it is not removed from the surface in a micromachined chip and sufficient adherence to the matrix that it is not pulled out. Most hardfacing alloys contain carbides which form on solidification as idiomorphic particles or as one constituent in a eutectic, can usually be represented as $(Cr,Metal)_xC_y$ carbides. Titanium and tungsten carbides are not usually used as solidification products. They are added to a hardfacing weld deposit as a carbide powder in the weld filler material.

An important factor in the design of a hardfacing alloy containing carbides is how the carbide is formed. Carbides formed by solid state phase transformations are not as large as those formed as solidification products. This is true in nickel- and cobalt-based alloys as well as iron-based alloys.

1.5.2 Alloys with Intermetallic Compounds

Intermetallic compounds are phases in which true metals and transition metals occur in simple ratios, like stoichiometric chemical compounds, and form characteristic crystal structures. Stoichiometries vary with the compound. Some intermetallics such as the Laves phases adhere closely to a B_2A stoichiometry while other intermetallic compounds such as the sigma phases range in stoichiometry from B_4A to BA_4.

Because of limited ductility and relatively high hardness, intermetallic compounds are most useful when present in an alloy as a fine precipitate in a ductile matrix. In fact, the predominant use of intermetallic compounds in structural alloys is as a strengthening precipitate. Intermetallic compounds play a major role in strengthening alloys such as Ni_3Al in the nickel-based superalloys and as $CuAl_2$ in aluminum alloys.

As an alternative to alloys containing carbides as a hard phase, several commercial hardfacing alloys and a few experimental alloys have been developed that use intermetallic compounds as the hard phase. The commercial alloys are all related and are marketed as the "Tribaloys". Both nickel-base and cobalt-base alloys, all Tribaloys, have been produced [73]. These alloys contain 8½ to 17½ wt.% chromium, 2½ to 3½ wt.% silicon,

and 28½ wt.% molybdenum with a cobalt or nickel base. The intermetallic compound in the Tribaloys has been identified as a ternary Laves phase (C-14, $MgZn_2$ type structure) with a stoichiometric limits of CoMoSi and Co_3Mo2Si.

Similar alloys based on iron have been investigated by Ohriner and Whelan [102,103]. These alloys contained 15 to 20 wt.% chromium, 10 wt.% nickel, 2 to 5 wt.% silicon, 20 to 30 wt.% molybdenum, and up to 4 wt.% niobium. The intermetallic compound was identified simply as a Laves phase and resided in an austenite matrix. The wear resistance of this iron-base alloy containing intermetallic compounds was equivalent to carbide-containing Stellite Alloy No.6.

The thrust of the present investigation is similar to that of Ohriner and Whelan: to develop an abrasion resistant hardfacing alloy which contained intermetallic compounds as the hard phase. An added constraint though was that the new alloy contain little or no chromium and/or cobalt. The Tribaloys and the alloys investigated by Ohriner and Whelan both contain up to 17½ wt.% chromium.

From other investigator's work on the relationships between microstructure and abrasive wear resistance it was apparent that a hardfacing alloy should have a microstructure containing more than 50% by volume fraction of a hard phase in a tough work-hardenable matrix. Based on commercial hardfacing alloys, this implies carbides in a face-centered--cubic matrix [99,101]. The present investigation, instead, was concerned with alloys containing at least 50% volume fraction of intermetallic compounds in a face-centered-cubic matrix. Consequently the alloy microstructure being sought would be one of at least 50% volume fraction

of intermetallic compounds in a face-centered-cubic matrix.

1.5.3 Alloy Design

As evidenced in commercial hardfacing alloys, at least three major constituent elements are used and some contain up to five elements. Thermodynamics limits the number of co-existing phases in any system as depicted by the Gibbs phase rule. The Gibbs phase rule states:

$$F + P = C + 2$$

where F = degrees of freedom

P = number of phases

C = number of components.

The degrees of freedom are composition, temperature, and pressure. Pressure is generally fixed in most metallurgical processes, leaving only temperature and composition free to change. Thus three phases can co-exist at equilibrium in a binary system, but with no degrees of freedom (i.e. a eutectic/eutectoid or peritectic/peritectoid point). Otherwise the maximum number of co-existing phases is only two, leaving one degree of freedom, the temperature or the composition. In a ternary system three phases can co-exist with one degree of freedom. As the number of elements in a system increases, the complexity of the phase relationships, both solidification and solid state, grows proportionately. For this reason, system selection began with ternary element systems.

Ternary systems were examined that exhibited the following:

1) An intermetallic plus face-centered-cubic phase two phase region that was present at high temperatures.

2) Intermetallic compounds that were stable at room

temperature and existed over a range of composition.

3) Elements in the system that were not considered strategic metals.

Since most applications for weld hardfacings are iron-based materials, candidate systems were limited to Fe-X-Y ternary systems and further limited to iron-rich regions of those systems. A survey of researched ternary phase diagrams, revealed that both Fe-Mo-Ni and Fe-Mn-Mo systems met these criteria.

Koster first investigated the Fe-Mo-Ni system in 1934 [104]. His work was later updated by Das, Beck, and Rideout [105], by Van Loo in 1980 [106], and reviewed by Raynor and Rivlin [107]. Most experimental work on the Fe-Mo-Ni system has been at isotherms from 1000 to 1200°C. Hoster [108], however, used calorimetric studies to extend isotherms of the system down to 700°C. Raynor and Rivlin in their review included several isopleths that extended down to 800°C. A 1200°C isotherm of the Fe-Mo-Ni system, shown in Figure 13,shows a large two phase region of an (Fe,Ni) austenite plus an intermetallic compound. Das, Beck, and Rideout identified the intermetallic as $(Fe,Ni)_3Mo_2$ [105]. In their review, Raynor and Rivlin identified the same intermetallic compound as $(Fe,Ni)_7Mo_6$ [107] citing recent x-ray diffraction studies. Hoster [108] analyzed the intermetallic compound and found a composition between that reported by Das et al and that by Raynor and Rivlin. Hoster also showed that the two phase region of the (Fe,Ni) austenite plus intermetallic extended down to at least 700°C (Figures 14 and 15).

Other intermetallic compounds which occur in the system are a Fe_2Mo Laves phase with a C-19 $MgZn_2$ type crystal structure and a ternary 'P'

phase with an orthorhombic crystal structure. The 'P' phase has been reported to be isomorphic with a similar phase in the Cr-Mo-Ni system [109]. Van Loo et al [106] in diffusion couple studies identified the 'P' phase as $Fe_{11}Ni_{36}Mo_{33}$. Van Loo et al also described a range of compositions, $Fe_{72}Ni_{14}Mo_{14}$ to $Fe_{82}Ni_5Mo_{13}$ in which an austenite to martensite transformation took place.

Das and Beck investigated a portion of the Fe-Mn-Mo system in 1960 [110]. They showed a large two phase region of an 'R' phase intermetallic compound plus an (Fe,Mn) austenite at high temperature (Figure 16). Raynor and Rivlin in a later review of the Fe-Mn-Mo system [107] pointed out inconsistencies in the isotherm produced by Das and Beck, including a question on the existence of a ternary 'R' phase at lower temperatures. They suggested that perhaps the 'R' phase was instead an iron-molybdenum intermetallic containing a solid solution of manganese. Raynor and Rivlin proposed a hypothetical reaction sequence for the Fe-Mn-Mo system which has an Fe_7Mo_6 intermetallic stable at temperatures below 1000°C. In the Fe-Mn-Mo isotherm by Das and Beck, the Fe_7Mo_6 phase only covers a small phase field. The Fe_7Mo_6 intermetallic may be the same as in the Fe-Mo-Ni system where nickel substitutes on iron lattice sites. Finally Raynor and Rivlin pointed out the lack of investigation into the Fe-Mn-Mo system as well as commenting on the difficulties of preparing and heat treating alloys containing large amounts of manganese and molybdenum.

The criteria for selecting an alloy system was best met by the Fe-Mo-Ni system. It possesses a large two phase field of a $(Fe,Ni)_7Mo_6$ intermetallic compound plus an (Fe,Ni) austenite and the field extends from above 1200°C to below 700°C. Also, none of the components in the Fe-Mo-Ni system is

considered strategically important in the U.S.

Silicon was considered as a fourth alloying element to the Fe-Mo-Ni system, since it stabilizes intermetallic compounds, particularly the sigma phases [111-115,118]. Fe-Mo-Si [116] and Fe-Ni-Si [117] systems exhibit a large number of intermetallic compounds which contain iron. Virkar and Raman [117] evaluated a large number of binary and ternary phases containing iron, molybdenum, nickel, and silicon occurring over a wide range of compositions and crystal structures. Raynor and Rivlin in reviews of the Fe-Mo-Si system [118] and the Fe-Ni-Si system showed detailed phase diagrams and reaction sequences for both systems which exhibit several ternary intermetallic compounds such as Fe_2MoSi_2, FeMoSi, and $FeMo_3Si$.

Carbon was also considered as an addition to the experimental alloys to investigate carbide formation and to simulate the dilution of carbon from base metal into the weld deposit. Most iron alloys which are hardfaced contain low to moderate amounts of carbon.

In this investigation the approach was first to synthesize arc-melted alloys in the iron-rich region of the Fe-Mo-Ni system. Using the 1200°C isotherm by Das and Beck as a map, a systematic survey of compositions in the intermetallic plus austenite region was made. Silicon and carbon additions were also added to a base composition which fell in the two-phase intermetallic plus austenite region of the Fe-Mo-Ni phase diagram. Based on hardness and microstructure of arc-melted alloys, compositions were selected for weld hardfacing deposits. Weld hardfacing deposits were made using the submerged-arc welding process and alloyed metal powders that were added to the weld. Weld hardfacing specimens were evaluated for hardness, microstructure and wear resistance.

Table 11

Hardness of Carbides and Abrasives [42,100].

Material	Knoop Hardness	
Diamond	5500-6950	
Chromium Boride	2900	
Boron Carbide	2580-2900	
Silicon Carbide	2250-2760	
Titanium Carbide	2350-2620	
Tungsten Carbide	1570-2140	
W_2C	1450	
WC	2100	
Chromium Carbide	1672-1960	
$Cr_{23}C_6$	1000	
Cr_7C_3	1600	
Iron Carbide	940	
Fe_3C	~1000	(840 Brinell)
Tantalum Carbide	1800-2400	
Al_2O_3	1860-2200, 1900	
Garnet	1240-2200, 670-750	
Quartz	750	
Olivene	650-750	
Magnetite/Hematite	370-600	
Fluorite	180	
Calcite	115	
Gypsum	70	
Martensite	390-640	
Austenite	412	
Ferrite	154	

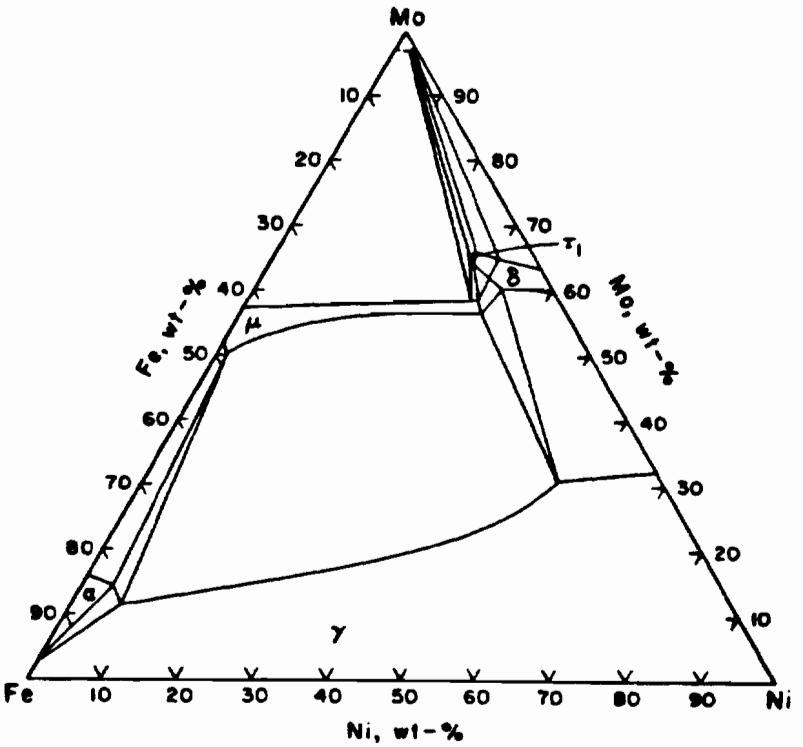

Figure 13. Fe-Mo-Ni phase diagram, hypothetical 1200°C isotherm [107].

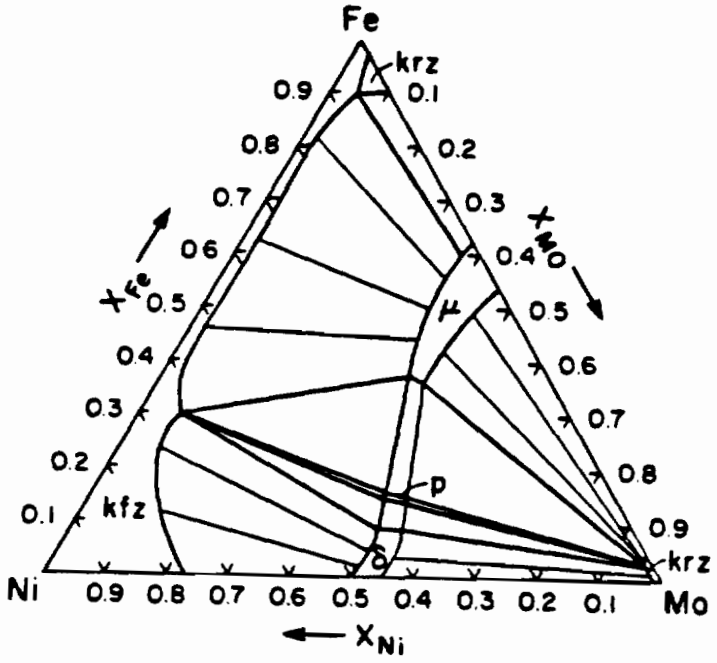

Figure 14. Fe-Mo-Ni phase diagram, 1100°C isotherm showing tie lines, in at.% [108].

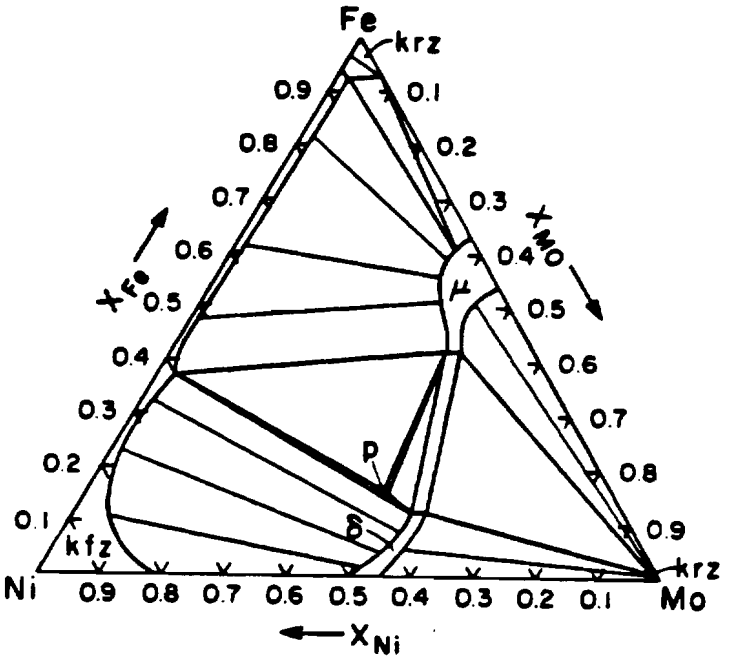

Figure 15. Fe-Mo-Ni phase diagram, 700°C isotherm showing tie lines, in at.% [108].

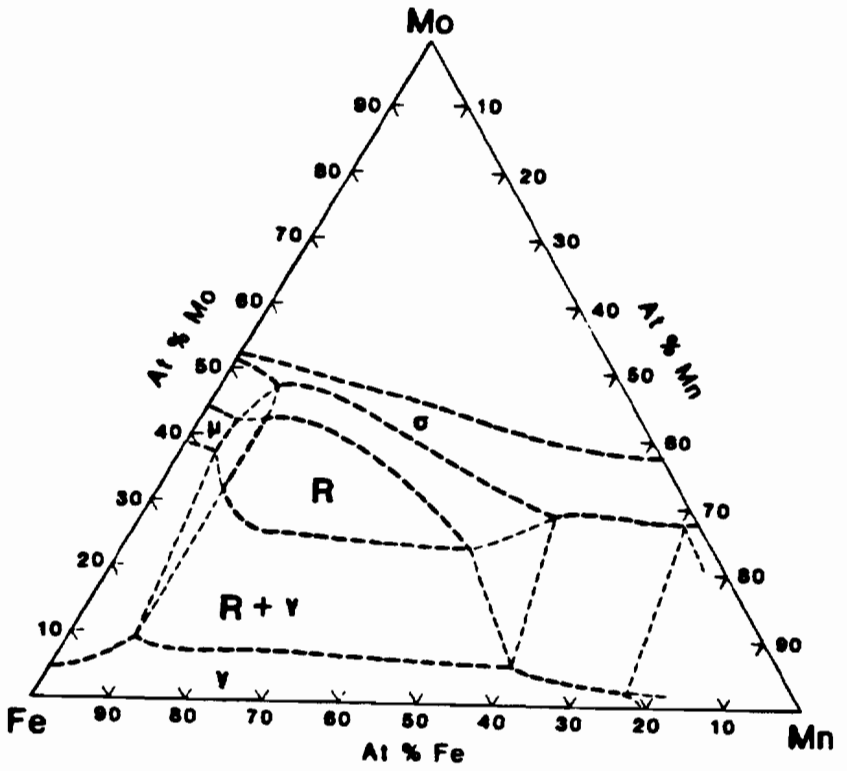

Figure 16. Fe-Mn-Mo phase diagram, 1200°C isotherm, in at.% [110].

2.0 Experimental Procedure

2.1 General Procedures

2.1.1 Metallography

Specimens for metallography were sectioned from weldments or buttons using either an abrasive cutoff saw or a bandsaw equipped with a carbide--edged blade. Two cutoff saws were used, one with a 26 inch wheel was used to cut large sections through weldments. The other, with a 12 inch wheel, was used for subsequent sectioning.

Specimens were polished using standard methods and materials down to 0.3μ alumina. All specimens were etched with a ferric chloride-hydrochloric acid-methanol etchant (10 gm $FeCl_3$-6 H_2O, 25 ml HCl, 200 ml Methanol). The etchant was used by alternately swabbing and washing the specimen with the etchant for up to 15 seconds.

The polished and etched specimens were examined on a Zeiss Ultraphot optical microscope at magnifications up to 2000X. Electron microscopy was done on a JEOL JSM-35 scanning electron microscope equipped with an ORTEC energy dispersive x-ray analyzer. Magnifications up to 5000X were used at an accelerating voltage of 25kV.

2.1.2 Hardness Testing

Alloy hardness was measured on a Rockwell hardness tester using the 'C' scale. Microhardness testing was done a Leitz microhardness tester using a 500 gm load and a Knoop diamond. Additional hardness testing was done using a diamond pyramid diamond at low loads.

2.1.3 Chemical Analysis

Chemical analysis of the alloys was performed at the U.S. Bureau of Mines using wet chemical methods. For wet chemical analysis, filings were taken from the various alloy buttons. Quantitative emission spectroscopy was used only intermittantly due to the high alloy content in the alloys and the lack of suitable calibration standards for spectroscopy. Both analyses were performed by personel at the U.S. Bureau of Mines, Albany, Oregon.

Energy dispersive x-ray (EDX) analysis was used to determine individual phase compositions in sample microstructures. Bulk analysis' by EDX were made of samples previously analyzed by wet chemical means. The results of both were plotted to obtain a calibration curve for the individual elements. The calibration curves are shown in figures 17, 18, 19, and 20 for iron, molybdenum, nickel, and silicon respectively.

2.1.4 X-Ray Diffraction Analysis

X-ray diffraction analysis was performed at the U.S. Bureau of Mines. An automatic powder diffractometer was used and the powder consisted of filings from button specimens or weld metal specimens.

2.1.5 Powder Preparation

Alloyed powders for welding and arc-melting were made from sintered compacts of pressed and sintered elemental powders. A flow chart of the alloy powder preparation process is shown in Figure 21. The elemental powders used were all -150 mesh or smaller in size. The purity of the individual powders were: iron, 99.9%; nickel, 99.9%; molybdenum, 99.995%;

silicon, 99.999%; and carbon, 99.99%. The powders were weighed and then blended. Moderate volumes of powder were blended for four to six hours in six inch diameter ball mills containing 4 to 6 1½ inch carbide balls. Small amounts of powder (less than 300 grams) were mixed in small bottles containing several clean carbide balls. These were rotated horizontally in a fixture for 4 to 6 hours and were manually turned through their vertical axis every half hour.

After blending the powders were pressed in a Mannesmann-Meer 29 ton powder compaction press (Figure 22). Several sets of dies were used over the course of the investigation; a 3/4 inch diameter cylinder, a 1¼ inch diameter cylinder, and a ½ by 2½ inch rectangle. Compactability of the powders varied with their alloy content. Powders high in nickel and iron pressed to a dense compact with high green strength. Powders with even small levels of carbon and/or silicon possessed little green strength after compaction. Due to this behavior, an additional processing step was performed on the non-compactable powders. Compactable powders were pressed immediately after blending.

Powders with a potential of low green strength after pressing were made compactable by adding a paraffin wax binder to the blended powder. To distribute wax in the powder, a solution of heptane saturated with dissolved wax was added to the powder at a rate 2.5-4 wt.% wax. After mixing the heptane was evaporated in a vacuum drying oven at 160°F for several hours. After deheptaning, the waxed powder was milled to an acceptable size and then pressed. The compacts of waxed powders had high green strength. The wax was removed by heating the powder to 650 to 850°F for four to six hours in a vacuum. A water-cooled trap captured

the wax vapors before they reached the vacuum pump. After dewaxing, the compacts were immediately moved to a high temperature vacuum furnace for sintering.

Sintering was performed under a vacuum at 1000 to 1200°C for one to two hours. Two furnaces were used. For large numbers of compacts a molybdenum element furnace was used and for smaller numbers of compacts, a graphite element furnace was used.

2.1.6 Arc-melting

The compacts were arc-melted directly after sintering when buttons were being made. The alloys were melted in a water-cooled copper skull to produce a 'button' ¼ to ½ inches thick and about 3 inches in diameter (Figure 23). A ½ inch diameter tungsten electrode was used for melting in a melting atmosphere of 50% Ar/50% He at a pressure of twenty inches absolute. Four paralleled constant current welding power supplies provided up to of 3000 amps for melting. Typically melting was done at 700-1200 amps. Before melting the chamber was evacuated to better than $1X10^{-4}$ torr and back filled with an inert gas several times. Once the compacts were melted, the molten pool was stirred with the arc to homogenize the melt.

2.2 Welding

2.2.1 Equipment Description

The welding equipment consisted of a Linde CVI-1200 constant voltage power supply with a wire feeder mounted on a ten foot long track beam (Figure 24). For automatic powder additions a TAPCO metal powder feeder and a TAPCO oscillating torch were used. Welds were made on A36 and A588

mild steel plate one to two inches thick which was clamped against a set of water-cooled copper shoes (Figure 25). These were used to maintain the weld interpass temperature below 350°F.

2.2.2 Welding Parameter Selection

Two sizes of welding wire were used in the investigation, 3/32 and 5/32 inch. Both were used with added metal powders. Parameters for optimum penetration and weld metal dilution were found by systematically varying the following welding parameters; voltage, current, travel speed, drag angle, amount of powder addition. Final welding parameters were selected to produce a good weld with minimum weld metal dilution by the base metal. For the selection of parameters using a powder addition, two types of metal powders were used: a mild steel powder and a high-carbon high-chromium powder.

2.2.3 Welding with Powder Additions

Powders for welding were produced by the previously described powder preparation method. Instead of arc-melting after sintering, sintered compacts were crushed in a laboratory-size jaw crusher. The final powder size after crushing was a Tyler number 5 mesh.

Powders were deposited on the plate by two methods. Fine uniform powders were deposited using the automatic powder feeder. Powders which were neither fine nor uniform were deposited manually, along the weld bead line, before welding. In the latter a weighed amount of powder was deposited along a given length of weld line. Welding parameters were

adjusted depending on the amount of powder added and the size of wire used.

2.2.4 Weld Sectioning and Examination

The welds were sectioned by first bandsawing the weld area from the mild steel plate. The resulting piece was again bandsawed to an appropriate thickness. Welds which included specimens for pin-on-drum testing were cut to a 1¼ inches thick and those for dry-sand-rubber-wheel testing were cut to a ½ inch thickness. Welds from which Charpy-sized specimens were made were cut to a ½ inch thickness as well. Except for Charpy-sized specimens, the welds were then sectioned on a 26-in. abrasive cut-off saw. Because of the heat evolved when making a cut with this saw, specimens were cut well over size and ground to final dimensions.

After sectioning, the weld pads were analyzed by chemical analysis, x-ray diffraction analysis, microscopy, hardness testing, pin-on-drum abrasive wear testing, and dry-sand-rubber-wheel abrasive wear testing. Not all welds underwent all tests.

2.3 Wear Testing

Two wear tests were used to evaluate the weld metals. One was a high stress abrasive wear test, the pin-on-drum test; and the other a low stress abrasive wear test, the dry-sand-rubber-wheel (DSRW) test. Both tests were performed at the U.S. Bureau of Mines in Albany, Oregon.

2.3.1 Pin-on-drum Abrasive Wear Testing

In the pin-on-drum test, the specimen pin is moved across a rotating 0.5 meter diameter drum covered with abrasive paper. The pin is under a 66.7 Newton dead weight load and is rotated at 17 rpm. The drum rotates at 1.7 rpm. The pin advances ½ inch per drum revolution, continually encountering fresh abrasive. A schematic drawing is shown in Figure 26.

The pin-on-drum test uses a ¼ inch diameter pin which runs along a drum covered with abrasive paper. The pin was machined by electrical discharge from the weld in the shape of a cylinder. It was then ground to a 0.250 ± 0.001 inch diameter. The test procedure began with running-in the pin on the drum for several revolutions. The sample and a reference pin were then ultrasonically cleaned and weighed. The sample pin was then run for a number of revolutions to produce a reasonable amount of wear, about 40 mg. For soft materials this was 6 drum revolutions (a 9.6 meter path length) and for hard materials, 12 revolutions (a 19.2 meter path length). The wear tracks of the sample pins were ½ inch apart. After the sample pin had been run the reference pin was run for the same number of revolutions in the unused abrasive track between worn abrasive tracks of the sample. After the test both sample pin and reference pin were cleaned ultrasonically and weighed. ASTM A514 steel with a 269 HB hardness was used as a reference material. The reference material was used to correct for the variations in the abrasivity of the cloth from lot to lot and from within each piece of cloth. A corrected mass loss for the sample was calculated using the equation:

$$W = \frac{W_x(S)}{1.6(S_x)}$$

Where W is the corrected mass loss of the sample pin per meter of path length; W_x is measured mass loss of the sample pin for x number of revolutions; S is the long term average mass loss of the reference specimen per revolution; and S_x is the measured mass loss of the reference pin for x number of revolutions.

Since the density of the alloy materials differed among themselves and from the reference material, corrected mass losses where converted to a volume loss after sample density was measured. This was done by two methods. In the first a section of the pin was cut off and the end ground square. It was then measured, a volume calculated, and then weighed. With the volume and weight known, a density was calculated. The second method utilized a picnometer at the U.S. Bureau of Mines.

Some pins were also examined using the scanning electron microscope after testing. The wear of the end of the pins was examined as-tested and after etching the worn end with a ferric chloride-hydrochloric acid--methanol etchant.

2.3.2 Dry-Sand-Rubber-Wheel Testing

The dry-sand-rubber-wheel (DSRW) abrasive wear test has been an ASTM standard (G65-81) since 1981. The test simulates the behavior of materials under low-stress abrasive wear conditions in the laboratory. The ASTM machine consists of a 22.86 cm diameter rubber rimmed steel wheel which is rotated at 200 rpm, a level arm arrangement which holds a specimen against the rubber rim, a sand feeding apparatus which feeds sand at a rate of 250-350 g/min, and a counter to measure the number of wheel revolutions (Figure 27). The sand is a 50-70 mesh silica sand and the rubber must have

a hardness of 60±2 durometer A. The test specimen is rectangular with nominal dimensions of ½x1x3 inches, with a ground surface on the 1x3 inch face.

Testing was performed at the U.S. Bureau of Mines. Their test equipment differed from the ASTM standard by including a tachometer and a strain gauge. The latter was placed in a direct line between specimen contact at the wheel and the level arm assembly pivot point. This permitted measurement of frictional force on the specimen. The tachometer and a variable speed drive made it possible to maintain a constant surface velocity on the wheel as the wheel diameter decreased due to either wear or surface dressing.

Specimens for dry-sand-rubber-wheel testing were cut from weld pads using a 26 inch abrasive cutoff saw. The specimens were cut wider than necessary and the excess ground away. This helped minimize any heat--affected-zone due to the abrasive saw. All the weld pads were multipass and the specimens were removed transverse to the weld. The DSRW blanks were then ground on all four sides to the nominal dimensions of ½x1x3 inches.

To test a specimen, it was first cleaned, dried, and weighed. The specimen was then mounted in the specimen holder and the lever arm loaded. The sand flow and motor were started, and then the arm released to allow the specimen to contact the wheel. The revolution counter starts when the specimen contacts the wheel. After the desired number of revolutions the test is stopped, the specimen removed, cleaned and reweighed. With the density of the specimen known, the weight loss is converted into a volume loss and reported as such. The test was repeated one or more times. To

meet ASTM specifications the coefficient of variation must not exceed seven percent.

ASTM recognizes standard procedures which use sliding distance and specimen load as the parameters. Table 12 lists the variations of the test procedure. Tests on experimental hardfacings and on several commercial hardfacings followed procedure B; with a 130N load and 2000 revolutions.

2.5 Heat-treatment

Specimens from two weld chemistries were heat-treated at temperatures from 300 to 1100°C in a box furnace for times of 1 to 100 hours. After heat-treatment specimens were sectioned, polished and etched for metallography, and then examined using both optical and scanning electron microscopes.

2.6 Melting point studies

Using the weld metal chemistry as a basis, alloys were mixed for melting point studies using powder preparation techniques. The melting point furnace is a Pirani type furnace [127] which uses resistance heating to heat a specimen between two watercooled electrodes. Heating is done in a vacuum or up to six atmospheres of inert gas. Since the specimen is held by the electrodes, a container is unnecessary, which reduces contamination problems. The specimen is in the shape of a bar or a rod with a small black body hole drilled in its midpoint. Figure 28 shows the specimen geometry used.

The furnace (Figure 29) is constructed with a stationary electrode

and one movable electrode. The latter pivots and a lever arm with a weight external to the furnace chamber provides the clamping force on the specimen. Power is supplied by a 50 kVA stepdown transformer with a secondary tap setting of 12 volts. A full wave silicon-controlled rectifier control circuit feeds the primary of the power transformer. A variable gain commercial magnetic amplifier type trigger unit (by Norbatrol) feeds the trigger circuit of the SCR's. A motor driven autotransformer, the output fed through a full-wave rectifier, supplies the DC current to the Norbatrol. Operator control of the of the motor yields power application rates that can be varied between 20 and 15000 watts per second.

Specimens were made from pressed and sintered powders. The wax/dewax procedure described previously was used to help fabricate the specimens. Alloy powders were pressed into the shape of a bar 0.45 by 0.45 by 3.0 inches. These dimensions changed slightly after sintering. Sintering was performed at 900°C under vacuum in a molybdenum element furnace. After sintering the bars were cut to a length of 1¼ to 1½ inches. The center of the bar was relieved to reduce the cross-sectional area and promote heating (Figure 30) and a blackbody hole drilled in the side of the specimen.

The specimen was inserted between the clamping electrodes after filing loose material from the ends to promote better electrical contact. The furnace chamber was evacuated and purged with inert gas several times before final evacuation. The specimen was then heated to incandecense under vacuum and held for a short period of time. This helped remove contaminants from the specimen. A micro-optical pyrometer was focussed on the blackbody hole and the power raised. If the approximate melting point was known, the temperature was raised to within 50° of the melting point. At that point

the power was raised in small increments.

Due to the steep temperature gradient between the specimen surface and the interior, molten liquid first appears in the bottom of the black body hole, allowing the observer sufficient time to adjust the pyrometer and measure the temperature. The run is finished when either the black body hole fills with liquid or the specimen collapses. Before this occurs slight power increases do not increase specimen temperature, but rather affect only the amount of liquid present.

After being analyzed in the melting point furnace specimens were arc-melted and then sectioned for metallography.

2.8 Oxidation Resistance Testing

Specimens from the weld metal alloys were tested at the U.S. Bureau of Mines for resistance to oxidation in a cyclic oxidation test. Samples were placed in a box furnace after cleaning and weighing. They were then removed at regular intervals for reweighing. An increase in weight was an indication of oxide growth. At the end of the test samples were mounted, polished, and etched such that the oxide layer could be examined in an electron microscope. Energy dispersive x-ray analysis was performed at the U.S. Bureau of Mines on the oxide layers.

Table 12

ASTM Dry-Sand-Rubber-Wheel Test Parameters.

	Force N(lb)	Revolutions	Linear Path Length
	N(lb)		m(ft)
Procedure A	130 (30)	6000	4309 (14138)
Procedure B	130 (30)	2000	1436 (4711)
Procedure C	130 (30)	100	71.8 (236)
Procedure D	45 (10.1)	6000	4309 (14138)

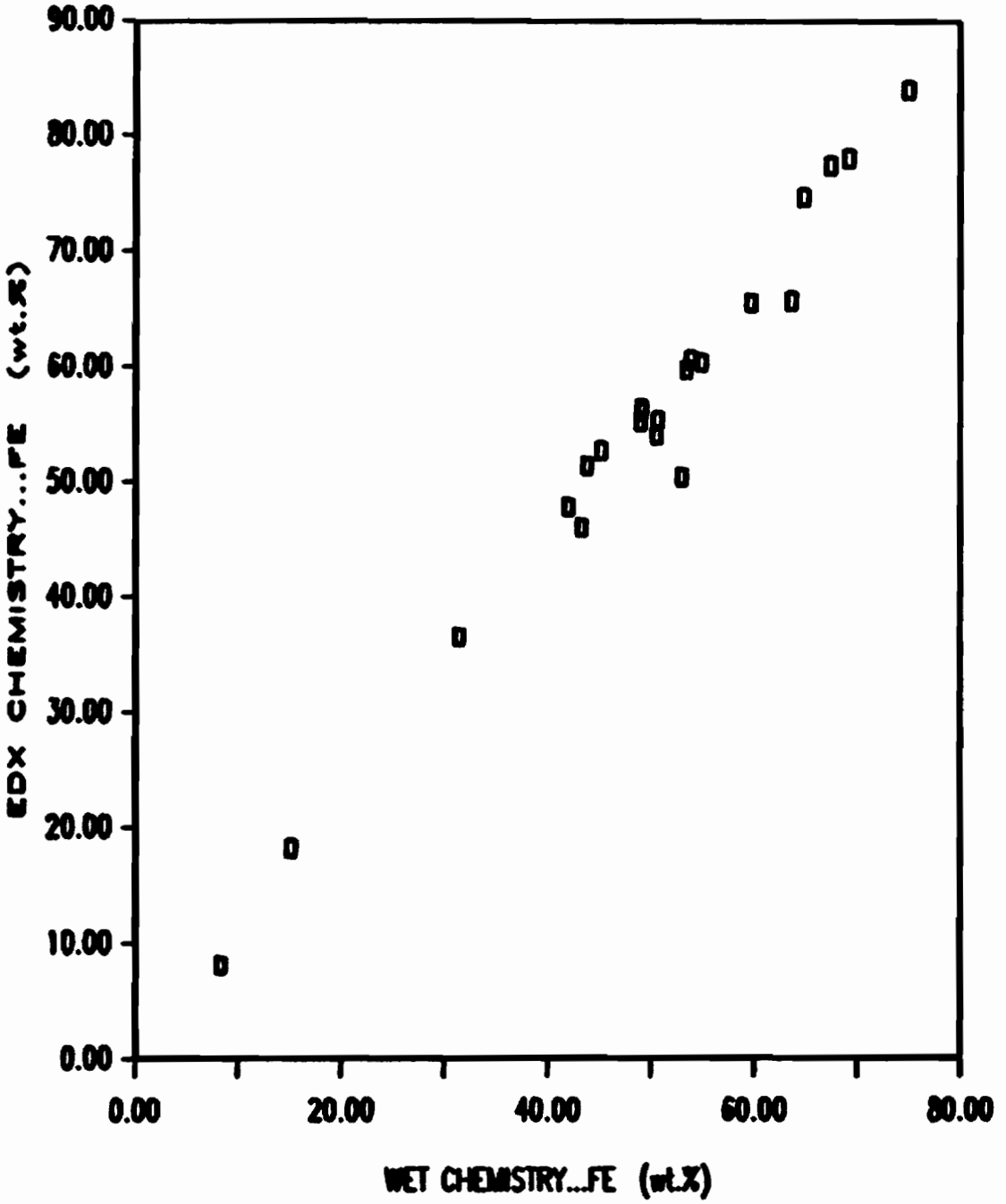

Figure 17. EDX calibration curve for iron.

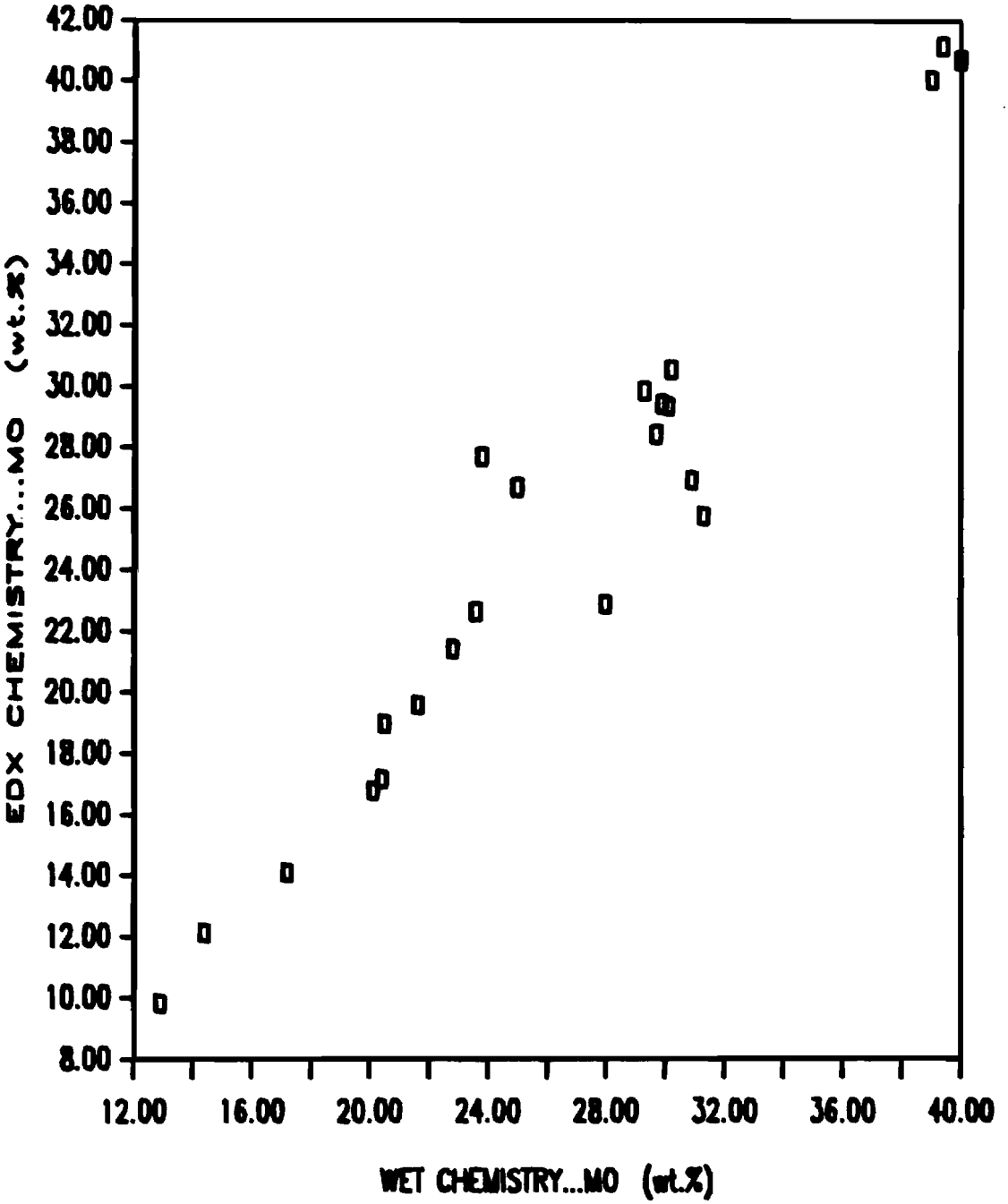

Figure 18. EDX calibration curve for molybdenum.

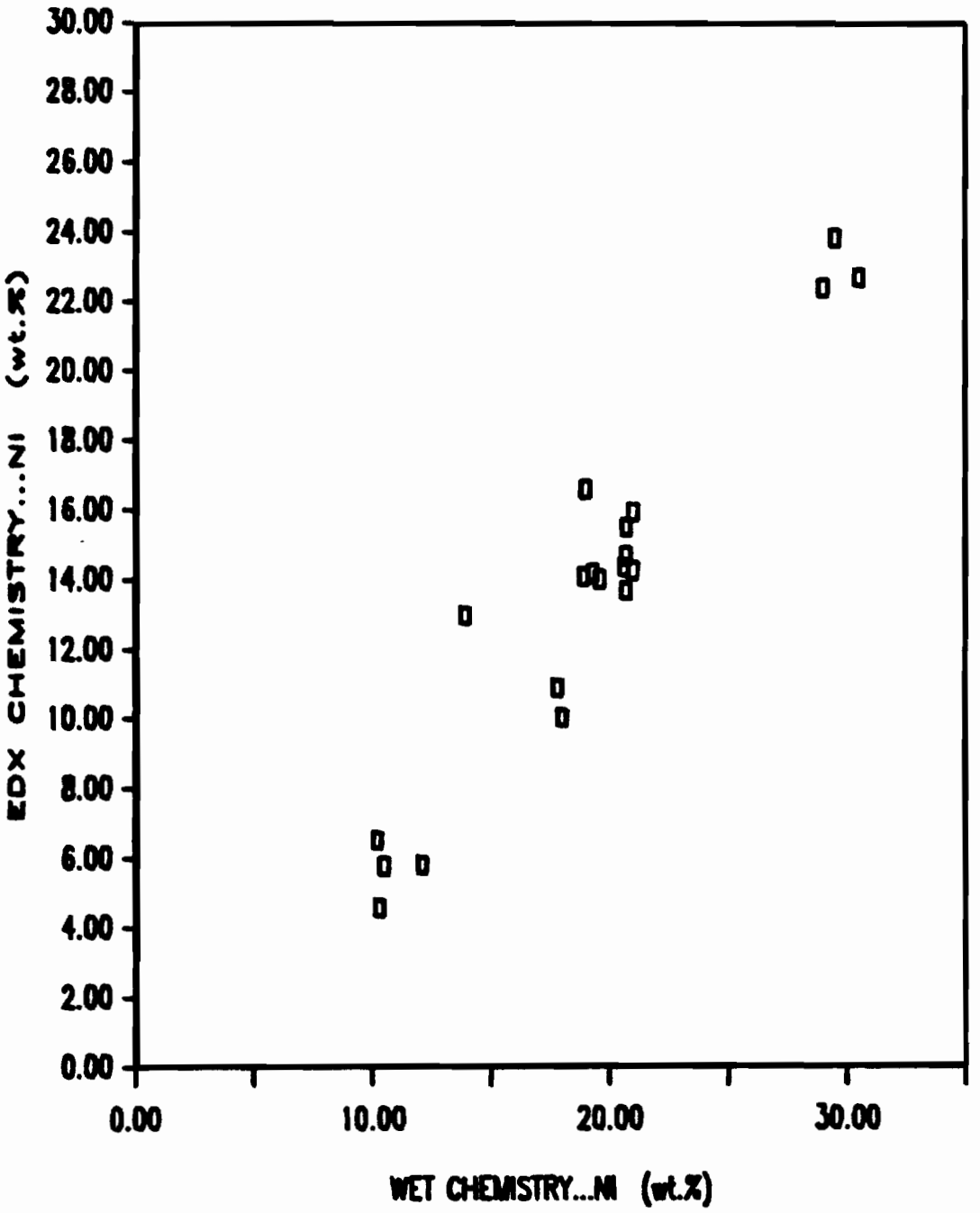

Figure 19. EDX calibration curve for nickel.

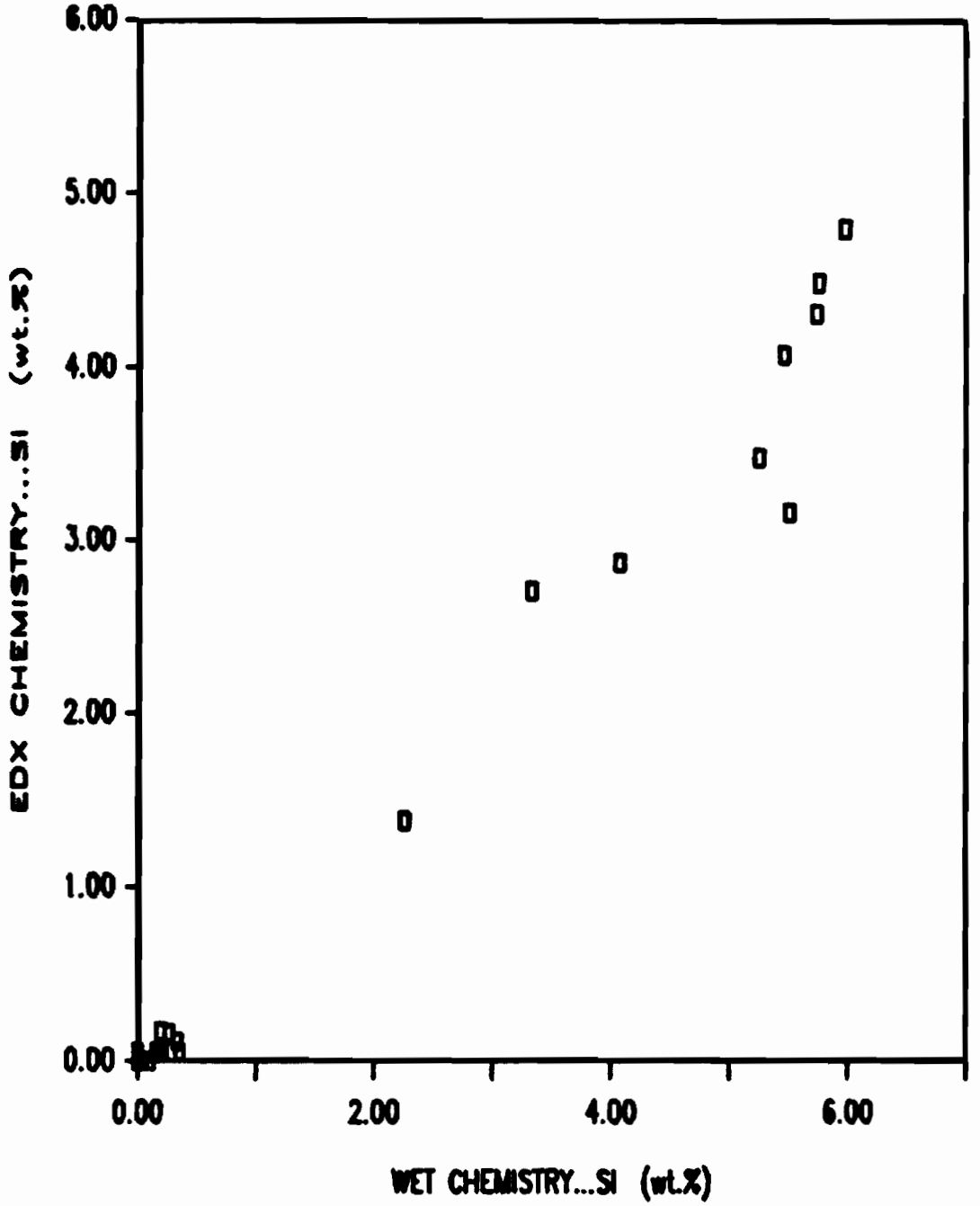

Figure 20. EDX calibration curve for silicon.

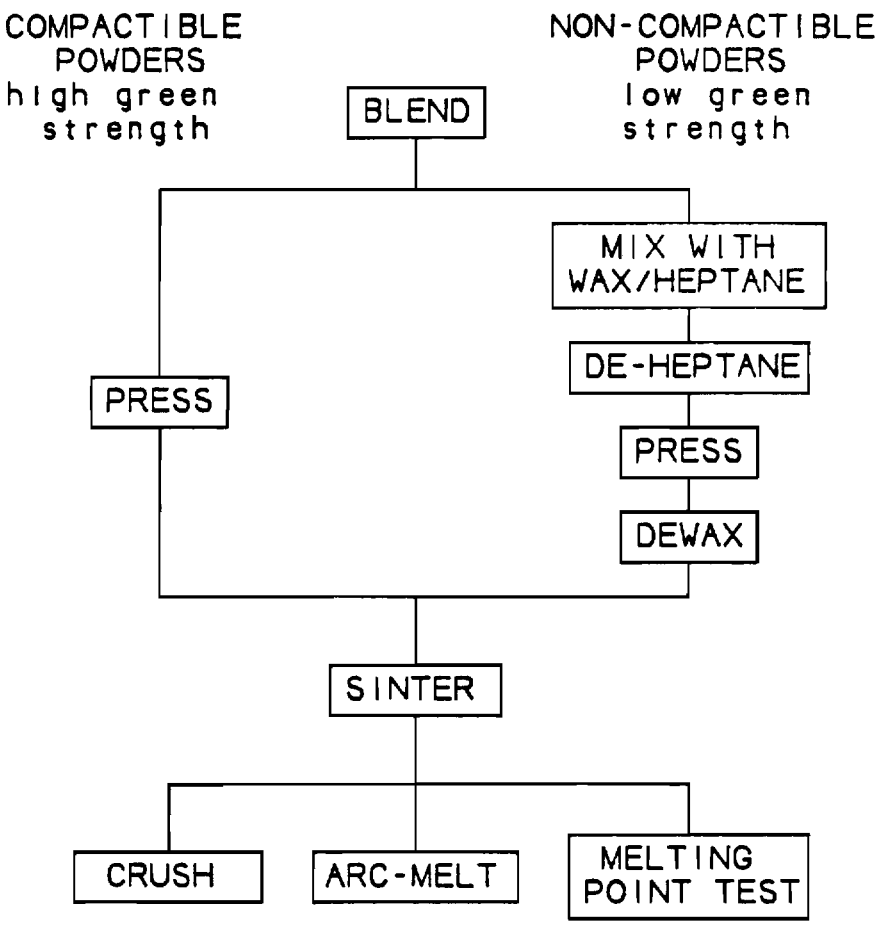

Figure 21. Flow chart of the powder preparation process.

Figure 22. Powder compaction press.

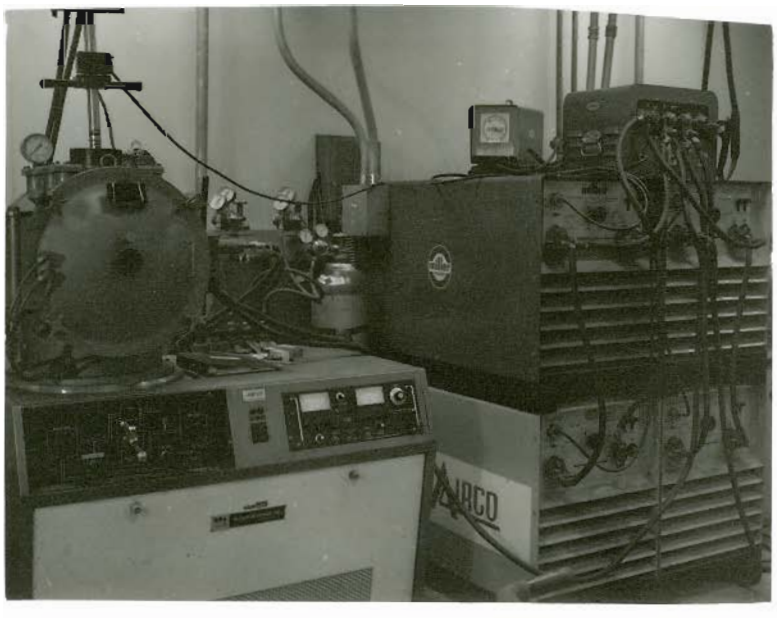

Figure 23. Arc-melting furnace.

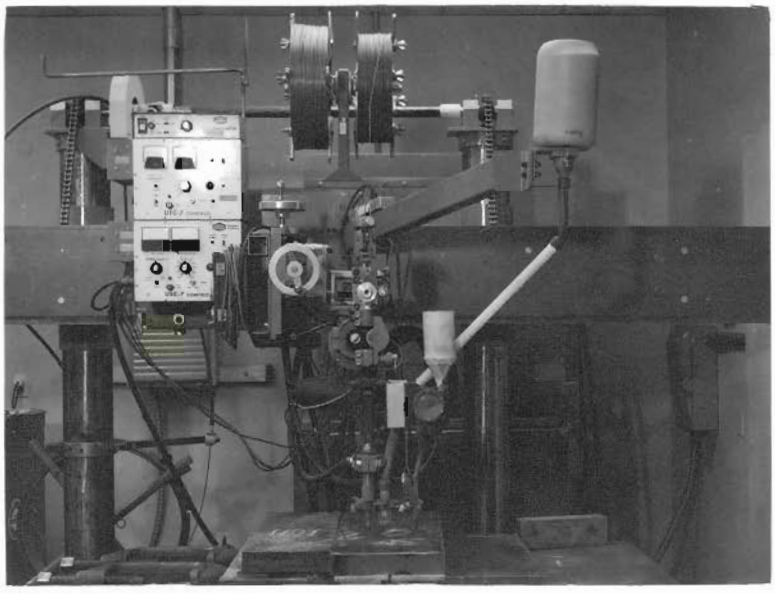

Figure 24. Submerged arc welding equipment set-up.

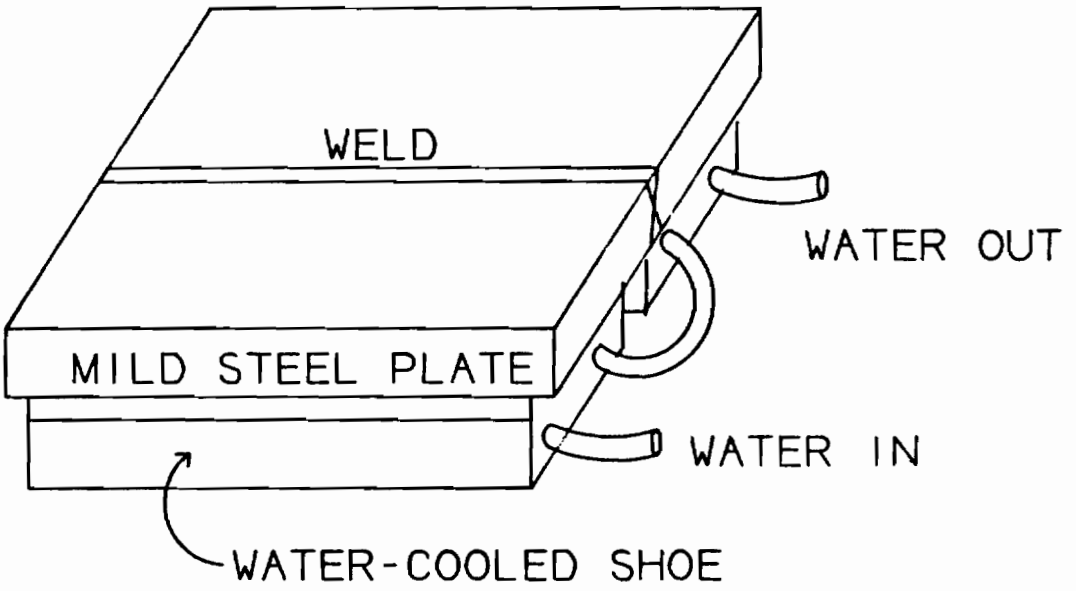

Figure 25. Plate set-up for welding.

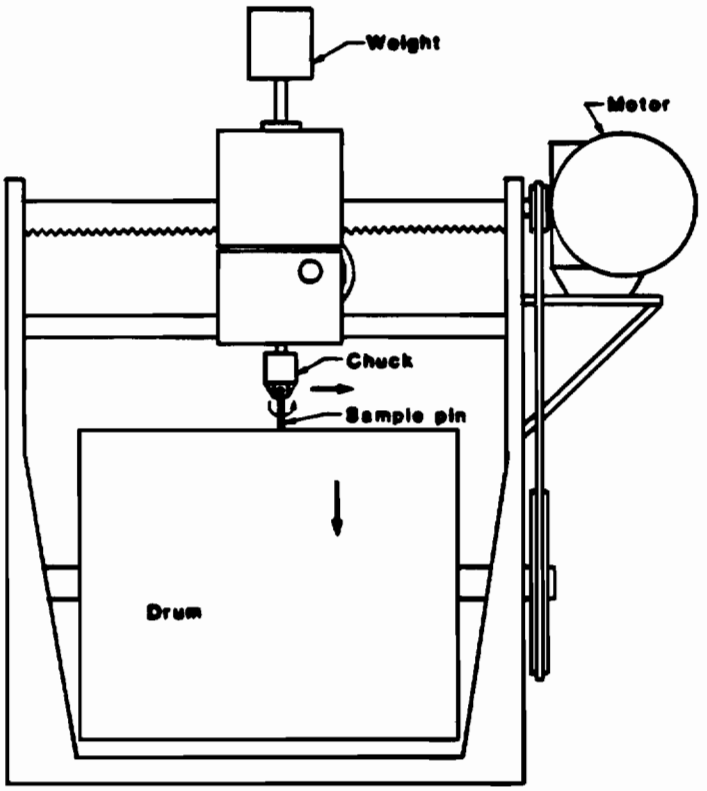

Figure 26. Diagram of pin-on-drum test.

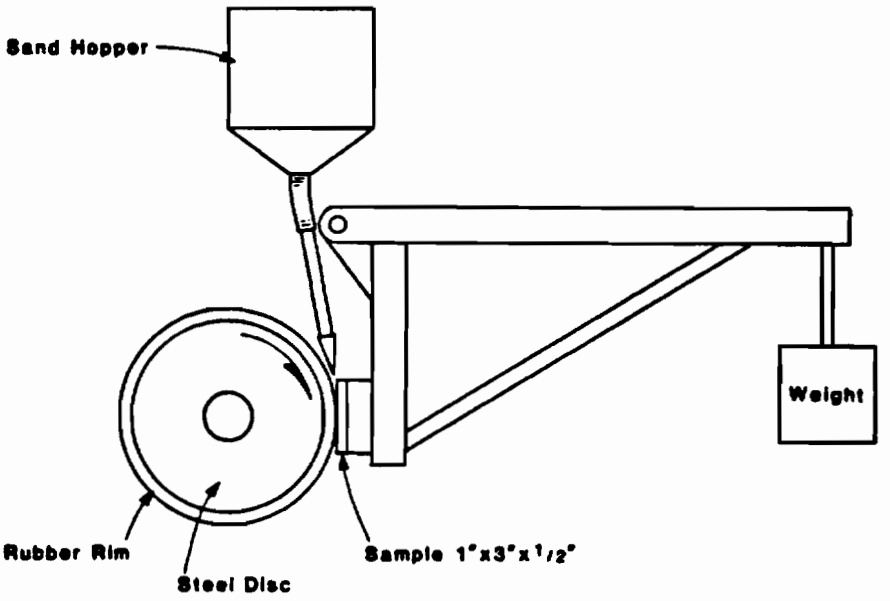

Figure 27. Diagram of the dry-sand-rubber-wheel test.

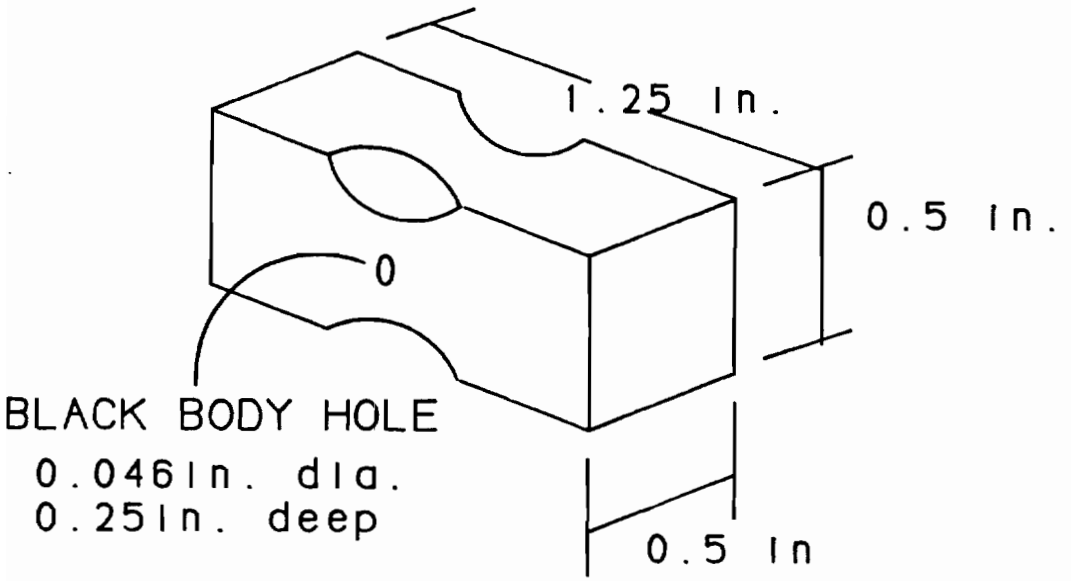

Figure 28. Melting point specimen geometry.

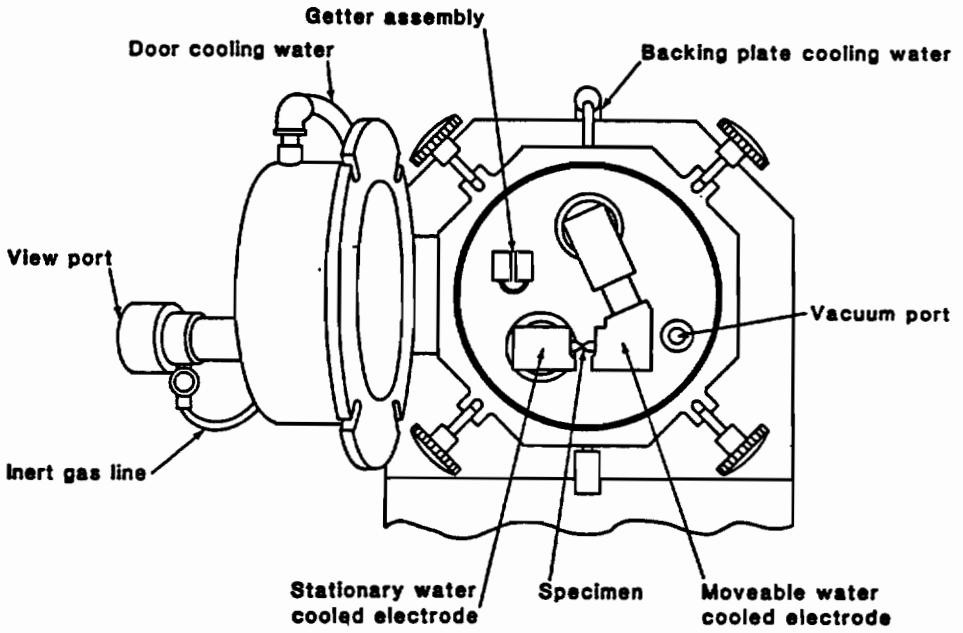

Figure 29. Melting point furnace.

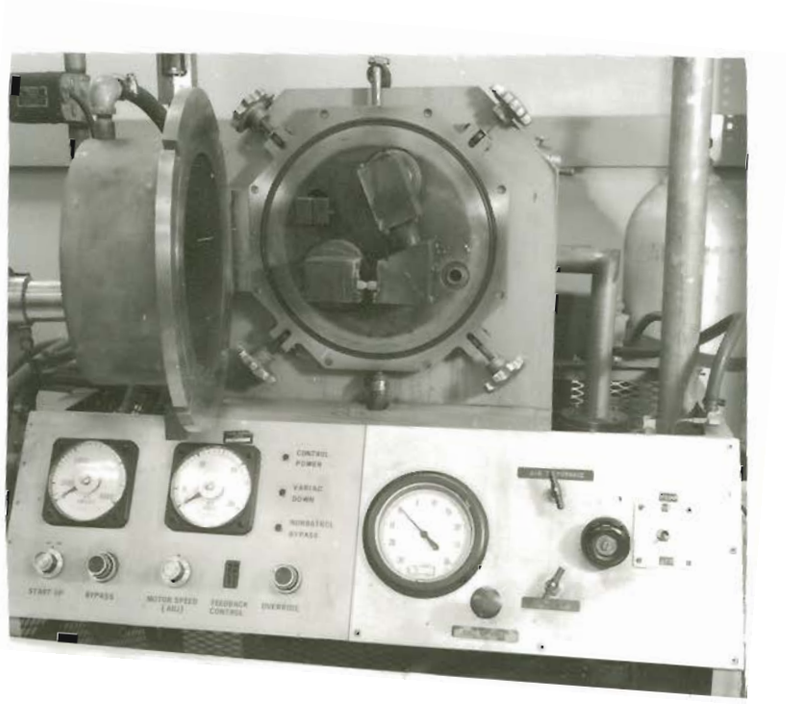

Figure 30. Photograph of melting point furnace.

3.0 Results

3.1 Arc-Melted Alloys

The arc-melted alloys produced in this investigation can be separated into four groups. The first group consisted of simple ternary alloys based on the Fe-Mo-Ni phase diagram. These constituted a traverse of the two phase austenite plus intermetallic region in the Fe-Mo-Ni phase diagram, as shown in Figure 31. The remaining three groups of alloys were based on a single composition, Fe-30Mo-20Ni. The second group of alloys contained additions of silicon, the third contained additions of carbon, and the fourth group of alloys contained additions of both silicon and carbon. Table 13 shows the Fe-Mo-Ni based alloys, their compositions, hardnesses, and a brief description of the microstructures. Several other alloys investigated initially were based on the Fe-Mn-Mo phase diagram.

The simple Fe-Mo-Ni ternary alloys could be divided further into three sections of constant molybdenum content, 20, 30, and 40 wt.% molybdenum; each containing alloys with 20, 30, and 40 wt.% nickel. Microstructures of the alloys are shown in Figure 32 (20 wt.% Mo), Figure 33 (30 wt.% Mo), and Figure 34 (40 wt.% Mo). The 20 wt.% Mo alloys containing 30 and 40 wt.% nickel had small amounts of an intermetallic compound in the interdendritic regions of an austenitic columnar dendritic structure. The Fe-20Mo-20Ni alloy may have transformed on cooling, forming a structure with a fine second phase dispersion. This alloy also lies on the boundary between two phase and three phase regions in the Fe-Mo-Ni phase diagram. The 30 wt.% molybdenum alloy microstructures consisted of an intermetallic compound plus austenite eutectic in inter-

dendritic regions of an austenitic dendrite solidification structure. The Fe-30Mo-20Ni alloy exhibited a microstructure of fine discontinuous lamella. This alloy was also of a composition near the boundary between the two phase and three phase regions in the Fe-Mo-Ni phase diagram. In the 40 wt.% molybdenum alloys, alloys containing 30 and 40 wt.% nickel had large idiomorphic particles of an intermetallic compound with an austenite matrix and an austenite plus intermetallic eutectic in the areas between the particles. Energy dispersive X-ray (EDX) analysis of the particles revealed a composition of 27Fe-57Mo-16Ni (in wt.%).

The second group of alloys were based on the composition of Fe-30Mo--20Ni and also contained ½, 1, or 5 wt.% silicon. Photomicrographs are shown in Figure 35. Silicon additions of up to 1 wt.% had little effect on a microstructure of austenite plus intermetallic eutectic in interdendritic regions of austenitic dendrites. At 5 wt.% silicon the microstructure became one of columnar dendrites of an intermetallic compound in an austenitic matrix. Composition of these dendrites by EDX analysis was 37Fe-9.5Ni-46Mo-7.5Si which corresponds to an intermetallic of the stoichiometry Fe_2Mo containing Si and considering nickel placement on iron sites of the crystal structure. The microhardness of this phase was measured as 670 to 780 DPH.

The third group of alloys were based on a composition of Fe-30Mo-20Ni and contained ¼, ½, and 1 wt.% carbon. Representative microstructures of these alloys are shown in Figure 36. The alloy containing ¼ wt.% carbon differed little from an alloy containing no carbon, having a structure of austenite plus intermetallic eutectic in the interdendritic regions of an austenitic dendrite solidification structure. The ½ wt.% carbon structure

differed in that the eutectic structure was much finer and of a slightly different morphology. At 1 wt.% carbon the structure was a 100% lamellar structure with an interlamellar spacing of 1.5μm. X-ray diffraction analysis of the 1 wt.% carbon alloy revealed the carbide formed in the lamella to be an eta carbide with an E9 type structure and a stoichiometry of $A_{1-x}B_xC$.

The fourth group of alloys was based on a composition of Fe-30Mo--20Ni-5Si with additions of ¼, ½, and 1 wt.% carbon. The microstructures are shown in Figure 37. The ¼ wt.% carbon alloy microstructure was much like the base Fe-30Mo-20Ni-5Si microstructure but with a slight change in dendrite morphology and presence of a small amount of a fine eutectic in interdendritic regions. The ½ wt.% carbon alloy contained a smaller volume fraction of the dendrites with an interdendritic eutectic and some large idiomorphic particles. With 1 wt.% carbon, the structure was very similar but with a greater number of the large particles. EDX analysis of the particles revealed their composition to be 19Fe-65Mo-10Ni-6Si. The microhardness of the particles was 1655 DPH which suggesting they are carbides. The hardness of the columnar dendrites, an intermetallic phase, was 1071-1177 DPH.

Several alloys based on the Fe-Mo-Mn system were made. The compositions were Fe-20Mo-20Mn, Fe-30Mo-20Mn, and Fe40Mo-20Mn. Microstructures of these alloys are shown in Figure 38. The Fe-20Mo-20Mn alloy had an acicular microstructure and the Fe-30Mo-20Mn alloy a microstructure with particles precipitated on parallel planes within the grain. The Fe-40Mo--20Mn alloy had a columnar dendritic solidification structure with an

unresolvable phase in interdendritic regions. These alloys were difficult to arc-melt because of the high manganese content.

Table 13

Composition (wt%) and Description of Arc-Melted Alloys.

Alloy	Analyzed Composition Fe	Mo	Ni	Si	C	Hardness	Microstructure
Fe-20Mo-20Ni	60.7	20.3	19.0	--	--	53.0 HRA	D plus IE
Fe-30Mo-20Ni	49.1	29.9	21.0	--	--	35.0 HRC	D plus IE
Fe-40Mo-20Ni	43.3	40.0	19.6	--	--	46.2 HRC	D plus IE
Fe-20Mo-30Ni	53.9	20.1	29.0	--	--	50.0 HRA	D plus I
Fe-30Mo-30Ni	42.0	29.3	30.5	--	--	25.2 HRC	D plus IE
Fe-40Mo-30Ni	31.4	39.4	29.5	--	--	44.4 HRC	D plus IE
Fe-30Mo-20Ni-1C	50.5	29.5	20.5	--	0.73	32.4 HRC	Lamellar E
Fe-30Mo-20Ni-1/2C	50.6	28.9	20.5	--	0.27	28.0 HRC	D plus IE
Fe-30Mo-20Ni-1/4C	50.0	29.6	20.4	--	0.07	29.0 HRC	D plus IE
Fe-30Mo-20Ni-1/2Si	49.1	30.1	20.7	0.05	--	34.8 HRC	D plus IE
Fe-30Mo-20Ni-1Si	49.0	30.2	20.6	0.17	--	37.8 HRC	D plus IE
Fe-30Mo-20Ni-5Si	43.8	30.9	21.0	4.31	--	38.0 HRC	CD, 2 phases
Fe-30Mo-20Ni-5Si-1/4C	45.4	31.5	20.6	5.1	0.11	35.6 HRC	CD + IE
Fe-30Mo-20Ni-5Si-1/2C	45.2	31.3	20.7	4.8	0.30	32.3 HRC	CD + IE + C
Fe-30Mo-20Ni-5Si-1C	55.9	20.9	22.5	4.3	0.87	29.8 HRC	CD + IE + C

C = Carbides
D = Dendritic
E = Eutectic
IE = Interdendritic Eutectic
CD = Columnar Dendritic
I = Interdendritic Phase

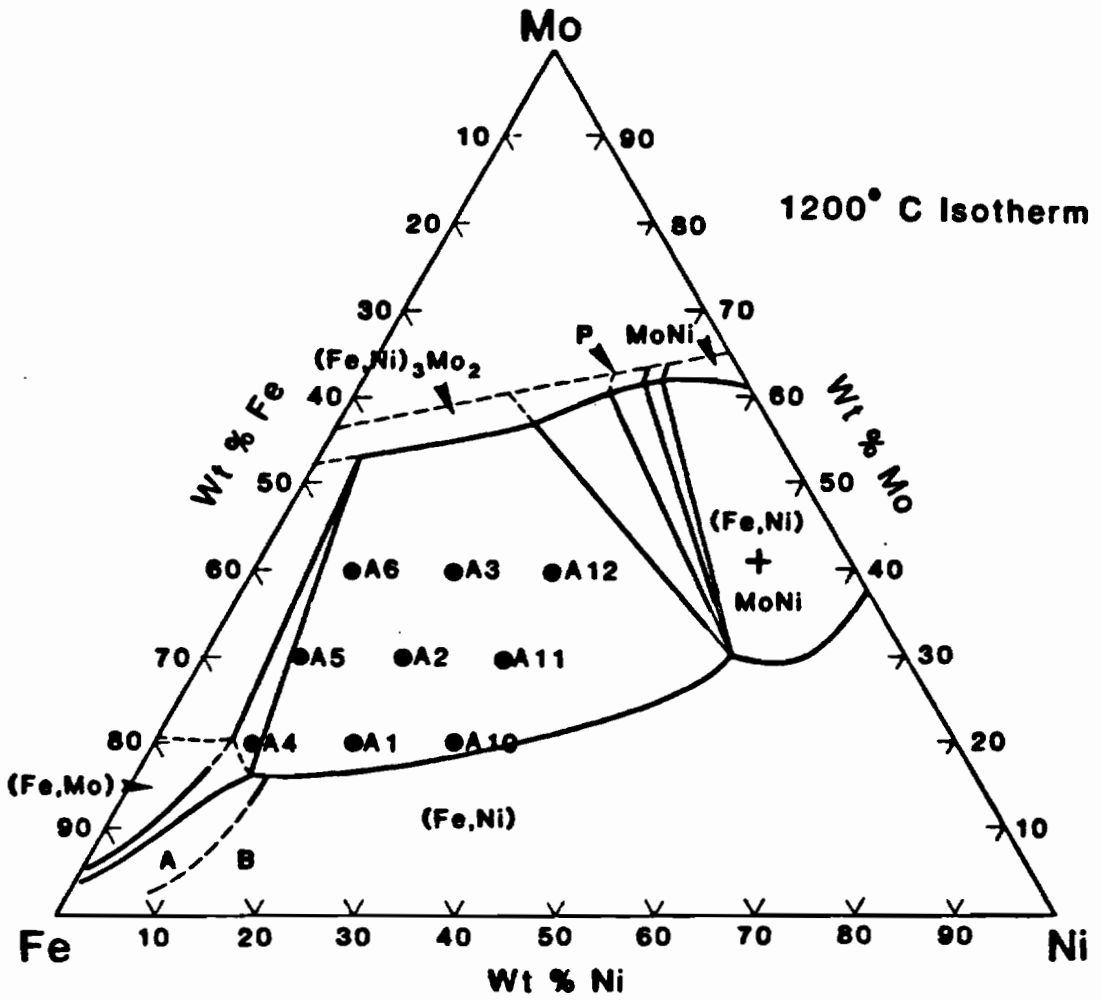

Figure 31. Location of arc-melted alloys within the Fe-Mo-Ni phase diagram.

(a)

Figure 32. Group I arc-melted alloy microstructures.

a) Fe-20Mo-20Ni b) Fe-20Mo-30Ni c) Fe-20Mo-40Ni

(a)

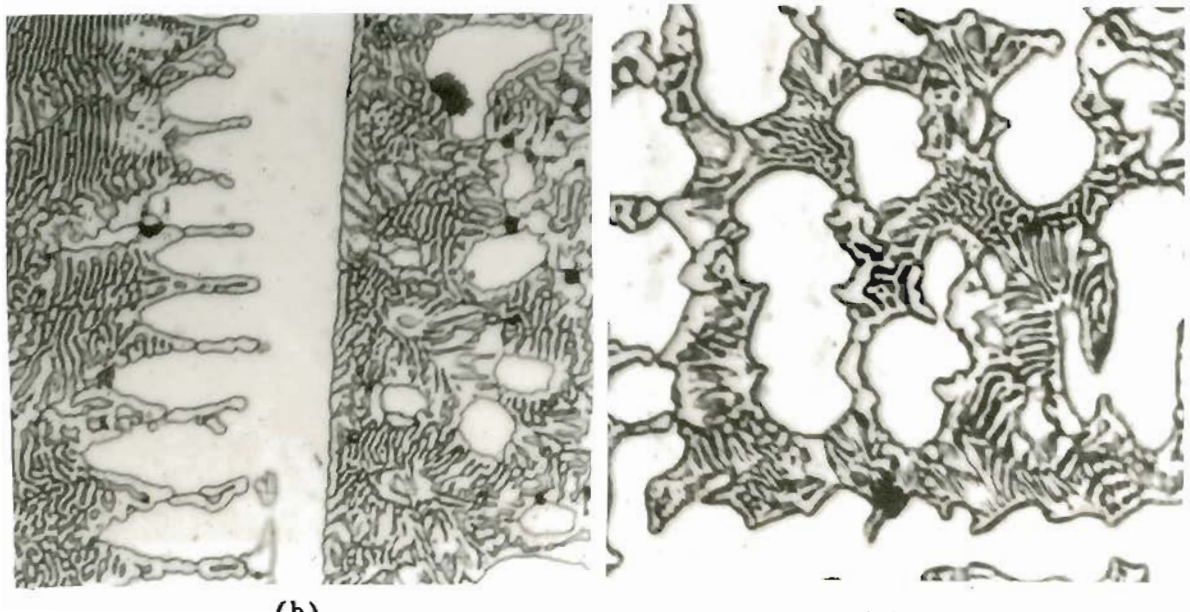

(b) (c)

20μm

Figure 33. Group I arc-melted alloy microstructures.

a) Fe-30Mo-20Ni b) Fe-30Mo-30Ni c) Fe-30Mo-40Ni

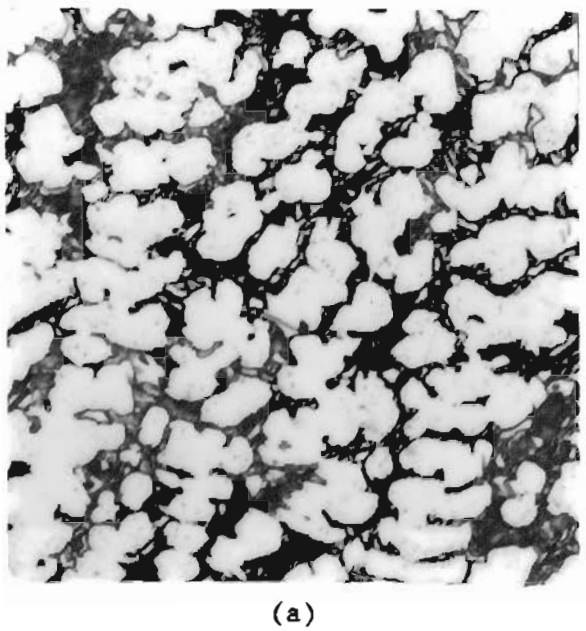

(a)

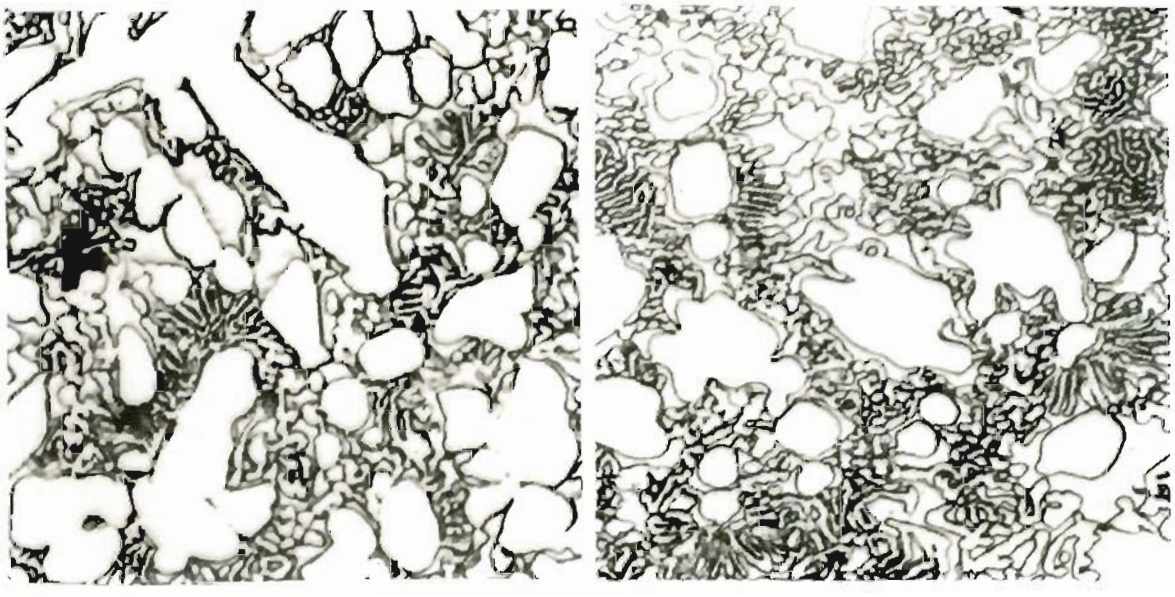

(b) (c)

20μm

Figure 34. Group I arc-melted alloy microstructures.

a) Fe-40Mo-20Ni b) Fe-40Mo-30Ni c) Fe-40Mo-40Ni

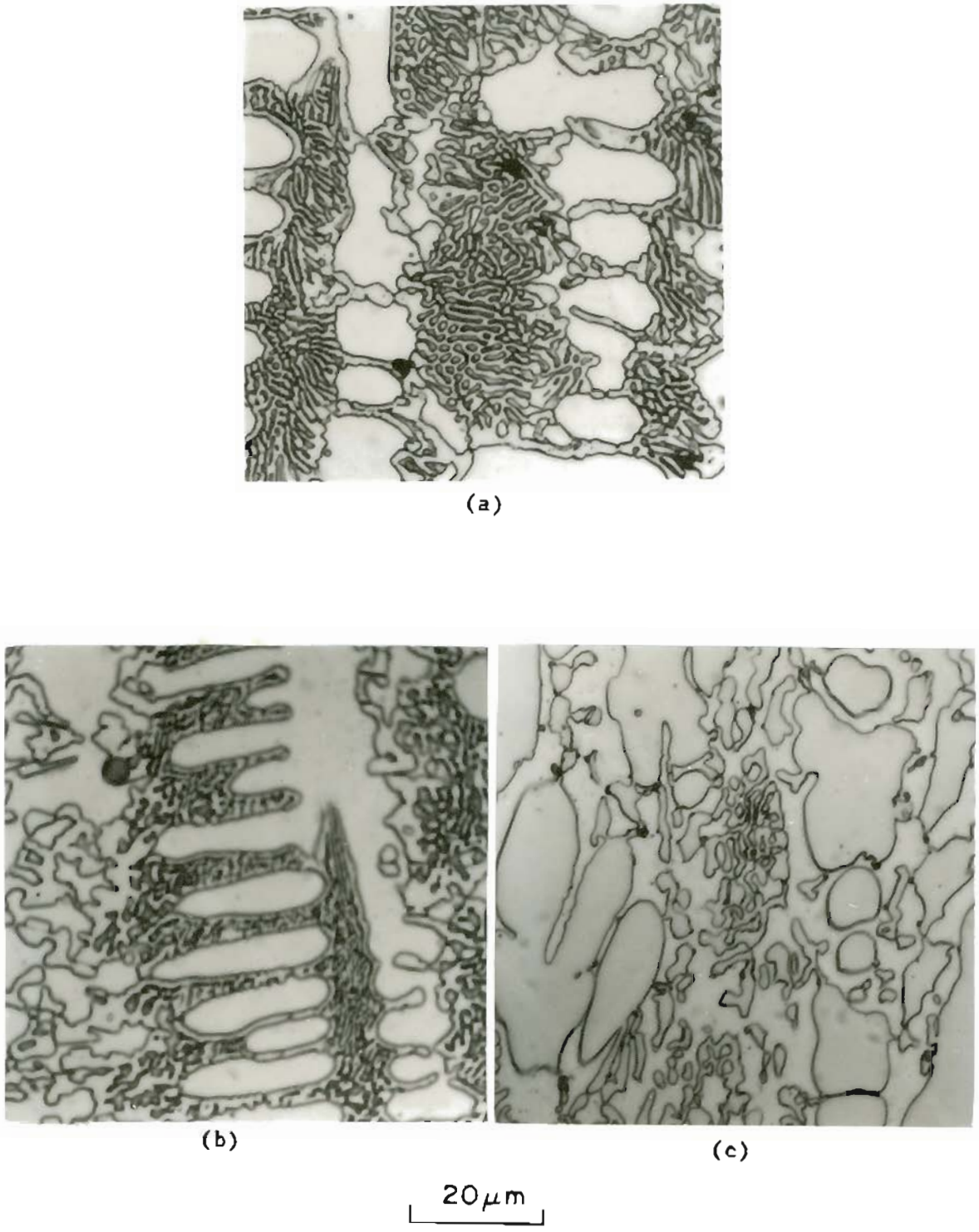

Figure 35. Group II arc-melted alloy microstructures.

a) Fe-20Mo-30Ni-0.5Si b) Fe-20Mo-30Ni-1Si c) Fe-20Mo-30Ni-5Si

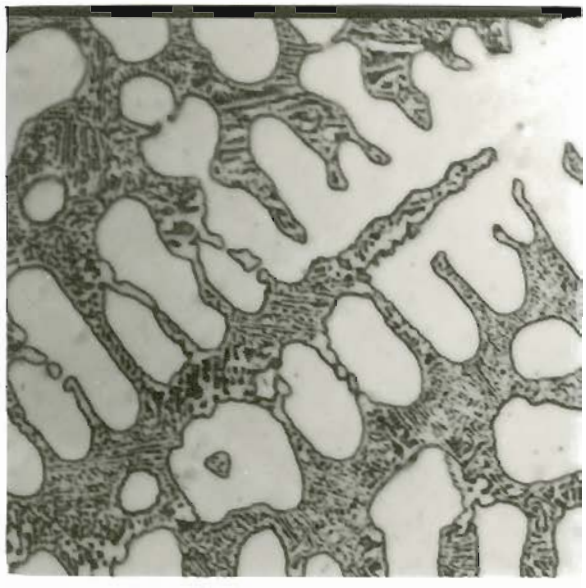

(a)

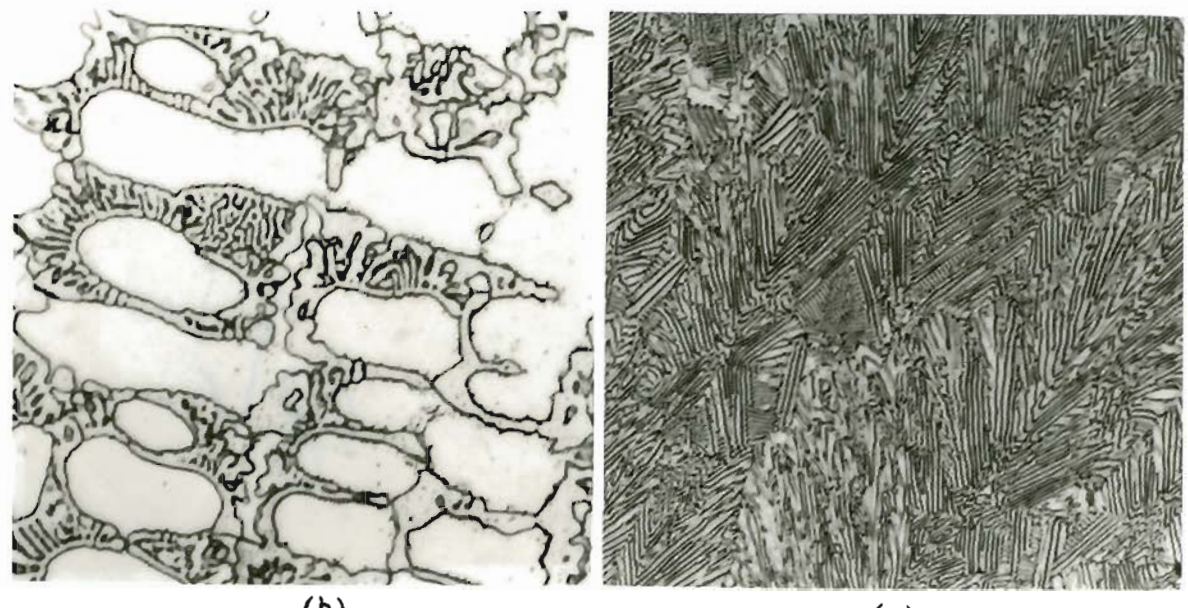

(b) (c)

20μm

Figure 36. Group III arc-melted alloy microstructures.

a) Fe-20Mo-30Ni-0.25C b) Fe-20Mo-30Ni-0.5C c) Fe-20Mo-30Ni-1C

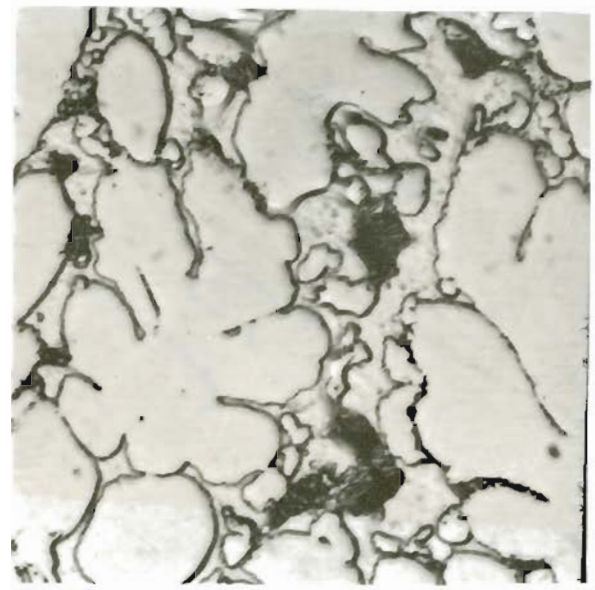

(a)

(b) 20 μm (c)

Figure 37. Group IV arc-melted alloy microstructures.

a) Fe-20Mo-30Ni-5Si-0.25C b) Fe-20Mo-30Ni-5Si-0.5C

c) Fe-20Mo-30Ni-5Si-1C

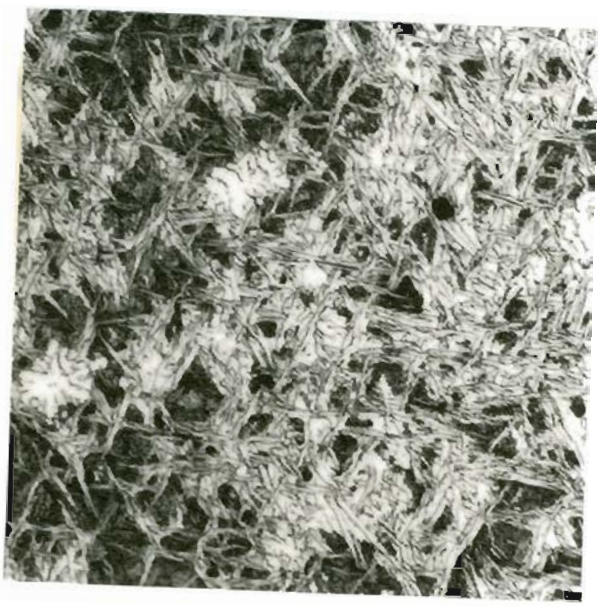

(a)

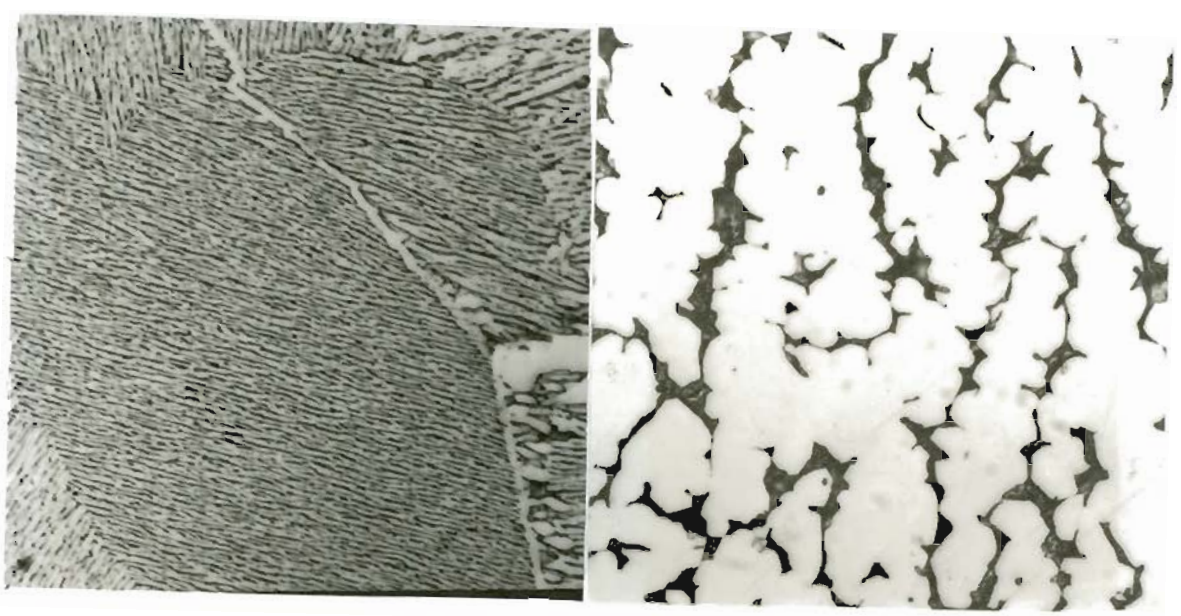

(b) (c)

20 μm

Figure 38. Fe-Mo-Mn arc-melted alloy microstructures.

a) Fe-20Mn-20Mo b) Fe-20Mn-30Mo c) Fe-20Mn-40Mo

3.2 Welding

3.2.1 Welding Parameters

The effect of weld metal dilution by the base metal was studied by varying the welding parameters and then examining transverse weld sections. The welding parameters varied were voltage, amperage, travel speed, lead angle, and powder feed rate. Heat input was calculated for all welding parameter variations. Only one parameter was varied at a time and in some cases two different wire sizes were used.

Changes in the arc voltage did not produce a great change in the weld metal dilution. Generally, dilution decreased with decreasing voltage as shown in Figure 39. For a voltage change of 45 to 25 volts, dilution dropped from 58% to only 48%. Excessively high voltages produced the greatest increase in dilution.

Amperage effected the weld metal dilution to a much greater degree than the voltage. This is shown in Figure 40. The behavior of two wire sizes, 5/32 inch and 3/32 inch in diameter, was examined. In general, as the amperage increased weld metal dilution increased. Dilution at high currents (900 amps for a 5/32 inch wire) was over 60%. At low currents (400 amps for 5/32 inch wire) the dilution was only 30%.

Changes in the travel speed also affected the weld metal dilution. Results are shown in Figure 41. As travel speed increased the dilution increased. Above travel speeds of 15 ipm (inches per minute), the dilution was over 50%. At a low travel speed of 5 ipm the weld metal dilution was only 30%.

In tests with metal powder additions, a 3/32 inch wire was used. Dilution behavior was examined for cases of a stationary electrode and an

oscillated electrode. The results are shown in Figure 42. In general as powder feed rate increased weld metal dilution decreased. At a 1:1 wire powder ratio (on a weight basis), an un-oscillated 3/32 inch wire plus powder weld had a weld metal dilution of only 15% while an oscillated wire using the same welding parameters had a dilution of 20%.

Changing lead angle had little effect on weld metal dilution as seen in Figure 43. Calculated heat input also showed little correlation with observed weld metal dilution. Heat input was calculated by using the equation

$$\text{Heat Input} = \frac{V*I*60}{S}$$

where the heat input is in Joule/inch and where V and I are respectively voltage and amperage and S is travel speed in inches per minute. Heat inputs calculated from all the various welds and plotted against respective weld metal dilution are shown in Figure 44. The only trend evident concerned a series of welds where amperage was varied from 400 to 900 amps.

A synopsis of all the results is shown in Table 14. From this welding parameter study, certain conditions of voltage, current, and travel speed were selected as a basis to use in making powder alloyed welds.

Table 14
Synopsis of Weld Parameters
and Thier Effect on Weld Metal Dilution

Parameter	Change in Parameter	Change in Dilution
Voltage	increase	increase
Amperage	increase	increase
Travel Speed	increase	increase
Lead Angle	increase	none
Powder Feed Rate	increase	decrease

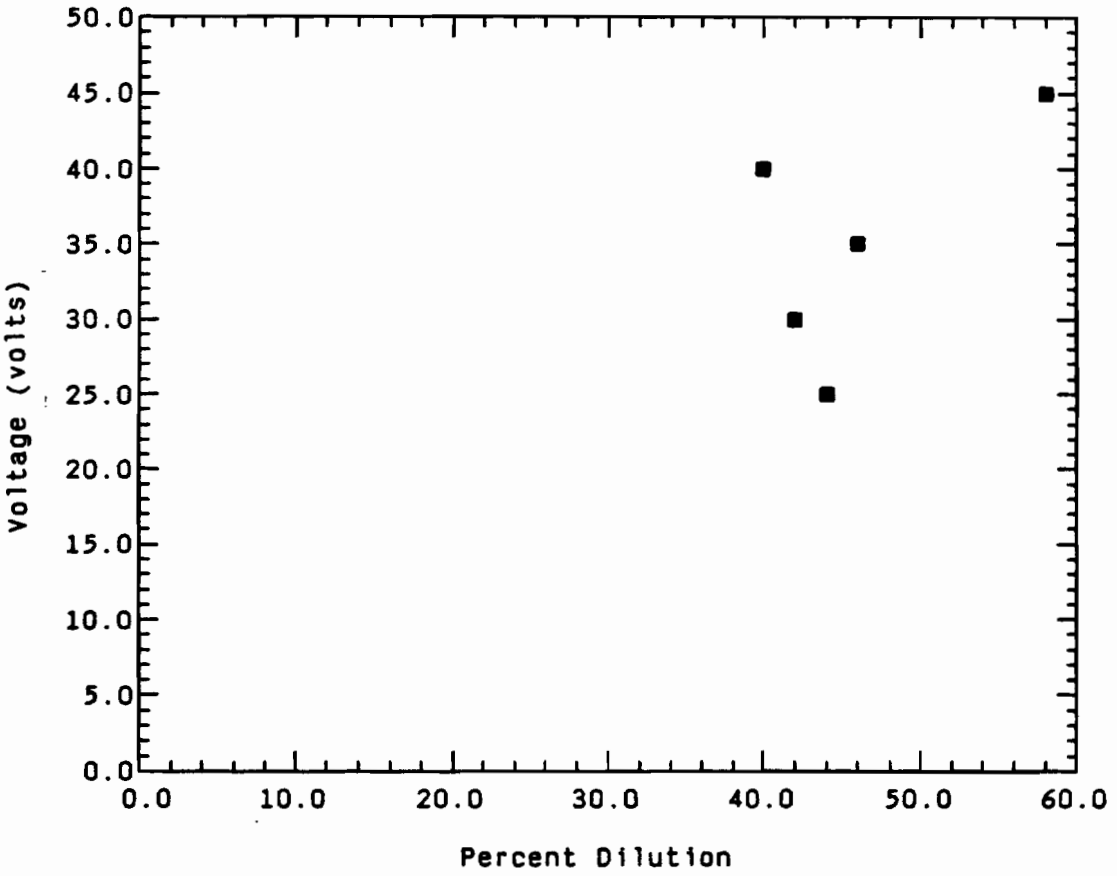

Figure 39. Voltage versus weld metal dilution.

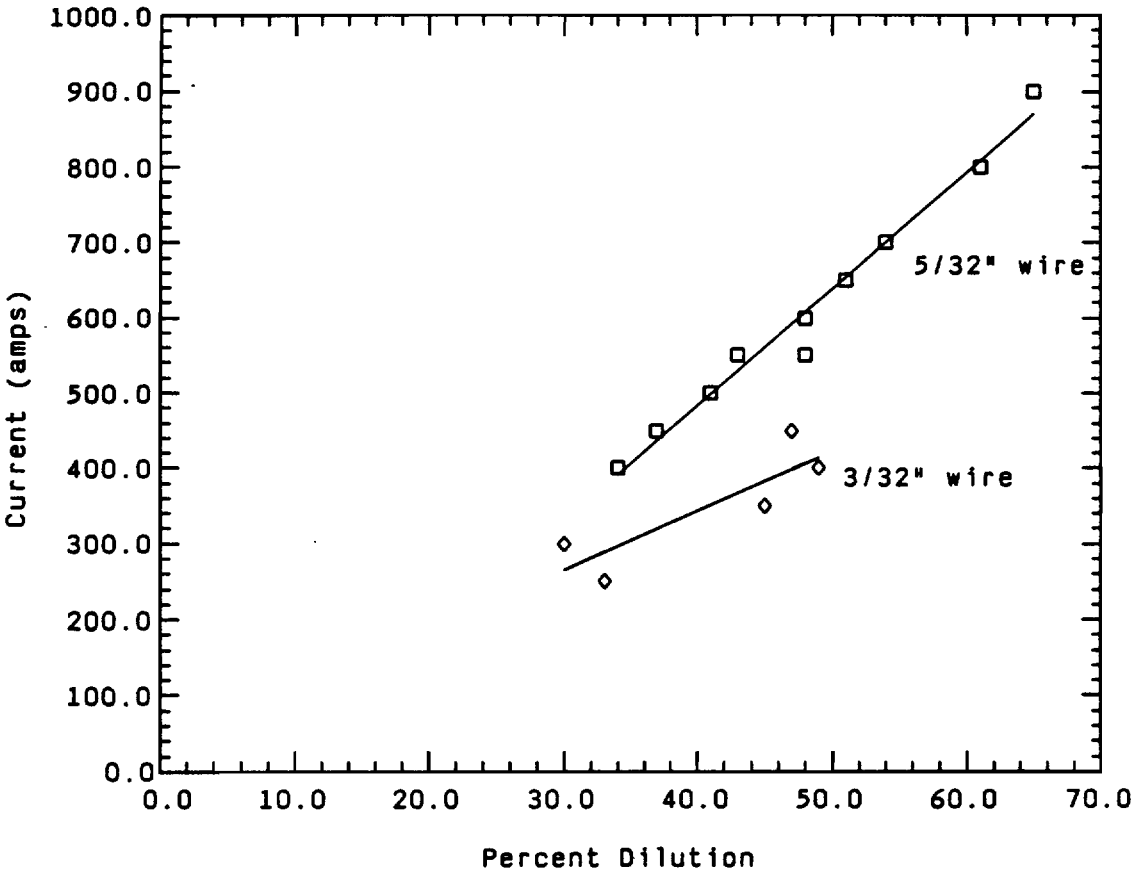

Figure 40. Amperage versus weld metal dilution.

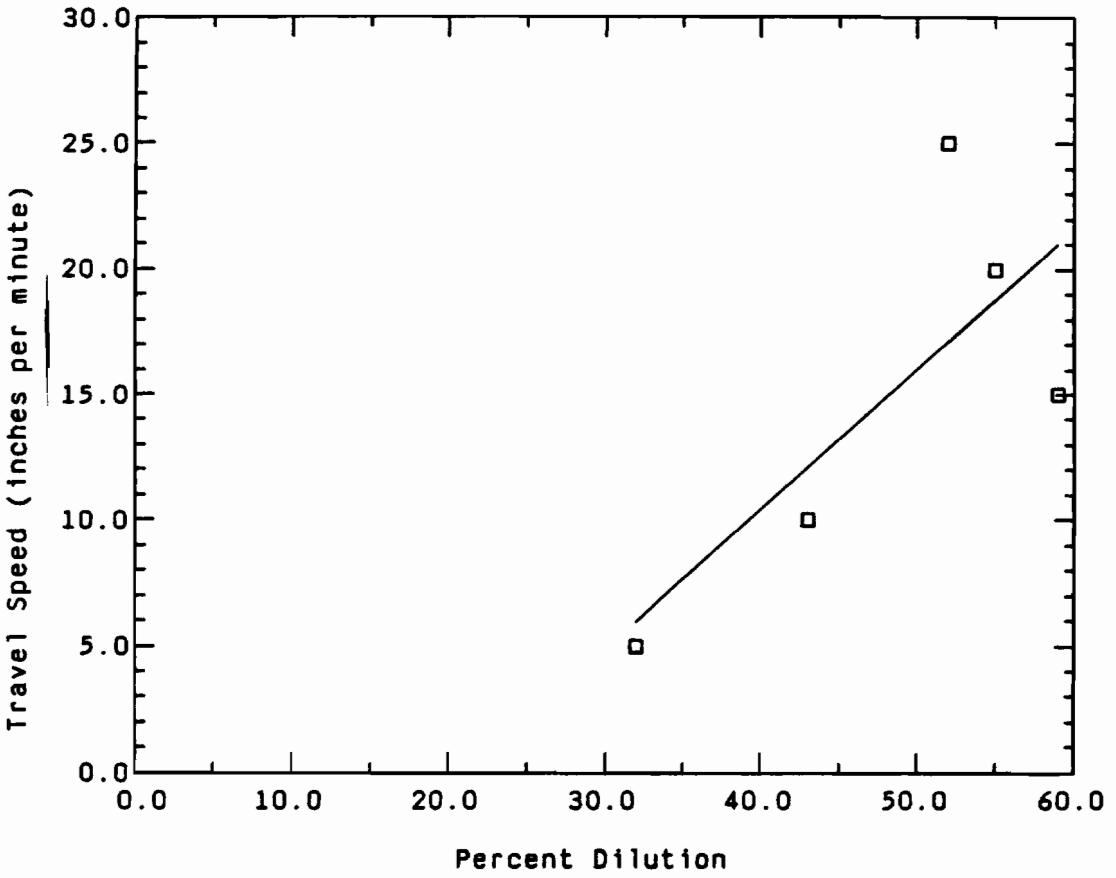

Figure 41. Travel speed versus weld metal dilution.

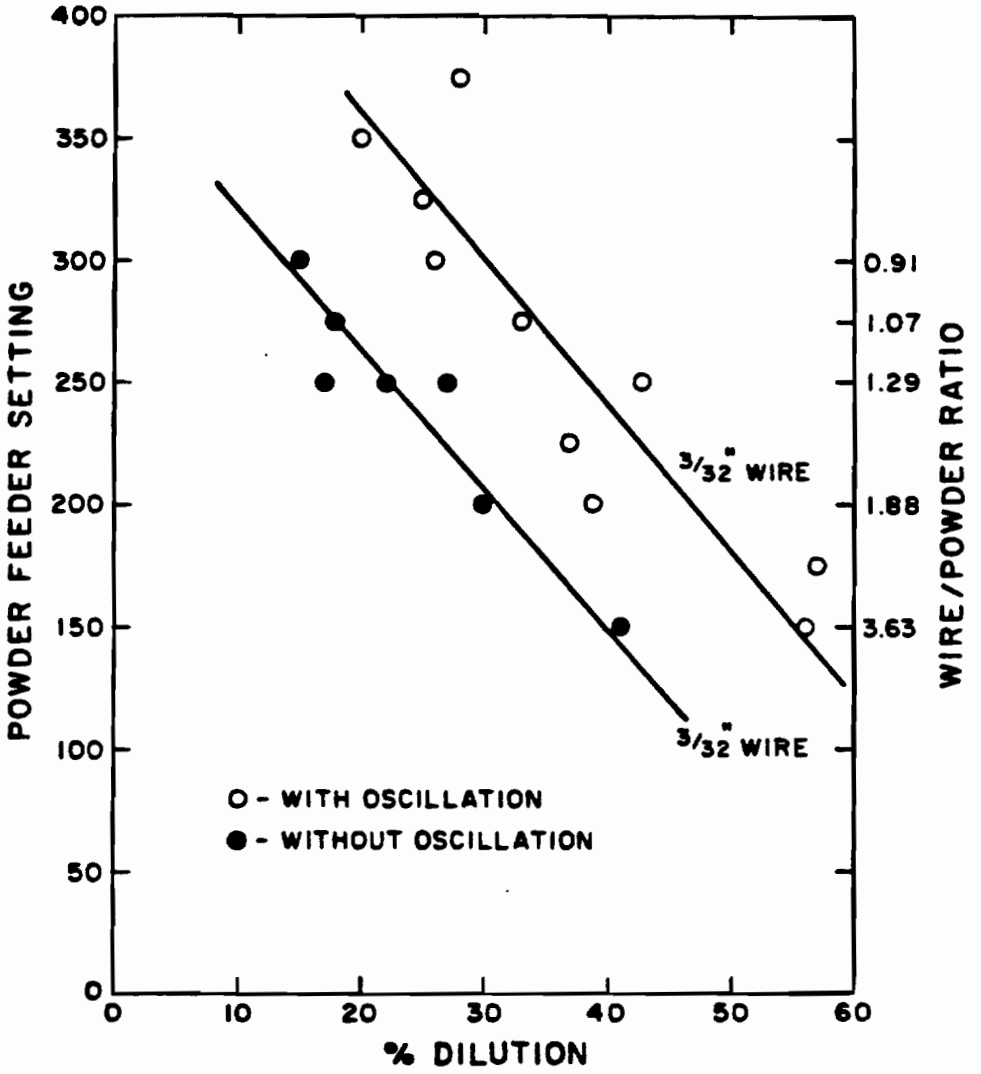

Figure 42. Powder feed rate versus weld metal dilution, with and without electrode oscillation.

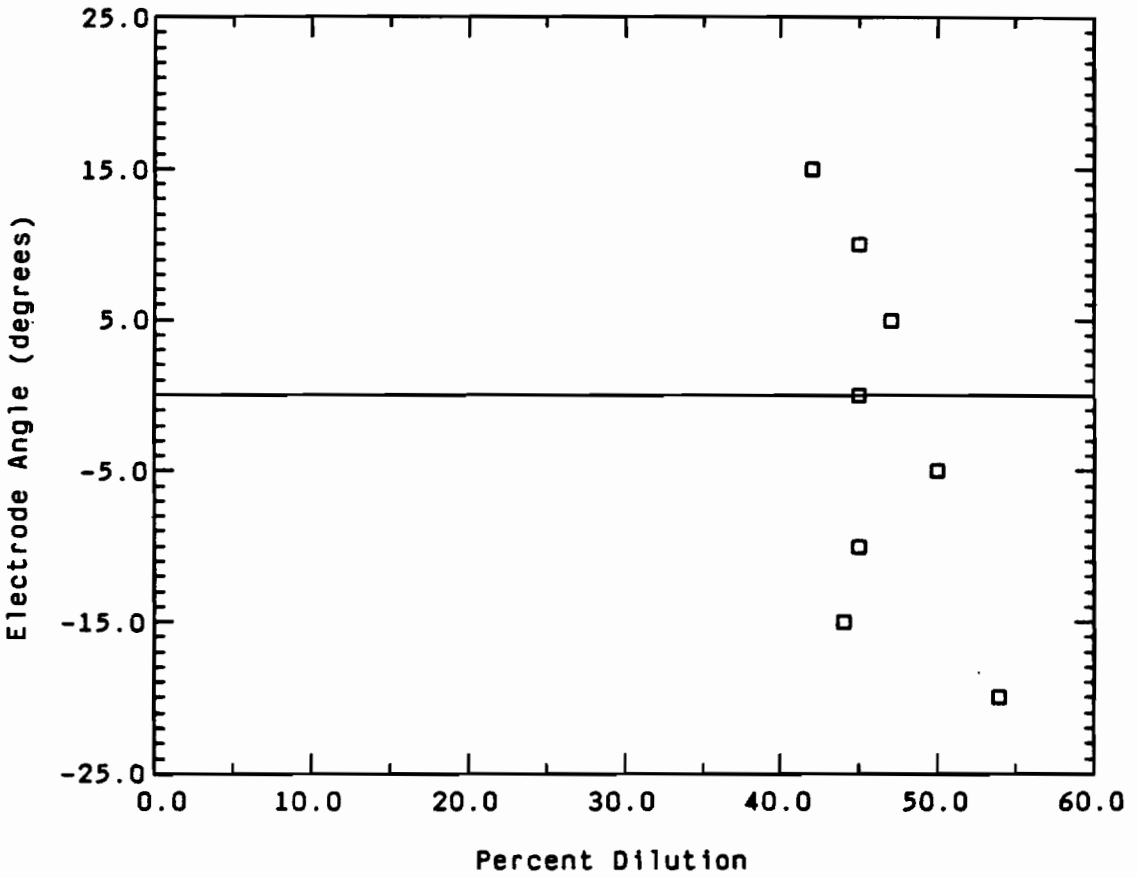

Figure 43. Electrode lead angle versus weld metal dilution.

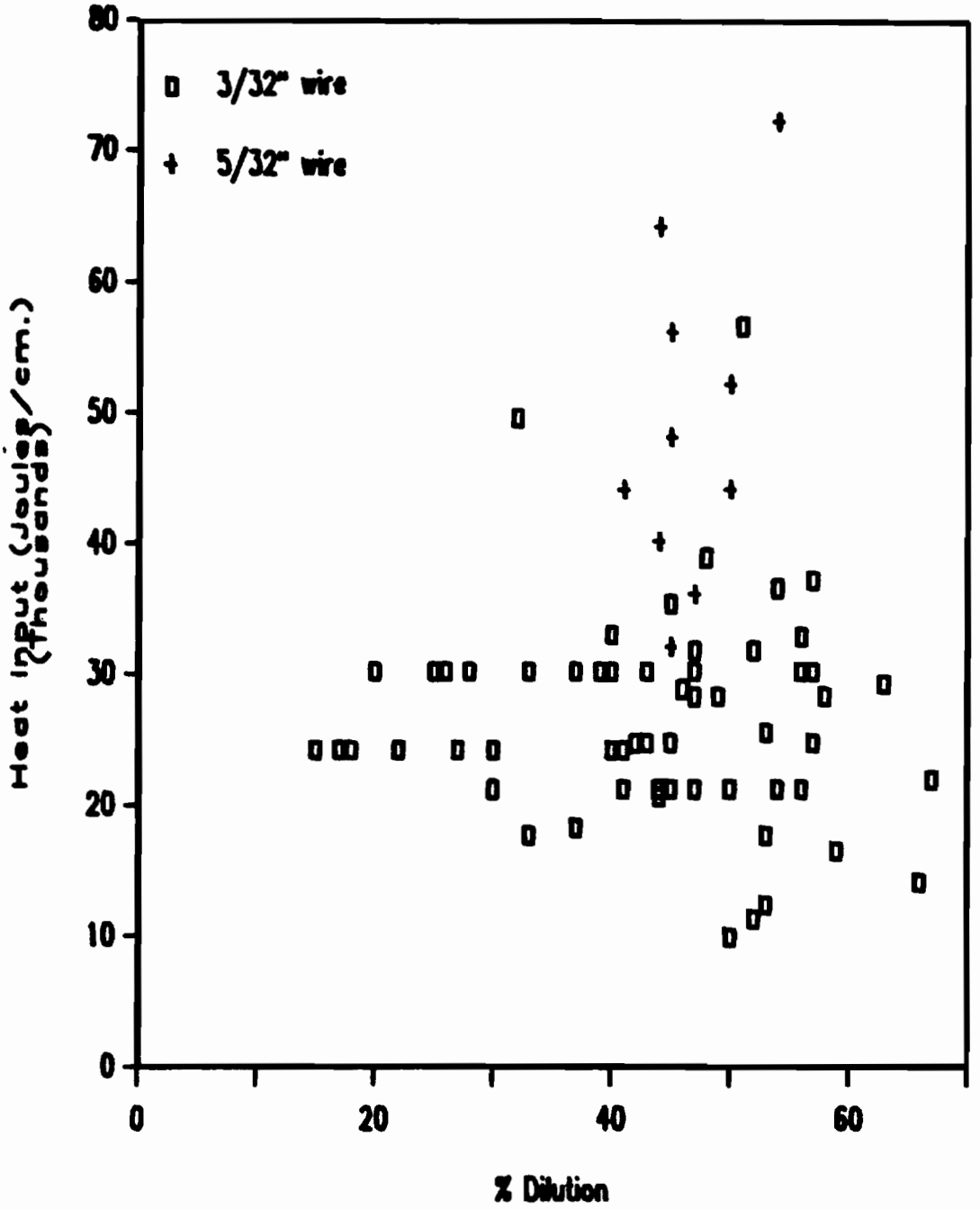

Figure 44. Heat input (Kilojoules/inch) versus weld metal dilution.

3.2.2 Weld Hardfacing Alloys

Initial weld hardfacing alloys were based on a simple ternary alloys. As experience with the alloying process grew and data on the wear resistances and microstructures of the weld deposits was obtained, subsequent hardfacing alloy compositions were adjusted accordingly.

Weld hardfacing alloys were produced using two different filler wires and several powder compositions. As-deposited wire compositions are shown in Table 15. Mild steels, A36 and A588, were used as base materials. The powder compositions are shown in Table 16. Table 17 shows wire and powder combinations used as well as powder addition rates for various welds. Welds were sectioned to provide samples for metallography, hardness testing, chemical analysis, x-ray diffraction, and wear testing using the pin-on-drum abrasive wear test and the dry-sand-rubber--wheel abrasive wear test. Welds were also made using an optimized composition and were sectioned to provide specimens for wear testing and metallography.

Some of the weld compositions produced are shown in Table 18. Table 19 shows results of hardness and pin-on-drum wear testing as well as a synopsis of the microstructures of some of the experimental overlays. The weld microstructures were classified into five groups similar to, but the same, as those of the arc-melted alloys. Group I was fully austenitic or austenitic/ferritic with a small amount of an interdendritic phase. Group II was a microstructure of austenite dendrites plus an intermetallic plus austenite eutectic. Group III alloys possessed an austenite matrix with a eutectic phase and idiomorphic carbide particles. Alloys of Group

IV had microstructures of a 90 to 100% lamellar structure. The difference between the Group IV alloys and the Group III alloys was that the latter contained about 1 wt.% carbon. The Group V microstructures had a multi-phase microstructure which included at least one eutectic, possibly two. Microstructures of the experimental welds are shown in Figures 45 to 56. They are grouped by the added powder composition.

The microstructures of the two filler wires used without any powder addition are shown in Figure 45. The experimental 15Mo-10Ni tubular wire produced an austenitic matrix plus an intermetallic microstructure. X-ray diffraction identified the intermetallic as FeMoSi. The other filler wire, a 5Mo-5Ni commercial tubular wire which also contained some carbon, produced a 100% martensitic microstructure.

Welds with the W1 powder (60Mo-40Ni) produced Group II microstructures, austenite dendrites with an austenite plus intermetallic eutectic in the interdendritic regions, as seen in Figure 46. The intermetallic was identified as FeMoSi by x-ray diffraction which also showed the presence of an eta (M_6C) carbide. Increasing alloy content did not decrease the wear rate, in fact it increased from 9.85 to 10.37 mg/m weight loss while the hardness increased from 15 to 32 HRC.

Using the W2 powder (54.5Mo-36.4Ni-9.1Si) also produced welds with a Group II microstructure as shown in Figure 47. X-ray diffraction analysis showed the presence of some ferrite as well as the austenite. It also identified the intermetallic as FeMoSi. Increasing alloy content increased the volume fraction of eutectic present in the microstructure and increased the hardness, from 17 to 28 HRC. The wear rate also increased, from 7.45 to 10.10 mg/m weight loss in the pin-on-drum wear test.

The W3 powder was a high nickel powder (25Mo-75Ni) and produced a weld with a Group I microstructure, an austenite matrix with second phase particles present in the boundaries between the austenite cells. These are shown in Figure 48. Hardnesses of these welds were low, around 50 HRA, and wear rates were high, from 10.03 to 10.62 mg/m weight loss.

The W4 powders contained silicon as well as the high nickel content (25Mo-70Ni-5Si). The microstructures produced were Group I tending toward Group II at the higher alloy contents. These microstructures are shown in Figure 49. The volume fraction of intermetallic compounds in these alloys was insufficient to detect with x-ray diffraction, only austenite peaks were seen. Hardnesses were low, 50-55 HRA, and were increased slightly by increasing alloy content. Wear rates increased with increasing alloy content, 8.97 to 10.34 mg/m weight loss.

The W5 powder contained some carbon as well as molybdenum, nickel, and silicon (49.7Mo-35.6Ni-13.9Si-1.8C). Microstructures produced are shown in Figure 50 and were of Group II microstructures. As powder additions increased, the amount of eutectic in the structure increased as did the hardness, from 56 HRA (~11 HRC) to 45.5 HRC. The wear rate did not, however, correlate with the hardness or the microstructure. The lowest wear rates were seen at the highest hardness and at the lowest hardness, 8.97 and 8.42 mg/m respectively. The highest wear rate in this weld series was 10.34 mg/m.

The W6 powder composition was similar to the W5 composition but without the carbon (49.7Mo-31.0Ni-19.3Si) and more silicon. This powder produced a Group V microstructure of austenite plus at least one eutectic as well as other phases, as shown in Figure 51. X-ray diffraction showed

only the presence of austenite, ferrite, and a FeMoSi intermetallic compound. Increasing alloy content decreased hardness in these alloys, from 50.5 HRC to 39.5 HRC, and the wear rate decreased as well. The lowest wear rate was seen on the alloy with the lower hardness, 6.333 mg/m weight loss. This weld microstructure had a larger volume fraction of large particles and a smaller volume fraction of a coarse eutectic than other welds using the W6 powder.

The W7 powder was similar to the W6 powder but with 3.7 wt.% carbon added (49.7Mo-29.9Ni-18.6Si-3.7C). Large alloy contents produced a Group III microstructure of austenite plus a eutectic plus large idiomorphic particles, and low alloy contents produced a Group IV microstructure of a lamellar eutectic. X-ray diffraction analysis identified the idiomorphic particle as an eta carbide and showed the presence of the FeMoSi intermetallic. These microstructures are shown in Figure 52. Hardnesses of these alloys did not vary appreciably, all alloys were about 34-36 HRC. The wear rates wear similar as well, 10.25-10.42 mg/m weight loss.

Figure 53 shows the weld microstructure using the W7 powder but with a high temperature carbide, tungsten carbide or titanium carbide, included in the alloy addition. The microstructures produced were of Group III and IV, with carbide particles seen in a lamellar eutectic. Hardnesses of these alloys were high, about 55 HRC, and pin-on-drum wear rates were low, 7.57 mg/m with added WC and 6.30 mg/m for added TiC.

The W8 powder was similar to the W7 powder but with more carbon (46.1Mo-28.8Ni-18.1Si-7C). Low powder additions produced a Group II microstructure while high powder addition rates produced a Group IV microstructure as seen in Figure 54. X-ray diffraction showed only the austenite

matrix and an eta carbide, no intermetallic phase was detected. Hardnesses ranged from 30 to 35 HRC and wear rates were relatively high 9.63 to 11.1 mg/m. Wear rates increased with increasing alloy content.

Figure 55 shows the microstructures of welds using the W8 powder and additional WC or TiC. The microstructures were a mixed Group II and Group V with a fine precipitate in the dendritic regions as well as the presence of a small blocky phase. Hardnesses were similar, from 41 to 44 HRC. Wear rates, however, differed greatly. The welds with the added TiC or WC had half the wear rate as welds made without additional carbide powder, 4.44 and 5.08 mg/m (TiC and WC additions respectively) versus 10.53 mg/m for no added carbide.

Microstructures of the welds made with the W9 powder (45.5Mo-28.4Ni--17.8Si-8.3C) are shown in Figure 56. The W9 powder was similar to the W7 and W8 powders, but even more carbon. Additions of hafnium carbide, titanium carbide, and tungsten carbide were made as well. The microstructure was a combined Group II and Group V, similar to some of the welds made with the W7 powder. Alloys with the Group II microstructure had large martensite plates running through the austenite dendrites. Hardnesses of the alloys were similar, 39.6 to 42.6 HRC. Wear rates were similar as well, 4.08 to 4.24 mg/m, all low and not seemingly affected by differences in microstructure. Additions of the different carbides did not produce differences in wear rates.

Table 15

Composition of weld filler wires (wt.%).

	Fe	Mo	Ni	Si	C
Fe-18Mo-18Ni experimental filler wire	bal.	15.44	16.4	0.10	0.047
Fe-5Mo-5Ni commercial filler wire	bal.	4.0	3.97	0.72	0.19

Table 16

Composition of metal powders used in welding (wt.%).

	Mo	Ni	Si	C
W1	60	40	--	--
W2	54.5	36.4	9.1	--
W3	25	75	--	--
W4	25	70	5	--
W5	49.7	35.6	13.9	1.8
W6	49.7	31.0	19.3	--
W7	47.8	29.9	18.6	3.7
W8	46.1	28.8	18.1	7.0
W9	45.5	28.4	17.8	8.3

Table 17
Wire/Powder Combinations Used

Weld No.	Wire	Powder	Addition Rate
T13-2	18Mo-18Ni	W1	2 g/cm
T13-3	18Mo-18Ni	W1	5.1 g/cm
T13-4	18Mo-18Ni	W2	1 g/cm
T13-5	18Mo-18Ni	W2	2 g/cm
T13-6	18Mo-18Ni	W2	3 g/cm
T13-7	18Mo-18Ni	W2	4 g/cm
T14-2	18Mo-18Ni	W3	1 g/cm
T14-3	18Mo-18Ni	W3	2 g/cm
T14-4	18Mo-18Ni	W3	3 g/cm
T14-5	18Mo-18Ni	W3	4 g/cm
T14-6	18Mo-18Ni	W4	1 g/cm
T14-7	18Mo-18Ni	W4	2 g/cm
T14-8	18Mo-18Ni	W4	3 g/cm
T15-2	18Mo-18Ni	W4	4 g/cm
T15-3	18Mo-18Ni	W5	1 g/cm
T15-4	18Mo-18Ni	W5	2 g/cm
T15-5	18Mo-18Ni	W5	3 g/cm
T15-7	5Mo-5Ni	W5	4 g/cm
T20-3	5Mo-5Ni	W6	5.9 g/cm
T21	5Mo-5Ni	W6	5.9 g/cm
T20-2	5Mo-5Ni	W6	7.09 g/cm
T20-4	5Mo-5Ni	W6	7.87 g/cm
T18-3	18Mo-18Ni	W7	3.93 g/cm
T18-2	18Mo-18Ni	W7	4.72 g/cm
T18-1	18Mo-18Ni	W7	6.3 g/cm
T22	5Mo-5Ni	W7	4.72 g/cm
T22-4A	5Mo-5Ni	W7 + WC	5.09 g/cm, 0.035 g/cm WC
T22-4B	5Mo-5Ni	W7 + TiC	5.09 g/cm, 0.035 g/cm TiC
T19-4	18Mo-18Ni	W8	2.36 g/cm
T19-1	18Mo-18Ni	W8	3.15 g/cm
T19-2	18Mo-18Ni	W8	3.93 g/cm
T19-3	18Mo-18Ni	W8	4.72 g/cm

(Table 17 continued)

T23-4A	5Mo-5Ni	W8 + WC	4.72 g/cm, 0.035 g/cm WC
T23-4B	5Mo-5Ni	W8 + TiC	4.72 g/cm, 0.035 g/cm TiC
T24-1A	5Mo-5Ni	W9	3.94 g/cm
T24-1B	5Mo-5Ni	W9 + TiC	3.94 g/cm, 0.035 g/cm TiC
T24-2A	5Mo-5Ni	W9 + HfC	3.94 g/cm, 0.035 g/cm HfC
T24-2B	5Mo-5Ni	W9 + WC	3.94 g/cm, 0.035 g/cm WC

Table 18

Analyzed Composition of Some of the Experimental Welds
Balance is Fe (in wt.%)

	Mo	Ni	Si	C
T12-4	13.3	13.9	0.05	<0.05
T12-7	17.2	17.8	0.16	<0.05
T13-2	22.3	19.3	0.09	<0.05
T13-3	27.1	21.9	0.08	<0.05
T13-5	18.8	16.1	1.01	<0.05
T13-7	22.7	18.2	1.67	<0.05
T14-2	17.8	22.9	0.11	<0.05
T14-5	19.3	33.3	0.07	<0.05
T14-6	15.7	19.2	0.05	0.06
T14-8	16.6	25.9	0.66	0.06
T15-3	17.4	15.0	0.65	0.13
T15-5	23.5	19.3	2.35	0.35
T18-1	23.8	19.0	3.48	0.72
T18-3	22.8	18.9	2.87	0.50
T19-1	23.1	19.8	2.39	0.79
T19-3	23.6	19.5	2.78	0.93
T20-2	17.6	13.2	5.04	0.14
T20-3	15.2	10.8	4.16	0.14
T20-4	19.8	14.9	5.38	0.14

Table 19
Structure and properties of some of the welds.

	Hardness	Pin-on-drum wear rate (mg/m)	Microstructure Group No.	Type
T14-2	49.5 HRC	10.03	1	A + 5% ID
T14-5	51 HRA	10.38	1	A + 5% ID
T12-4	51 HRA	8.48	2	AD + 5% IE
T12-7	52.5 HRA	8.03	2	AD + 5% IE
T13-2	15 HRC	10.85	2	AD + 10% IE
T13-3	32 HRC	10.37	2	AD + 50% IE
T13-5	15 HRC	8.39	2	AD + 40% IE
T13-7	28 HRC	10.10	2	AD + 70% IE
T14-6	50.6 HRA	8.97	2	A + 5% E
T14-8	51.7 HRA	10.39	2	A + 15% IE
T15-3	56 HRA	8.43	2	A + 40% IE
T15-5	38 HRC	10.34	2	A + 90% IE
T23-4	44 HRC	4.44	2	AD + 80% IE
T18-1	34 HRC	10.25	3	A + E + C
T18-3	36.1 HRC	10.43	4	100% LE
T19-1	35.4 HRC	10.33	4	95% LE
T19-3	33.3 HRC	11.10	4	100% LE
T23	43.6 HRC	10.53	4	80% LE
T20-2	45.5 HRC	7.31	5	Multi-phase
T20-3	50.8 HRC	7.47	5	Multi-phase
T20-4	39.5 HRC	6.33	5	Multi-phase
T21	50.7 HRC	7.43	5	Multi-phase
T24-1A	39.6 HRC	4.14	5	Multi-phase

AD = Austenite Dendrites
C = Carbide
E = Eutectic
LE = Lamellar Eutectic
ID = Interdendritic Phase
IE = Interdendritic Eutectic

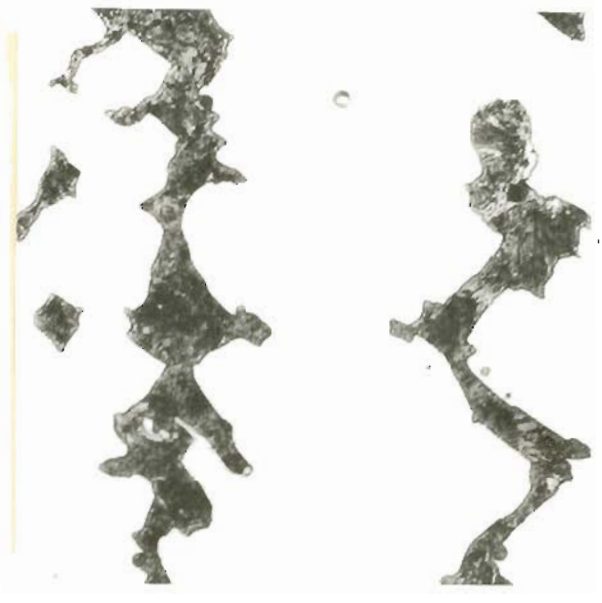

(a)

20μm

(b)

Figure 45. Weld metal micrographs, no powder added.

a) 18Mo-18Ni filler wire, 51 HRA, 8.164 mg/m wear rate
Fe-16.5Mo-16.2Ni-0.10Si
b) 5Mo-5Ni filler wire, 44 HRC, 8.972 mg/m wear rate
Fe-4.0Mo-3.97Ni-0.72Si-0.19C

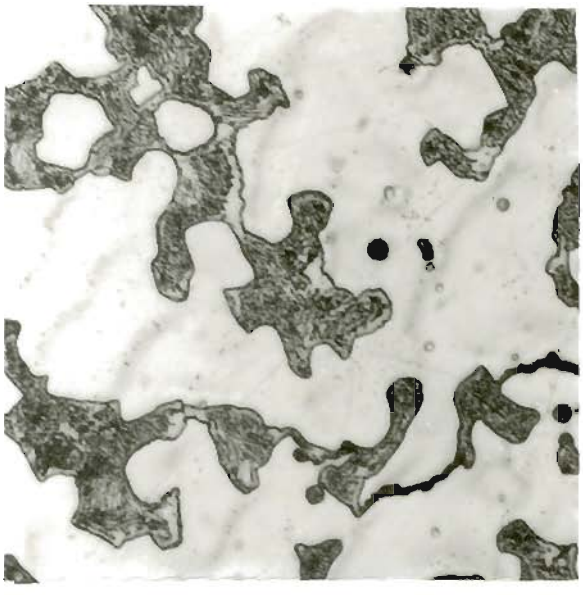

(a)

20μm

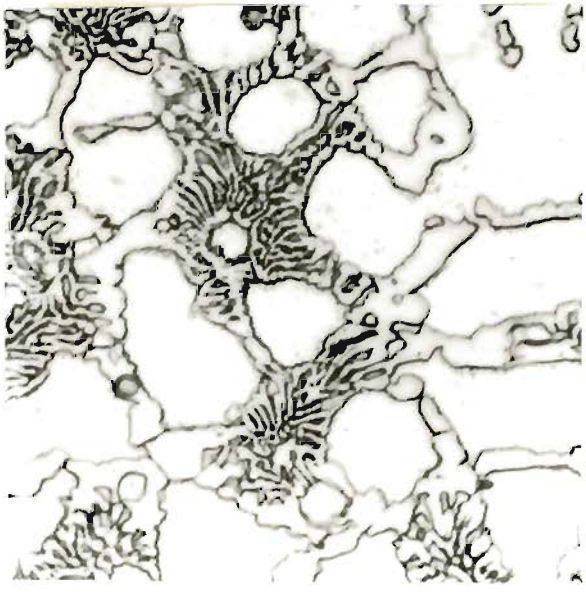

(b)

Figure 46. Weld metal micrographs, W1 powder.

a) Weld T13-2, 15 HRC, 9.85 mg/m wear rate
Fe-22.3Mo-19.3Ni-0.09Si
b) Weld T13-3, 32 HRC, 10.37 mg/m wear rate
Fe-27.1Mo-21.9Ni-0.08Si

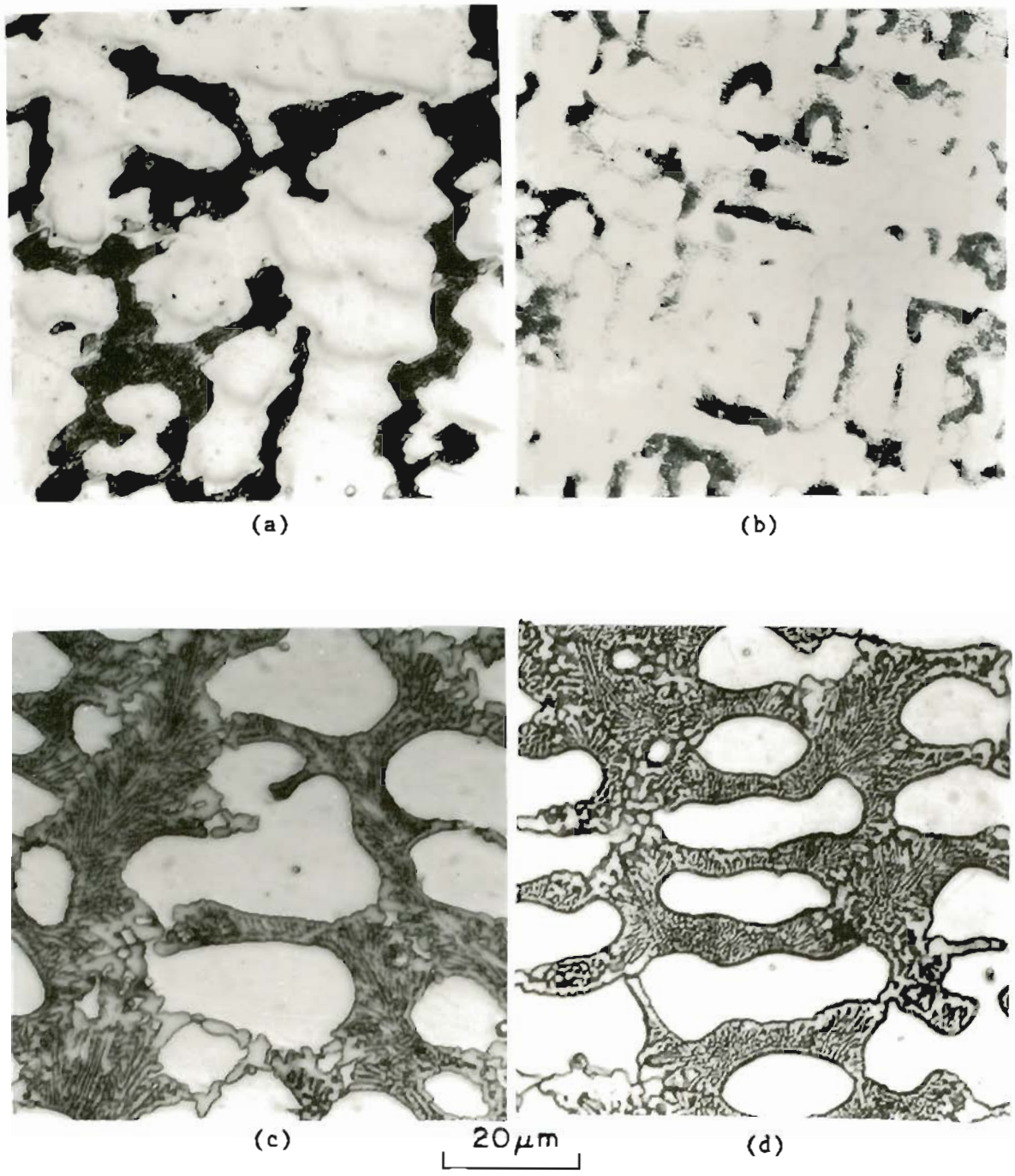

Figure 47. Weld metal micrographs, W2 powder.

a) T13-4, 17 HRC, 7.45 mg/m wear rate
Fe-17.2Mo-14.8Ni-0.45Si
b) T13-5, 15 HRC, 8.39 mg/m wear rate
Fe-18.8Mo-16.1Ni-1.01Si
c) T13-6, 24.5 HRC, 9.03 mg/m wear rate
Fe-21.7Mo-17.3Ni-1.41Si
d) T13-7, 28 HRC, 10.02 mg/m wear rate
Fe-22.7Mo-18.2Ni-1.67Si

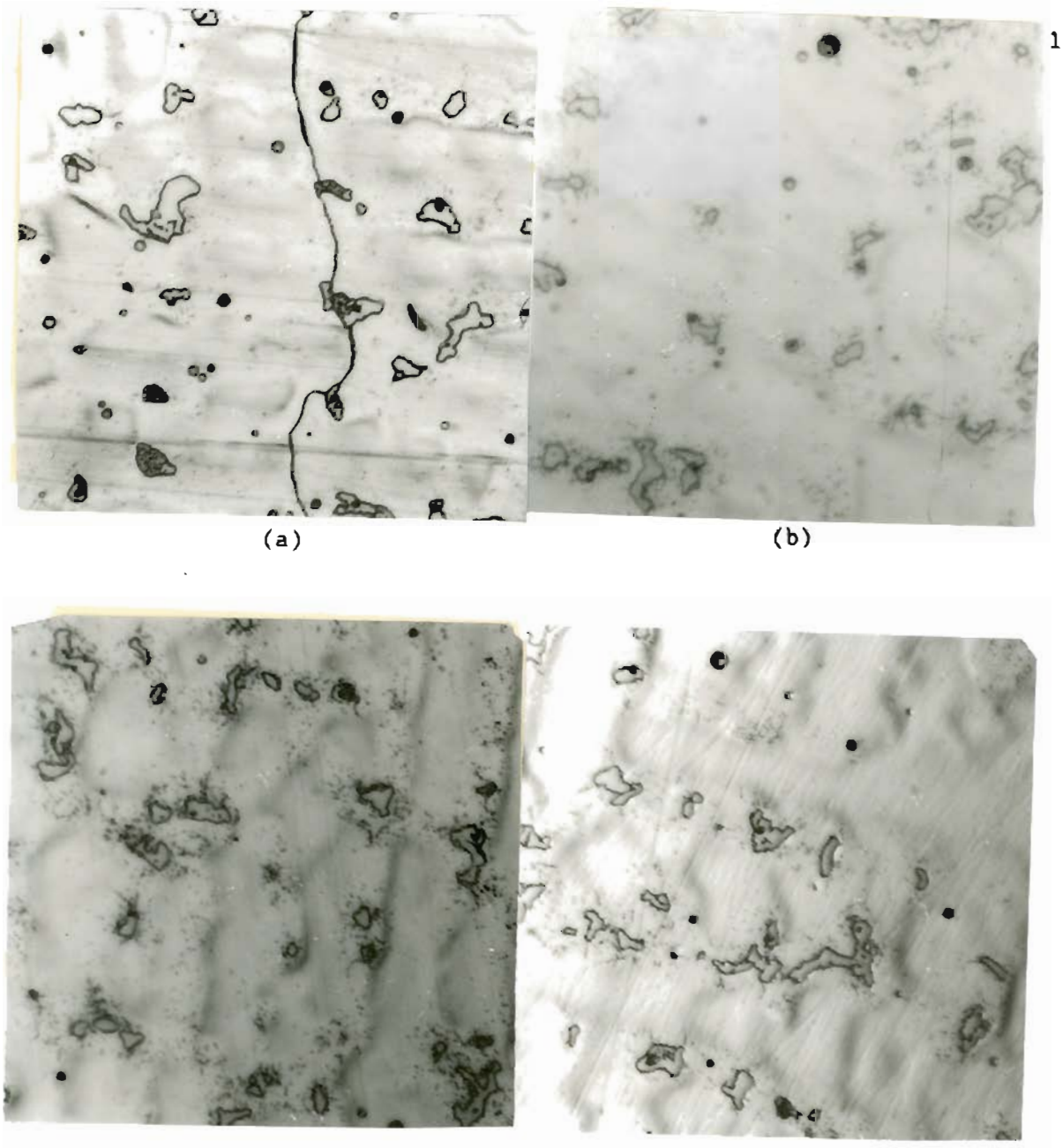

Figure 48. Weld metal micrographs, W3 powder.

a) T14-2, 49.5 HRA, 10.03 mg/m wear rate
Fe-17.8Mo-22.9Ni-0.11Si
b) T14-3, 50.5 HRA, 10.23 mg/m wear rate
Fe-18.0Mo-26.7Ni-0.18Si
c) T14-4, 51.0 HRA, 10.62 mg/m wear rate
Fe-19.4Mo-29.5Ni-0.07Si
d) T14-5, 50.5 HRA, 10.38 mg/m wear rate
Fe-19.3Mo-33.3Ni-0.07Si

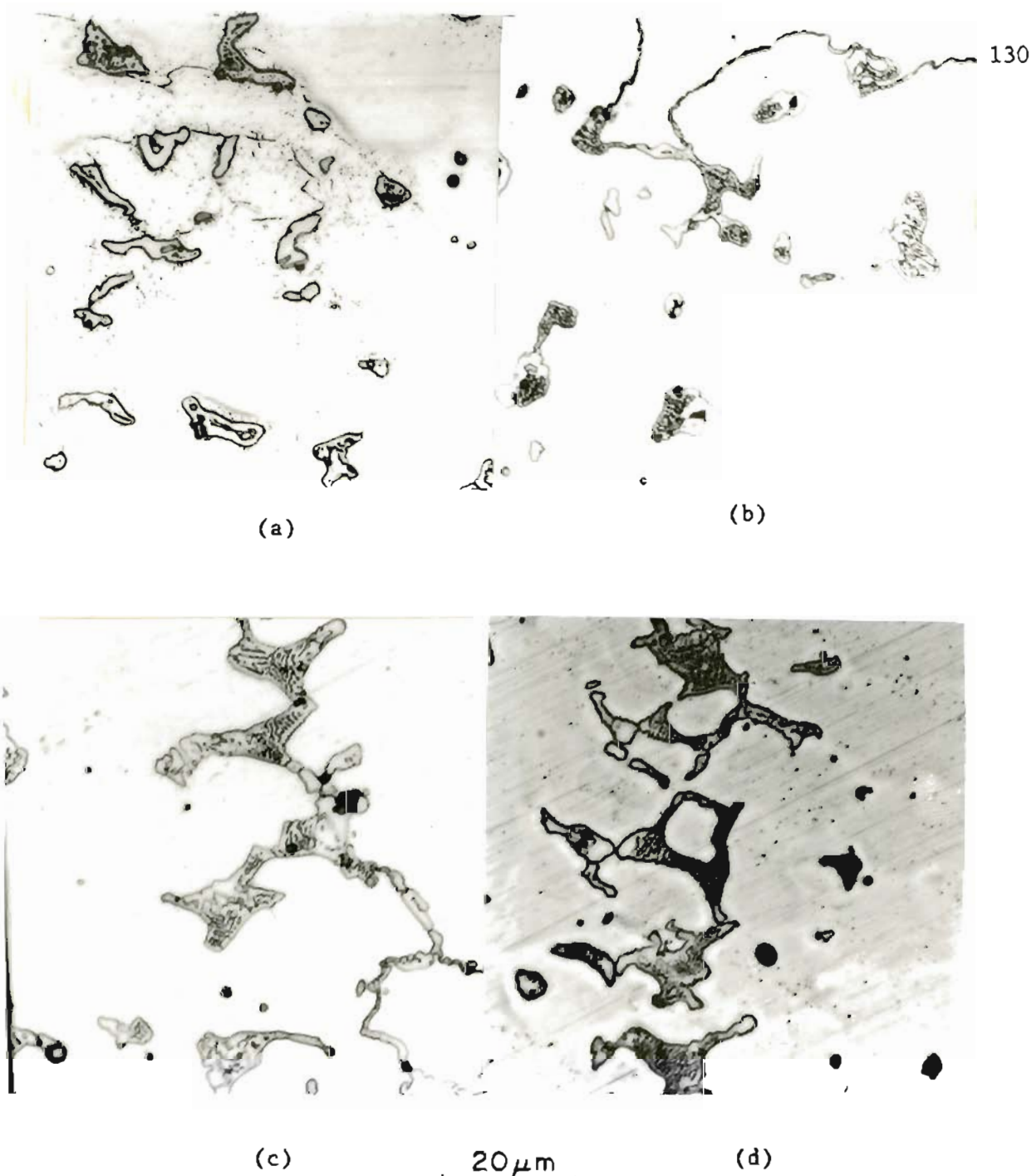

Figure 49. Weld metal micrographs, W4 powder.

a) T14-6, 50.6 HRA, 8.97 mg/m wear rate
Fe-15.7Mo-19.2Ni-0.05Si-0.06C
b) T14-7, 51.3 HRA, 10.54 mg/m wear rate
Fe-15.1Mo-21.4Ni-0.27Si-0.08C
c) T14-8, 51.7 HRA, 10.39 mg/m wear rate
Fe-16.6Mo-25.9Ni-0.66Si-0.06C
d) T15-2, 55 HRA, 10.34 mg/m wear rate
Fe-17.5Mo-26.0Ni-0.83Si-0.056C

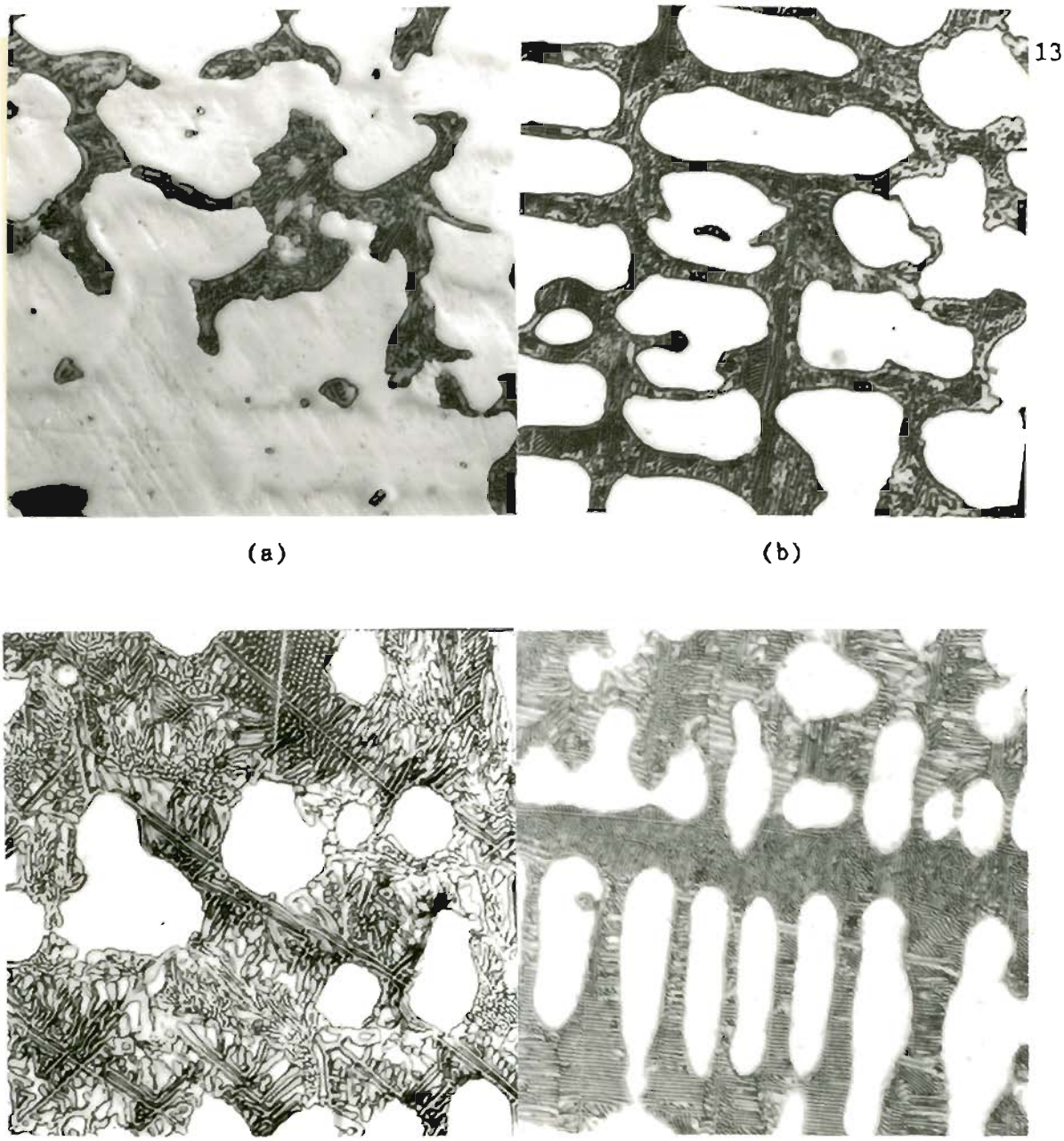

Figure 50. Weld metal micrographs, W5 powder.

a) T15-3, 56.0 HRA, 8.43 mg/m wear rate
Fe-17.4Mo-15.0Ni-0.65Si-0.13C
b) T15-4, 22.7 HRC, 9.65 mg/m wear rate
Fe-19.4Mo-17.4Ni-1.16Si-0.21C
c) T15-5, 38 HRC, 10.34 mg/m wear rate
Fe-23.5Mo-19.3Ni-2.35Si-0.35C
d) T15-6, 45.5 HRC, 9.05 mg/m wear rate
Fe-15.3Mo-11.0Ni-3.42Si-0.51C

(a)

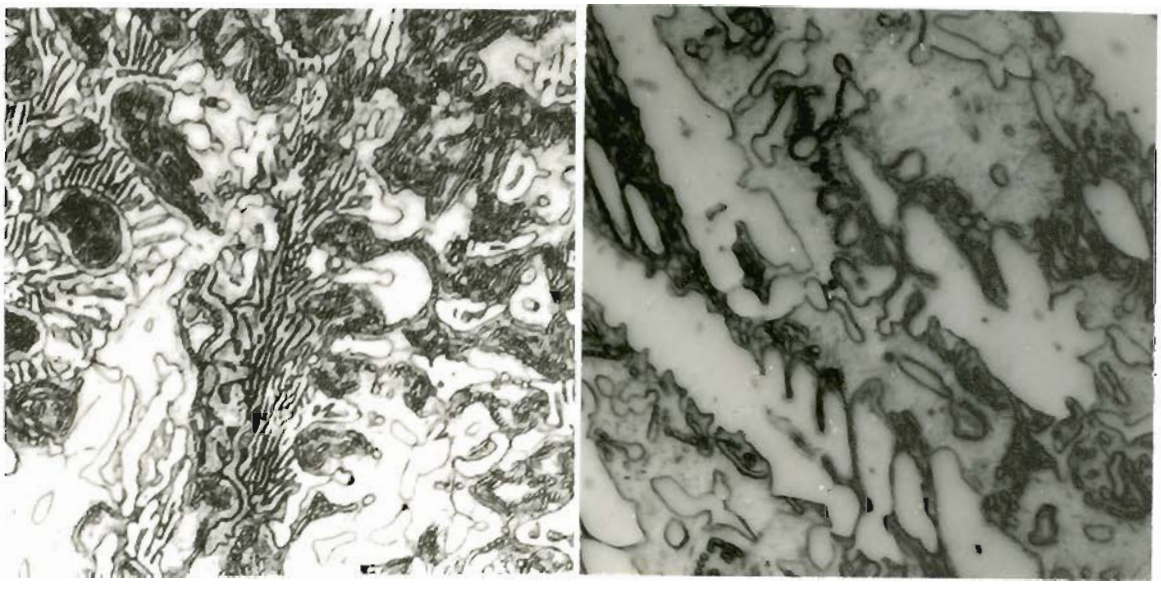

(b) 20μm (c)

Figure 51. Weld metal micrographs. W6 powder.

a) T20-3, 50.8 HRC, 7.49 mg/m wear rate
Fe-15.2Mo-10.8Ni-4.16Si-0.14C
b) T20-2, 45.4 HRC, 7.31 mg/m wear rate
Fe-17.6Mo-13.2Ni-5.04Si-0.14C
c) T20-4, 39.5 HRC, 6.33 mg/m wear rate
Fe-19.8Mo-14.9Ni-5.38Si-0.14C

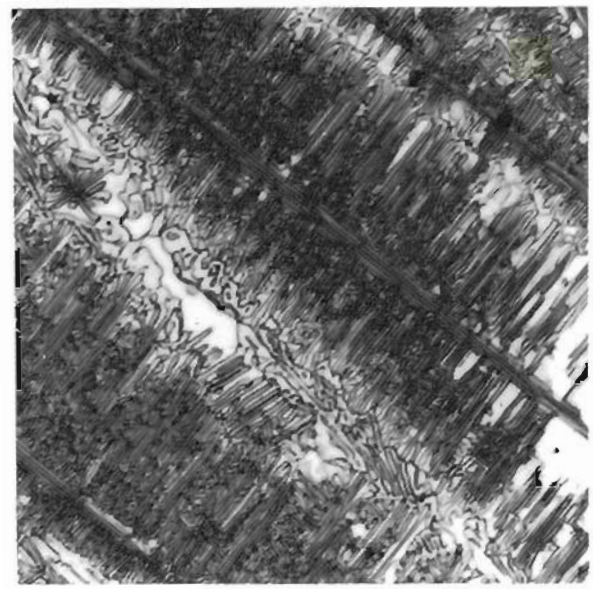

(a)

(b) 20μm (c)

Figure 52. Weld metal micrographs, W7 powder.

a) T18-3, 36.0 HRC, 10.43 mg/m wear rate
Fe-22.8Mo-18.9Ni-2.87Si-0.50C
b) T18-2, 36.8 HRC
Fe-25.0Mo-20.7Ni-3.16Si-0.56C
c) T18-1, 34.0 HRC, 10.25 mg/m wear rate
Fe-23.8Mo-19.0Ni-3.48Si-0.72C

(a)

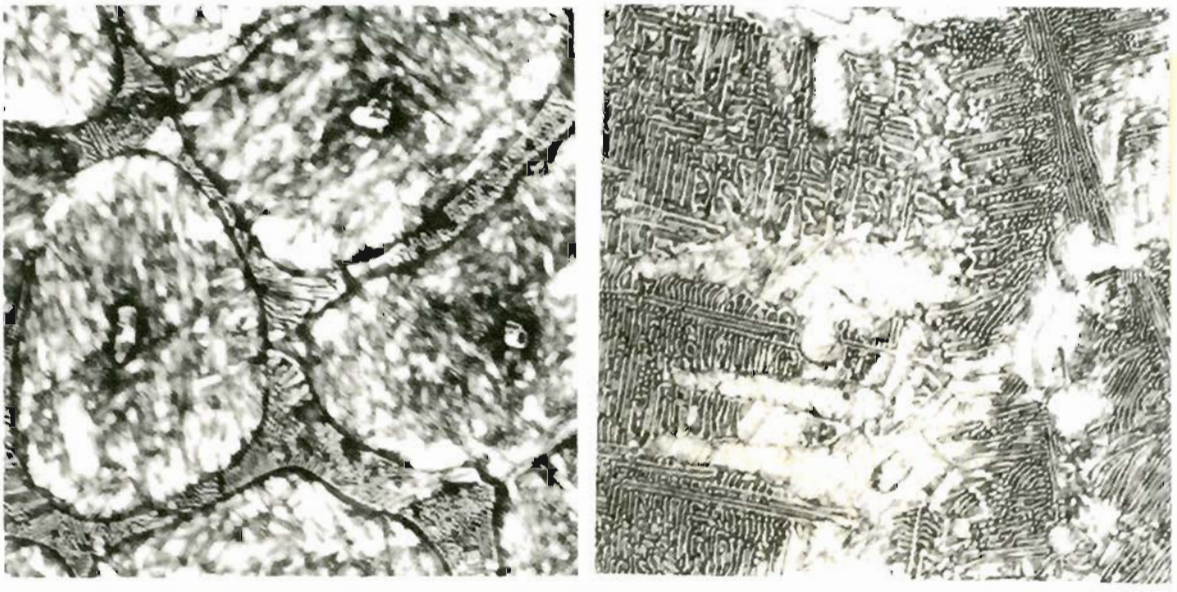

(b) 20μm (c)

Figure 53. Weld metal micrographs, W7 powder plus carbides.

a) T22-D, 52.9 HRC,
   7.44 mg/m wear rate
b) T22-4B1, 0.035 g/cm WC, 56 HRC
   7.57 mg/m wear rate
c) T22-4A1, 0.035 g/cm TiC, 55.6 HRC
   6.31 mg/m wear rate

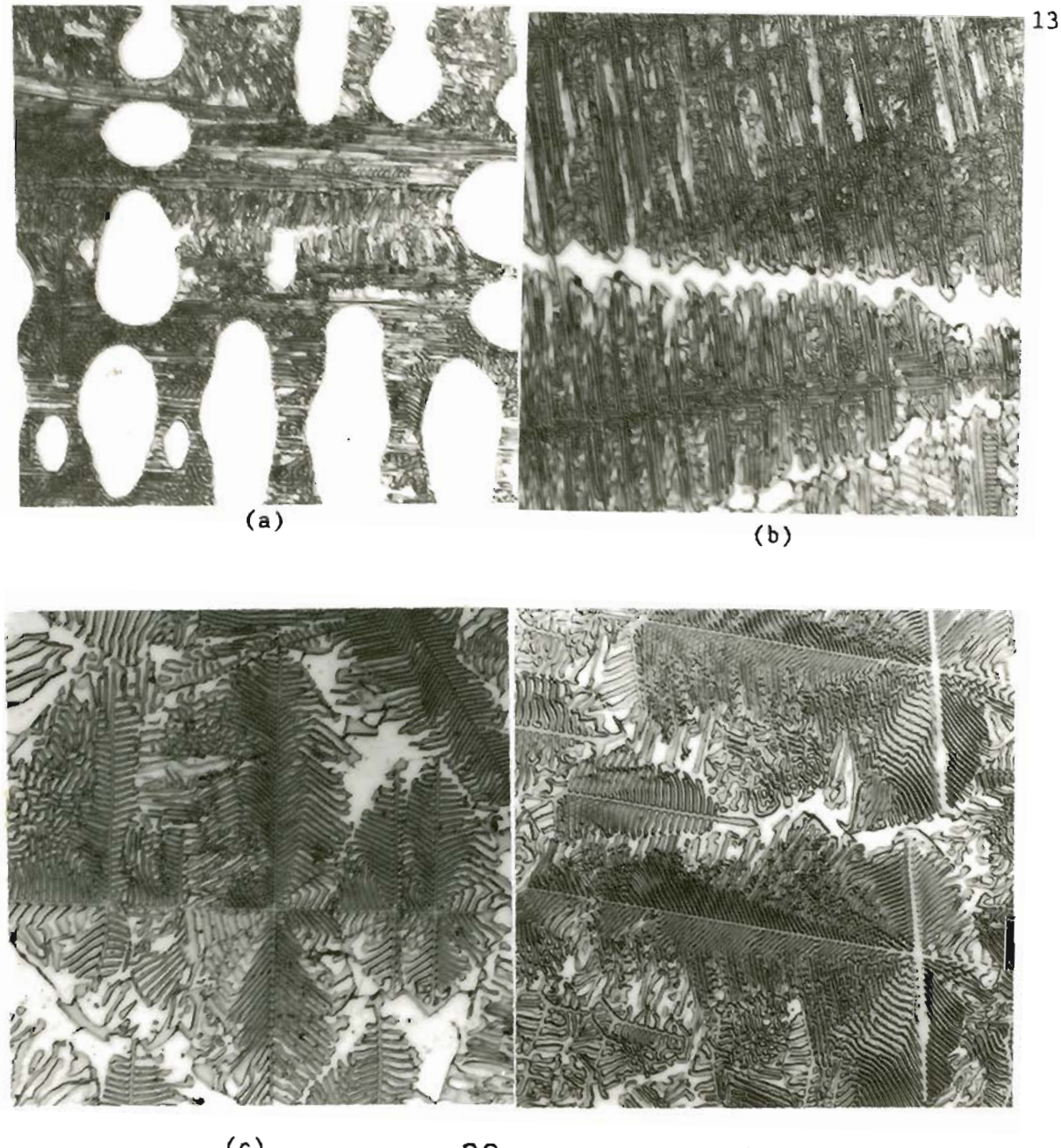

Figure 54. Weld metal micrographs, W8 powder.

a) T19-4, 31 HRC, 9.63 mg/m wear rate
Fe-20.5Mo-13.9Ni-1.38Si-0.57C
b) T19-1, 35.4 HRC, 10.3 mg/m wear rate
Fe-23.1Mo-19.8Ni-2.39Si-0.79C
c) T19-2, 32 HRC, 10.16 mg/m wear rate
Fe-23.6Mo-19.3Ni-2.71Si-0.94C
d) T19-3, 33 HRC, 11.1 mg/m wear rate
Fe-23.6Mo-19.5Ni-2.78Si-0.93C

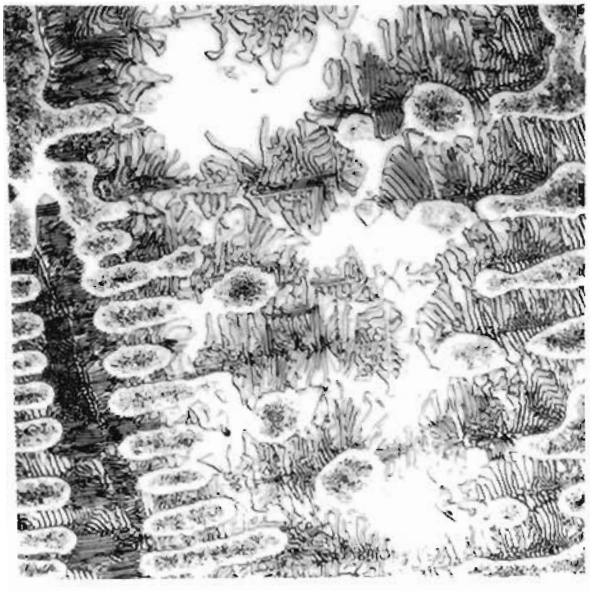

(a)

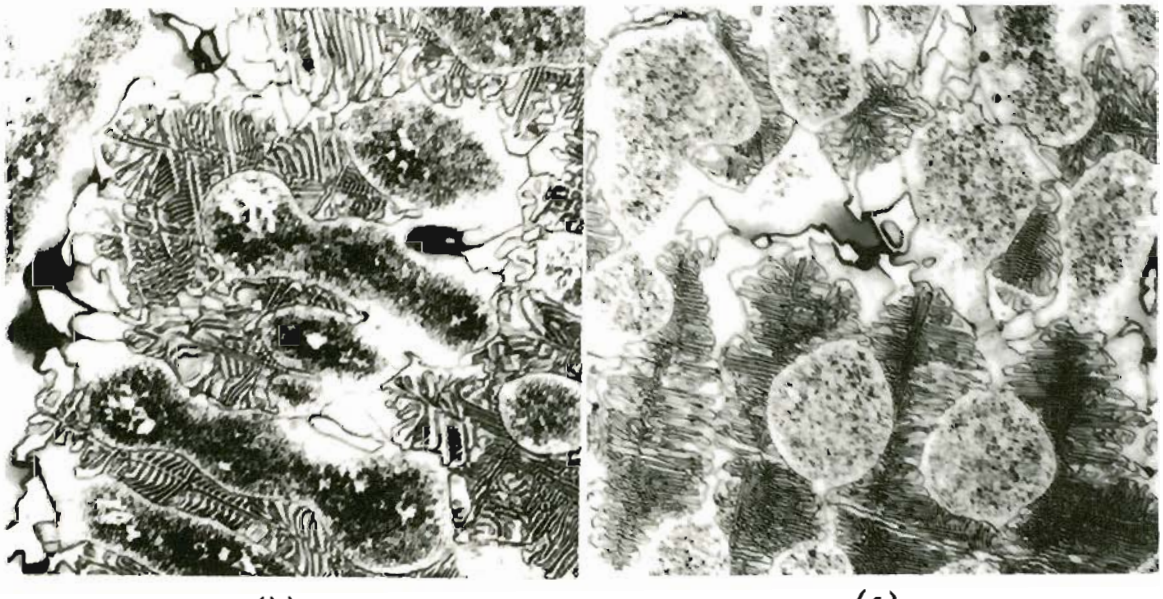

(b) (c)

20μm

Figure 55. Weld metal micrographs, W8 powder plus carbides.

a) T23-D, 43.6 HRC, 10.53 mg/m wear rate
b) T23-4A1, 0.035 g/cm TiC, 44 HRC, 4.44 mg/m wear rate
c) T23-4B1, 0.035 g/cm WC, 41.4 HRC, 5.08 mg/m wear rate

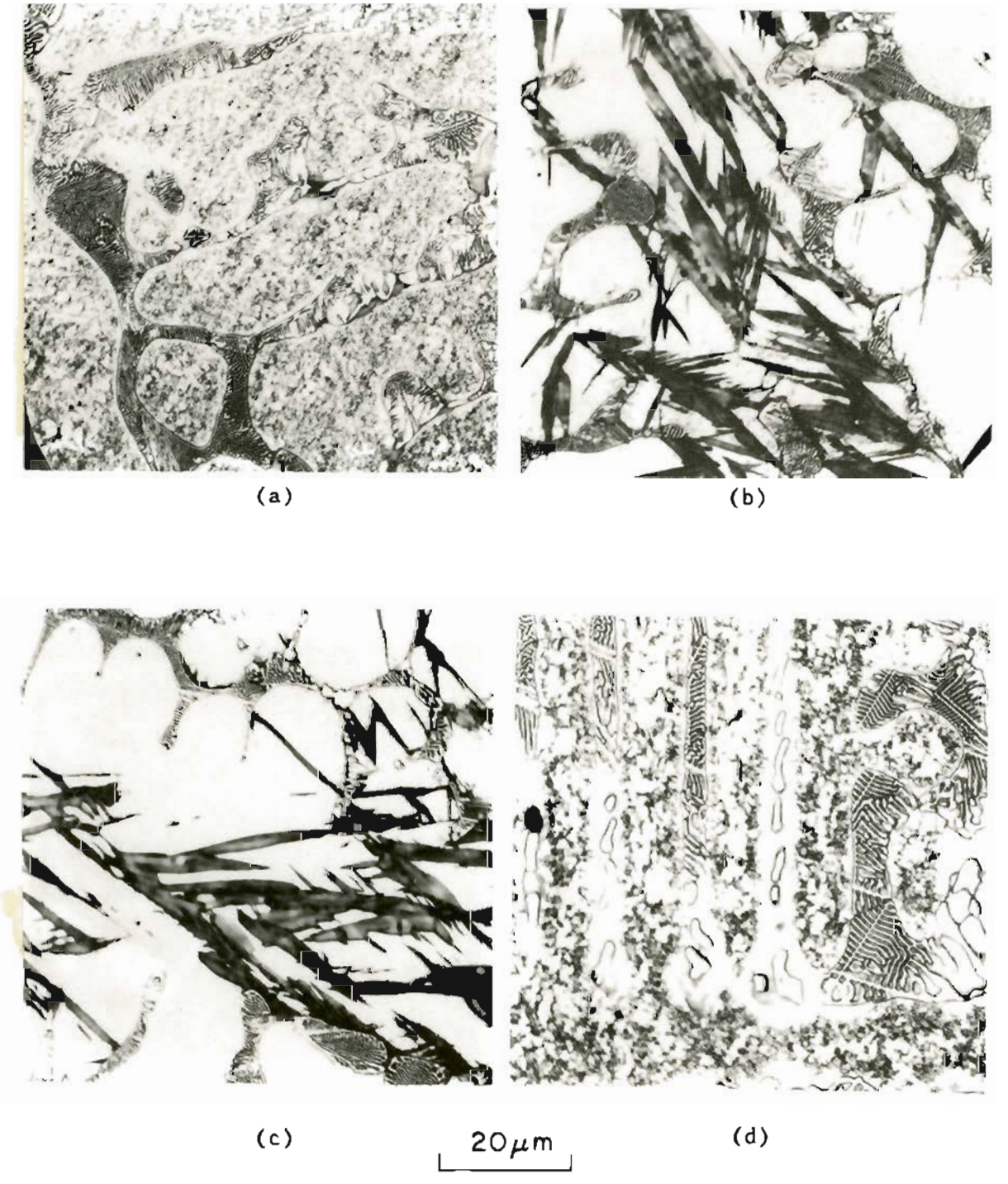

Figure 56. Weld metal micrographs, W9 powder plus carbides.

a) T24-1B1, 39.6 HRC, 4.14 mg/m wear rate
b) T24-1A1, 0.035 g/cm TiC, 42.6 HRC, 4.08 mg/m wear rate
c) T24-2A1, 0.035 g/cm HfC, 41.8 HRC, 4.24 mg/m wear rate
d) T24-2B1, 0.035 g/cm WC, 40.1 HRC, 4.15 mg/m wear rate

3.3 Melting Point Analysis

Alloys of 27 different compositions were produced by powder techniques and were tested in a Pirani-type melting point furnace. The compositions are shown in Table 20 along with melting point results. The melting point recorded in Table 20 represents the average of three different tests.

The alloys were based on the composition Fe-21Mo-15Ni-5Si which corrosponded to the weld composition with the best wear resistance while not having carbides in the microstructure. High and low molybdenum contents were 25 and 17 wt.% respectively. High and low nickel contents were 20 and 10 wt.%. For silicon the high content was 6 wt.% and the low was 4 wt.%. Figure 57 shows the region of the three-dimensional quartenary tetrahedron phase diagram in which the alloys were made. Figures 58, 59, and 60 show contour maps of the measured solidus surface at molybdenum contents of 17, 21, and 25 wt.%. A Student's T-test at a confidence interval of 99.9% was made between each adjacent point to insure that their values, the mean of six tests, were different.

After melting points were measured, samples were arc-melted to form a button which was sectioned, polished, and etched for metallography. Table 20 includes a synopsis of the microstructures produced after arc-melting. Photomicrographs of the various structures are shown in Figures 61 to 69. These are arranged into three groups of molybdenum contents each with three sub-groups of nickel levels. Figures 61 to 63 are of 25 wt.% Mo alloys, Figures 64 to 66 are for 21 wt.% Mo alloys, and Figures 67 to 69 the 17 wt.% Mo alloys.

From examination of the microstructures and melting point results, few trends were evident. In general, as silicon content increased the

melting point tended to decrease. Other than this observation there was no apparant correlation between the melting point, the composition, and the microstructure observed. Microstructures ranged from a 100% coarse lamellar structure to mixtures of coarse and fine lamellar phases to columnar dendrites plus a coarse interdendritic eutectic.

Table 20
Synopsis of melting point study results

CD = Columnar dendrites CE = Coarse eutectic
IL = Interlamellar phase ID = Interdendritic phase
M = Matrix phase FL = Fine lamellar phase

	Composition	Melting Point	Microstructure*
1.	25Mo-20Ni-6Si	1263.8±5.11°C	50% CD + 50% CE
2.	25Mo-15Ni-5Si	1290.5±5.92°C	30% CD + 70% CE
3.	25Mo-10Ni-4Si	1355.8±4.95°C	20% CD + 80% CE + IL
4.	25Mo-20Ni-4Si	1312.5±9.05°C	20% CD + 80% CE + IL
5.	25Mo-10Ni-6Si	1310.2±7.44°C	20% CD + 80% CE
6.	25Mo-20Ni-5Si	1282.8±2.40°C	40% CD + 60% CE
7.	25Mo-15Ni-6Si	1267.0±5.44°C	60% CD + 40% CE
8.	25Mo-10Ni-5Si	1317.2±7.83°C	60% CD + 40% CE
9.	25Mo-15Ni-4Si	1317.8±4.35°C	30% CD + 70% CE + IL
10.	21Mo-15Ni-5Si	1283.3±10.39°C	20% CD + 75% CE + IL/ID
11.	21Mo-10Ni-4Si	1333.8±14.22°C	5% CD + 95% CE + IL
12.	21Mo-20Ni-6Si	1238.5±4.72°C	40% CD + 40% CE + 20%M
13.	21Mo-15Ni-4Si	1325.8±4.71°C	20% CD + 50% CE + 30% M + IL/ID
14.	21Mo-10Ni-5Si	1327.0±6.96°C	20% CD + 80% CE + IL
15.	21Mo-15Ni-6Si	1279.3±4.68°C	30% CD + 70% CE + IL
16.	21Mo-20Ni-5Si	1295.3±5.20°C	10% CD + 90% CE
17.	21Mo-10Ni-6Si	1308.3±7.92°C	10% CD + 85% CE + 5%FL
18.	21Mo-20Ni-4Si	1313.3±6.02°C	5% CD + 95% CE
19.	17Mo-10Ni-4Si	1344.8±8.28°C	25% CD + 25% CE + 50%M
20.	17Mo-15Ni-5Si	1301.2±6.99°C	80% CE + 20% FL
21.	17Mo-20Ni-6Si	1259.0±6.57°C	10% CD + 90% CE

(Table 20 continued)

22.	17Mo-10Ni-6Si	1297.5±12.44°C	5% CD + 95% CE
23.	17Mo-20Ni-4Si	1319.3±6.56°C	70% CE + 30% FL
24.	17Mo-10Ni-5Si	1334.7±12.43°C	75% CE + 25% FL
25.	17Mo-15Ni-4Si	1322.0±10.1°C	20% CE + 50% FL + 30% M + IL
26.	17Mo-15Ni-6Si	1264.3±4.84°C	5% CD + 95% CE
27.	17Mo-20Ni-5Si	1270.3±5.08°C	95% CE + 5% M

*Microstructure percentages from visual observation only.

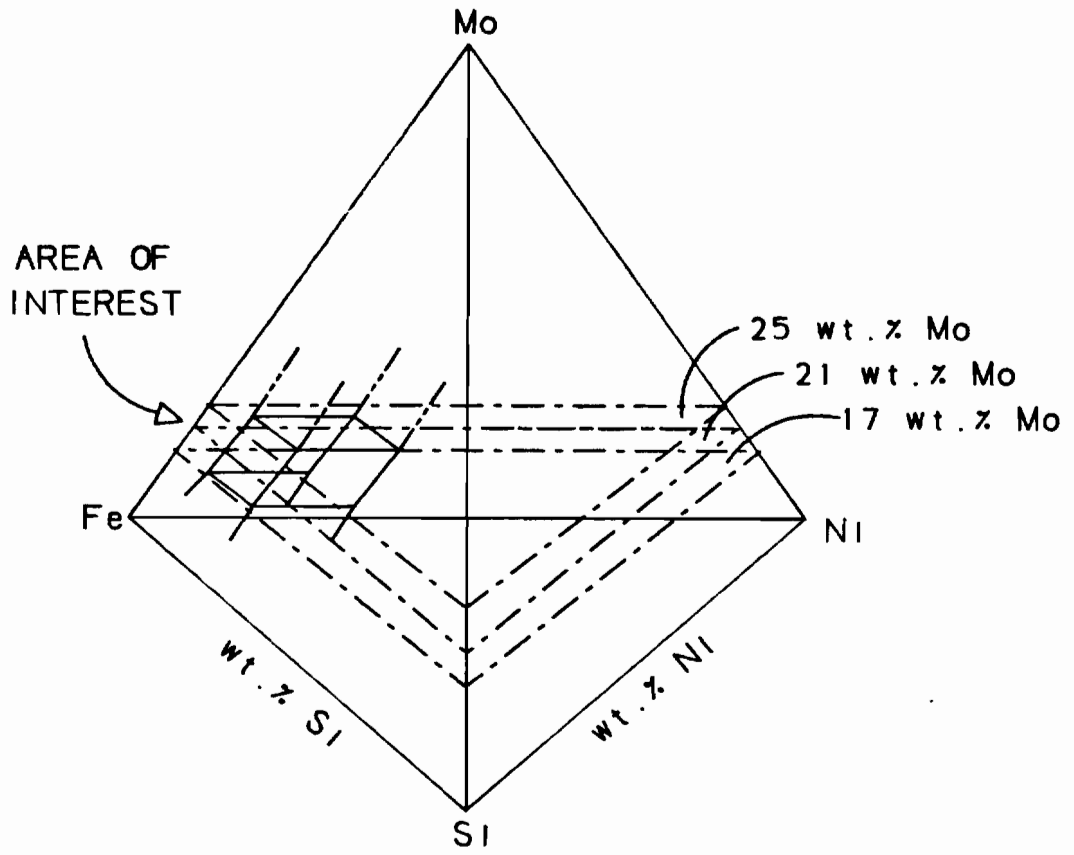

Figure 57. Area of interest in Fe-Mo-Ni-Si quartenary phase tetrahedron.

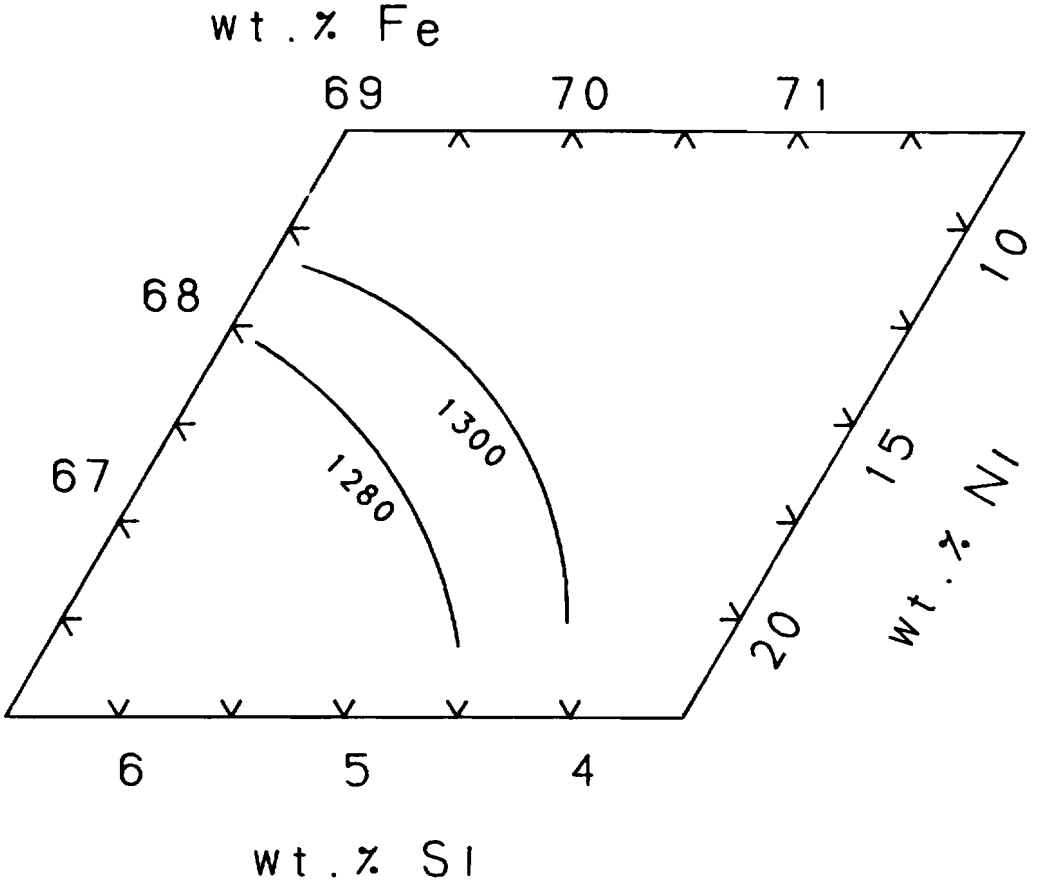

Figure 58. Temperature contours of solidus surface for alloys containing 17 wt.% molybdenum.

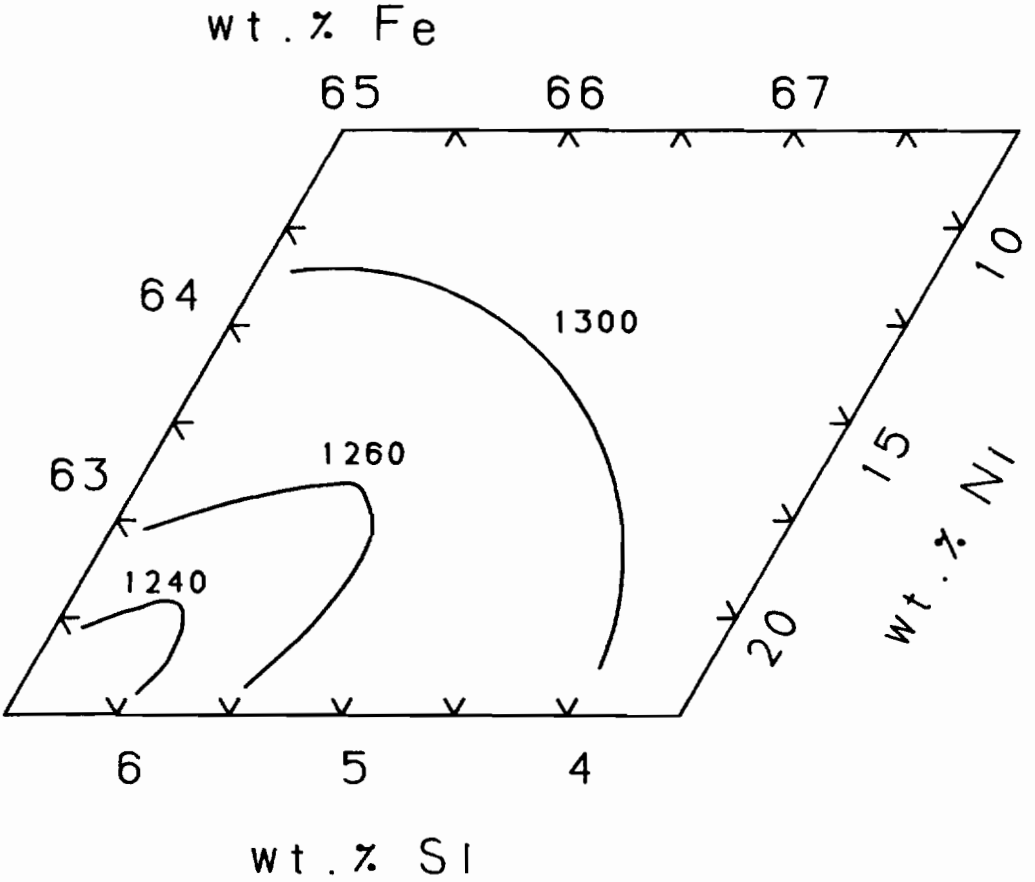

Figure 59. Temperature contours of solidus surface for alloys containing 21 wt.% molybdenum.

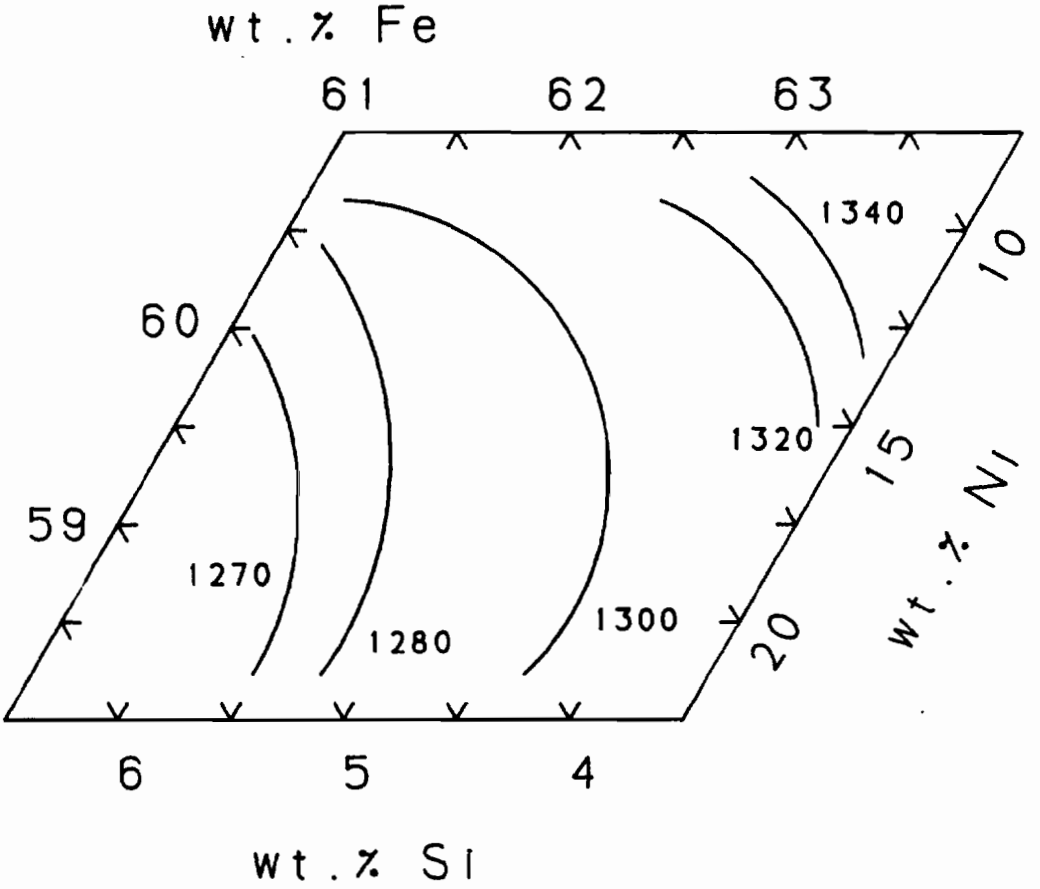

Figure 60. Temperature contours for solidus surface of alloys containing 25 wt% molybdenum.

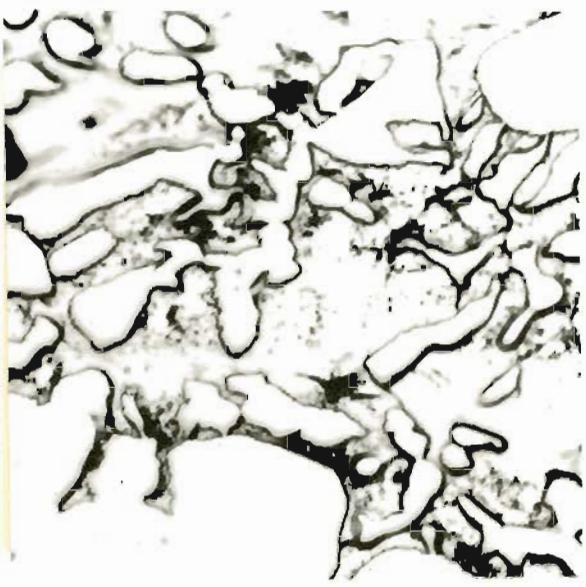

(a)

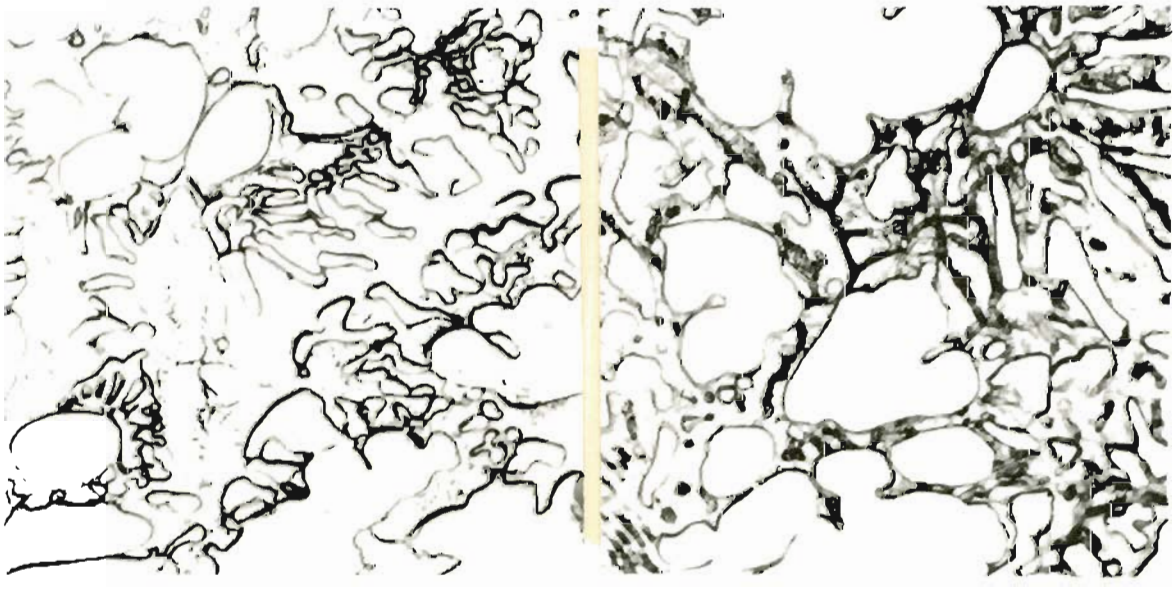

(b) (c)

20μm

Figure 61. Arc-melted melting point sample microstructures.

a) Fe-25Mo-20Ni-6Si b) Fe-25Mo-20Ni-5Si c)Fe-25Mo-20Ni-4Si

(a)

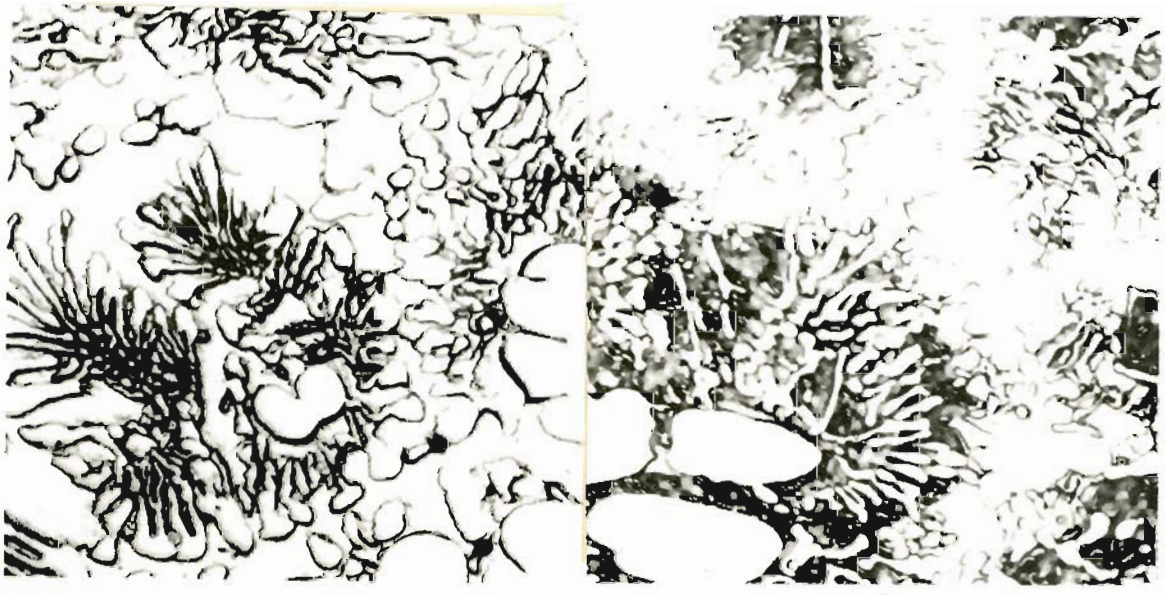

(b) (c)

20μm

Figure 62. Arc-melted melting point sample microstructures.

a) Fe-25Mo-15Ni-6Si b) Fe-25Mo-15Ni-5Si c) Fe-25Mo-15Ni-4Si

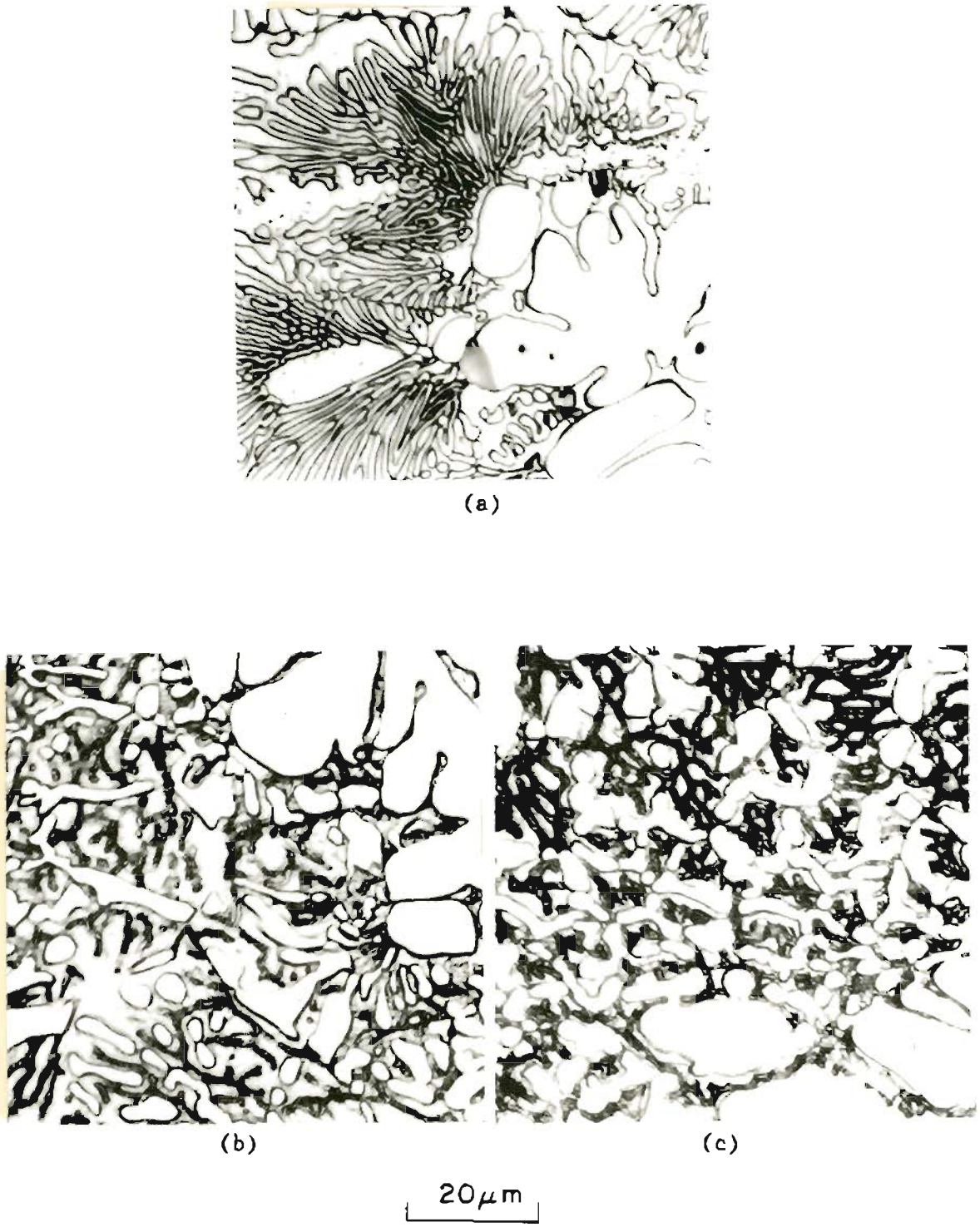

Figure 63. Arc-melted melting point sample microstructures.

a) Fe-25Mo-10Ni-6Si b) Fe-25Mo-10Ni-5Si c) Fe-25Mo-10Ni-4Si

(a)

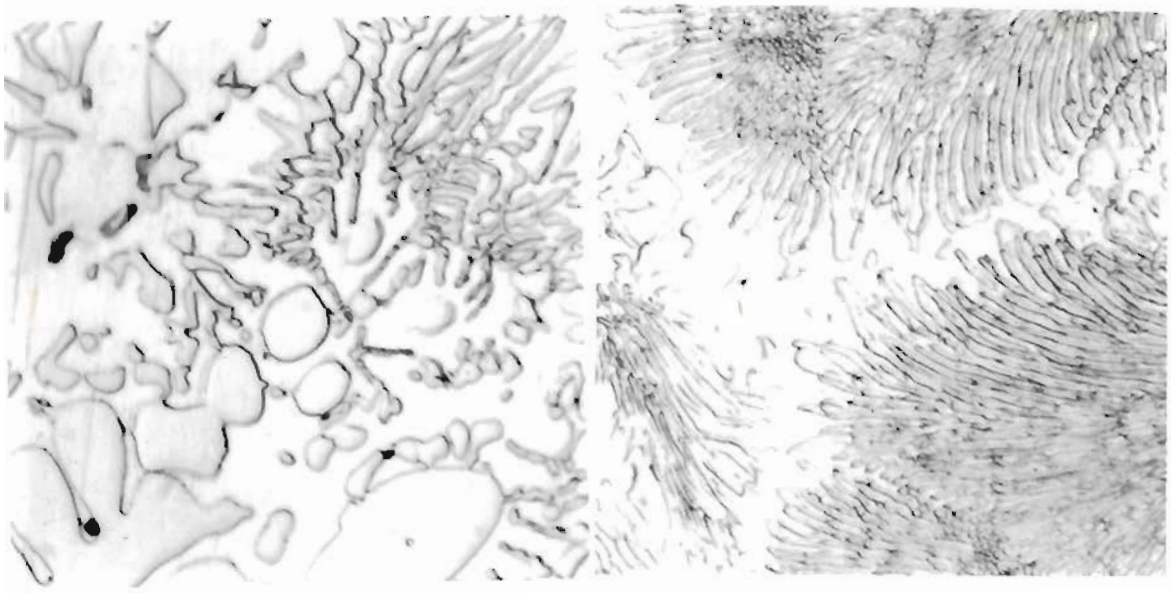

(b) (c)

20μm

Figure 64. Arc-melted melting point sample microstructures.

a) Fe-21Mo-20Ni-6Si b) Fe-21Mo-20Ni-5Si c) Fe-21Mo-20Ni-4Si

(a)

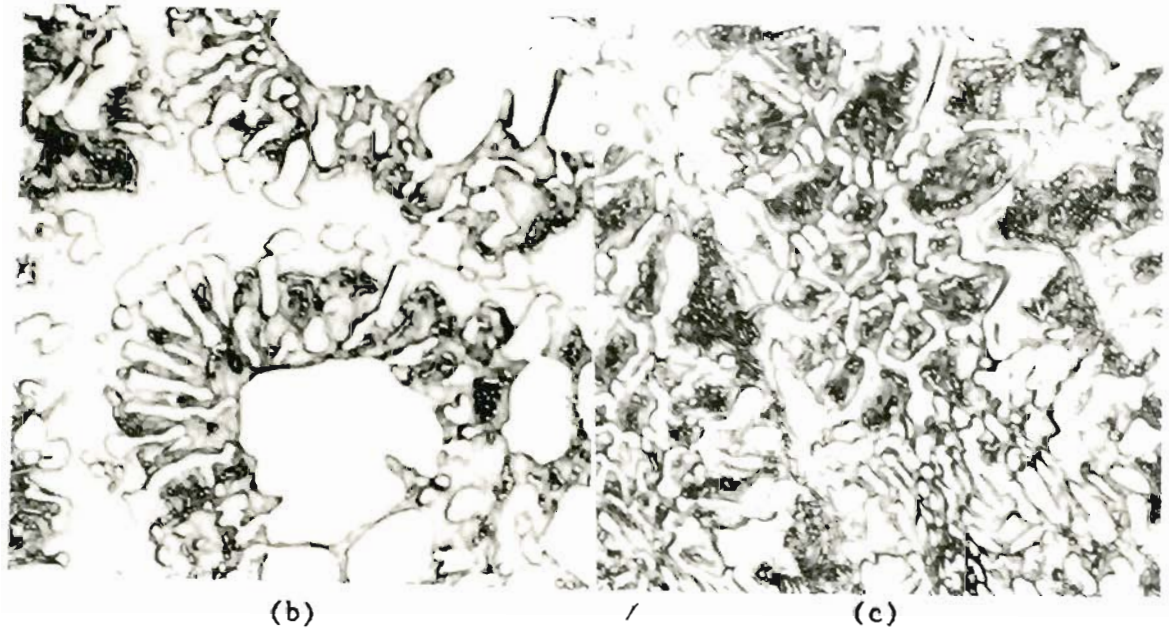

(b) (c)

20μm

Figure 65. Arc-melted melting point sample microstructures.

a) Fe-21Mo-15Ni-6Si b) Fe-21Mo-15Ni-5Si c) Fe-21Mo-15Ni-4Si

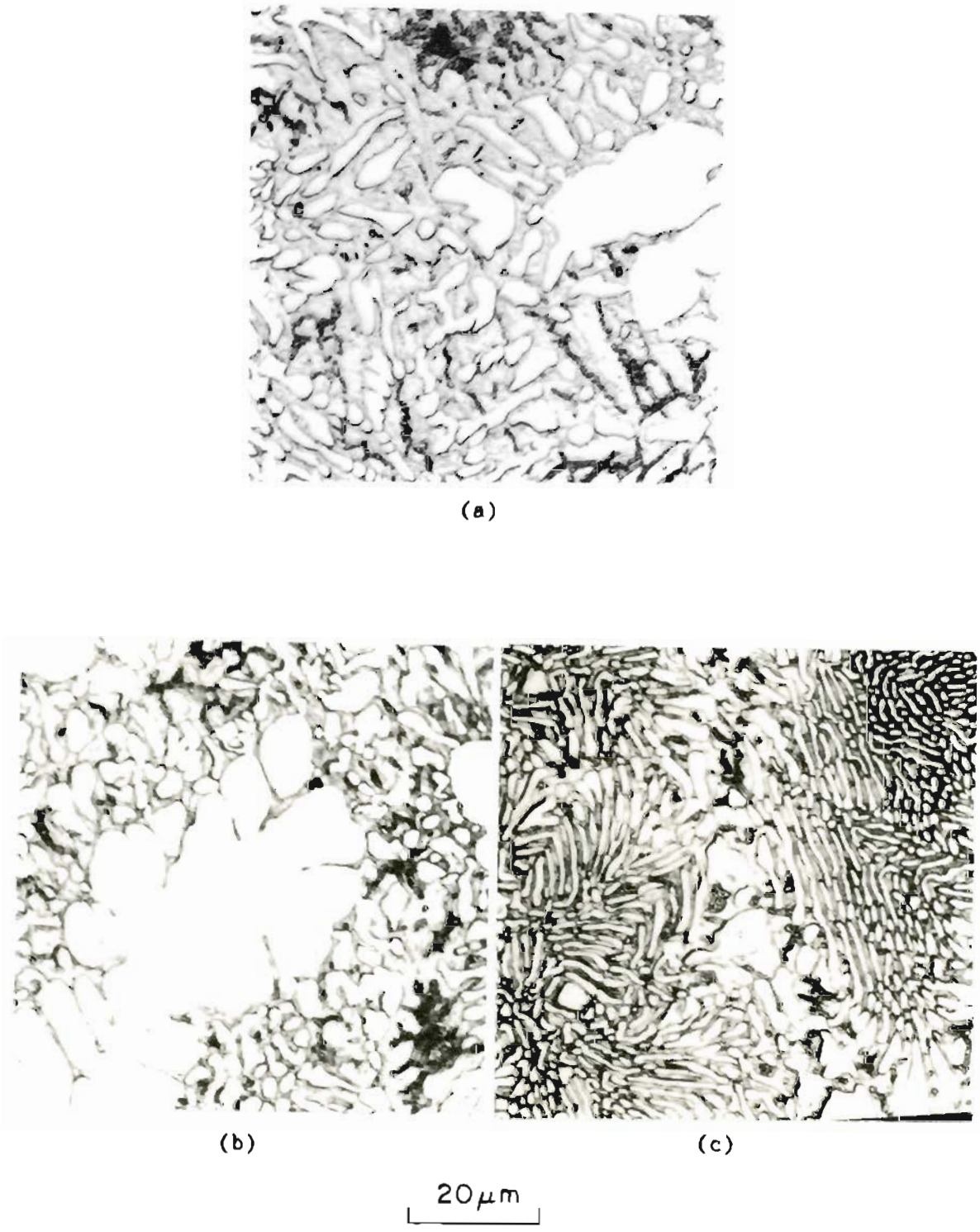

Figure 66. Arc-melted melting point sample microstructures.

a) Fe-21Mo-10Ni-6Si b) Fe-21Mo-10Ni-5Si c) Fe-21Mo-10Ni-4Si

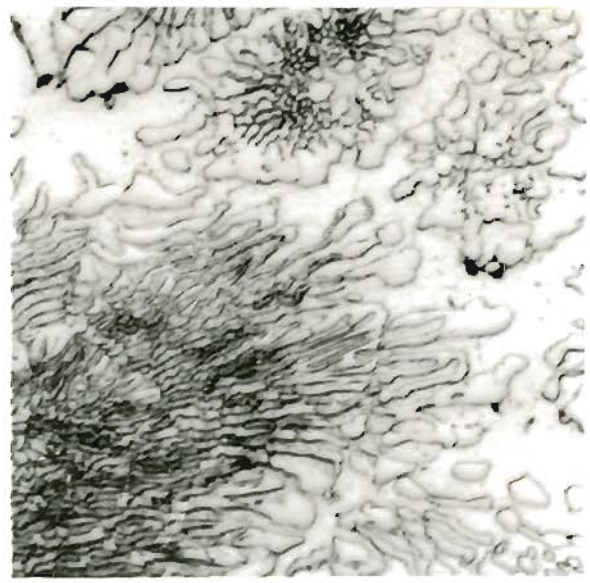

(a)

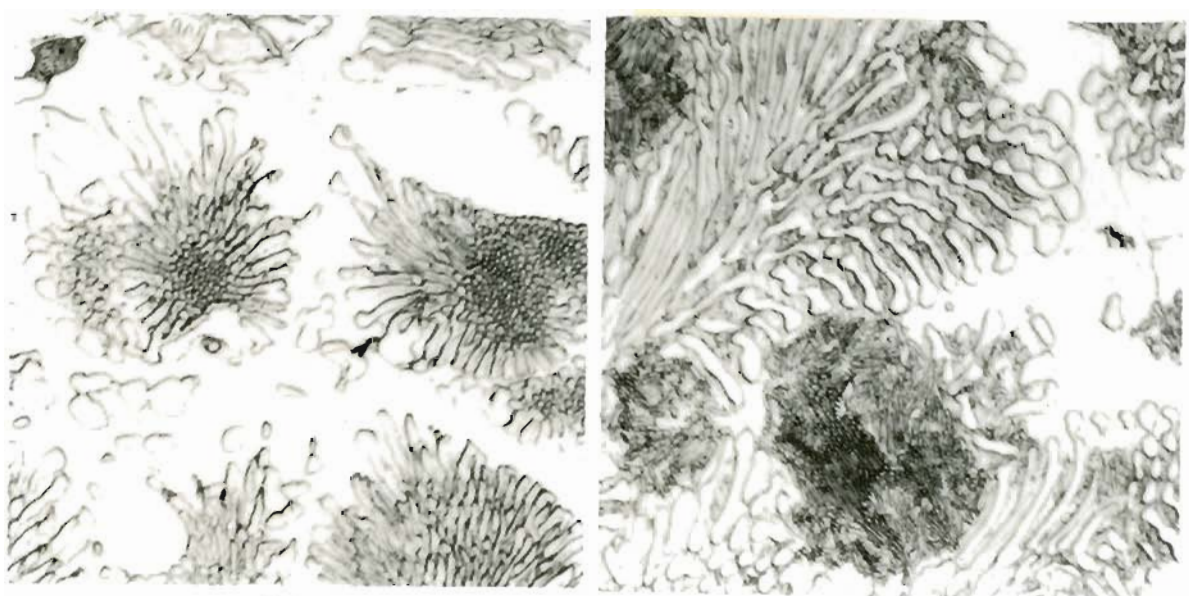

(b) (c)

20μm

Figure 67. Arc-melted melting point sample microstructures.

a) Fe-17Mo-20Ni-6Si b) Fe-17Mo-20Ni-5Si c) Fe-17Mo-20Ni-4Si

(a)

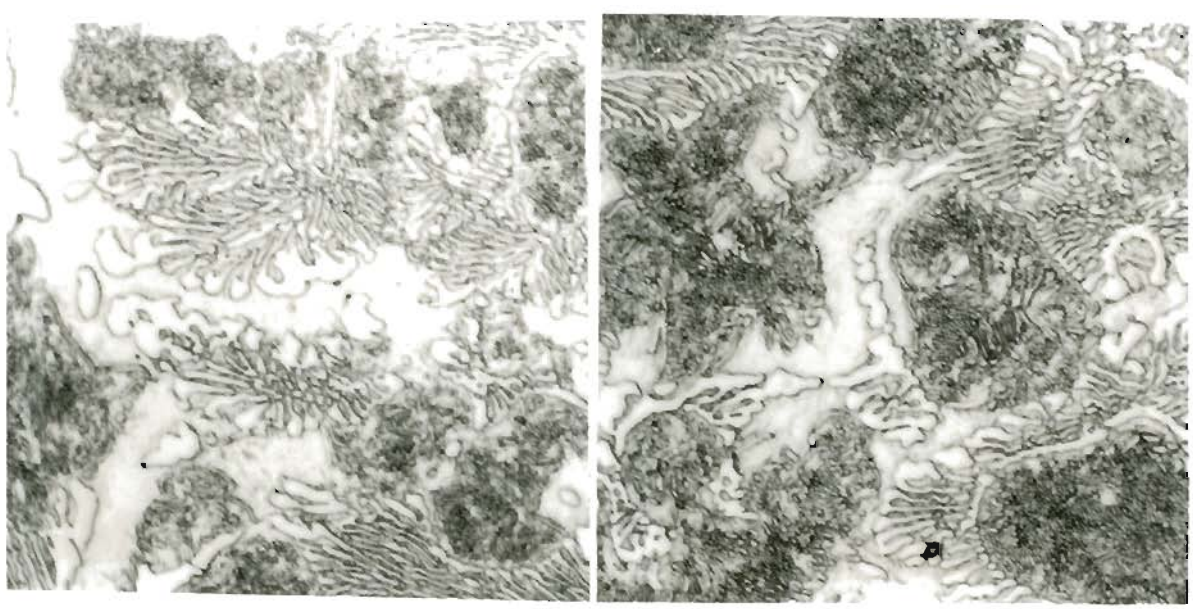

(b) (c)

20μm

Figure 68. Arc-melted melting point sample microstructures.

a) Fe-17Mo-15Ni-6Si b) Fe-17Mo-15Ni-5Si c) Fe-17Mo-15Ni-4Si

(a)

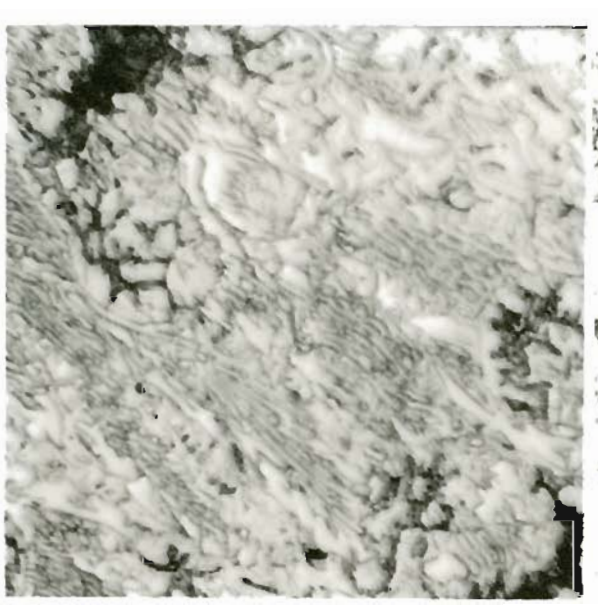

(b)

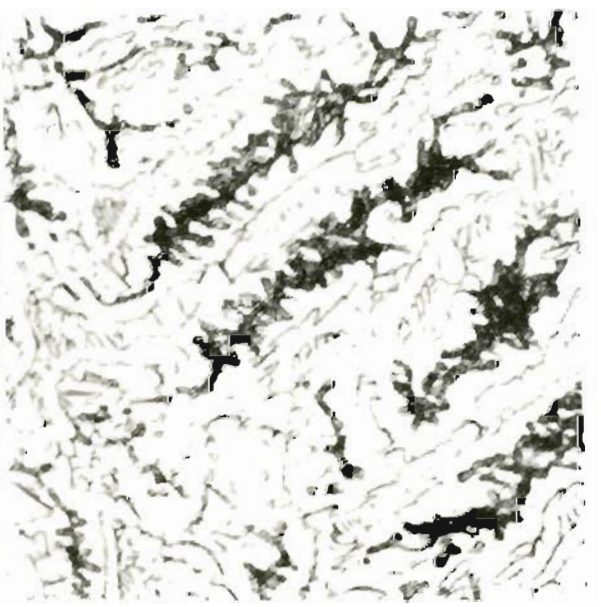

(c)

20μm

Figure 69. Arc-melted melting point sample microstructures.

a) Fe-17Mo-10Ni-6Si b) Fe-17Mo-10Ni-5Si c) Fe-17Mo-10Ni-4Si

3.4 Heat-Treatment Analysis

Weld deposits with a chemistry similar to intermetallic-containing welds with the best wear resistance were heat-treated to investigate the relative stability of the intermetallic compounds and any subsequent hardness changes. The heat- treatments thus served a two-fold purpose; 1) they enabled some prediction on the response of the weld deposit to multipass welds, and 2) they provided an indication of the ability to increase wear resistance through heat-treatment.

Using a 5Mo-5Ni filler wire and the W6 powder shown in Table 16 a series of optimized welds were made on a mild steel plate to study effects of time and temperature on the weld metal microstructure and hardness. Two weld series were produced. The T25 series used 15 g/in of W6 powder and the T26 series used 20 g/in of the W6 powder. The welds were sectioned into bars 1.2 cm wide by 1.1 cm thick transverse to the weld. These bars were cut to a length of approximately 15 cm and surface ground to a thickness of 10 cm, essentially the size of standard Charpy bars. The bars were heat-treated in an air furnace at temperatures from 300 to 1100°C for times of 1 to 100 hours. The complete heat-treatment matrix is shown in Table 21. Results of the heat treatments in terms of hardness change were plotted versus temperature (Figures 70 and 71) and time (Figures 72 and 73). A plot showing only data from 2 hour heat treatments of T25 and T26 welds is shown in Figure 74.

The T25 and T26 weld series showed similar behaviours with the changing heat treatment times. Generally, hardnesses increased with time in both weld series at the 400°C heat treatment. Hardnesses decreased with time

at all other temperatures. With respect to temperature, both weld series showed a peak in hardness increase between 400 and 600°C and a gradual decrease in hardness at temperatures above 700°C.

Metallography was performed on all the heat treated samples. Structures produced at various times and temperatures between the two weld series were similar. Photomicrographs of the T25 weld series are shown in Figures 75 to 88. Throughout the heat treatments the structure of the coarse eutectic visible in untreated samples remained relatively unchanged, even up to 1100°C. Changes were seen in the dendritic regions, in the regions of matrix between eutectic cells, and between the non-intermetallic lamella of the coarse eutectic. At 500 to 600°C a second phase begins to appear in the matrix. As times increase at 600°C this second phase grows from the lamella of the coarse eutectic into matrix regions. At high temperatures discrete particles form in the matrix and by 1100°C the particles are numerous and visible with optical microscopy.

Table 21

Heat Treatment Schedule

	1hr	2hrs	4hrs	8hrs	24hrs	100hrs
300		X			X	
400	X	X	X	X	X	X
500		X			X	
600	X	X	X	X	X	X
700		X			X	
800	X	X	X	X	X	X
900		X			X	
1000	X	X	X	X	X	X
1100		X			X	

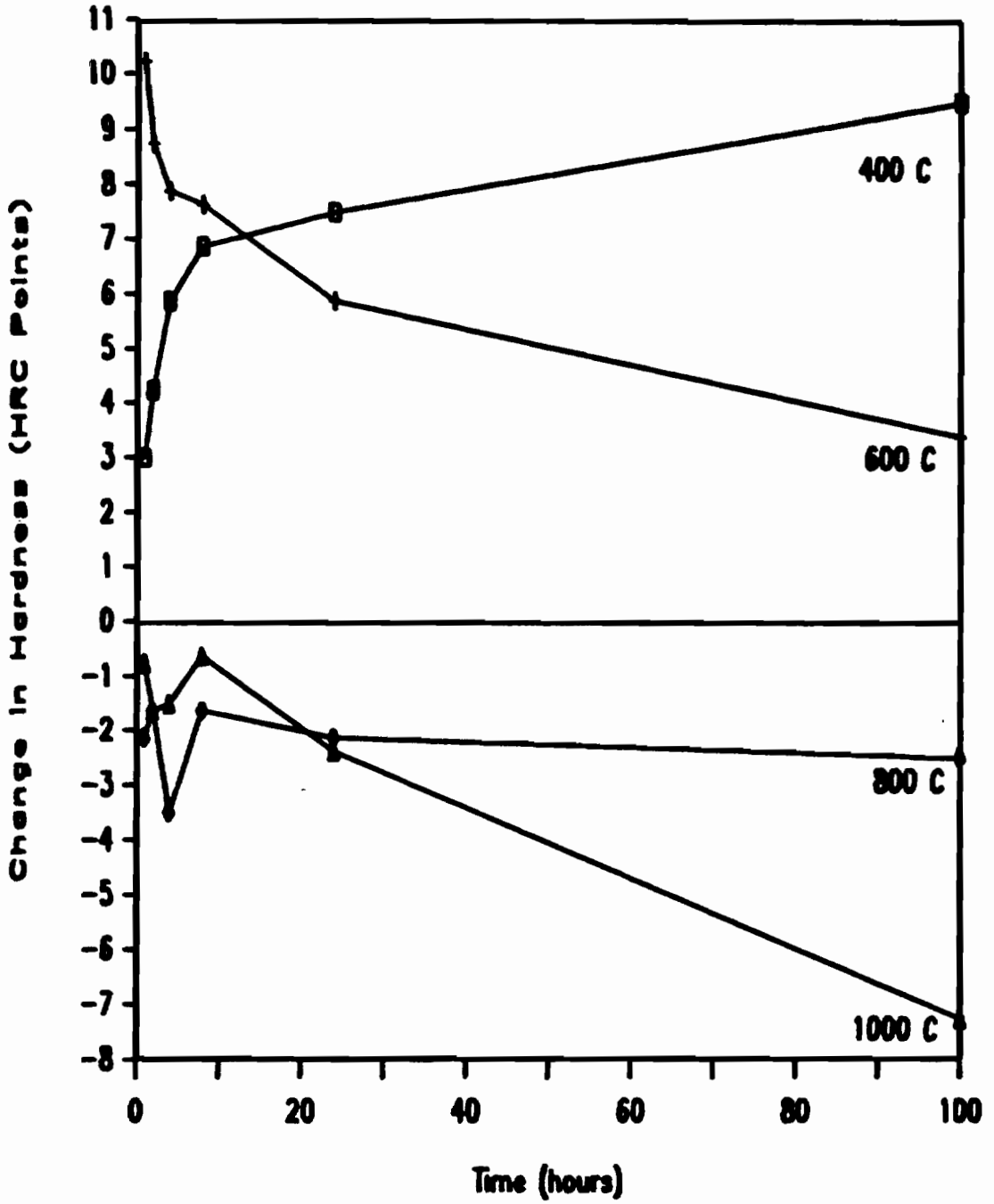

Figure 70. Change in hardness versus time for T25 weld series.

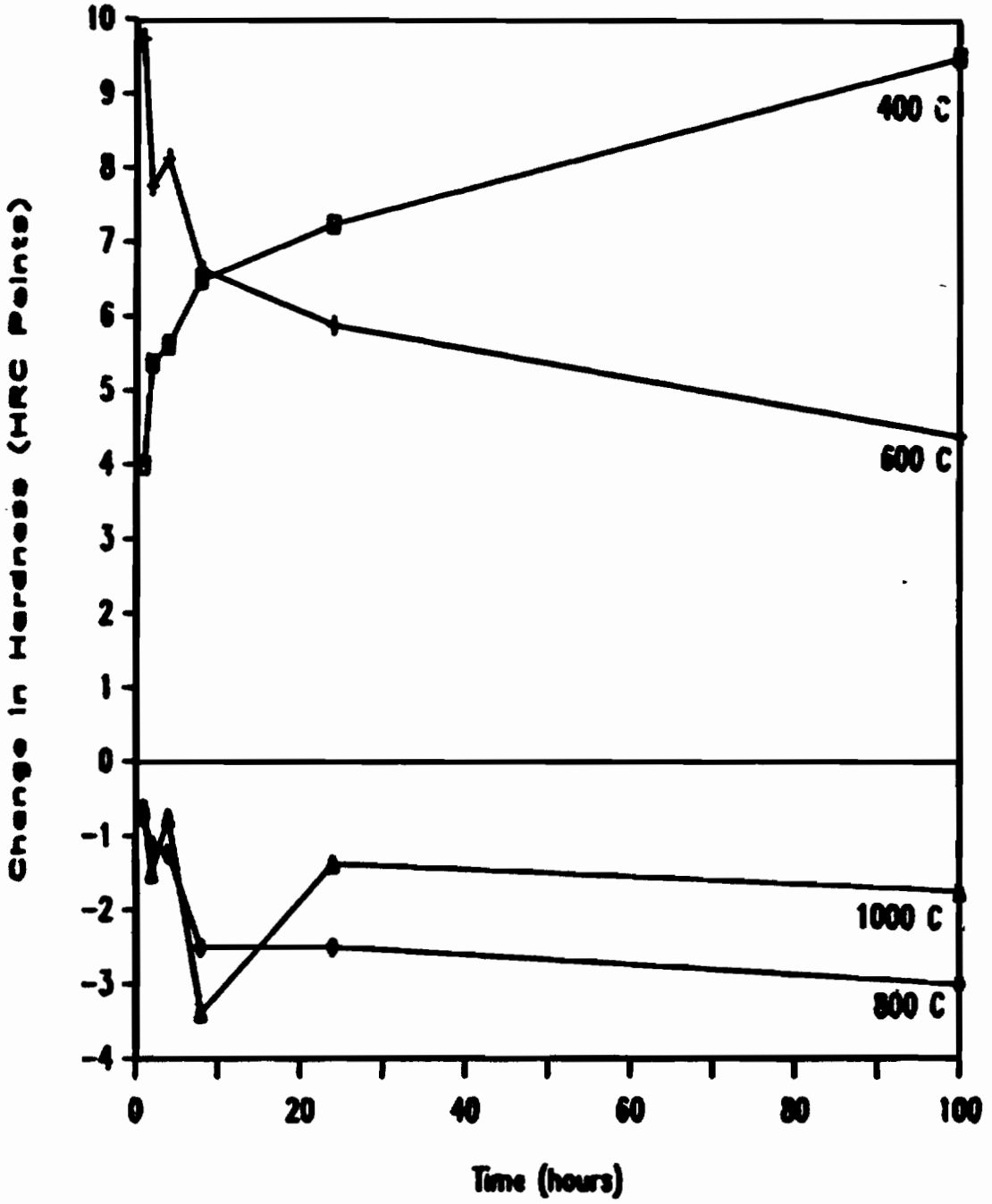

Figure 71. Change in hardness versus time for T26 weld series.

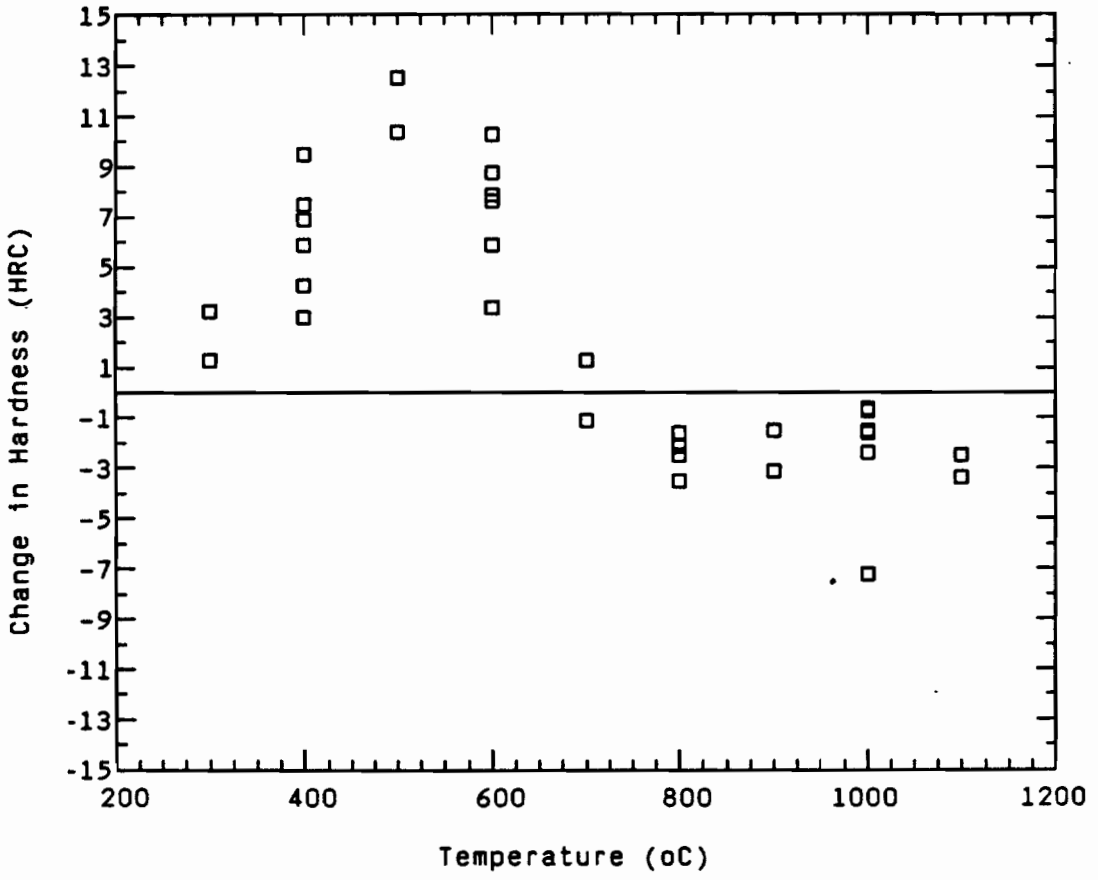

Figure 72. Change in hardness versus temperature for T25 weld series.

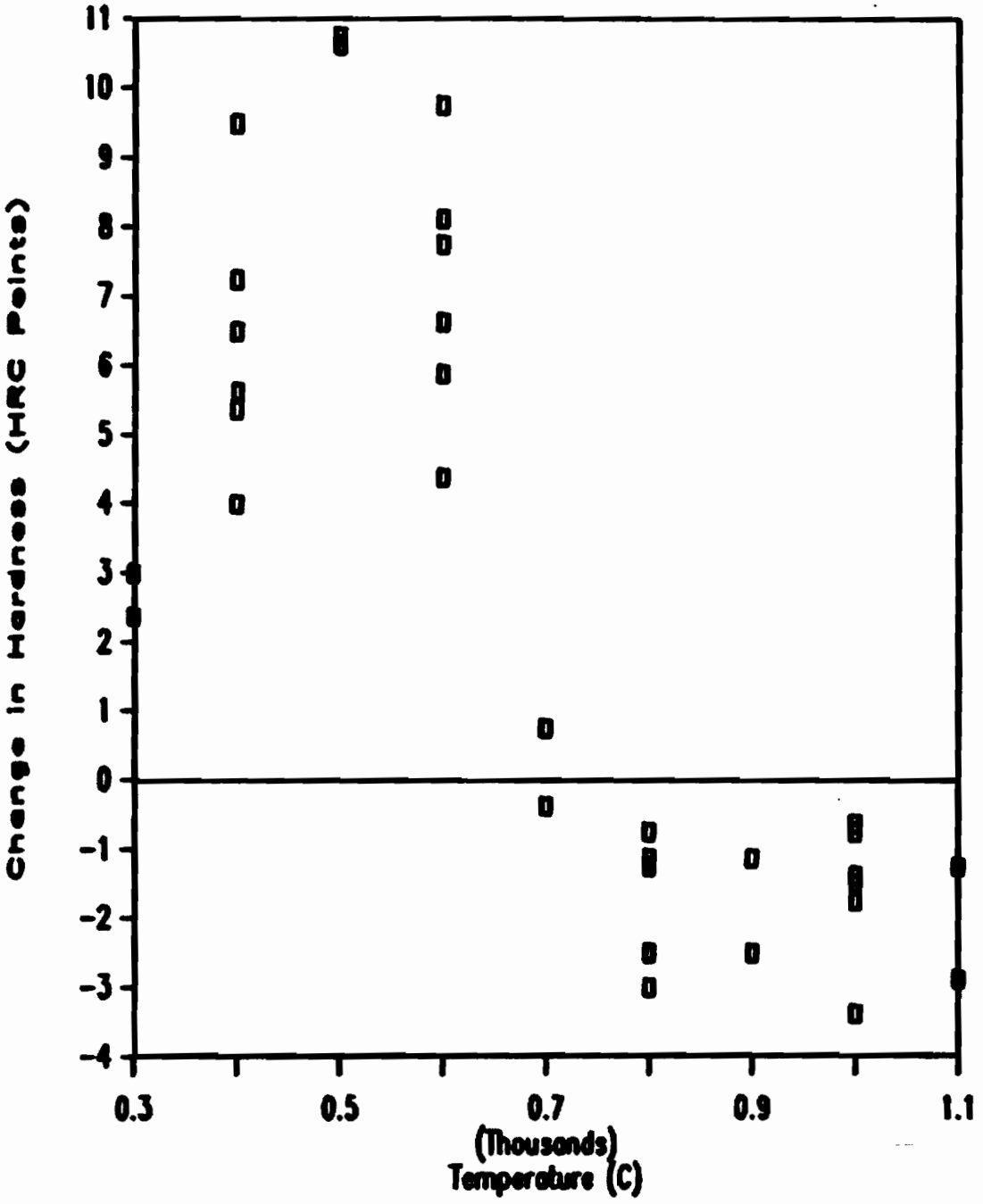

Figure 73. Change in hardness versus temperature for T26 weld series.

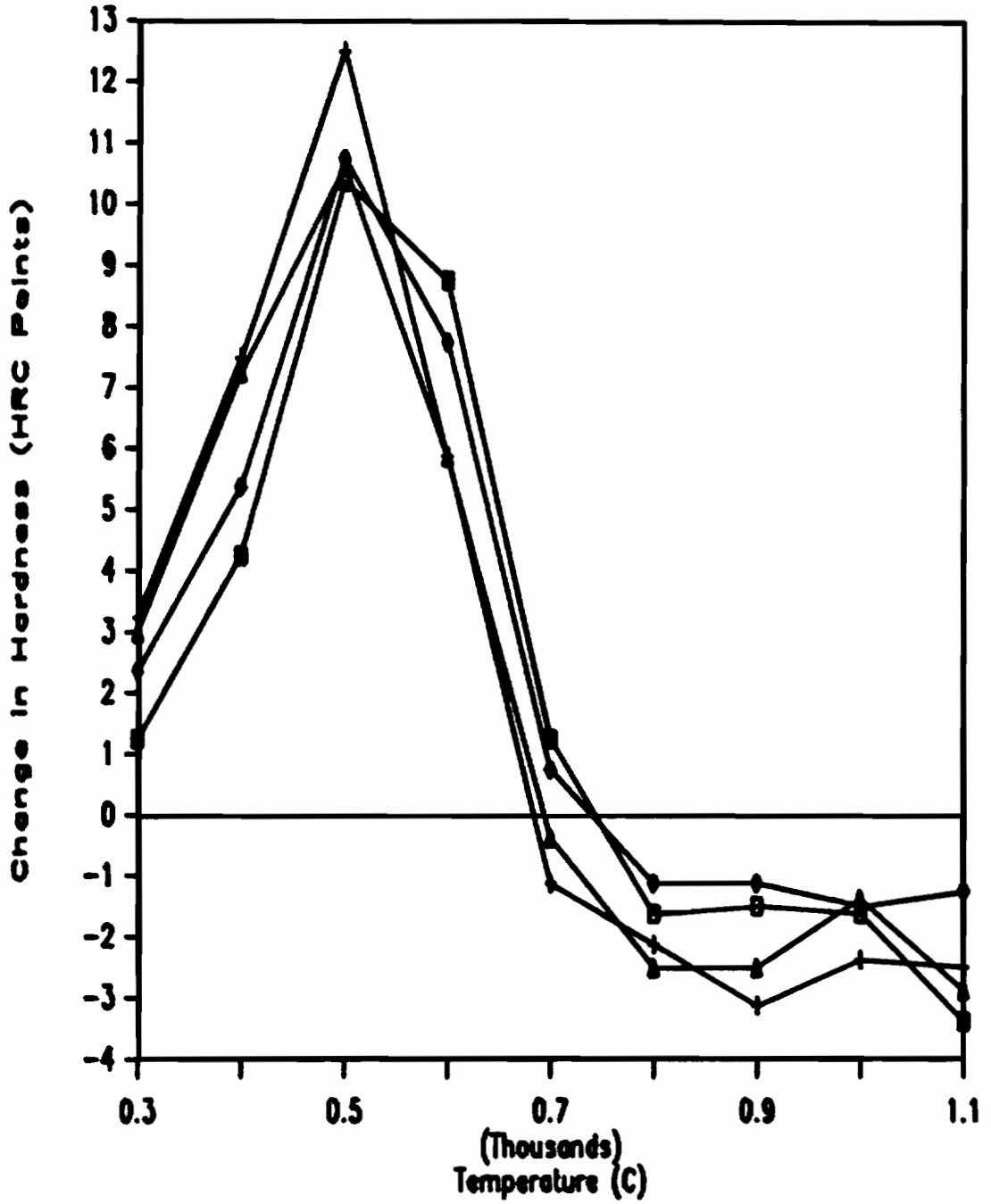

Figure 74. Change in hardness versus temperture for 2 hour heat treatment of T25 and T26 weld series.

Figure 75. Microstructure of un-heat-treated weld metal, T25 weld series.

(a)

20μm

(b)

Figure 76. Microstructure of 300°C heat treatment, T25 weld series.

a) 2 hours b) 24 hours

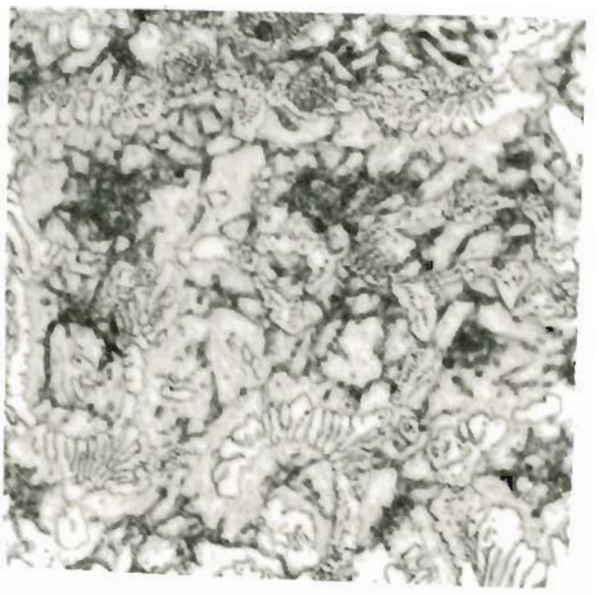

(a)

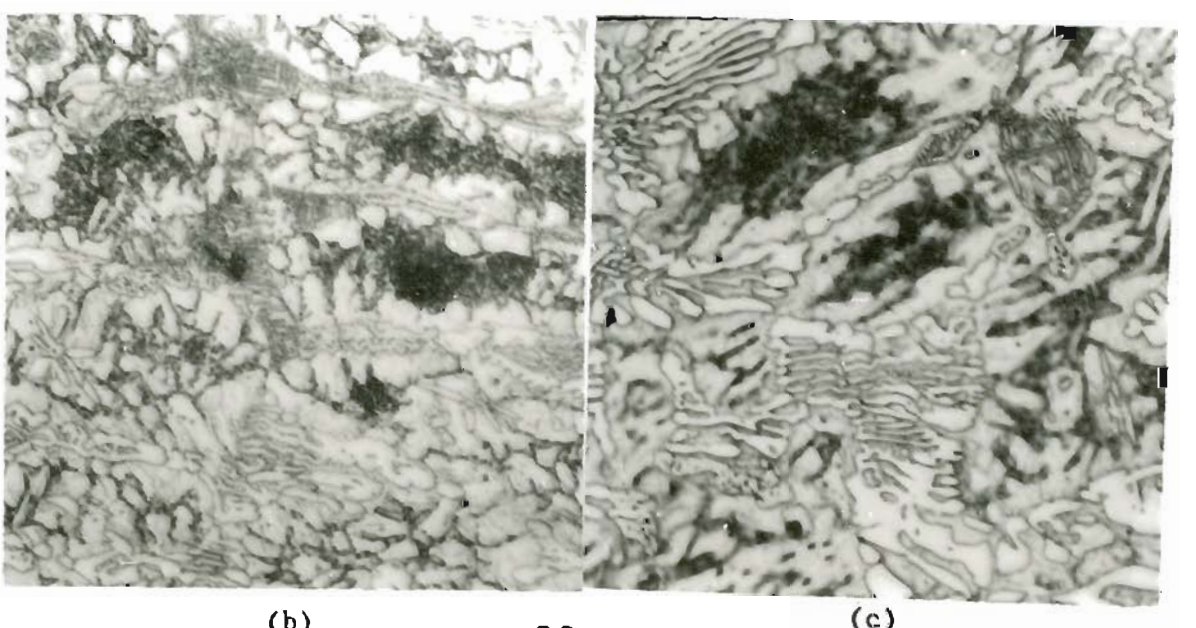

Figure 77. Microstructure of 400°C heat treatment, T25 weld series.

a) 1 hour b) 2 hours c) 4 hours

(a)

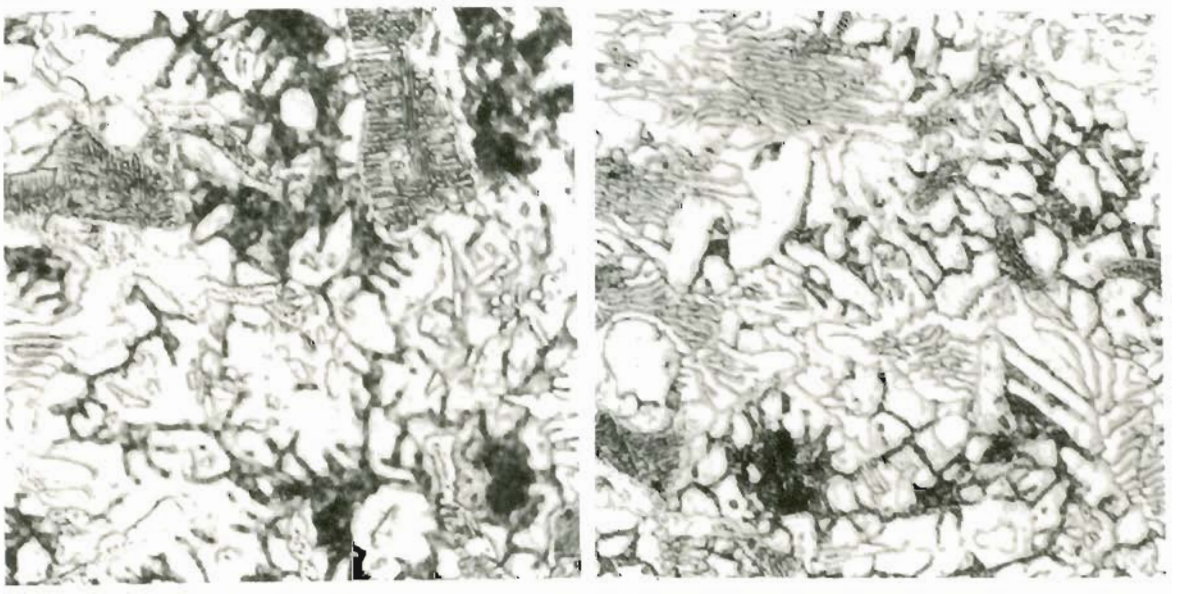

(b) 20μm (c)

Figure 78. Microstructure of 400°C heat treatment, T25 weld series (continued).

a) 8 hour b) 24 hours c) 100 hours

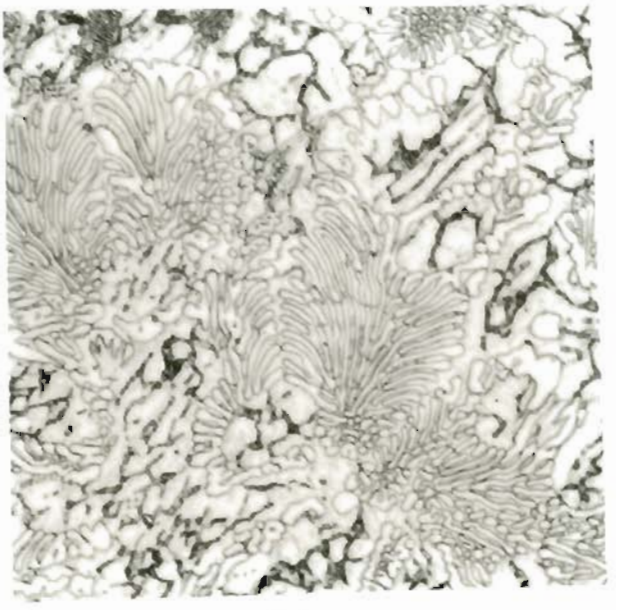

(a)

20μm

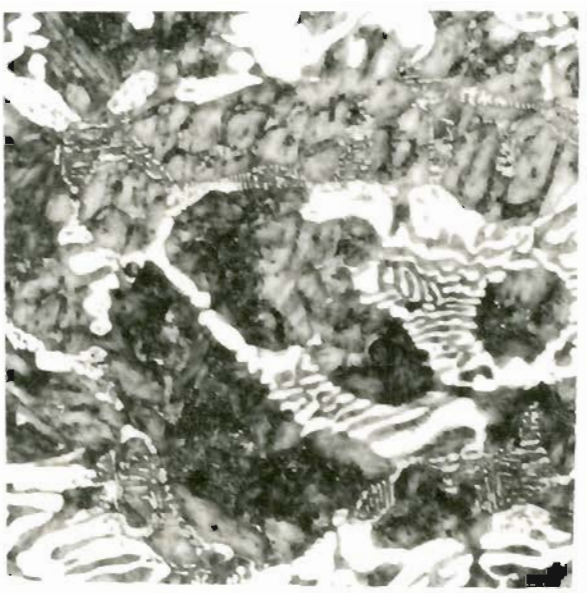

(b)

Figure 79. Microstructure of 500°C heat treatment, T25 weld series.

a) 2 hours b) 24 hours

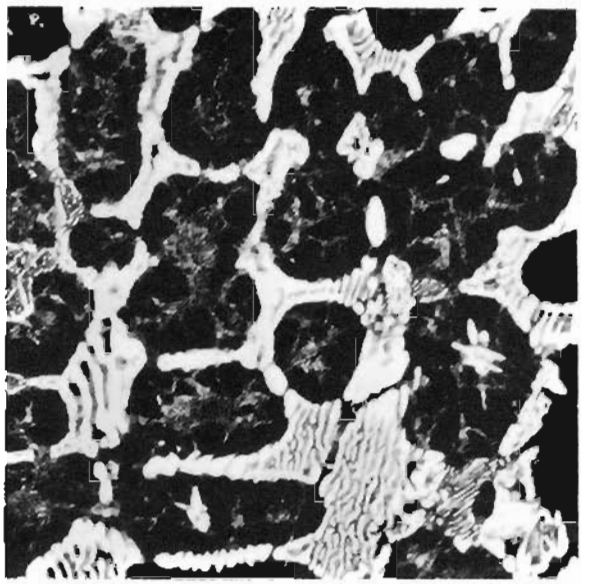

(a)

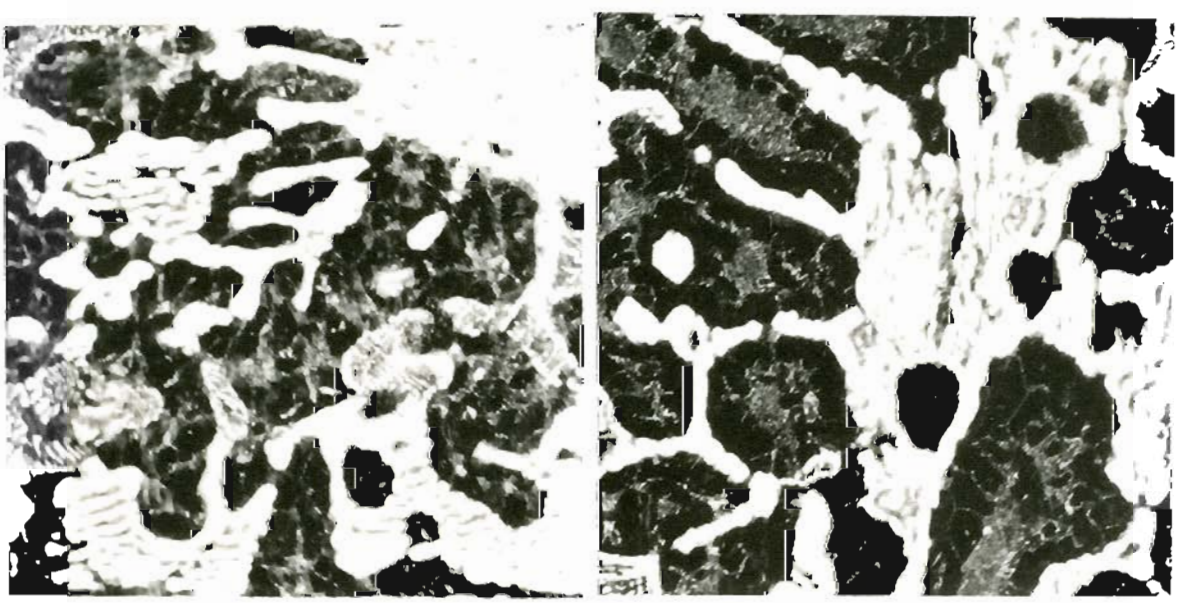

(b) 20μm (c)

Figure 80. Microstructure of 600°C heat treatment, T25 weld series.

a) 1 hour b) 2 hours c) 4 hours

(a)

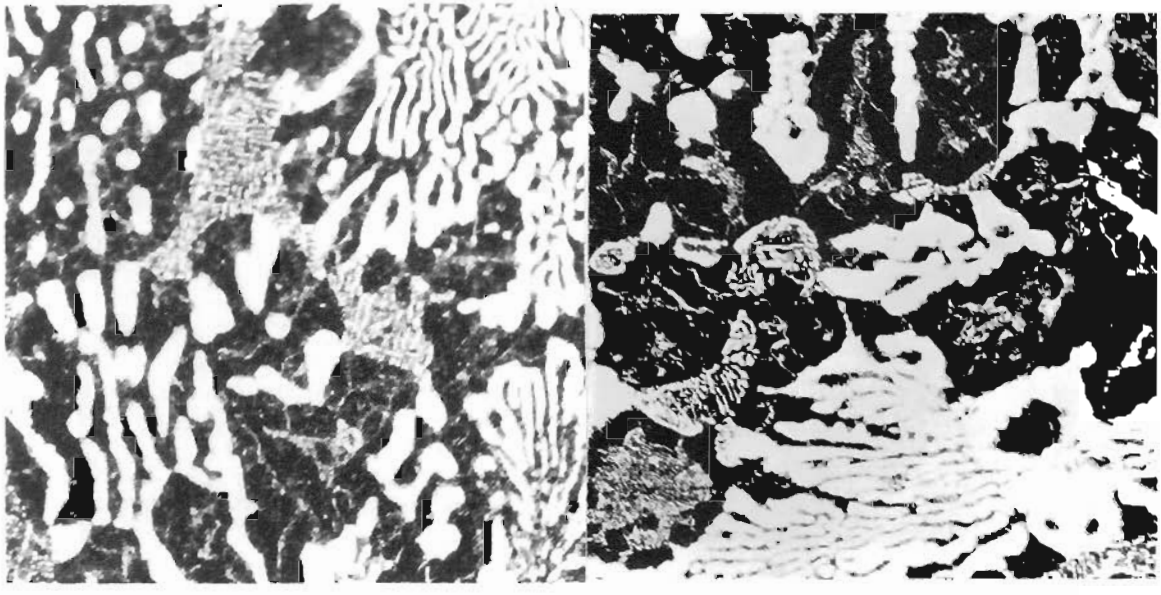

(b) 20μm (c)

Figure 81. Microstructure of 600°C heat treatment, T25 weld series (continued).

a) 8 hours b) 24 hours c) 100 hours

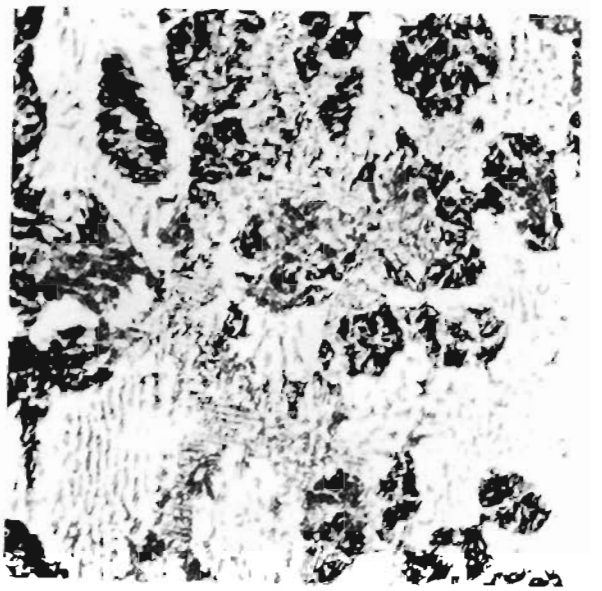

(a)

20μm

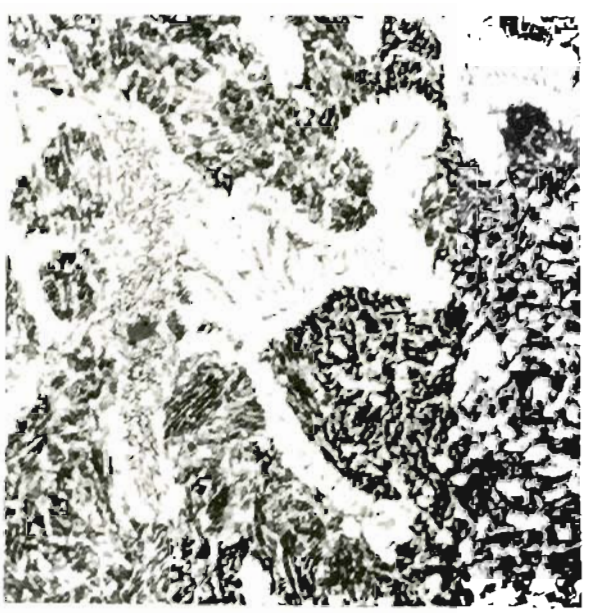

(b)

Figure 82. Microstructure of 700°C heat treatment, T25 weld series.

a) 2 hours b) 24 hours

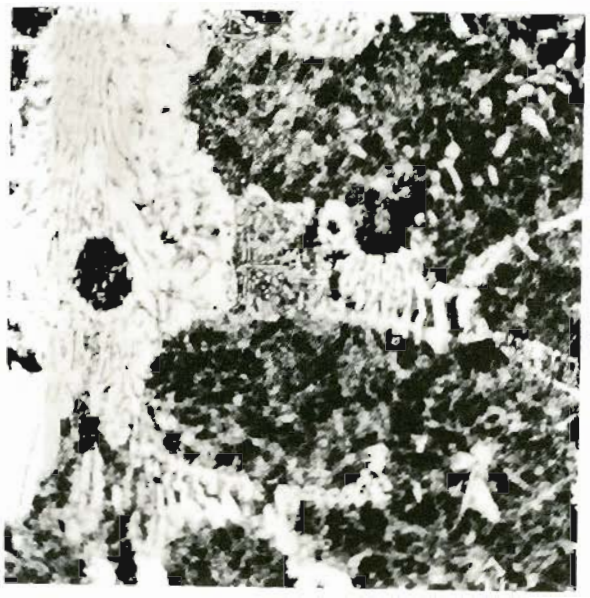

(a)

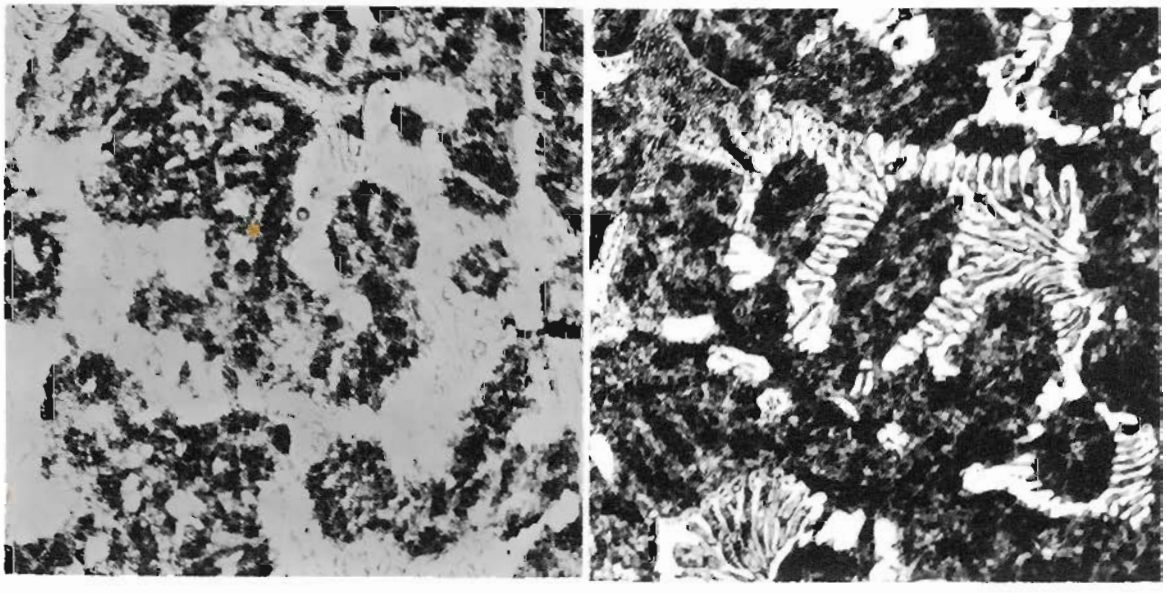

(b) (c)

20μm

Figure 83. Microstructure of 800°C heat treatment, T25 weld series.

a) 1 hour b) 2 hours c) 4 hours

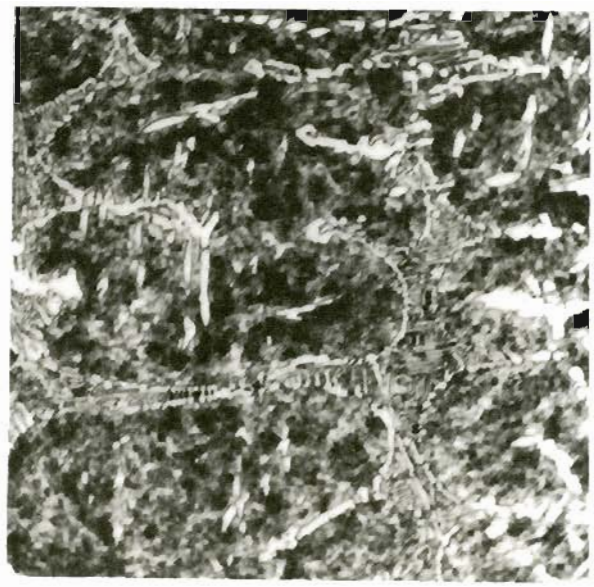

(a)

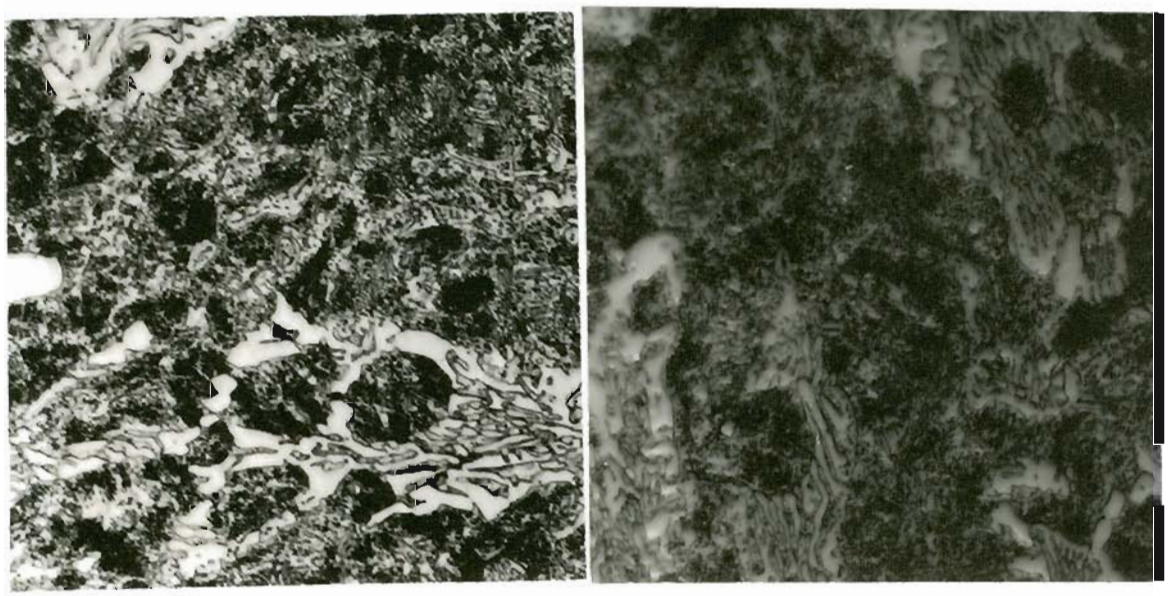

(b) 20μm (c)

Figure 84. Microstructure of 800°C heat treatment, T25 weld series (continued).

a) 8 hours b) 24 hours c) 100 hours

(a)

20μm

(b)

Figure 85. Microstructure of 900°C heat treatment, T25 weld series.

a) 2 hours b) 24 hours

(a)

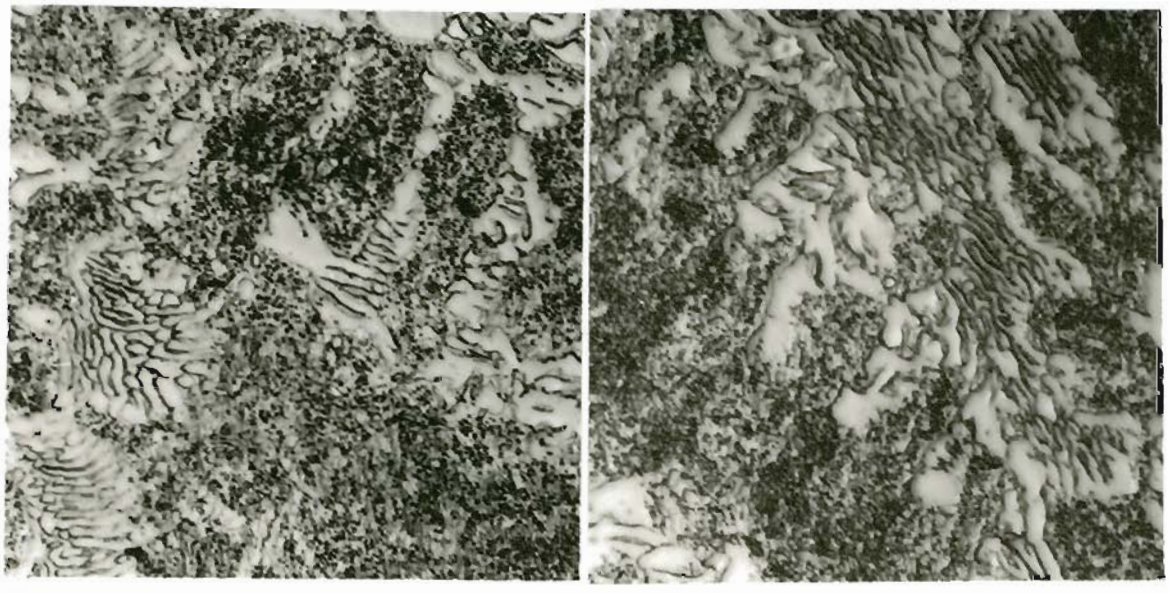

(b) (c)

20μm

Figure 86. Microstructure of 1000°C heat treatment, T25 weld series.

a) 1 hour b) 2 hours c) 4 hours

(a)

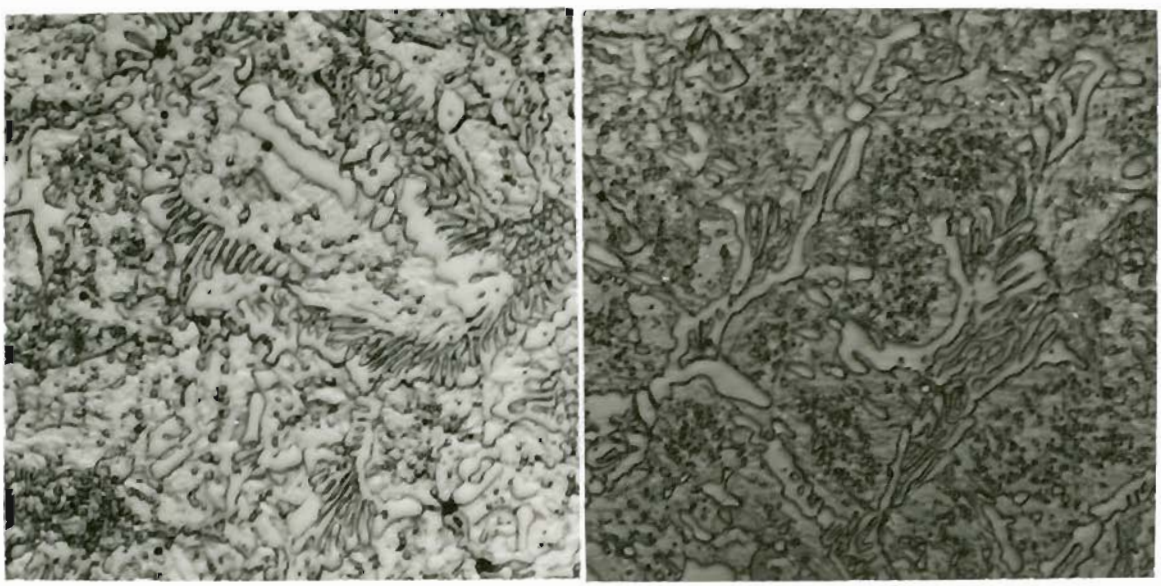

(b) 20μm (c)

Figure 87. Microstructure of 1000°C heat treatment, T25 weld series (continued).

a) 8 hours b) 24 hours c) 100 hours

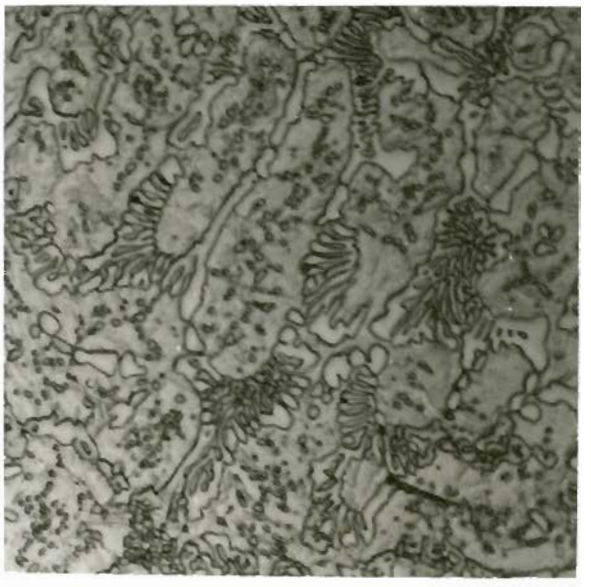

(a)

20μm

(b)

Figure 88. Microstructure of 1100°C heat treatment, T25 weld series.

a) 2 hours b) 24 hours

3.5 Cyclic High Temperature Oxidation Tests

Two samples, one of each of the weld series used in the heat treatment study, were tested for cyclic oxidation resistance at the U.S. Bureau of Mines, Albany, Oregon. The samples were tested at 1000°C for up to 152 hours. The resulting weight changes are shown in Table 22. The results are inconclusive because of spalling of the oxide coating which occured during the heating and cooling cycles of the test.

The oxide layer produced by oxidation of the samples was examined at the U.S. Bureau of Mines and analyzed by energy dispersive x-ray techniques. The oxide layer was divided into three regions. An outer layer was formed which contained two sub-zones, a inner layer, and a sub-oxide layer which contained two phases and lay next to the metal. There was also a thin layer between inner and sub-oxide regions. Composition of these layers and their constituent phases are shown in Table 23 and schematically in Figure 89. The outer region was composed principly of iron oxide. The outer part of this region was almost pure iron oxide while the inner part contained about 10 at.% nickel. The inner region of oxide contained 65 to 72 at.% iron, 7 to 8 at.% nickel, and 20 to 26 at.% silicon. The thin layer which lay betwen the inner region and the two phase sub-oxide region contained 45 at.% iron, 2 to 6 at.% nickel, 7 to 17 at.% silicon, and 31 to 45 at.% molybdenum. Of the two phases in the sub-oxide region, one contained almost no molybdenum. The low molybdenum phase contained 46 to 56 at.% iron, 6 to 35 at.% nickel, 12 to 37 at.% silicon, and only upto 6 at.% molybdenum. The high molybdenum phase contained 29 to 46 at.% iron, 9 to 43 at.% nickel, 2 to 17 at.% silicon,

and 25 to 27 at.% molybdenum. Some of the ranges of these compositions are large because the data are drawn from from samples of the T25 and T26 weld series which have different compositions.

Table 22

Results of Cyclic Oxidation Tests at 1000° C

Time	Weight Loss T25 Sample	Change*	Weight Loss T26 Sample	Change*
1/2 hr	$-5.37X10^{-4}$	decrease	$+1.11X10^{-3}$	increase
1 hr	$-4.60X10^{-5}$	increase	$+1.72X10^{-3}$	increase
2 hrs	$+5.68X10^{-4}$	decrease	$+2.44X10^{-3}$	increase
4 hrs	$+2.32X10^{-3}$	increase	$+3.35X10^{-3}$	increase
8 hrs	$+3.68X10^{-4}$	decrease	$+7.22X10^{-4}$	decrease
16 hrs	$-9.59X10^{-3}$	decrease	$+5.39X10^{-4}$	decrease
32 hrs	$-2.56X10^{-2}$	decrease	$-4.18X10^{-3}$	decrease
64 hrs	$-5.36X10^{-2}$	decrease	$-2.02X10^{-2}$	decrease
152 hrs	$-1.07X10^{-1}$	decrease	$-3.68X10^{-2}$	decrease

*A decrease is a loss of weight between weighings, an increase is a weight gain between weighings.

Table 23

Composition of Oxide Layers, Cyclic Oxidation Test (in wt.%).

Region		Fe	Mo	Ni	Si	Cr
Outer Oxide	T25					
Overall	T26	93.62	0	0	0.24	0.12
Outer Oxide	T25	98.8	0	0.26	0.7	0.25
Outer	T26	99.64	0	0	0.35	0.01
Outer Oxide	T25	89.46	0	9.89	0.28	0.38
Inner	T26	89.36	0	9.91	0.46	0.27
Inner Oxide	T25	65.3	0	8.28	26.11	0.31
Overall	T26	72.95	0	7.03	19.62	0.39
Sub-Oxide	T25	47.66	13.19	14.89	23.94	0.32
Overall	T26	51.62	13.43	11.66	23.1	0.19
Bright	T25	45.15	31.8	6.2	16.85	0
Layer	T26	46	44.57	2.21	7.22	0
Light Phase	T25	46.3	27.01	9.59	17.09	0
in Sub-Oxide	T26	29.12	25.15	43.27	2.47	0
Dark Phase	T25	46.47	6.2	34.87	12.3	0.16
in Sub-Oxide	T26	56.61	0	6.1	37.29	0

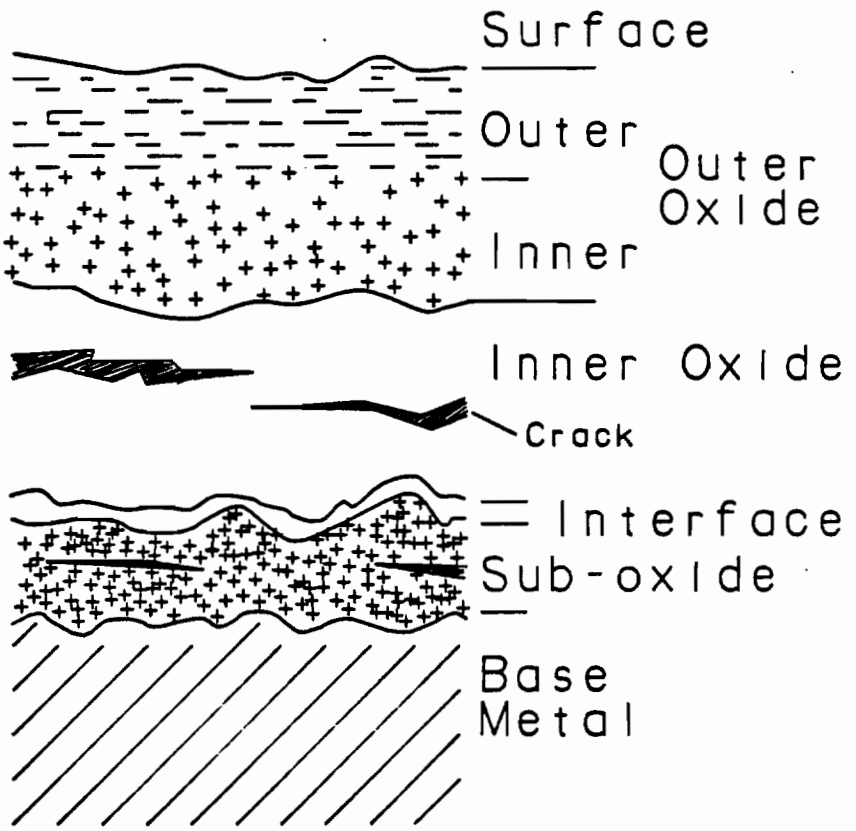

Figure 89. Schematic representation of oxide layers.

4.0 Discussion

4.1 Arc-Melted Alloy and Weld Metal Phase Analysis

In the initial stages of this investigation arc-melted buttons made from powder compacts were used to ascertain the solidification phase morphologies of Fe-Mo-Ni, Fe-Mo-Ni-Si, and Fe-Mo-Ni-Si-C alloys. At the same time a literature search was performed. Through this search solidification data on the Fe-Mo-Ni system, and on the quartenary and quinary systems, was found to be almost non-existant. The arc-melted alloys were useful as an indication of the solidification structures formed over the composition range of interest.

From solidification structures formed in the ternary arc-melted alloys (Fe-Mo-Ni) and their respective hardnesses, it was apparent that a fourth alloying element was necessary to alter the solidification morphologies and increase the bulk hardness. The Fe-Mo-Ni arc-melted alloys possessed a microstructure of austenite dendrites with an intermetallic plus austenite eutectic in interdendritic regions. Phase diagrams of this system as compiled by Rivlin, Hoster, and Das, shown in Figures 90, 91, and 92 respectively, reveal the intermetallic to be Fe_7Mo_6 (Rivlin and Hoster) or Fe_3Mo_2 (Das) with placement of nickel on the iron sites in the intermetallic. As can be seen in Figure 93, the intermetallic regions proposed by the different investigators vary chiefly on the amount of nickel substitution in the intermetallic, molybdenum contents are predicted to be relatively stable. At 1100 and 1200°C isotherms, Hoster and Das agree that the maximum nickel substitution on iron sites is about 50% while Rivlin proposes up to 67% replacement. Rivlin's Fe-Mo-Ni phase diagram compilation is the most recent.

Some of the arc-melted alloy compositions and their phase compositions are shown in Figure 94. The composition of the intermetallic phase, analyzed by EDX, does not extend into the intermetallic region shown on the equilibrium phase diagram. The compositions, however, are close and the discrepancy can be attributed to the fact that the alloys examined are solidification structures formed through a relatively fast cooling cycle, rather than structures formed after slow or equilibrium cooling.

All the Fe-Mo-Ni alloys investigated contained some volume fraction of the austenite plus Fe_7Mo_6 eutectic. The formation of this eutectic was unexpected. With one exception investigators of this system have not published any information on the liquidus/solidus surfaces. Koster published the first information on the Fe-Mo-Ni system in 1934 [104] and included a proposed liquidus surface, shown in Figure 94. Koster's liquidus surface projection shows only a univariant reaction 'Liq = (Mo) + Fe_3Mo_2' extending from a peritectic reaction 'Liq + (Mo) = Fe_3Mo_2' on the Fe-Mo binary diagram to a similar peritectic on the Mo-Ni binary diagram. He also shows a univariant line from a Fe-Mo eutectic, 'Liq = bcc_{Fe} s.s. + Fe_3Mo_2', to a eutectic, 'Liq = fcc_{Ni} s.s. + MoNi', on the Mo-Ni binary diagram. This univariant line passes through a minima in the ternary. Connecting to this line is another univariant reaction, 'Liq = bcc_{Fe} s.s. + $fcc_{Fe,Ni}$ s.s.', approaching from the Fe-Ni binary diagram. Where the two lines meet Koster proposed a quasi-peritectic reaction, 'Liq + bcc_{Fe} s.s. = $fcc_{Fe,Ni}$ s.s. + Fe_3Mo_2'.

Koster based much of his liquidus surface on the behaviour of the binary systems which make up the ternary diagram. Later phase diagram

investigations show some differences in the binary diagrams, particularly the Fe-Mo diagram. The greatest difference lies in the Fe-Mo minima which lies at Fe-20 at.% Mo and near the peritectic reaction 'Liq + R = bcc_{fe}'. These two points are separated vertically by only a few degrees centigrade and by only a few at.% (6.6 at.%, [122]). Koster perceived the combination of the two reactions as a eutectic. Koster also was not aware of the presence of a second peritectic reaction in the Fe-Mo binary; the reaction 'Liq + (Mo) = sigma'.

From examination of the arc-melted alloys some inferences on the nature of liquidus/solidus surfaces of the Fe-Mo-Ni phase diagram can be made. Since the microstructures of the arc-melted alloys contained austenite dendrites, at least in the area investigated, solidification must start in a 'Liq = fcc_{Fe} s.s..' region. This reaction occurs until the liquid composition changes to meet a univariant reaction which could possibly be 'Liq = Fe_7Mo_6 + fcc_{Fe} s.s.'. The solidification would proceed along that line until a ternary invariant reaction is met. A univariant reaction would explain the presence of eutectic structure in the interdendritic regions of the austenite dendrites.

The Fe-Mo-Ni system proved to be limited to the structures of austenite dendrites with an austenite plus Fe_7Mo_6 eutectic in the interdendritic regions. Austenite was the primary solidification phase in the Fe-Mo-Ni alloys rather than an intermetallic compound. It was decided to use the Fe-Mo-Ni system as a base for other alloying element additions.

Two elements were added, silicon and carbon, to examine Fe-Mo-Ni-Si and Fe-Mo-Ni-Si-C alloys. Carbon was added solely to study the effects

of carbon pick-up from the base metal on the structure of Fe-Mo-Ni weld deposits. The result was that for alloy carbon contents of up to 0.5 wt.% in a Fe-30Mo-20Ni alloy, little change was seen in the microstructure. At higher carbon contents, however, a 100% lamellar structure resulted. The lamellar structure was composed of austenite plus an eta carbide. The lamella structure, contained in well defined cells with no grain boundaries visible, was a eutectic structure. This structure could prove useful in other applications other than those demanding abrasive wear resistance.

Silicon additions were made to the arc-melted Fe-30Mo-20Ni alloy as well. Below 1 wt.% silicon little effect was seen on the structure. However at 5 wt.% silicon the structure became columnar dendritic. Microhardness tests on this structure showed the columnar dendrites to be much harder than the matrix phase, revealing the dendrites to be an intermetallic phase. This composition of alloy and its solidification structure promised to be attractive for use as a weld hardfacing alloy; provided that the hard phase could be produced in a large enough volume fraction in a weld metal alloy.

When considering nickel seperately, i.e a quartenary system, alloys with base compositions of Fe-15Mo-10Ni-5Si to Fe-30Mo-20Ni-5Si lie closest to the Fe-Mo-Si face of the quartenary tetrahedron (Figure 95). From this geometry on the tetrahedron and the results of the microstructural survey of Fe-Mo-Ni-Si arc-melted alloys, an in-depth look was made at the Fe-Mo-Si ternary system. Considering the Fe-Mo-Si phase diagram and assuming that there was total placement of nickel atoms on iron sites in the crystal structure, an examination of the Fe-Mo-Si solidification

paths was performed.

A search of the literature revealed a surprising amount of information on the Fe-Mo-Si system, though none on the Fe-Mo-Ni-Si system. The Fe-Mo-Si system was treated in a recent review by Raynor and Rivlin [118]. Besides producing a high temperature (800°C) isotherm (Figure 96), Raynor and Rivlin proposed a hypothetical room temperature isotherm (Figure 97) and a projection of the liquidus surface (Figure 98). Solid state reaction sequences from the liquid state to room temperature were also proposed. The latter proved useful in an solidification analysis of the weld metal alloys.

The hypothetical room temperature isotherm shows a number of possible intermetallic compounds. Of greatest interest were a tau_1 ternary intermetallic, with an orthorhombic crystal structure and a stoichiometry of approximately Fe_2MoSi_2, and a Fe_2Mo Laves phase intermetallic with a $MgZn_2$ crystal structure and a solid solubility of silicon up to a stoichiometry of FeMoSi. A large two phase region of the $Fe_{(2-x)}MoSi_x$ (Laves phase) intermetallic plus a bcc_{Fe} solid solution phase exists as well. This region is bounded on the ends by the Laves phase and by the bcc_{Fe} solid solution and bounded on the silicon-rich side by a ternary phase triangle of tau_1, the Laves phase, and the bcc_{Fe} solid solution.

Silicon exists in the Fe_2Mo intermetallic by virtue of the high solubility of the Laves phase crystal structure for silicon. In the Fe-Mo-Si system, Laves phases can contain up to 33.3 at.% silicon, the stoichiometry terminating at FeMoSi. The ternary Laves phase $Fe_{(2-x)}MoSi_x$ has been reported by a number of investigators [113, 114, 121, 125,

126]. Gladyshevskii [125] reported FeMoSi to have a $MgZn_2$ crystal structure with lattice dimensions of a_o=4.751 Å and c_o=7.662 Å. Bardos et al [114] looked at a range of silicon concentrations in Fe_2Mo alloys with the silicon content ranging from 16.5 to 50 %. They found that the Laves phase lattice parameters varied from a_o=4.737 Å and c_o=7.727 Å for low silicon, to a_o= 4.766 Å and c_o=7.601 Å at higher concentrations of silicon. Some investigators have attributed the Laves phase solubilty of silicon to a decrease in the effective atomic radius of the silicon atom [114] which would enable it to fit the $MgZn_2$ crystal structure of the Laves phase. Bardos, et al, reported the effective atom radius of silicon in $Fe_{(2-x)}MoSi_x$ ternary Laves phases to be 1.18 Å while the calculated radius for silicon at a C.N. of 12 was 1.34 Å.

The liquidus surface projection (Figure 99) exhibits the presence of several quasi-peritectic reactions and two ternary eutectic reactions. The invariant reactions are shown in Table 24. Figure 99 shows an expanded view of the liquidus projection in the iron-rich region. Compositions of the weld metal (shaded area in Figure 99) straddle the reaction line p_4-U_5 which leads to the E_1 eutectic. The U_5 reaction is the quasi-peritectic 'Liq + R = tau_1 + bcc_{Fe} s.s.' and the E_1 ternary eutectic is 'Liq = tau_1 + FeSi + bcc_{Fe} s.s.'.

Room temperature phases in weld metal alloys were determined by x-ray diffraction analysis to be bcc_{Fe} and fcc_{Fe} solid solution and FeMoSi. Assuming these are equilibrium phases and tracing back through reaction sequences proposed by Raynor and Rivlin, initial solidification could be either via the U5 or the U_7 quasi-peritectic invariant reaction or the E_1 ternary eutectic. For the weld metal compositions studied, the

U_7 invariant reaction is inaccessible as a solidification path as both the U_5 and E_1 reaction must be traversed first. It would also mean an increase in the temperature of the liquid to reach the U_7 reaction point. The reaction sequence for the iron-rich region of the Fe-Mo-Si system from liquid to 800°C is shown in Figure 100 and a hypothetical reaction sequence from 800°C to room temperature in Figure 101.

Since the U_7 reaction is not possible for the compositions in question, two solidification and solid state reaction paths are possible: through the U_5 invariant reaction or through the E_1 ternary eutectic. If the U_5 reaction is the path followed then the reaction sequence would be:

U_5 [Liq + R = tau_1 + bcc_{Fe} s.s.]

yielding

tau_1 + R + bcc_{Fe} s.s.

to

[tau_1 + bcc_{Fe} s.s. = Fe_5Si_3 + Fe_2Mo]

yielding

Fe_5Si_3 + Fe_2Mo + bcc_{Fe} s.s.

to

[Fe_5Si_3 = FeSi + Fe_2Mo + bcc_{Fe} s.s.]

yielding

FeSi + Fe_2Mo + bcc_{Fe} s.s.

to

[FeSi + Fe_2Mo = tau_1 + bcc_{Fe} s.s.]

yielding

tau_1 + Fe_2Mo + bcc_{Fe} s.s.

Solidification from the ternary eutectic would follow the same path

except for the ternary transition reaction which immediately follows solidification. In this case the sequence would be:

E_1 [Liq = tau_1 + FeSi + bcc_{Fe} s.s]

yielding

tau_1 + FeSi + bcc_{Fe} s.s.

to

[FeSi + bcc_{Fe} s.s. = Fe_5Si_3 + tau_1]

yielding

tau_1 + Fe_5Si_3 + bcc_{Fe} s.s.

to

[tau_1 + bcc_{Fe} s.s. = Fe_5Si_3 + Fe_2Mo]

yielding

Fe_5Si_3 + Fe_2Mo + bcc_{Fe} s.s.

to

[Fe_5Si_3 = FeSi + Fe_2Mo + bcc_{Fe} s.s.]

yielding

FeSi + Fe_2Mo + bcc_{Fe} s.s.

to

[FeSi + Fe_2Mo = tau_1 + bcc_{Fe} s.s.]

yielding

tau_1 + Fe_2Mo + bcc_{Fe} s.s.

Lack of the tau_1 phase in x-ray diffraction results of the weld metal alloys can be accounted for by the fact that cooling was not through equilibrium states, and also the presence of up to 15 wt.% nickel. Traces of the silicides, FeSi and Fe_5Si_3, were also not found.

Data from the arc-melted alloys made for the melting point study

supported this analysis on the weld metal alloys. The melting point alloy composition range is shown on Figure 100. The range is bounded by molybdenum contents of 17 and 25 wt.% and silicon contents of 4 and 6 wt.%. The microstructures observed confirmed analysis of weld metal and usefulness of the Fe-Mo-Si phase diagram for this phase analysis, as well more concrete evidence that the 100% nickel-on-iron site assumption may be used for the compositions investigated.

On the Fe-Mo-Si phase diagram the melting point alloys lie across the p_4-U_5 univariant reaction line (Liq = bcc_{Fe} s.s. + R). This reaction line descends from the 1449°C p_4 peritectic reaction (Liq + R = bcc_{Fe} s.s) to the U_5 quasi-peritectic reaction at 1186°C. Figure 102 shows the average volume fraction of lamellar phase in the microstructure of alloys which lie across the p_4-U_5 univariant line. The volume fraction of the lamellar phase increases with proximity to the univariant line. This corrosponds to the eutectic valley of the univariant reaction.

For the arc-melted melting point alloys two initial modes of solidification are possible, 'Liq = bcc_{Fe} s.s.' and 'Liq = R', depending on which side of the univariant line the composition lies on. In both cases solidification proceeds down to the univariant line. Once at the p_4-U_5 univariant reaction, liquid composition would follow the eutectic valley down to the U_5 quasi-peritectic reaction, and then down the U_5-E_1 univariant reaction (Liq = tau_1 + bcc_{Fe} s.s.) line to the E_1 ternary eutectic. This ternary eutectic occurs at 1170°C at composition of 75Fe-6.5Mo-18.5Si. These reactions are shown in greater detail in Figure 103. As discussed previously, two possible paths of final solidification are possible, through the U_5 quasi-peritectic or through the E_1 ternary

eutectic. For reasons to be detailed next, the E_1 eutectic reaction was determined to be dominant.

Weld metal alloys fall in the Liq = bcc_{Fe} s.s. field of initial solidification. With the liquid composition falling to the p_4-U_5 univariant reaction line during solidification, the formation of the R phase would be minimized. This would subsequently limit the extent of the U_5 quasi-peritectic reaction, leading to an increased influence of the E_1 eutectic reaction. Observations of the microstructure of the weld metal alloys seem to confirm this hypothesis. In many cases the eutectic cell in the interdendritic region of the microstructure is surrounded by a rim of an intermetallic as can be seen in Figure 104. This rim could be due to the U_5 quasi-peritectic reaction. When liquid composition reaches the U_5 point, liquid would react with any R phase at the liquid/-solid interface to form 'bcc_{Fe} s.s. + tau_1'. This new layer of 'bcc_{Fe} s.s. + tau_1' would then limit extent of the U_5 reaction by physically preventing liquid from contacting the R phase as well as providing an effective diffusion barrier. For the U_5 reaction to continue, silicon and/or molybdenum would need to diffuse to the solid/liquid interface and then transform the phases there to more of the R phase. Liquid compositions instead fall towards the E_1 ternary eutectic reaction along the U_5-E_1 univariant reaction line, forming the lamellar structure seen in inter-dendritic spaces.

The solidification and solid state phase analysis using the Fe-Mo-Si phase diagram produced results confirmed by the observation of Fe-Mo-Ni-Si melting point alloys. These observations were made in two seperate studies, one examining microstructures of arc-melted alloys used in a

melting point study and the other examining microstructures of weld metal alloys. An initial assumption was made that there was complete placement of nickel atoms on iron sites of the microstructure. The presence of nickel does not appear to effect Fe-Mo-Si reaction sequences appreciably, the Fe-Mo-Ni-Si behaving as Fe-Mo-Si alloys. Nickel's primary effect appears to promote formation of an $fcc_{(Fe,Ni)}$ solid solution phase.

The weld metal alloys mimicked the microstructure of the arc-melted alloys closely, particularly in the Fe-Mo-Ni compositions which possessed a microstructure of austenite dendrites plus a austenite + Fe_7Mo_6 eutectic. Some differences were seen though between the arc-melted alloys and the weld metal alloys in the Fe-Mo-Ni-Si compositions. These weld metal compositions had the best wear resistance of intermetallic--containing weld metal alloys which were wear tested. The microstructure of these weld metal alloys was a Laves phase intermetallic plus ferrite ($Fe_{(2-x)}MoSi_x$ + bcc_{Fe} s.s.) eutectic in a bcc_{Fe} s.s./$fcc_{(Fe,Ni)}$ s.s. matrix. The Fe-Mo-Si phase diagram predicts only the bcc_{Fe} solid solution. X-ray diffraction showed the presence of $fcc_{(Fe,Ni)}$ as well. The weld metal alloys contain up to 15 wt.% nickel which would promote formation of a $fcc_{(Fe,Ni)}$ phase. EDX analysis of the phases, corrected using standards, revealed an average matrix composition of 80Fe-5Mo--10Ni-5Si. This amount of nickel would promote the formation of $fcc_{(Fe,Ni)}$ with the moderate amounts of molybdenum and silicon present.

When plotted on the Fe-Mo-Si phase diagram and considering 100% placement of nickel atoms on iron sites in the matrix, compositions of the intermetallic in the eutectic in the weld metal alloys tended toward

the Fe_2Mo region and matrix compositions tended toward the bcc_{Fe} solid solution region of the phase diagram. This is shown in Figure 105 where several compositions are plotted in at.% at the iron-rich corner of the Fe-Mo-Si phase diagram. Table 25 shows matrix and intermetallic compositions of several of the Fe-Mo-Ni-Si weld metal alloys. The discrepancies between measured phase compositions and the phase diagram could be attributed to non-equilibrium cooling of the weld metal alloys and the alloy nickel content.

A similar analysis was done on heat-treated weld metal alloys. The heat-treated alloys had an overall composition of about 70Fe-15Mo-9Ni-6Si. Comparing phase compositions of heat-treated alloys to the Fe-Mo-Si phase diagram yielded more consistent results than as-welded alloys. Heat--treatments of up to 100 hours at 1000°C and 24 hours at 1100°C were employed. Results of EDX analysis of the phases were plotted on the Fe-Mo-Si phase diagram and are shown in Figure 106 as well as listed in Table 26. A trend was quickly evident. The matrix compositions varied little with heat-treatment, remaining about 85Fe-6Mo-4Ni-5Si. Composition of the intermetallic in the eutectic was seen to vary with heat treatment. Generalization of changes in alloy chemistry could be made on two levels; variations with temperature given a 24 hour heat treatment and variations with times of 24 and 100 hours over a range of given temperatures.

For a heat treatment time of 24 hours, the silicon content of the hard phase decreased almost 10 at.% as the heat treatment temperature increased from 400 to 700°C. Changes in the molybdenum content were only a few at.% and could be attributed to differences in the overall alloy compositions. From 700 to 1100°C, the silicon content of the intermetallic

increased almost 15 at.%. Greater variation was seen in the molybdenum content in this temperature range, it decreasing about 5 at.% from 700 to 800°C then rising to previous levels by 1100°C.

Examining phase analysis results for the 24 and 100 hour heat treatments at singular temperatures reveals only small changes in the molybdenum and silicon content of the intermetallic. Though the silicon content of the intermetallic changed with heat treatment temperature and time, the matrix composition did not change appreciably. Small precipitates in the matrix became visible at higher heat treating temperatures (Figure 107).

The formation of a visible precipitate coincided with the hardness change with increasing heat treatment temperature (Figure 73). Hardness increased with heat-treatment temperature up to about 650°C and then decreased abruptly. This was also the point at which precipitates were easily observed. The particles seen at 800°C were about 0.1 μ in diameter, 0.5 μ at 1000°C, and 1-2 μ at 1100°C. Unfortunately these precipitates were too small for EDX analysis on the SEM, but it is likely they are an $Fe_{(2-x)}MoSi_x$ Laves phase intermetallic. Since degradation of the Laves phase intermetallic in the eutectic did not occur even at temperatures approaching the melting point, heat treating the weld metal alloys at 550-650°C to form a precipitate in the matrix should have a beneficial effect on weld metal properties. By increasing matrix hardness by precipitates, wear resistance alloy should improve. A discussion of weld metal abrasive wear properties follows in the next section.

Table 24 Part I

Fe-Mo-Si Ternary Invariant Reactions [118].

Reaction	Nature of Reaction
U_1	Liq + (Mo) = Mo_3Si + sigma
U_2	Liq + sigma = Mo_3Si + R
U_3	Liq + Mo_3Si = R + Mo_5Si_3
U_4	Liq + Mo_5Si_3 = R + tau_1
U_5	Liq + R = tau_1 + bcc_{Fe} s.s.
U_6	Liq + Mo_5Si_3 = tau_1 + $MoSi_2$
U_7*	Liq + Fe_2Si = FeSi + bcc_{Fe} s.s.
E_1	Liq = bcc_{Fe} s.s. + tau_1 + FeSi
E_2	Liq = tau_1 + $MoSi_2$ + FeSi
P_1*	Liq + $MoSi_2$ + (Si) = $FeSi_2$
U_8*	Liq + $MoSi_2$ = FeSi + $FeSi_2$

*Hypothetical reaction

Table 24

Part II. Compositions and Temperatures

Fe-Mo-Si Ternary Invariant Reactions

Reaction	Composition (wt.%) Fe	Mo	Si	Temp., °C
U_1	35	55	10	~1620
U_2	37	51	12	~1575
U_3	39	48	13	~1550
U_4	52	27.5	20.5	1356
U_5	76	7.5	16.5	1186
U_6	49.5	23	27.5	1342
U_7*	~77	~4	~19	?
E_1	75	6.5	18.5	1170
E_2	53	18.5	28.5	1331
P_1*	~40	~5	~55	?
U_8*	~57	~3	~40	?

*Hypothetical Reaction

Table 25

Weld Metal Phase Compositions (in at.%).

	Intermetallic				Matrix			
Sample	Fe	Mo	Ni	Si	Fe	Mo	Ni	Si
T14-2	49.8	25.4	17.7	7.1	66.6	8.9	20.2	4.3
T20-2	45.7	27.7	12.0	14.7	68.2	8.1	15.8	7.9
T20-3	51.6	24.0	10.9	13.5	72.8	9.0	12.6	5.5
T20-4	48.6	29.6	11.6	13.2	69.9	8.1	14.9	7.0
T18-1	25.4	45.4	17.4	11.9	63.0	10.0	22.9	4.2
T18-2	26.3	45.5	14.3	13.9	61.7	10.3	22.8	5.2
T12-7/10	60.7	27.7	11.6	0.0	73.1	11.3	15.7	0.0

Table 26

Heat Treated Weld Metal Phase Compositions (in at.%).

	Intermetallic				Matrix			
Sample*	Fe	Mo	Ni	Si	Fe	Mo	Ni	Si
400/24	46.7	28.8	9.6	14.9	74.6	8.2	10.3	6.9
400/100	47.9	26.4	10.2	15.4	73.0	8.2	11.3	7.5
500/24	46.7	29.7	9.3	14.4	73.5	8.2	10.5	7.7
600/24	53.9	27.3	9.3	9.6	74.5	8.6	9.7	7.3
600/100	53.7	30.7	8.9	6.6	75.3	8.3	9.9	6.5
700/24	52.7	28.4	9.1	9.8	71.1	12.0	9.4	7.5
800/24	55.8	22.5	9.5	12.2	75.6	7.6	9.8	7.0
800/100								
900/24	45.1	28.7	9.7	16.5	75.7	6.6	11.2	8.9
1000/24	46.7	25.8	9.0	18.5	74.7	7.0	9.9	8.3
1000/100	44.5	33.1	9.1	16.3	76.8	6.5	10.6	6.2
1100/24	44.5	27.1	8.9	18.6	74.9	6.8	10.1	8.2

*Temperature in °C/Time in hours

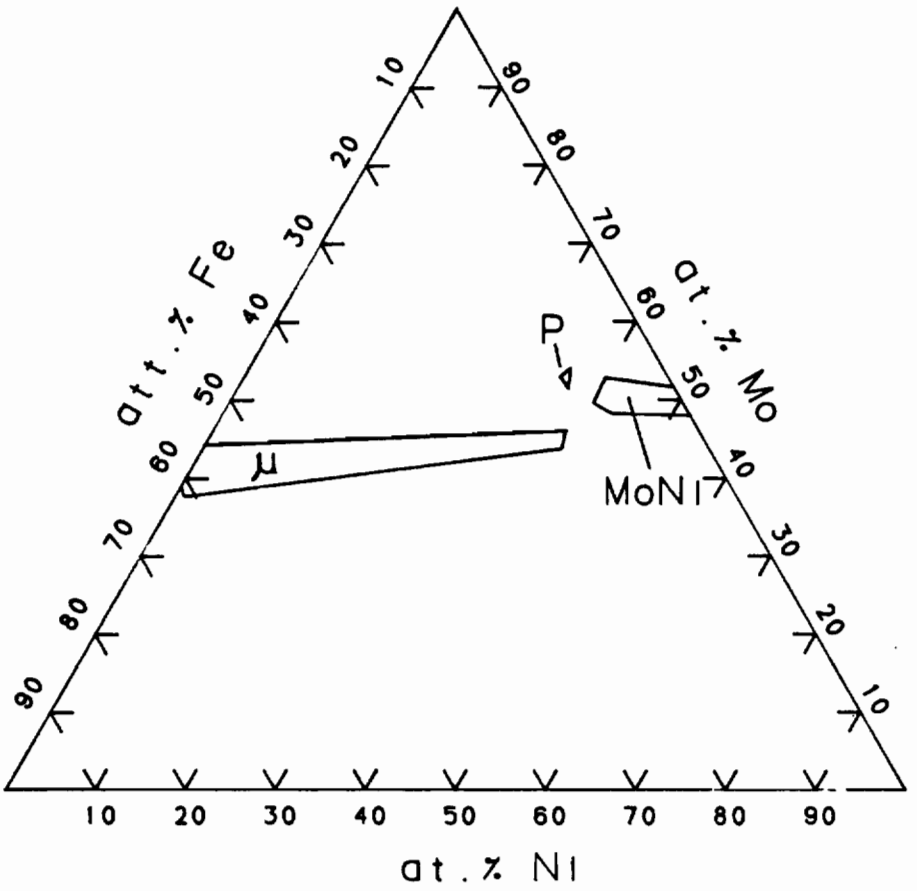

Figure 90. Fe-Mo-Ni 1200°C isotherm showing intermetallic regions, in at.%, after Rivlin [107].

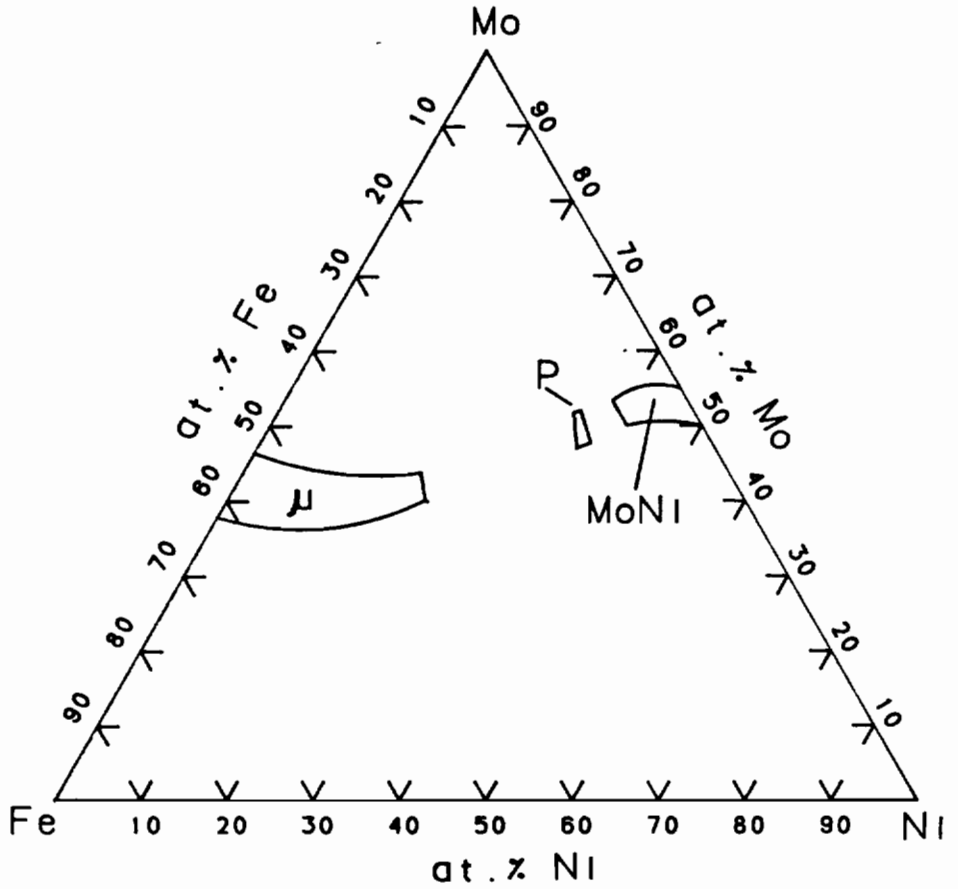

Figure 91. Fe-Mo-Ni 1100°C isotherm showing intermetallic regions, in at.%, after Hoster [108].

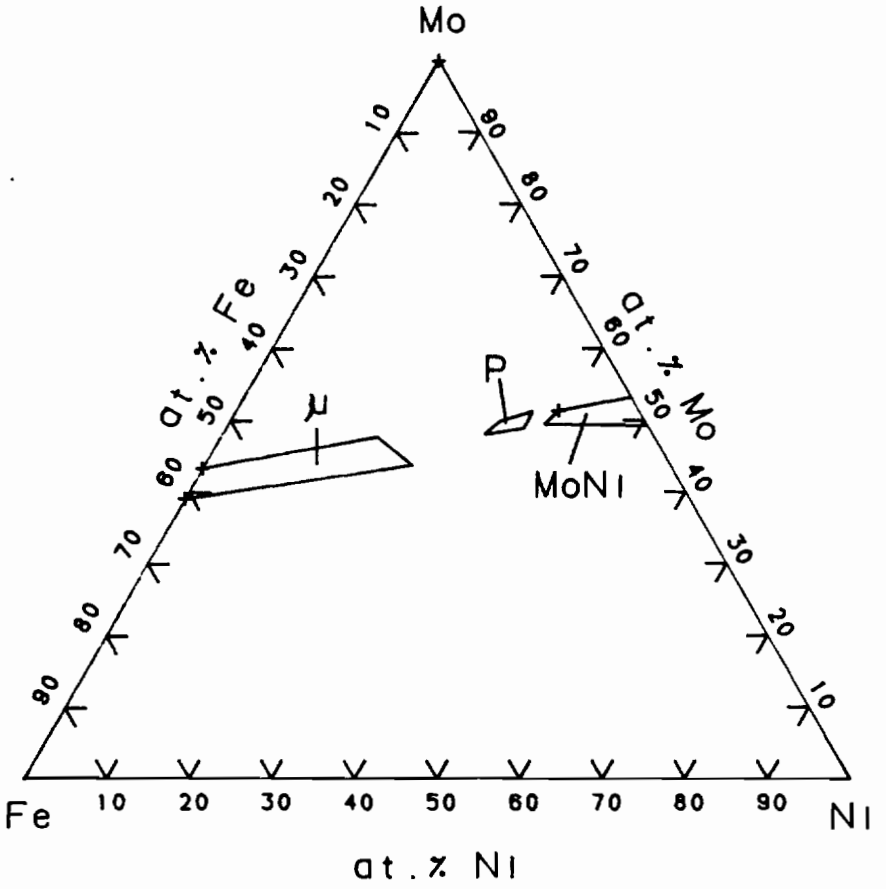

Figure 92. Fe-Mo-Ni 1200°C isotherm showing intermetallic regions, in at.%, after Das [105].

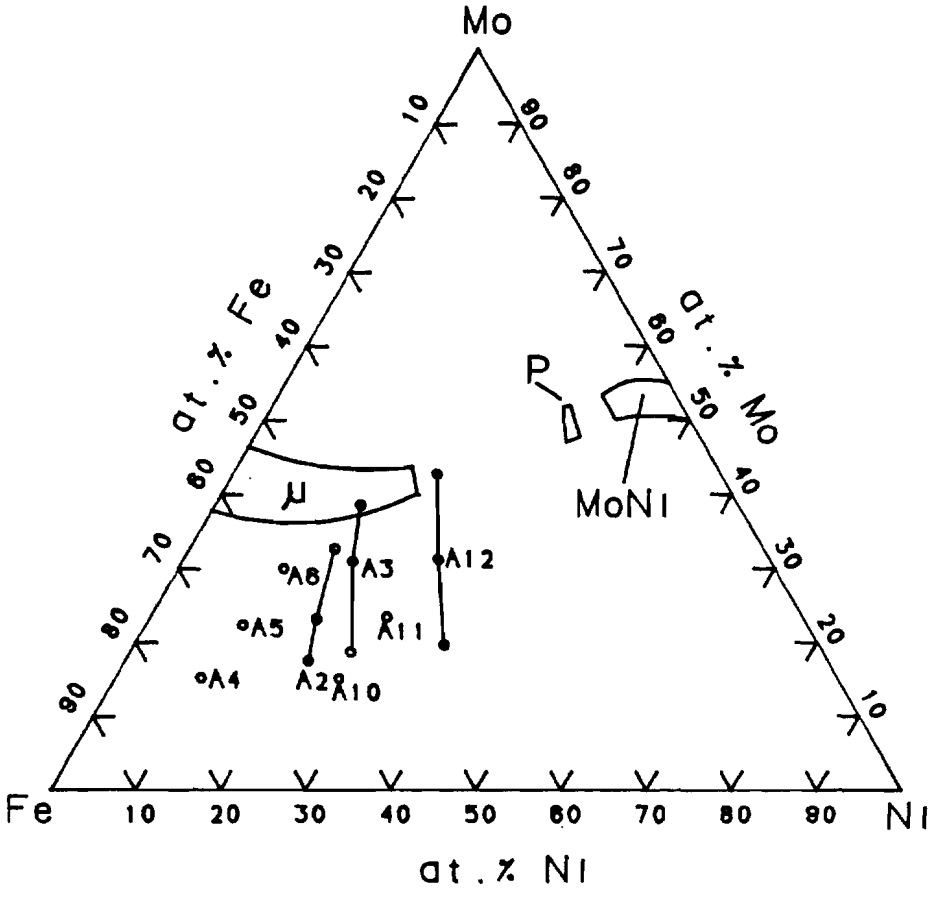

Figure 93. Fe-Mo-Ni phase diagram showing intermetallic regions and location of arc-melted alloy compositions.

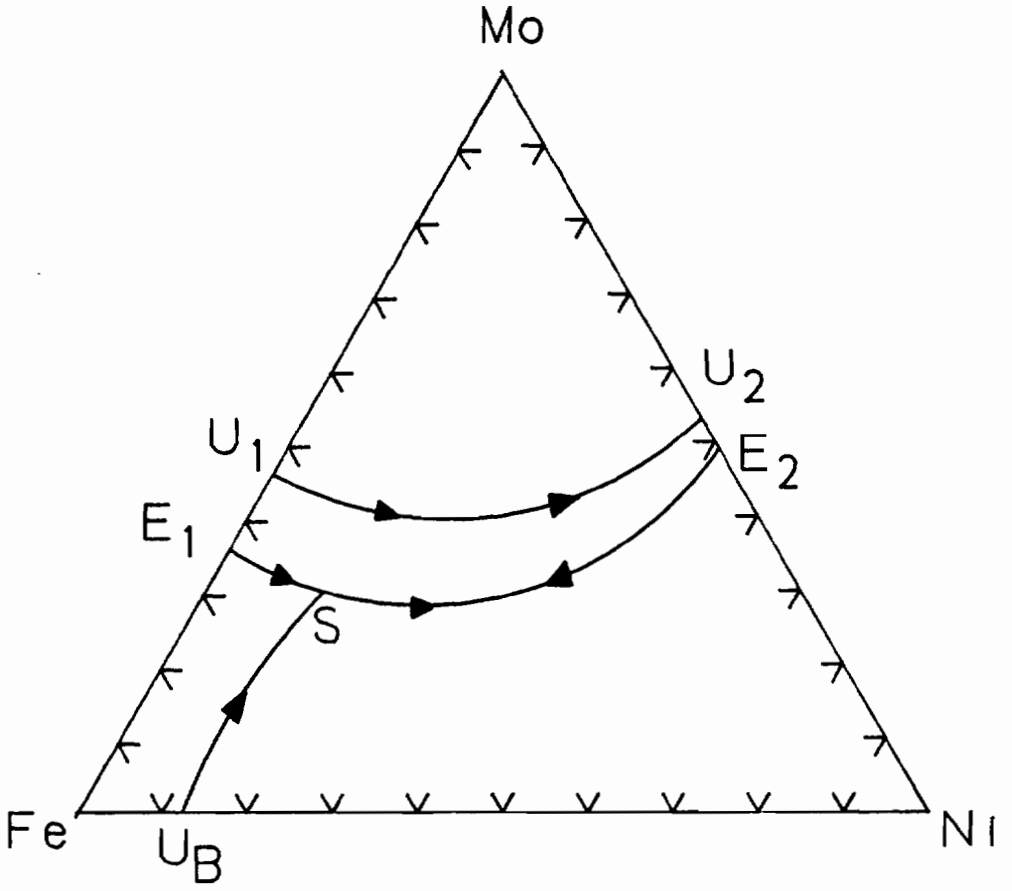

Figure 94. Primary liquidus surface projection of Fe-Mo-Ni phase diagram, with location of arc-melted alloys, after Koster, 1934 [104].

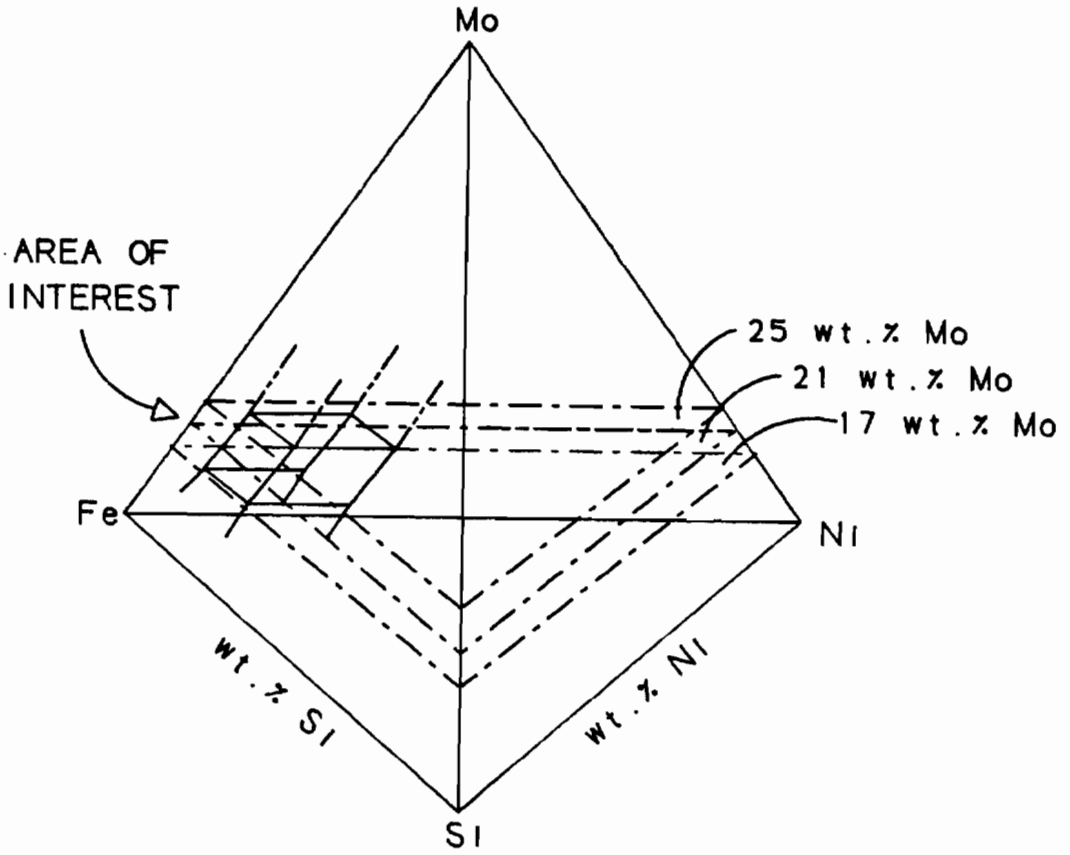

Figure 95. Fe-Mo-Ni-Si quartenary phase tetrahedron showing area of interest.

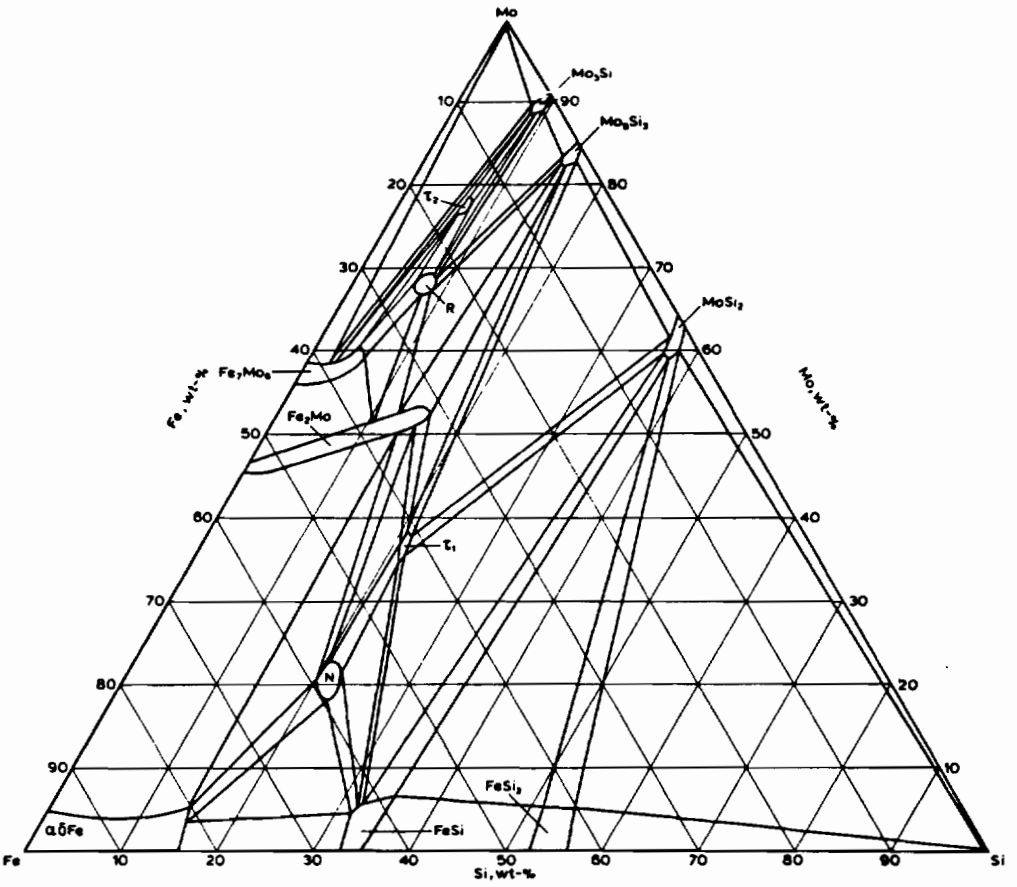

Figure 96. Fe-Mo-Si phase diagram, 800°C isotherm, after Raynor [118].

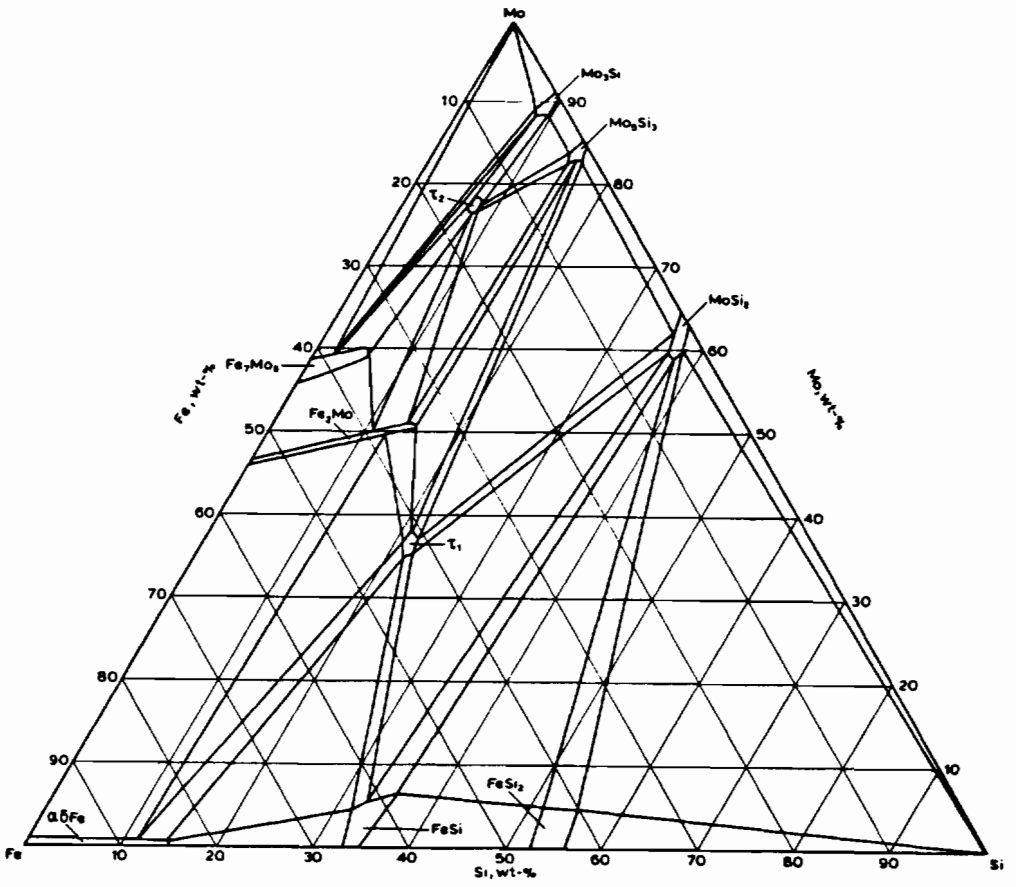

Figure 97. Fe-Mo-Si phase diagram, probable room temperature isotherm, after Raynor [118].

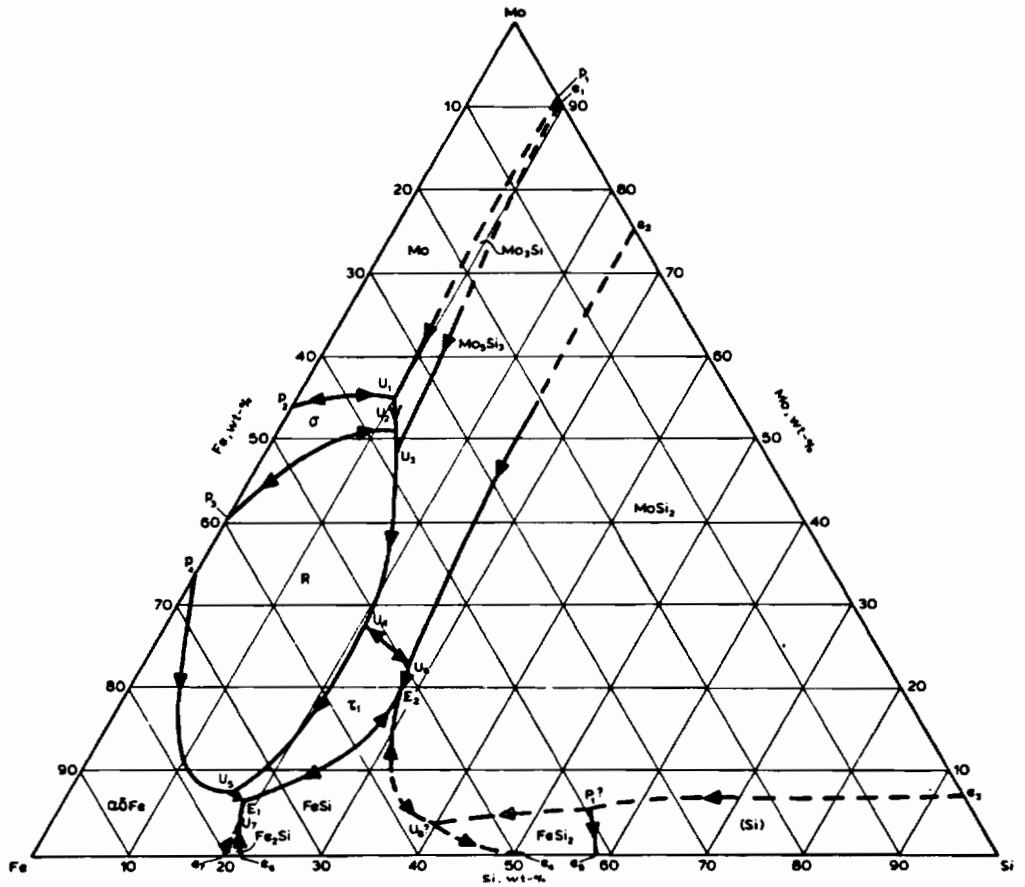

Figure 98. Fe-Mo-Si phase diagram, projection of primary surfaces, after Raynor [118].

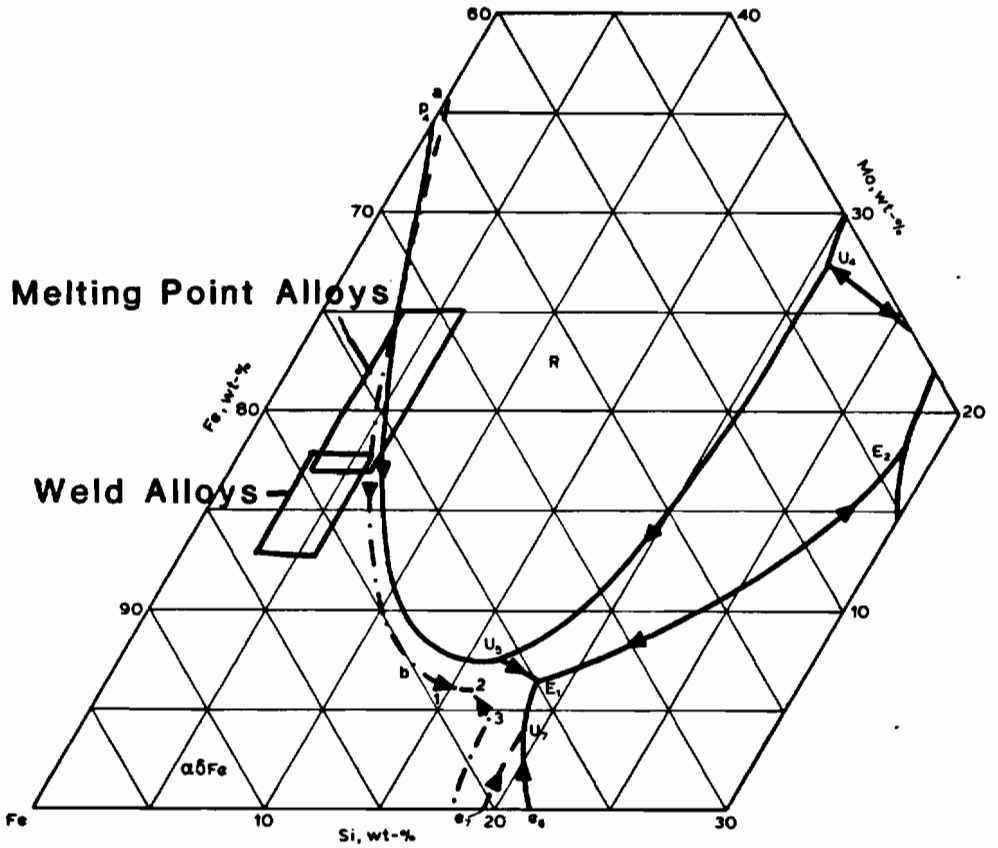

Figure 99. Projection of the liquidus surface in iron-rich corner of the Fe-Mo-Si phase diagram, showing composition ranges of melting point and weld metal alloys.

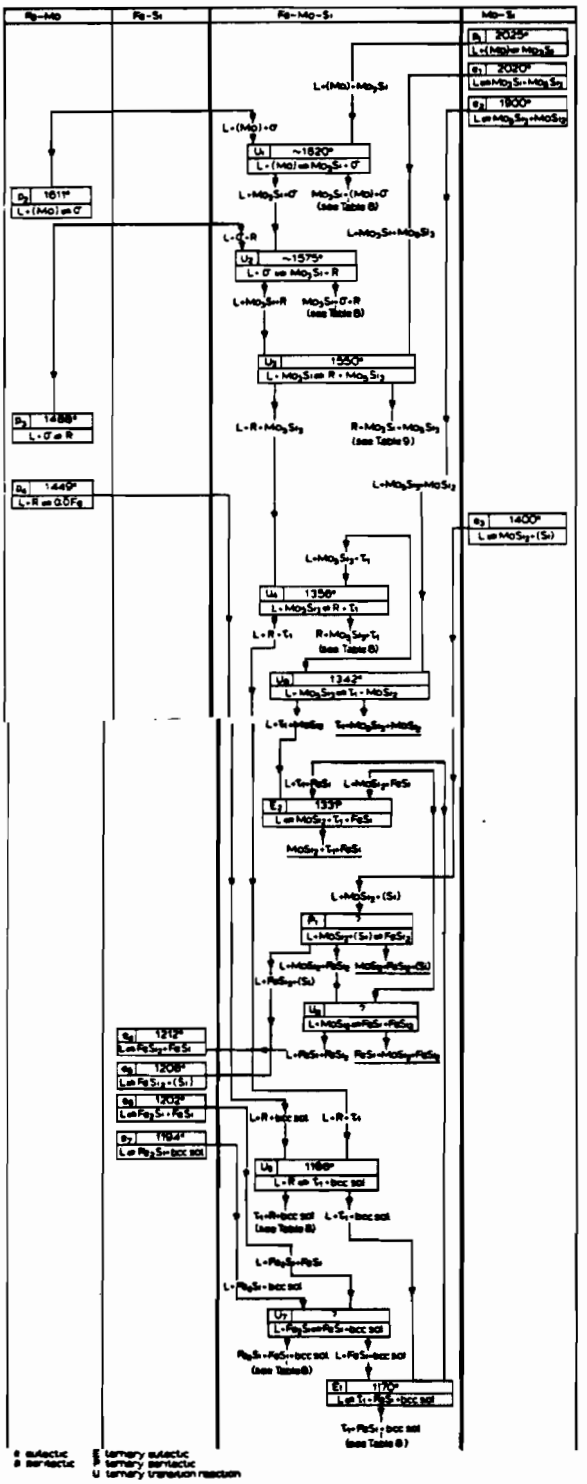

Figure 100. Liqiud-solid state reaction sequences for the Fe-Mo-Si phase diagram, after Raynor [118].

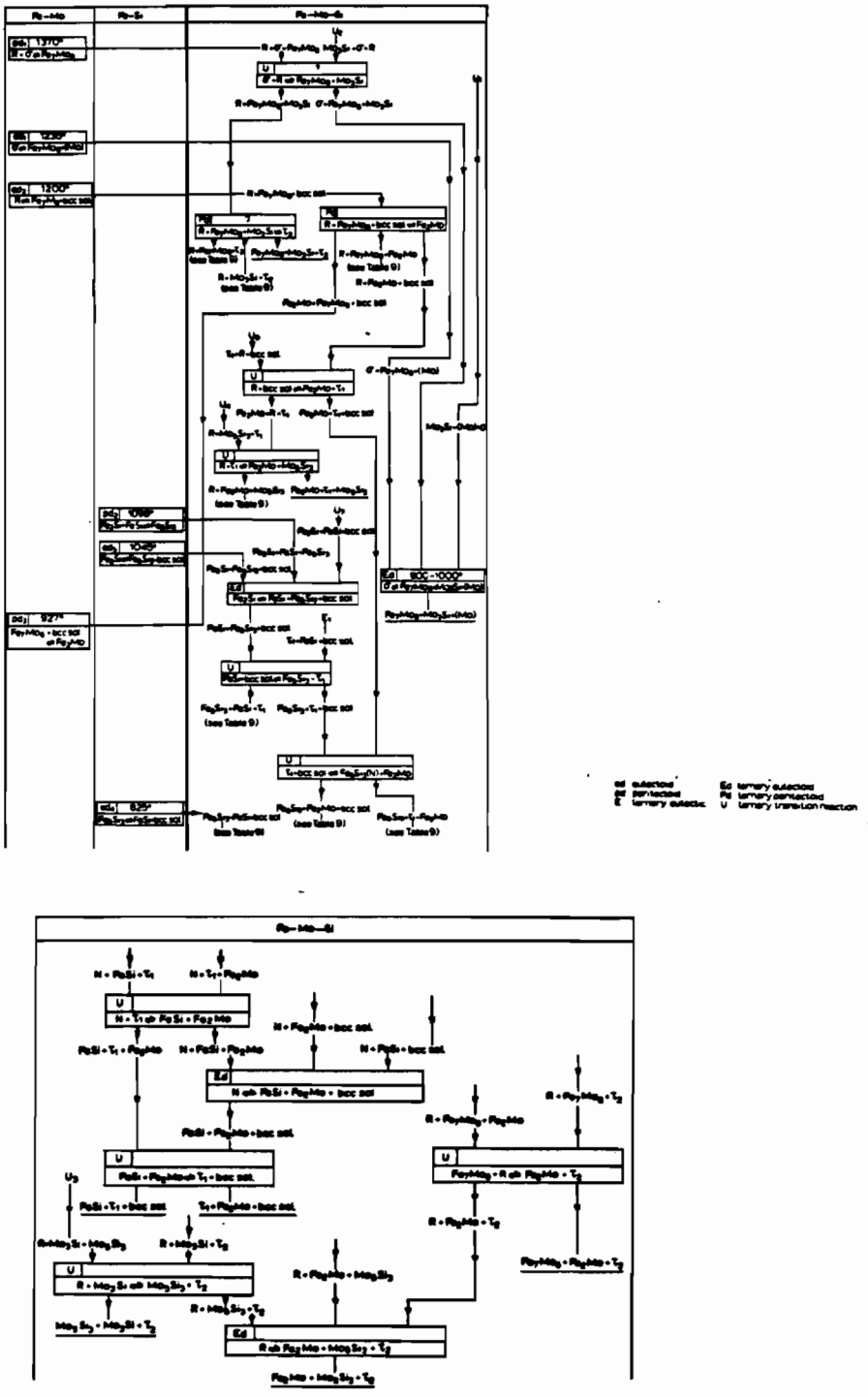

Figure 101. Solid state reaction sequences for the Fe-Mo-Si phase diagram, after Raynor [118].

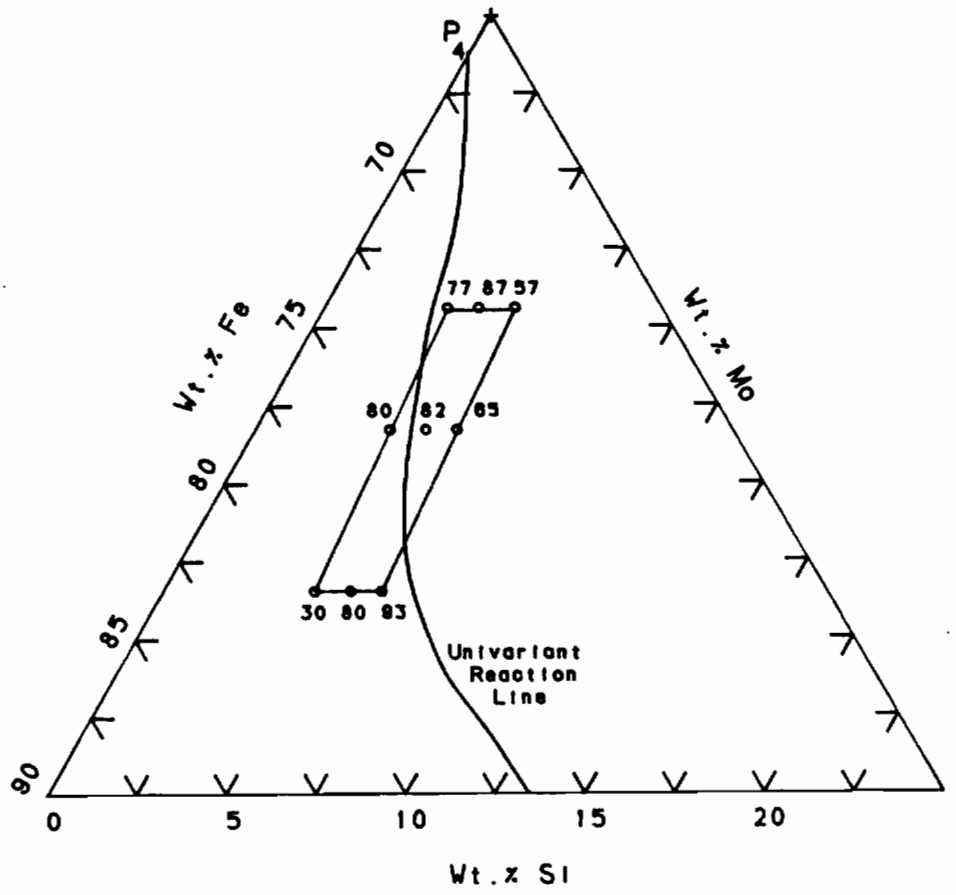

Figure 102. Portion of the Fe-Mo-Si liquidus projection showing melting point alloy eutectic percentage.

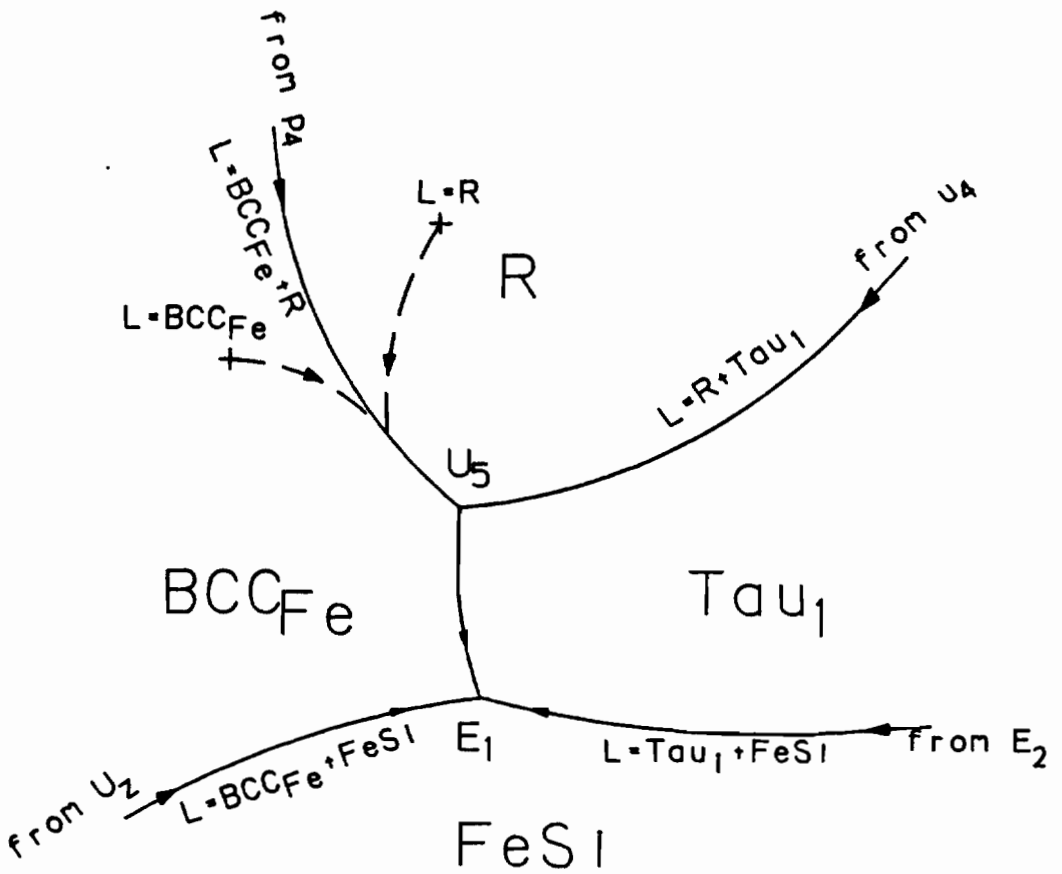

Figure 103. Possible solidification paths.

Figure 104. Microstructure of weld metal alloy showing intermetallic rim around eutectic cell.

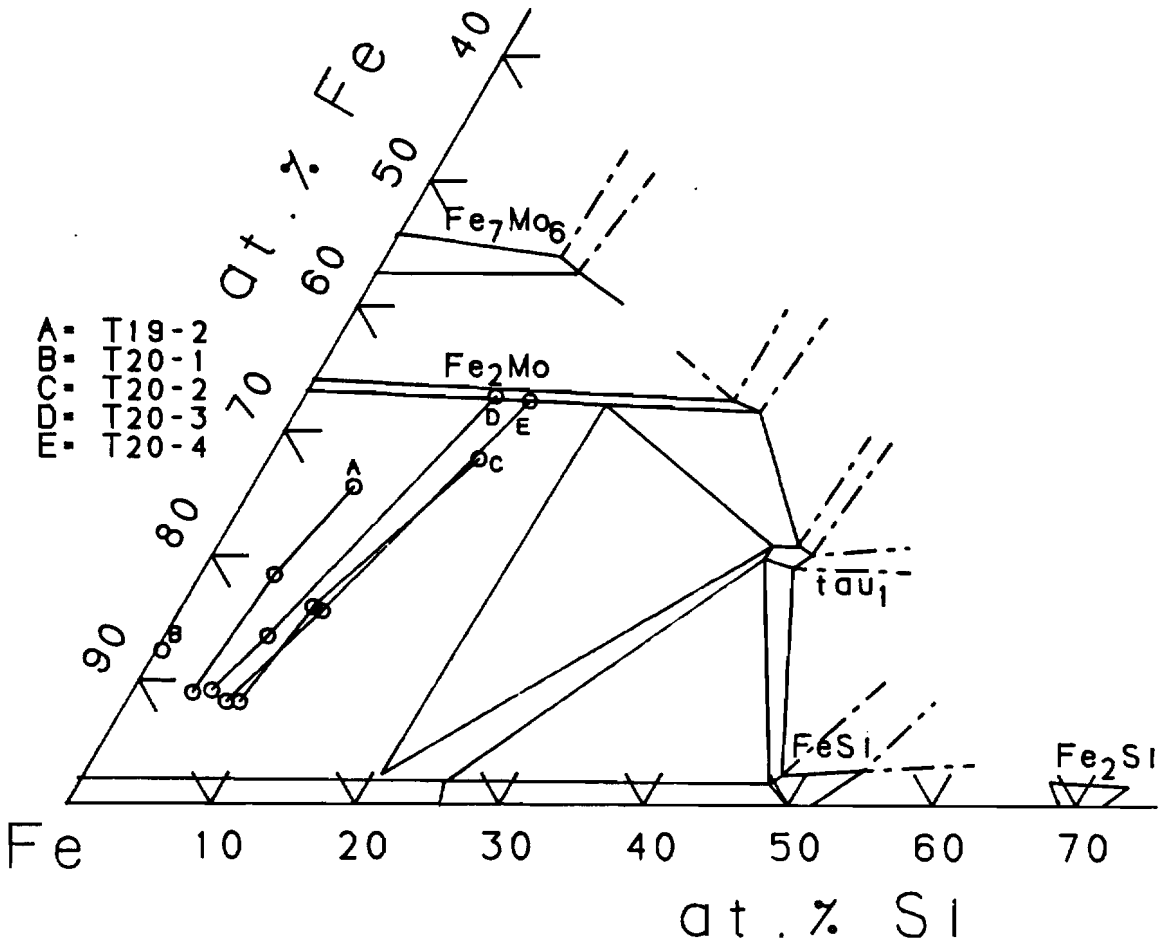

Figure 105. Iron-rich portion of the Fe-Mo-Si phase diagram showing phase compositions of some weld metal alloys, in at.%.

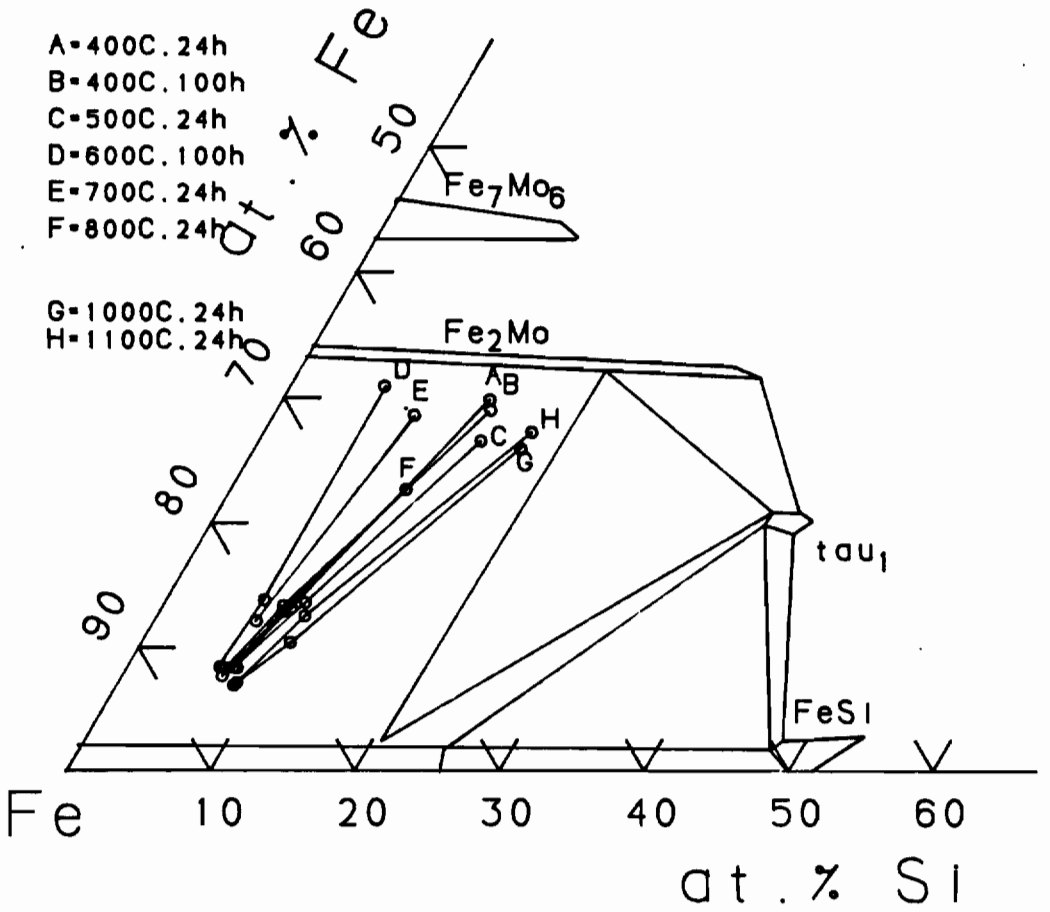

Figure 106. Iron-rich portion of the Fe-Mo-Si phase diagram showing phase compositions of some of the heat treated weld metal alloys, in at.%.

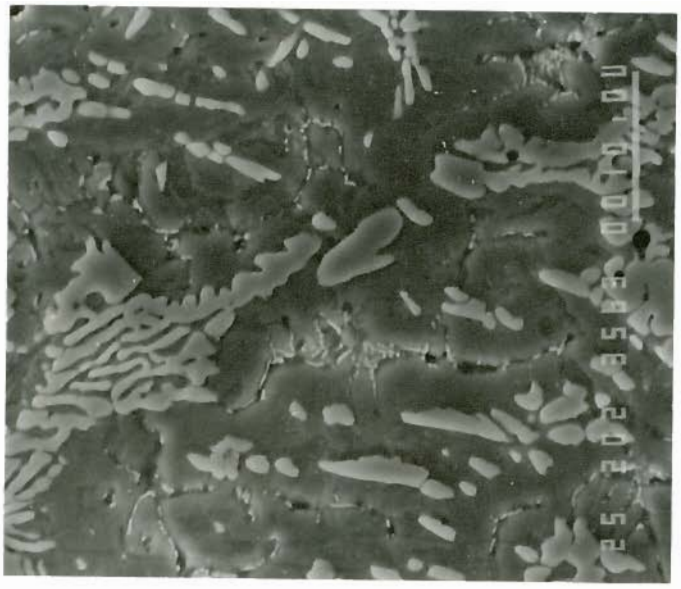

(a)

(b)

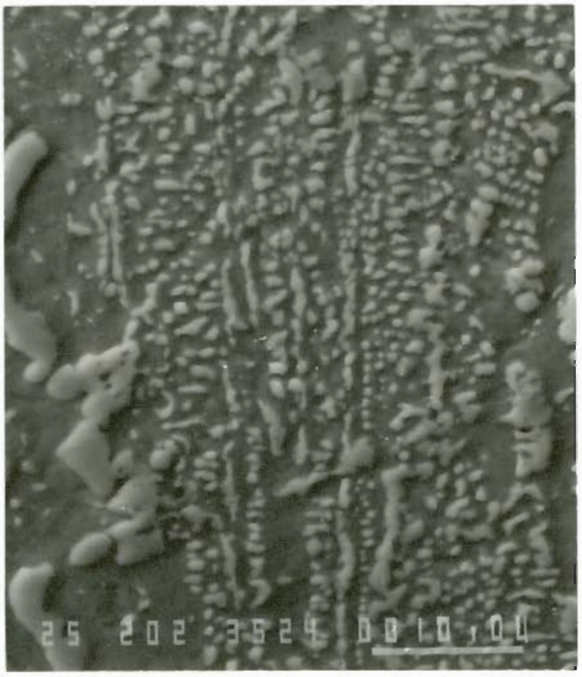

(c)

Figure 107. Photomicrographs of heat-treated alloys showing precipitate formation.

a) 700°C, 24 hours b) 900°C, 24 hours c) 1100°C, 24 hours

4.2 Wear Test Analysis

The wear resistance of the weld metal alloys was tested using the pin-on-drum abrasive wear test. Additional abrasive wear tests were performed using the dry-sandrubber-wheel (DSRW), but only on selected alloys. The major difference between the two wear tests is that the pin-on-drum test could be best described as a high-load test with a two-body abrasive system while the DSRW test is a low-load test with a three-body abrasive wear system. In a comparison of two- and three-body tests, including the pin-on-drum and DSRW tests, Blickensderfer et al [123] showed only a 4% difference between the two when considering a variety of abrasive wear tests in terms of specific wear. Pin-on-drum testing was performed almost exclusively on the weld alloys, primarily because of the ease of specimen fabrication.

While considering weld alloy abrasive wear resistance it should be noted that there are a number of variables which are interdependent and affect the wear resistance. These interdependent variables include alloy composition, hardness, and the microstructure. One microstructural variable which has a large influence on wear resistance is the volume fraction of hard phase. A large amount of research has been performed to determine the relationship between volume fraction hard phase and wear resistance [20-24]. Generally, the higher the volume fraction of hard phase, the greater the wear resistance, often only up to a point.

The elements of the alloy composition were treated as independent variables and evaluated versus the pin-on-drum wear resistance. Graphs of these are shown in Figures 108, 109, 110, and 111. Hardness versus

the pin-on-drum wear resistance was also plotted (Figure 112). From these graphs it was observed that there was a fair amount of datum scatter, and any trends were not readily evident. There was no apparent relationship between hardness and wear resistance.

Since the hardness was dependent on microstructure which was dependent on composition, the effect of the independent composition variables on hardness was examined. Plots of hardness versus wt.% molybdenum, wt.% nickel, wt.% silicon, and wt.% carbon are shown in Figures 113, 114, 115, and 116 respectively. Again there was a good deal of scatter in the data points, and again trends were not readily evident.

Multiple linear regression analysis was performed using hardness, wt.% molybdenum, wt.% nickel, wt.% silicon, and wt.% carbon as variables. Permutations using reciprocal values of wear and square and cube roots of some variables were tried. However, singular correlation coefficients never rose above 0.5 and plots of real versus calculated values showed only a small degree of correlation. Figure 117 shows a graph of real versus calculated values for regression using the hardness and composition variables and reciprocal wear. As can be seen, the regression equation differs substantially from reality, which was typical of the regressions tried.

From examination of attempts to correlate wear rate with the various variables it became obvious that trends could not be inferred. Since a multi-phase microstructure performed the best in terms of pin-on-drum wear resistance, the new alloy chemistry approximated those compositions which produced multi-phase structures. The new composition was then modified to accept the following compositional ranges: maximum wear

resistance at 12-16 wt.% molybdenum, 14-17 wt.% nickel, and greater than 5 wt.% silicon. This aim composition ended up leaner after welding with a final composition of approximately 14 wt.% molybdenum, 10 wt.% nickel, and 4.5 wt.% silicon. This alloy did have a multi-phase microstructure and a high wear resistance relative to other weld metal alloys. This weld metal composition range was also used in the heat-treatment studies of the weld metal alloys. Wear rates of these alloys in pin-on-drum tests were twice as high as high-chromium high-carbon alloys, 6.3-6.6 mg/m versus 2.5-3.5 mg/m, but still less than the wear rates produced by low alloy steels, 8.22 mg/m for AISI 5160 for example [128,129].

Wear surfaces of some pin-on-drum specimens were examined in the SEM. Typical wear scars for a number of different weld metal microstructures and compositions are shown in Figure 118 and 119. Photographs in Figure 118 are of pins with wear rates greater than 7 mg/m, and those in Figure 119 are of pins with less than 7 mg/m wear rates. Deformation of the matrix phase was clearly visible at edges and walls of grooves left by abrasive particles. The extent of deformation however, was limited to groove edges in alloys of lower wear rates. The wear grooves were 5-10 microns wide, measured from photomicrographs, on alloys with low wear rates. Abrasive particle grooves on alloys with higher wear rates were more than twice as wide, over 20 microns. These higher wear rate alloys also exhibited more plastic deformation in and at edges of wear grooves. Prows of deformed material left by abrasive particles were seen as well, as shown in Figure 120.

Some tested pins were etched in a $FeCl_3$-HCl-Methanol etchant and re-examined. The results are shown in Figure 122, along with photo-

micrographs of the actual microstructure. Effects of microstructure morphology can be seen. In a microstructure consisting of almost 100% of a lamellar phase, Figure 121(a), deformation of the lamella can be observed. In this case, though the volume fraction of the hard phase was large, the actual thickness of the hard phase particles was small, much less than the width of the groove left by an abrasive particle. Such thin plates of a hard material were easily sheared by passage of an abrasive particle since there is only a similar thin layer of the tougher matrix phase present to support the hard phase.

Photomicrographs shown in Figure 121(b) and 121(c) are of multiphase alloys with greater wear resistance than the alloy in Figure 121(a). In these two alloys the volume fraction of hard phases were similar, but the size of intermetallic compound particles was greater. The size was still less than the 10 micron width of the abrasive particle groove but large enough to resist the cutting forces imposed by passage of the abrasive particles.

Both hardness and size of abrasive particles were greater than that of the hard phase in the most wear resistant of the weld metal alloys. The abrasive paper used in the pin-on-drum test was a 150 grit garnet cloth with garnet particles with a mean size of 100-110 microns and a hardness of about 1400 HV. The Laves phase intermetallic in the weld alloys had a hardness of approximately 800 HV. Cutting and grooving of the hard phase, the Laves phase, in the weld alloys could be seen in the photomicrographs of etched wear scars of the pins.

On the whole the experimental intermetallic-hardened weld hardfacing alloys did not perform as well as commercial high-chromium high-carbon

alloys. Wear rates of intermetallic-hardened alloys were a factor of two higher. Two commercial chromium-carbon alloys tested had pin-on-drum wear rates of 2.078 mg/m at a hardness of 53.8 HRC and 3.492 mg/m at a hardness of 43.2 HRC. Besides differing in hardness, the commercial alloys possessed microstructures with a higher hard phase volume fraction, and the size of the hard phase particles was greater. Figure 122 shows photomicrographs of these commercial alloys which can be compared to photomicrographs of intermetallic-hardened alloys in Figures 104 and 121. The carbides formed in high-chromium high carbon alloys were much harder than the intermetallic compounds; 1200-1600 HV [124] versus 700-820 HV for a $Fe_{(2-x)}MoSi_x$ Laves phase intermetallic in a Fe-Mo-Ni-Si arc-melted alloy.

To further increase abrasive wear resistance of intermetallic-hardened alloys, two principal microstructural parameters would need to be modified. These would be hard phase volume fraction and hardness of the hard phases. The tau_1 phase (Fe_2MoSi_2) in the Fe-Mo-Si system has been reported to have a hardness of almost 1100 HV [115]. This is much closer to the hardness of common abrasives than the hardness of silicon-modified Fe_2Mo. Changing the microstructure of Fe-Mo-Ni-Si weld metal alloys to contain the tau_1 intermetallic, as well as increasing overall volume fraction of hard phases, could be accomplished by modifying overall alloy composition in accordance with liquid/solid and solid state reaction sequences proposed by Raynor and Rivlin for the Fe-Mo-Si system.

As discussed previously, solidification of Fe-Mo-Ni-Si weld metal alloys takes place along the univariant reaction lines, p_4-U_5 and U_5-E_1, and at the ternary eutectic E_1, 'Liq = FeSi + Fe_2Mo + bcc_{Fe} s.s.'. After

solid state reactions this yields a structure of 'tau_1 + Fe_2Mo + bcc_{Fe} s.s'. By modifying the overall alloy composition such that it is closer to either the U_5 quasi-peritectic or the E_1 eutectic, solidification products would be modified so that more of the harder tau_1 phase is formed.

Increasing weld alloy silicon content (Line 1, Figure 123) by 5 wt.% would change the composition such that the R phase would be the first solid to form, rather than the bcc_{Fe} solid solution. Solidification would then follow first the p_4-U_5 univariant reaction 'Liq = R + bcc_{Fe} s.s.' to the quasi-peritectic U_5 and then along the U_5-E_1 univariant reaction 'Liq = tau_1 + bcc_{Fe} s.s' to finally the ternary eutectic E_1. The R phase transforms to tau_1 and Fe_2Mo through a series of solid state reactions. By increasing the silicon content further, about 10 wt.% overall, solidification would follow the U_4-U_5 invariant reaction, 'Liq = tau_1 + R', after solidification of primary R phase.

Increasing molybdenum content by 5 wt.% (Line 2, Figure 123) would, as with the 5 wt.% increase in silicon content, promote primary solidification as R phase, followed by solidification along the p_4-U_5 univariant reaction. Adding 5 wt.% of both silicon and molybdenum (Line 3, Figure 123) would place the alloy composition in the midst of the 'Liq = R' region. From this point either univariant reaction, p_4-U_5 or U_4-U_5, could be followed, depending on the liquidus and solidus surface shape. This increase in composition would lengthen the solidification path while following the univariant reaction lines, allowing a great fraction of R phase to form. Exact prediction of phases and their compositions is not possible as orientation of tie lines crossing two phase regions are

unknown, as are relative effects of cooling rates and the presence of 5 to 10 wt.% nickel. Relative proportions of final phases to form, tau_1, Fe_2Mo, and bcc_{Fe} s.s., are not predictible for the same reasons.

Examination of the room temperature equilibrium phase diagram for the Fe-Mo-Si system shows that increases in molybdenum, or molybdenum and silicon, content would increase the volume fraction of $Fe_{(2-x)}MoSi_x$ formed. The diagram also shows that increasing silicon content by 10-15 wt.% overall, the alloy composition would fall into a three phase region of $Fe_{(2-x)}MoSi_x$, tau_1, and bcc_{Fe} solid solution. Thermodynamics dictate that vertices of three phase triangles have invariant compositions. In this case these would be:

$$bcc_{Fe} \text{ s.s.} = 85Fe\text{-}3Mo\text{-}12Si$$

$$tau_1 = 43Fe\text{-}36Mo\text{-}21Si$$

$$Fe_{(2-x)}MoSi_x = 38Fe\text{-}50Mo\text{-}12Si$$

If the weld metal composition were to be increased from 85(Fe+Ni)-15Mo-5Si to 65(Fe+Ni)-20Mo-15Si, phase proportions predicted by the equilibrium phase diagram would be 52% bcc_{Fe} s.s., 15% $Fe_{(2-x)}MoSi_x$, and 33% tau_1; or 48% volume fraction hard phase. The current alloy yields about 30% $Fe_{(2-x)}MoSi_x$ and 70% bcc_{Fe} solid solution. The modified composition would yield more of the harder tau_1 phase, but the molybdenum and silicon contents would have to be increased substantially. Increased volume fraction of hard phases and harder intermetallic compounds should increase abrasive wear resistance. Although much of this reasoning is based on evidence which is insufficient for proof, the previous solidification analysis on Fe-Mo-Ni-Si arc-melted and weld metal alloys affirms the validity of using the Fe-Mo-Si phase diagram and the liquid/solid and

solid state reaction sequences for predictions of phases in other iron-rich Fe-Mo-Ni-Si alloys.

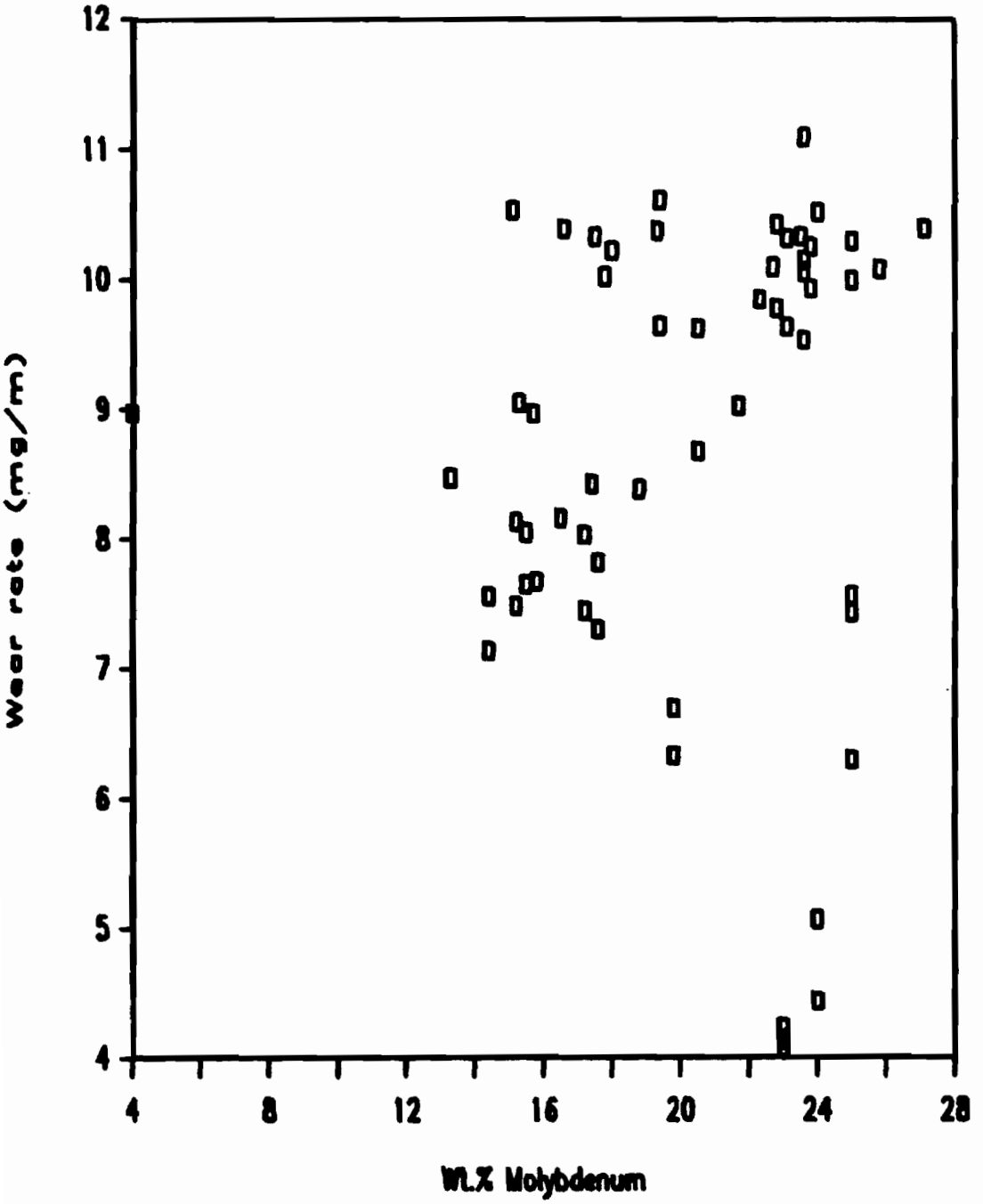

Figure 108. The effect of molybdenum on wear resistance, pin-on-drum abrasive wear test.

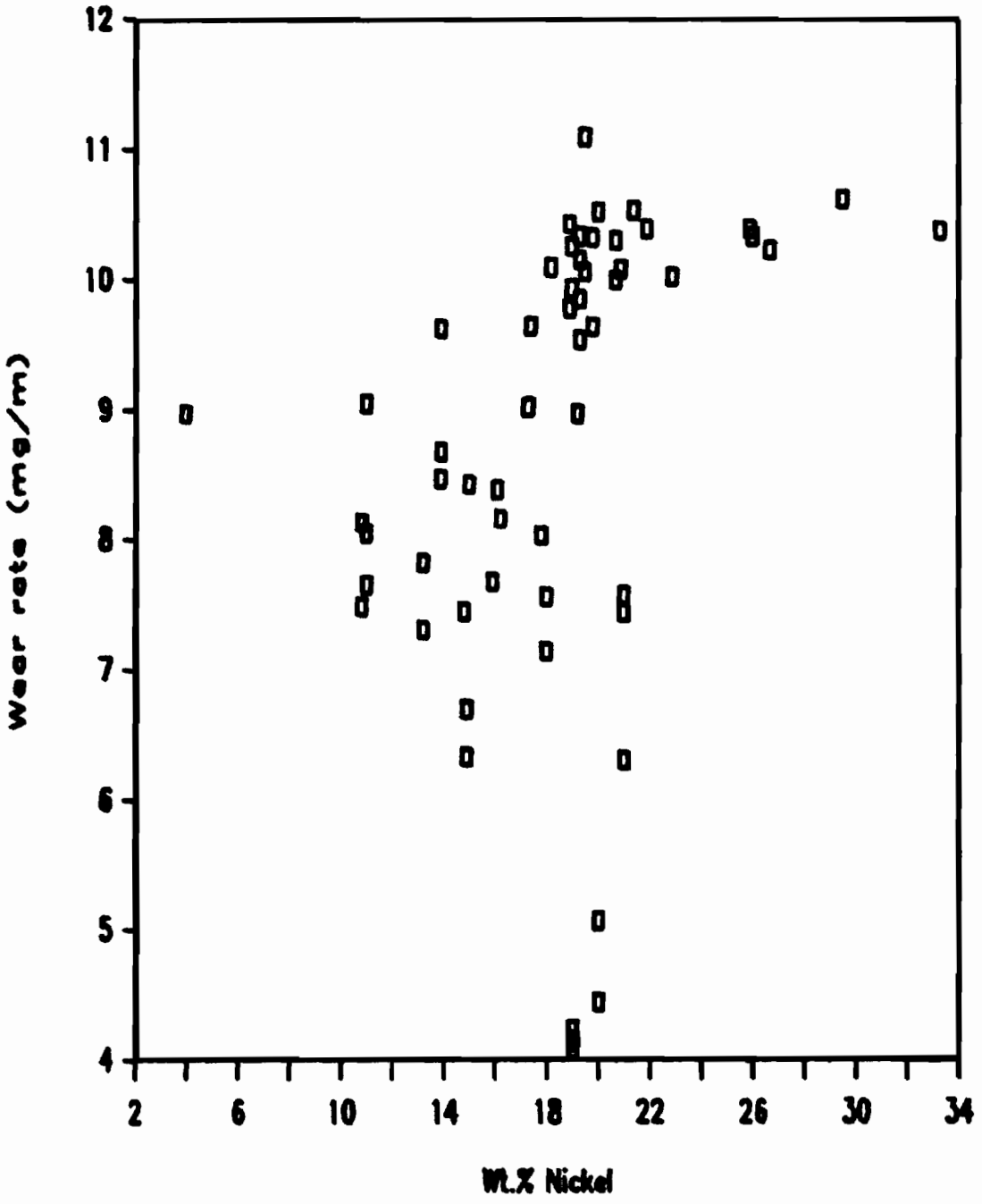

Figure 109. The effect of nickel on wear resistance, pin-on-drum abrasive wear test.

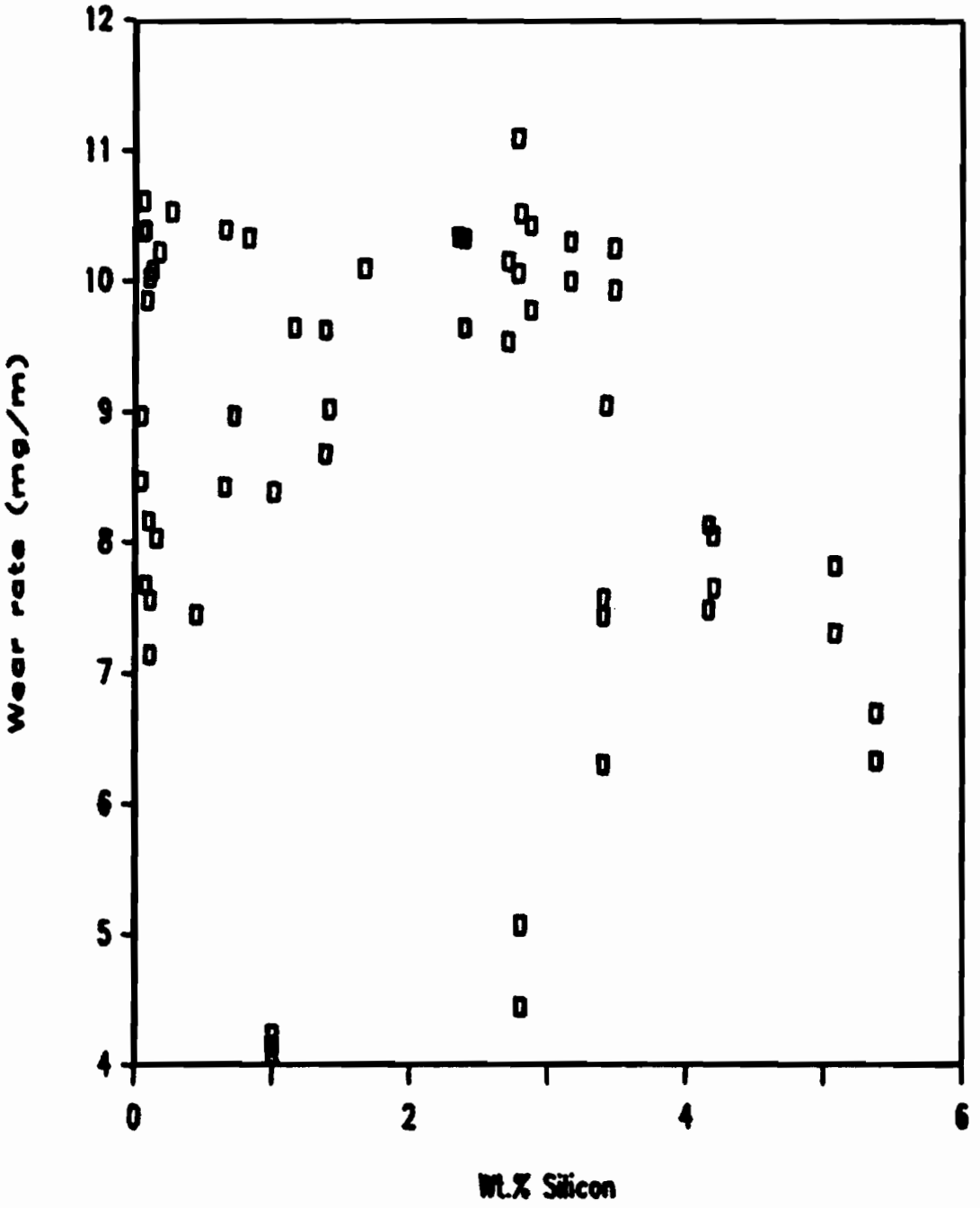

Figure 110. The effect of silicon on wear resistance, pin-on-drum abrasive wear test.

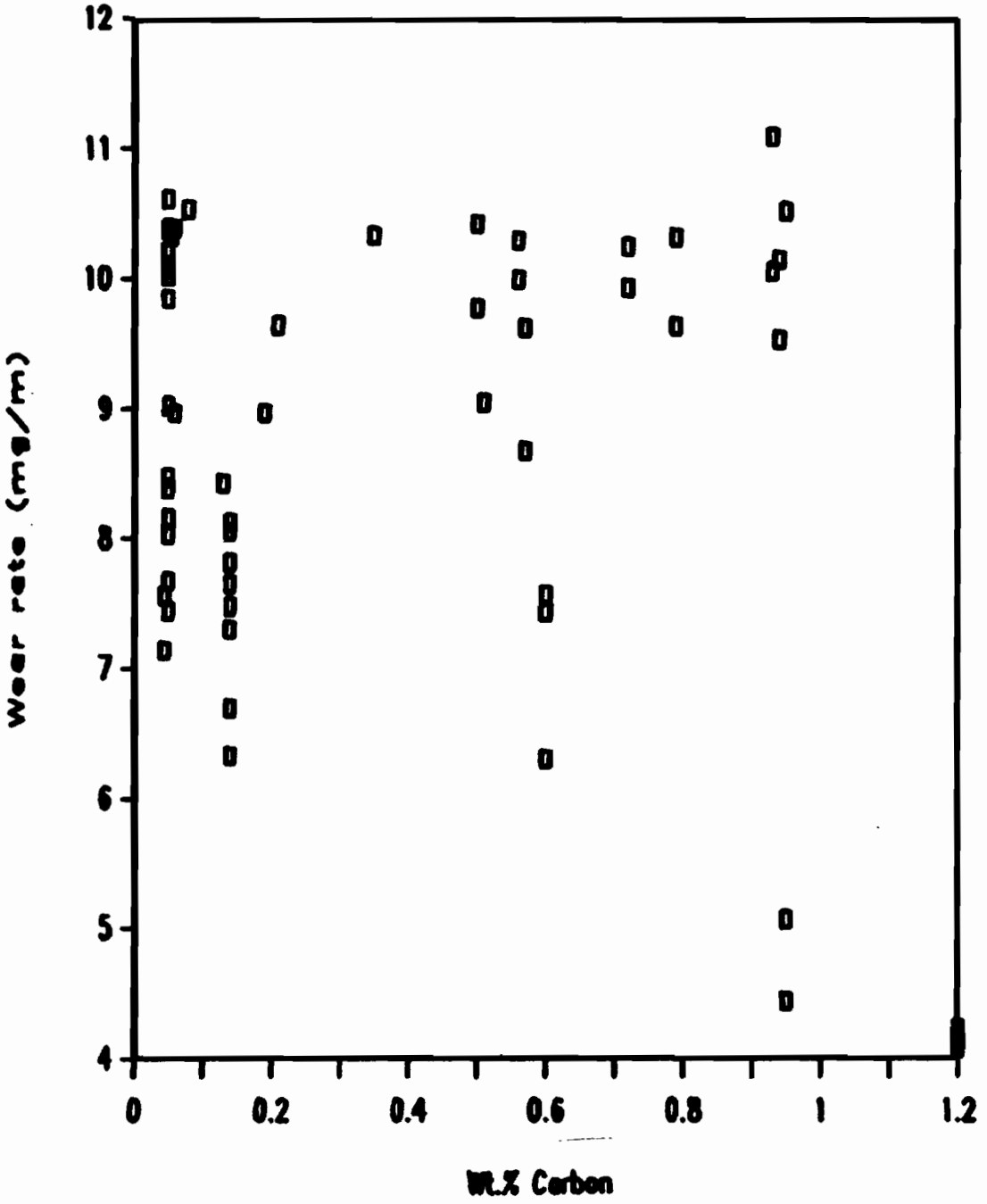

Figure 111. The effect of carbon on wear resistance, pin-on-drum abrasive wear test.

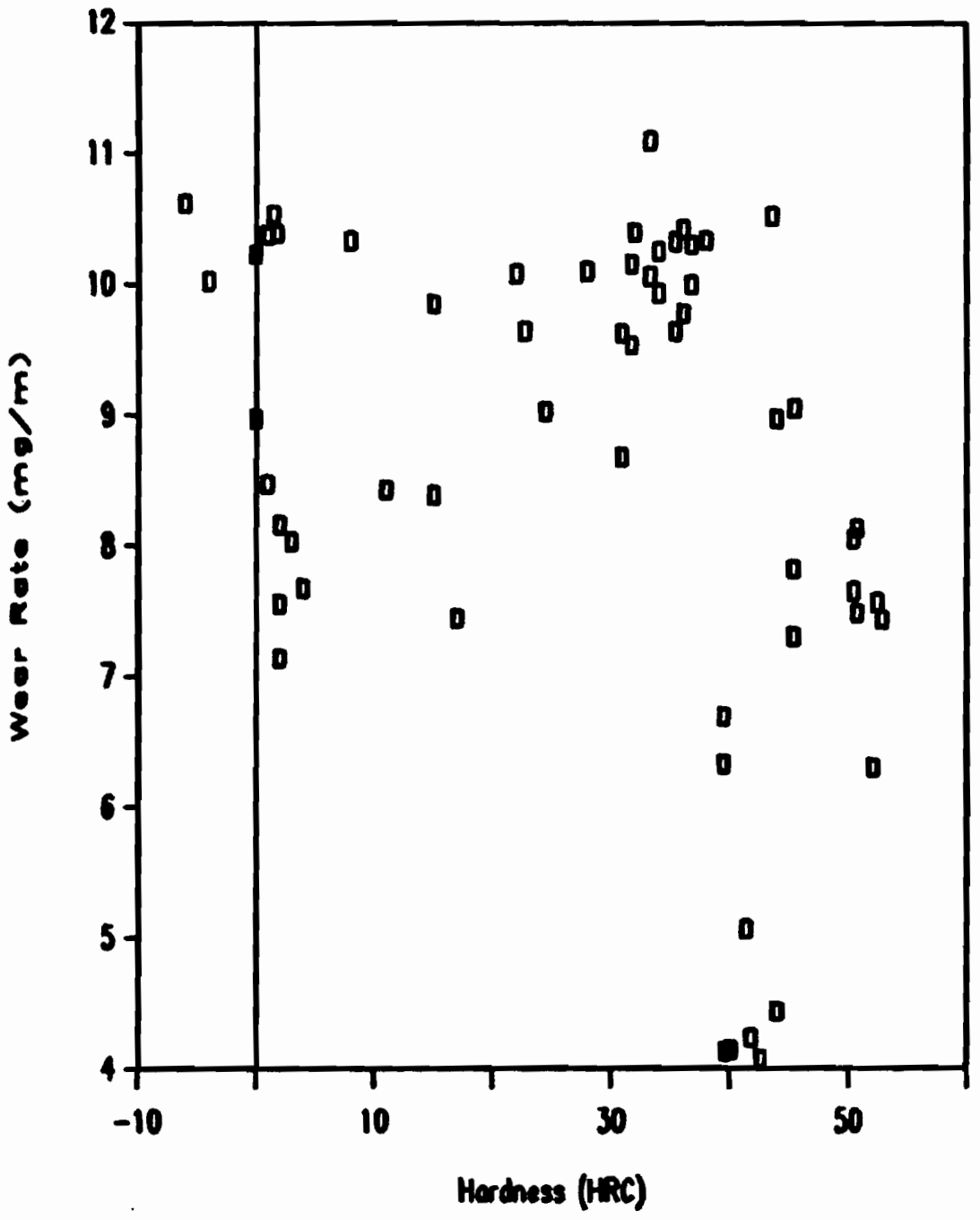

Figure 112. The effect of hardness on wear resistance, pin-on-drum abrasive wear test.

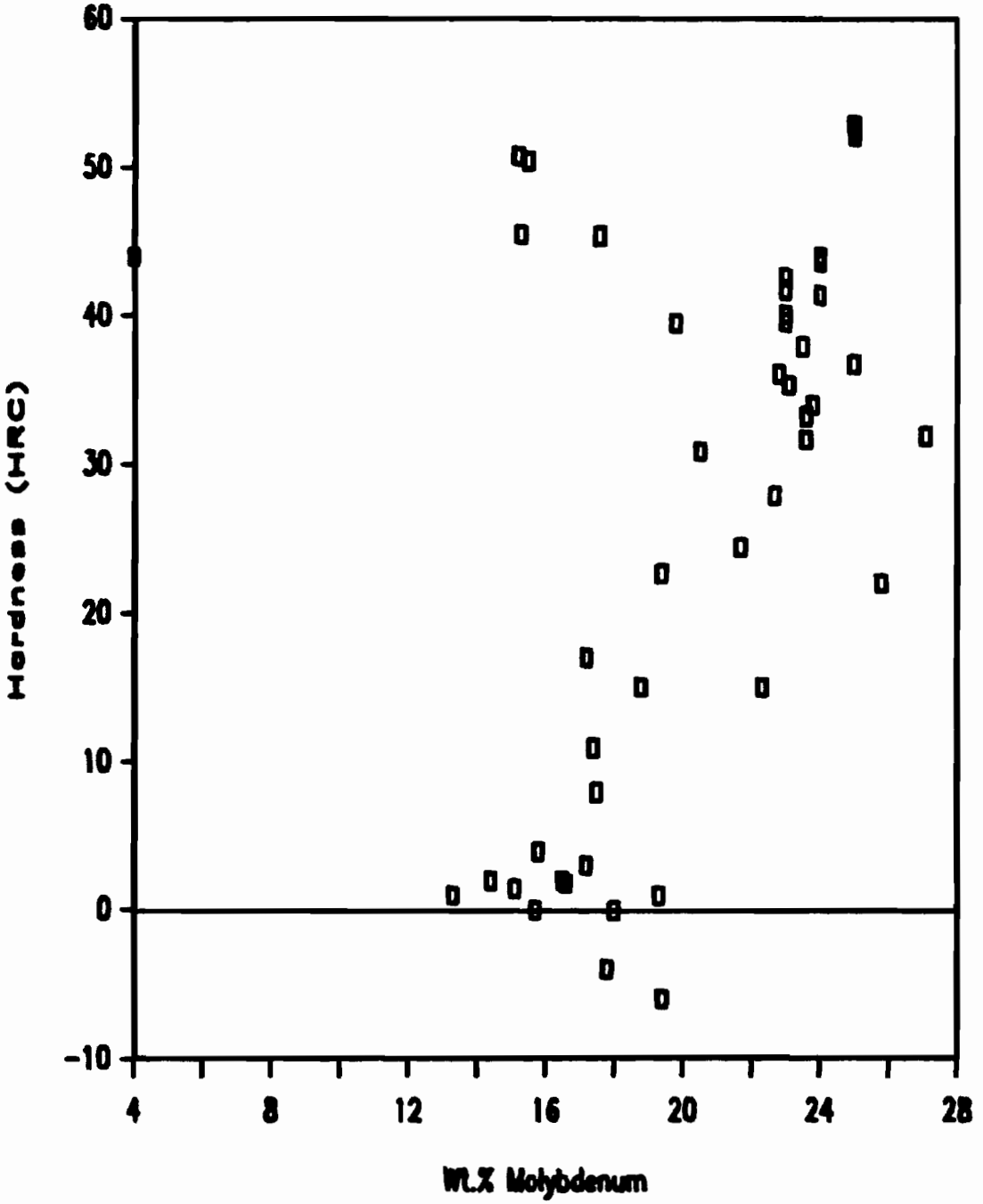

Figure 113. The effect of molybdenum on hardness.

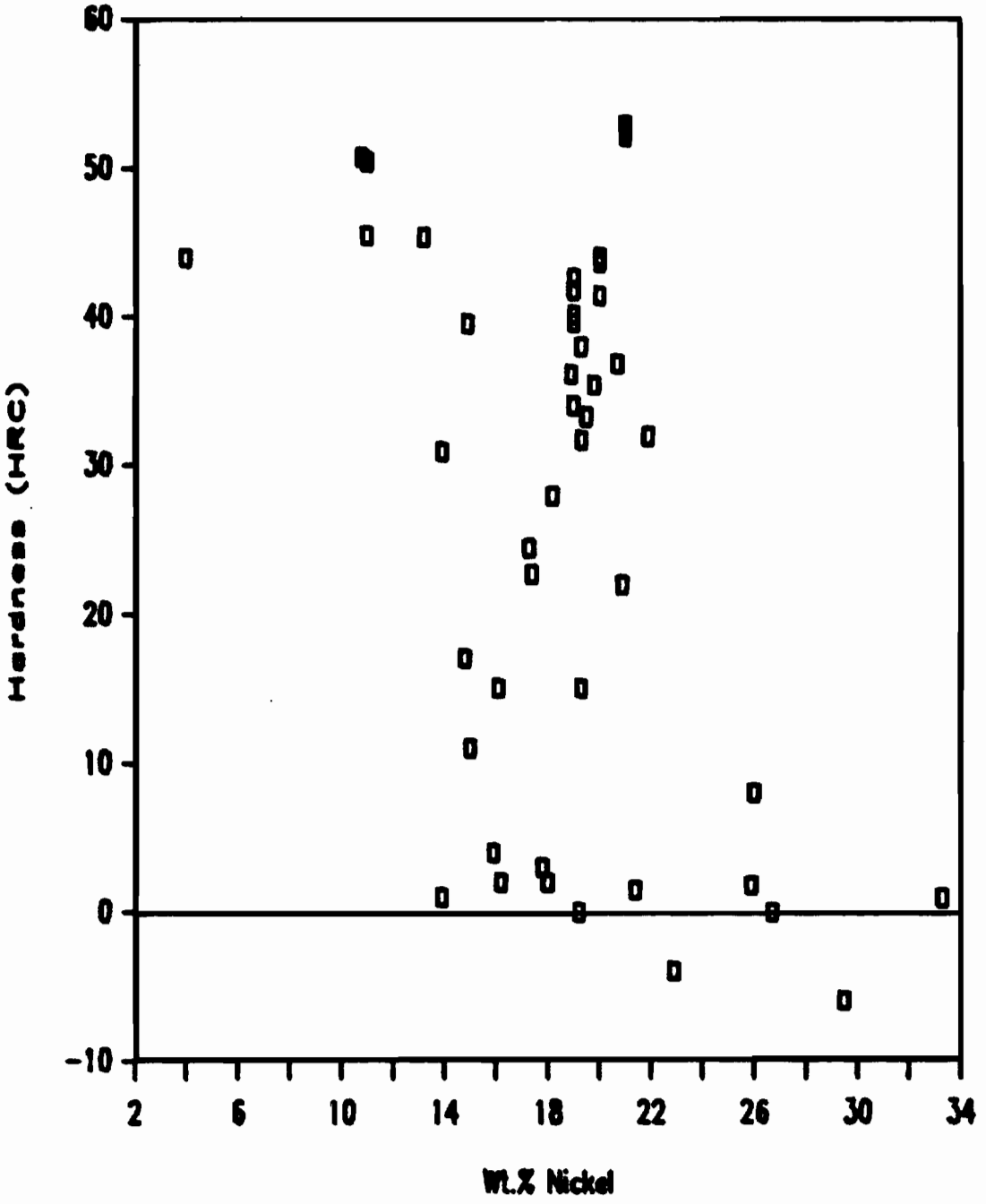

Figure 114. The effect of nickel on hardness.

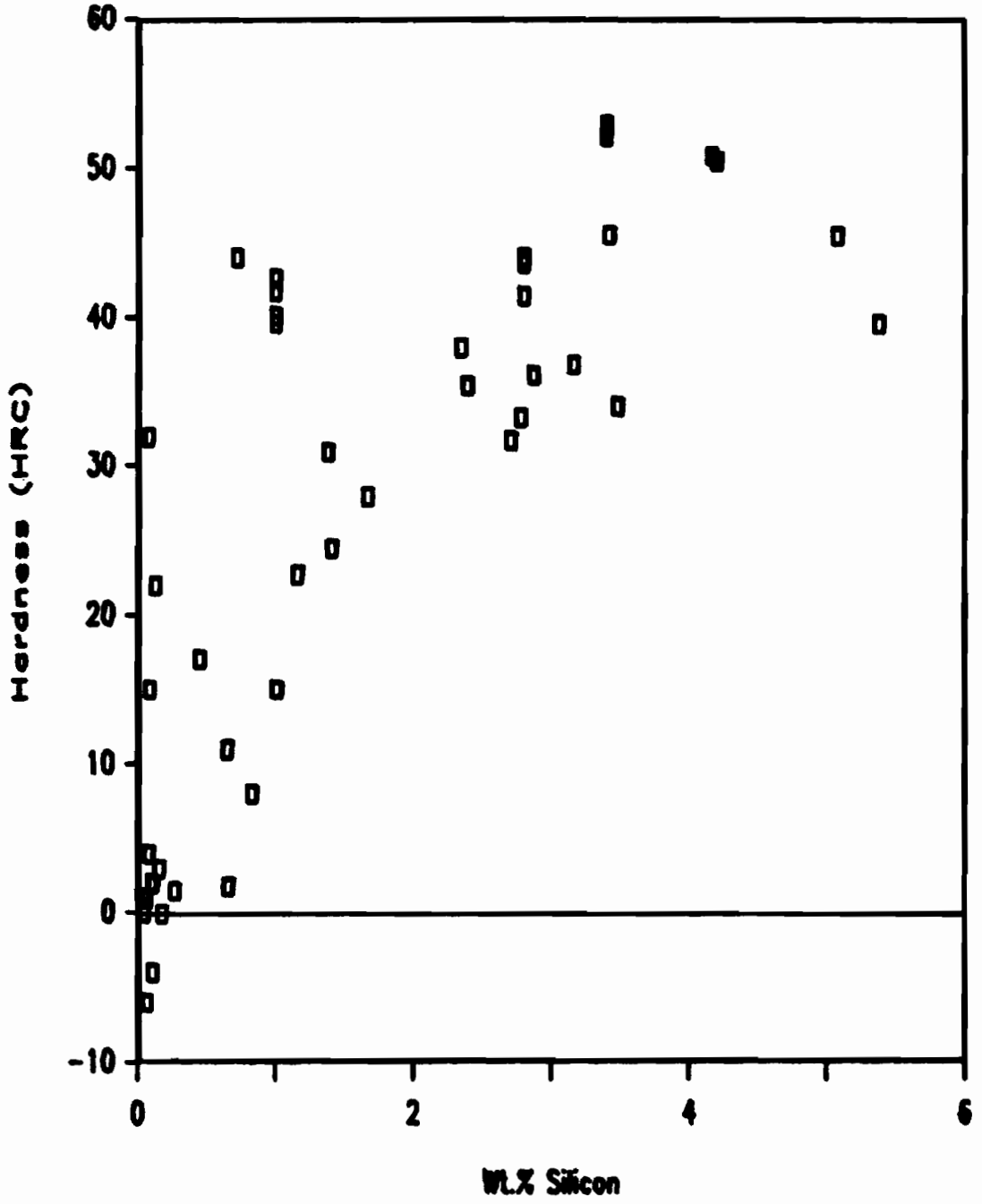

Figure 115. The effect of silicon on hardness.

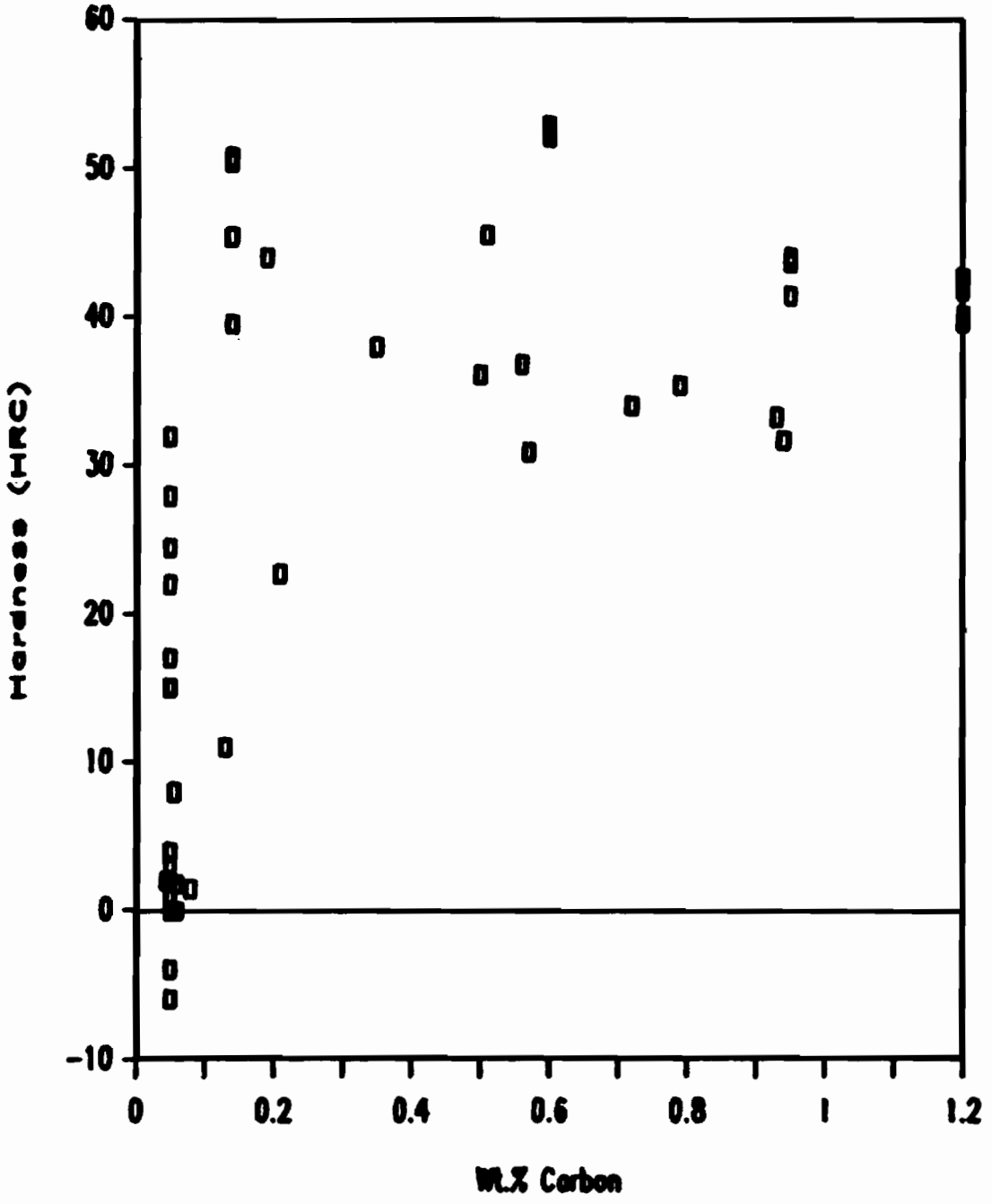

Figure 116. The effect of carbon on hardness.

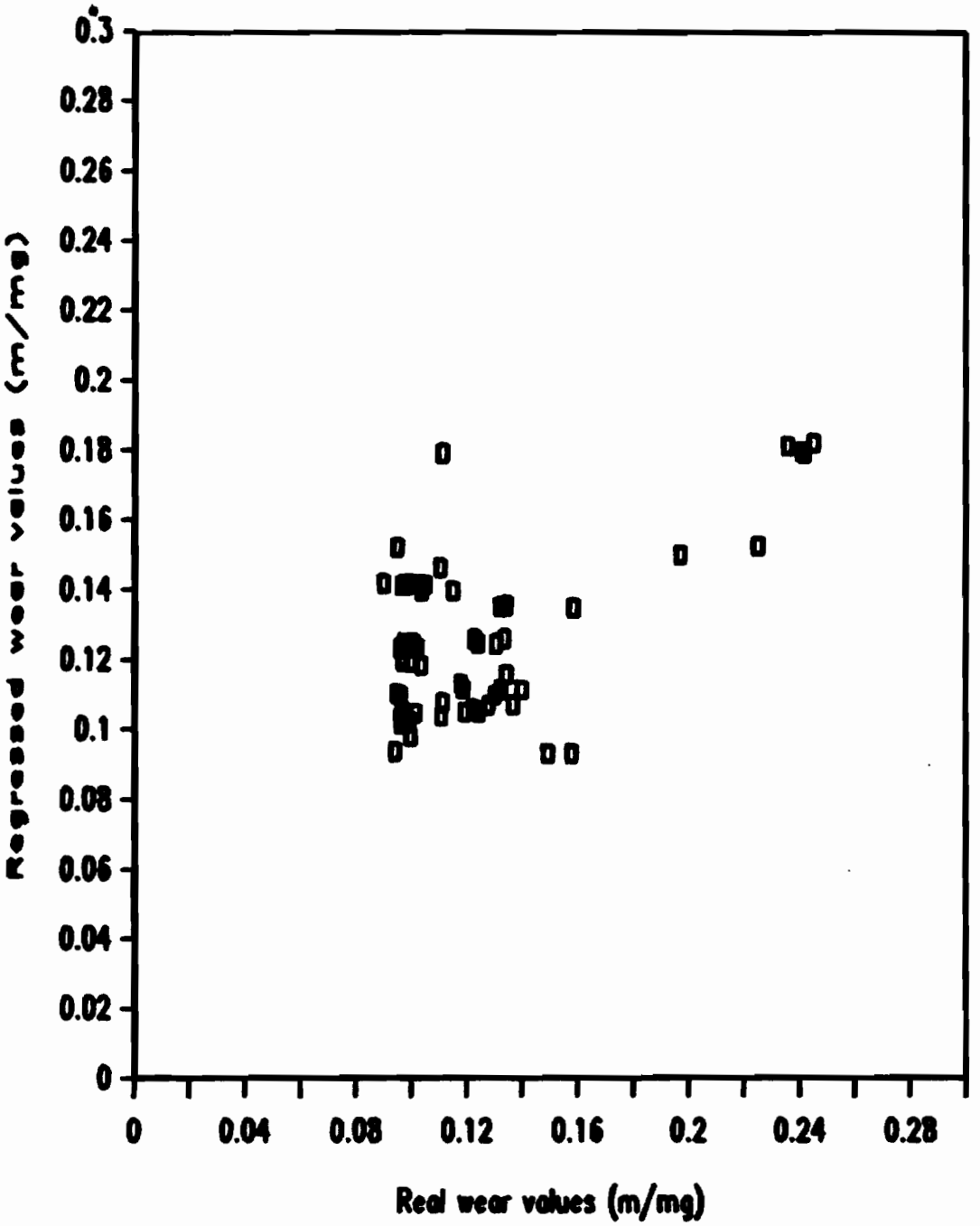

Figure 117. Regressed values versus real values for the equation:

1/wear = hardness + wt.%Mo + wt.%Ni + wt.%Si + wt.% C

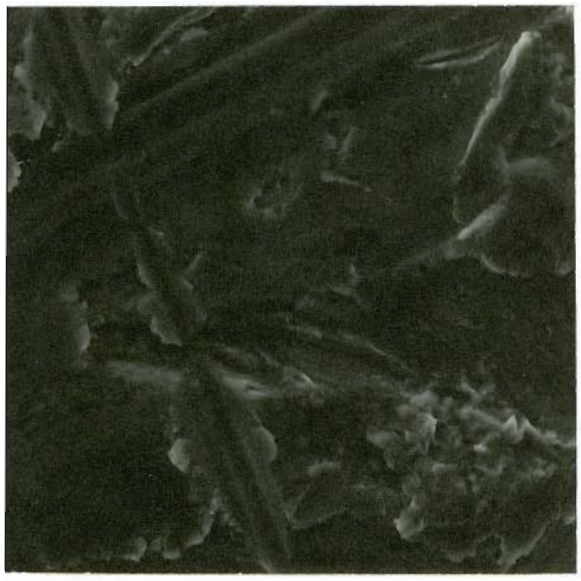

(a)

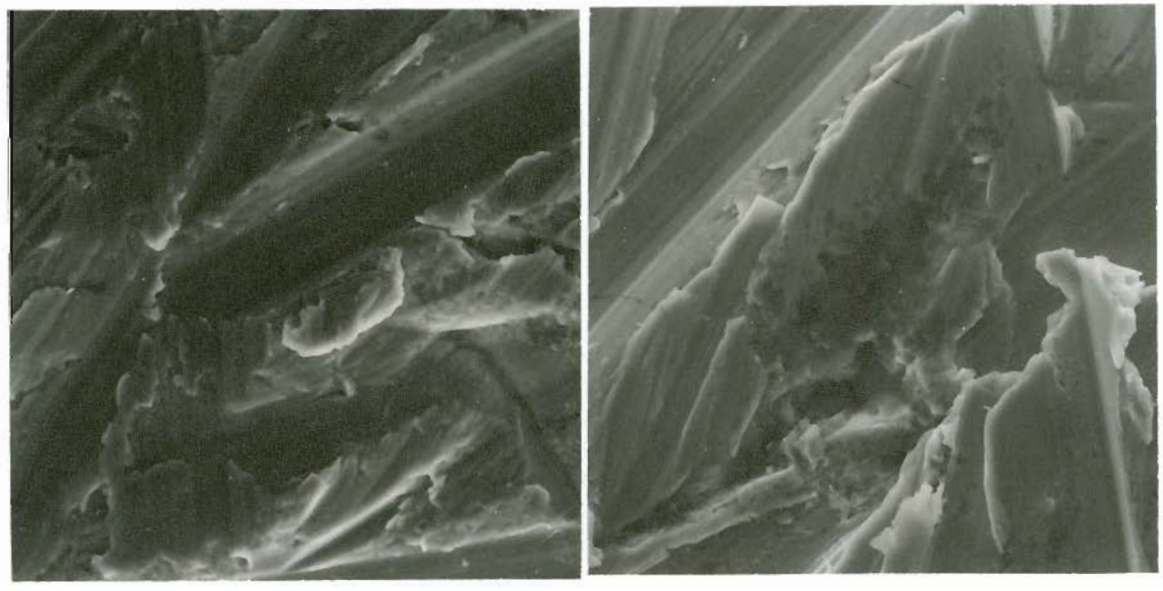

(b) 20μm (c)

Figure 118. Wear scars of high (> 7 mg/m) wear rate weld metal pins, from pin-on-drum test.

a) T19-3, 11.099 mg/m wear rate, 22.3 HRC
b) T19-1, 10.325 mg/m wear rate, 34 HRC
c) T20-1, 7.558 mg/m wear rate, 47.6 HRC

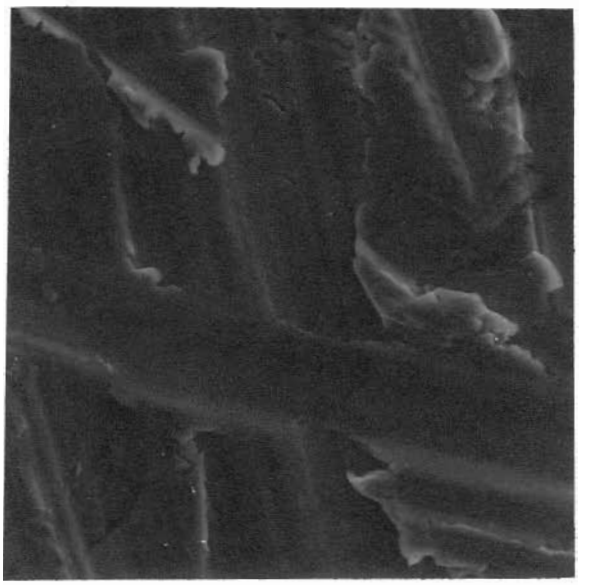

(a)

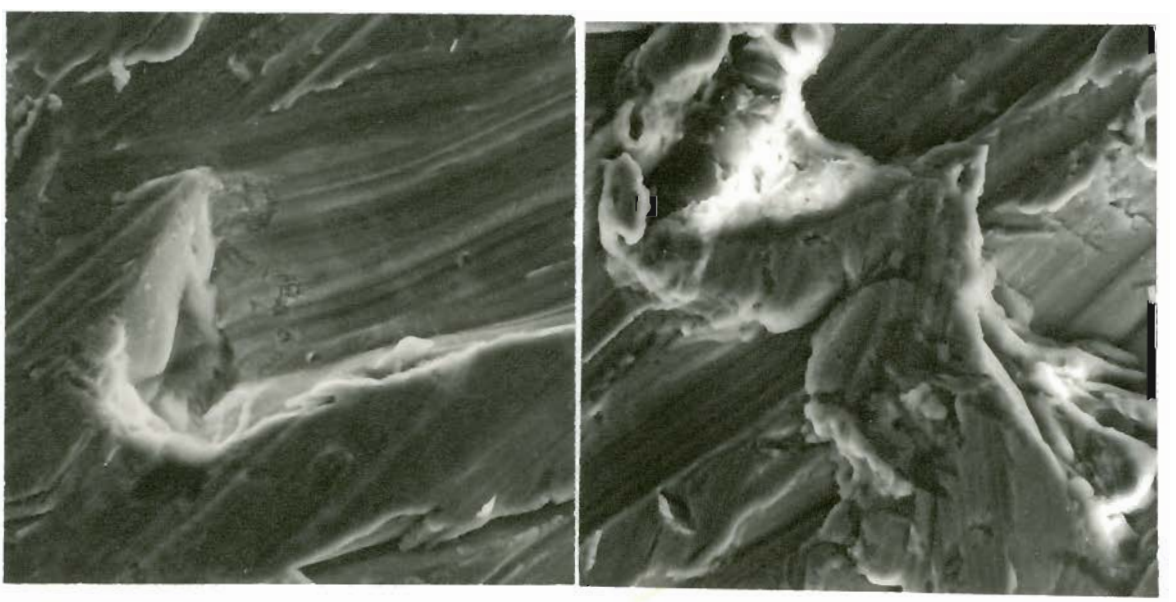

(b) 20μm (c)

Figure 119. Wear scars of low (< 7 mg/m) wear rate weld metal pins, from pin-on-drum test.

a) T20-4, 6.333 mg/m wear rate, 40 HRC
b) T22-4D, 6.305 mg/m wear rate, 55.6 HRC
c) T23-4C, 5.079 mg/m wear rate, 41.4 HRC

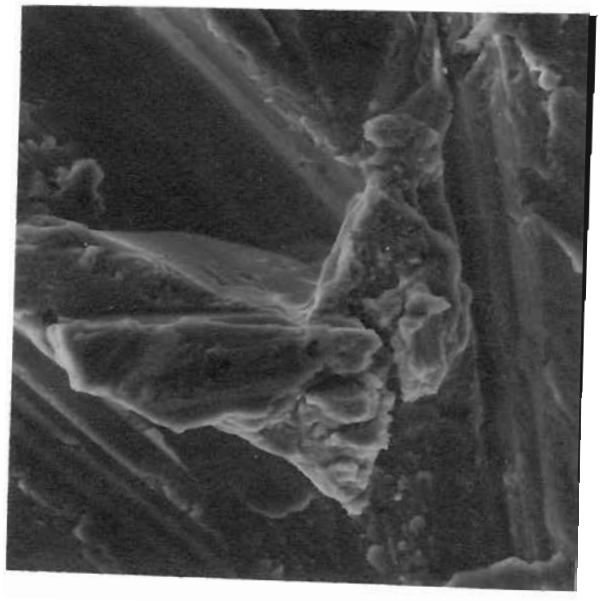

(a)

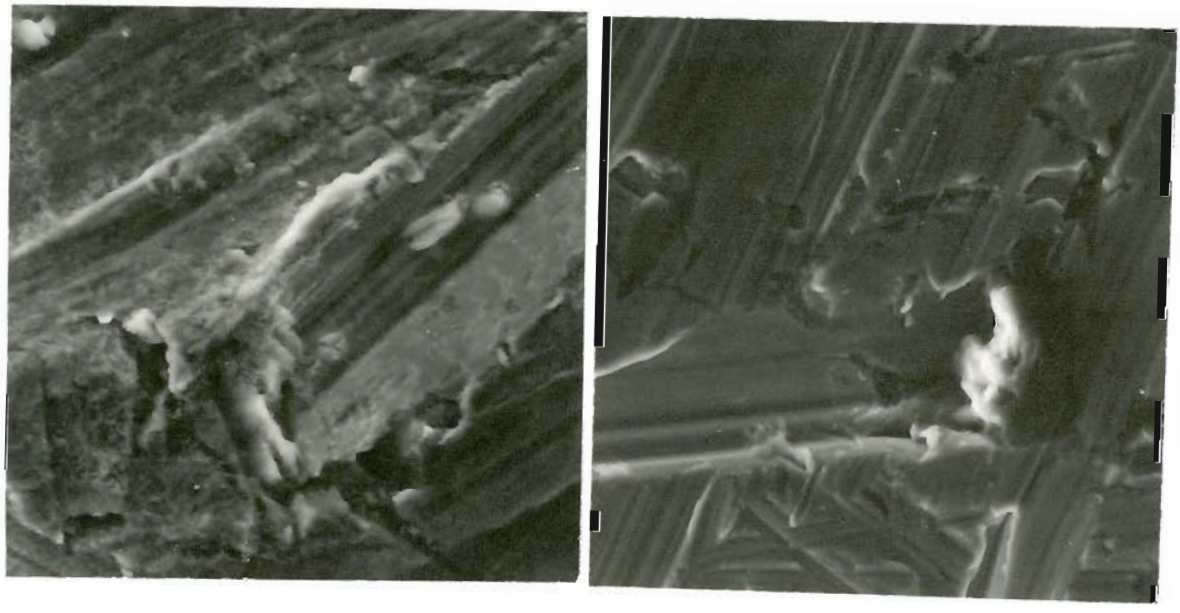

(b) 20μm (c)

Figure 120. Prow formation at end of wear groove left by abrasive particle.

a) T19-3, 11.099 mg/m wear rate, 22.3 HRC
b) T22D, 7.439 mg/m wear rate, 52.9 HRC
c) T24-1E, 4.138mg/m wear rate, 39.6 HRC

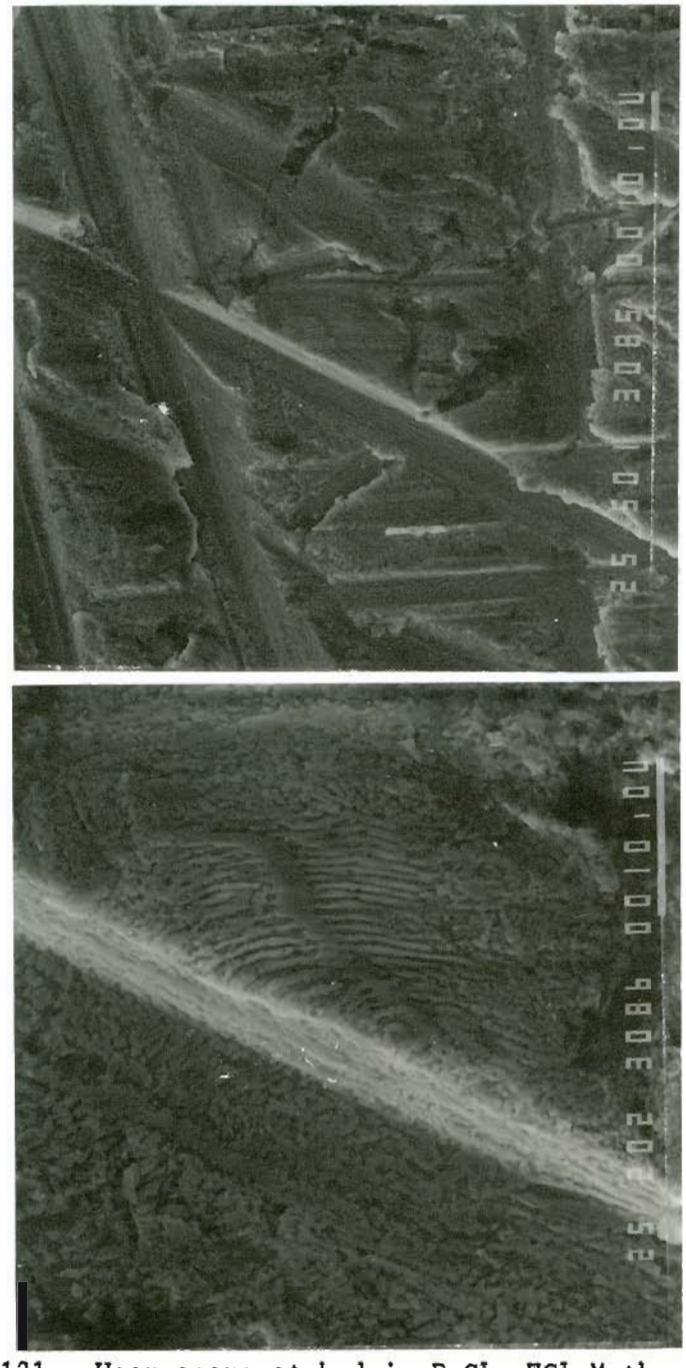

Figure 121. Wear scars etched in $FeCl_3$-HCl-Methanol etchant to reveal microstructure.

a) T19-3, 11.099 mg/m wear rate.

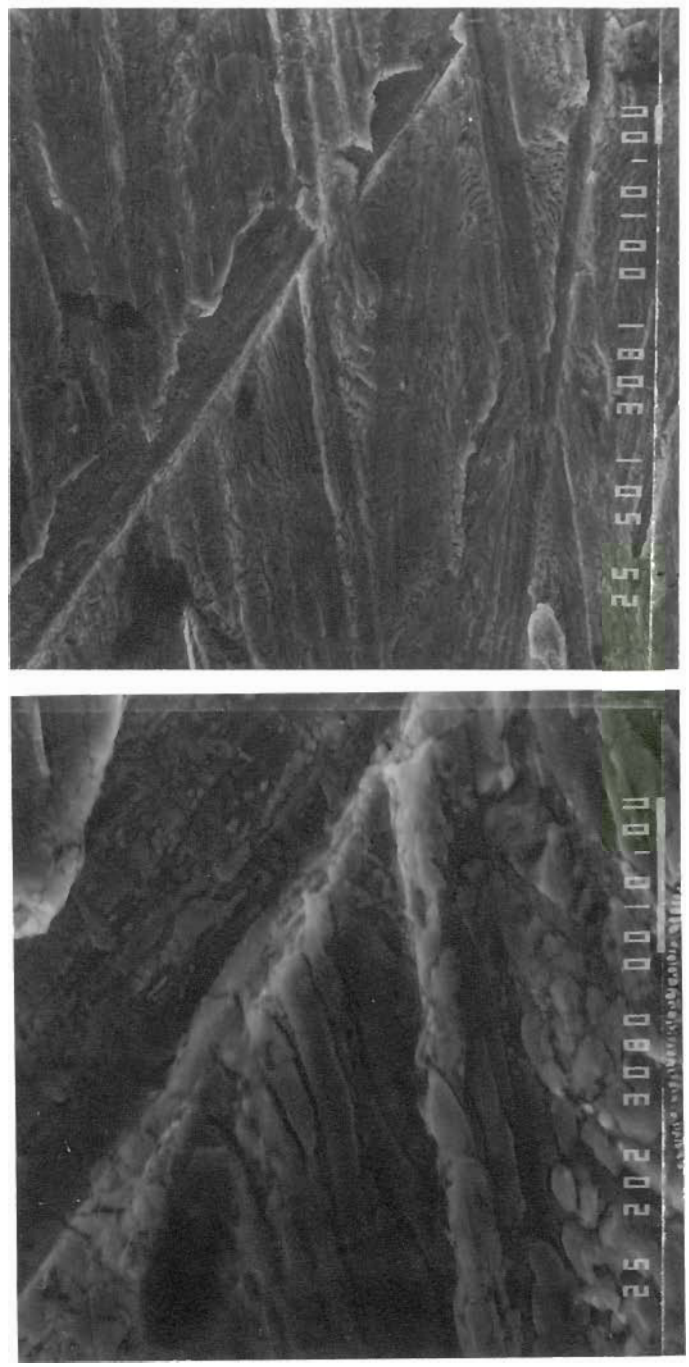

Figure 121. Wear scars etched in $FeCl_3$-HCl-Methanol etchant to reveal microstructure.

b) T20-2, 7.306 mg/m wear rate.

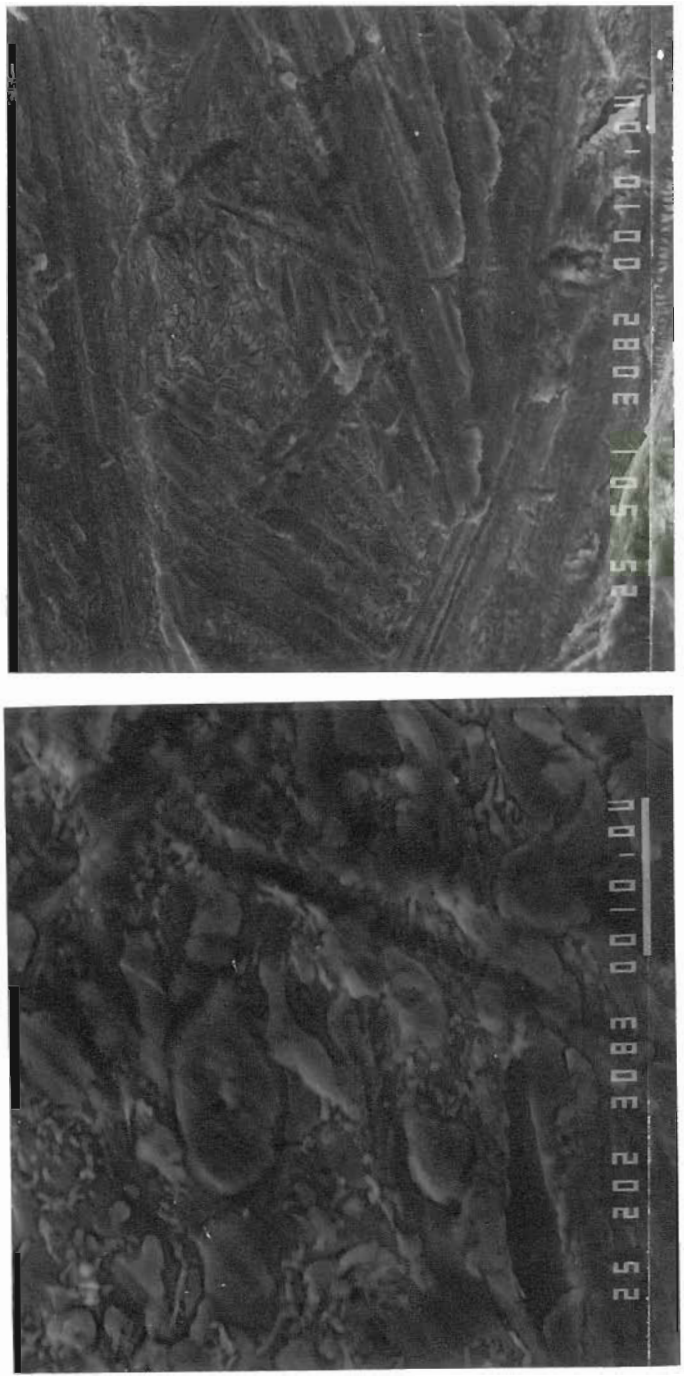

Figure 121. Wear scars etched in $FeCl_3$-HCl-Methanol etchant to reveal microstructure.

c) T20-4, 6.333 mg/m wear rate.

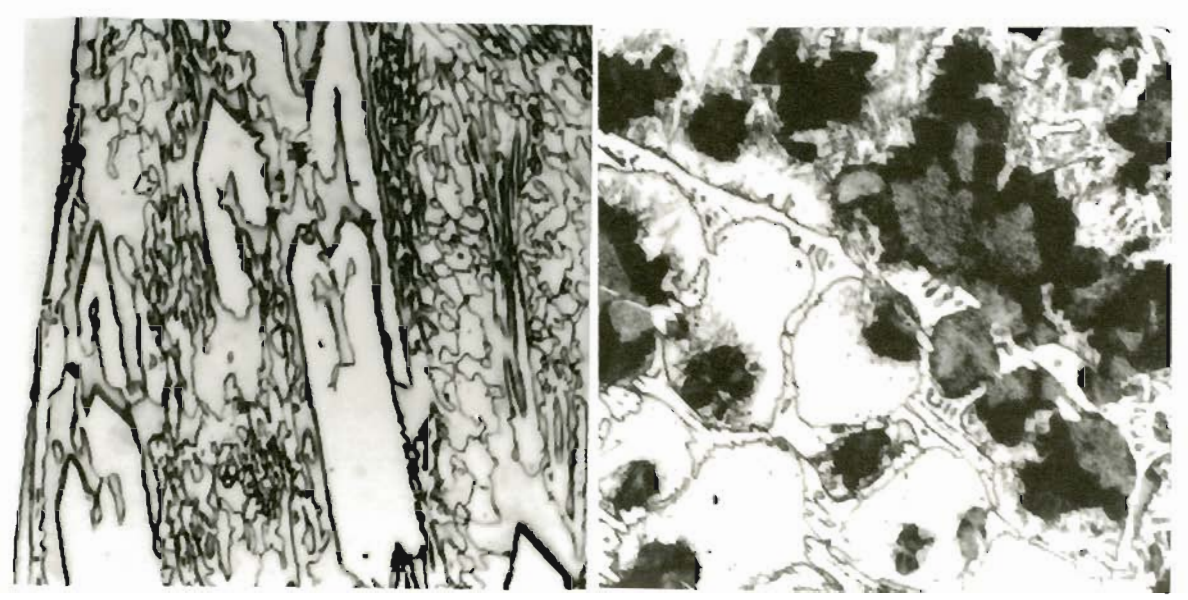

Figure 122. Microstructures of commercial high-chromium high-carbon hardfacing alloys.

a) Stoody 2134, 2.078 mg/m wear rate, 53.8 HRC

b) Abrasoweld, 3.492 mg/m wear rate, 43.2 HRC

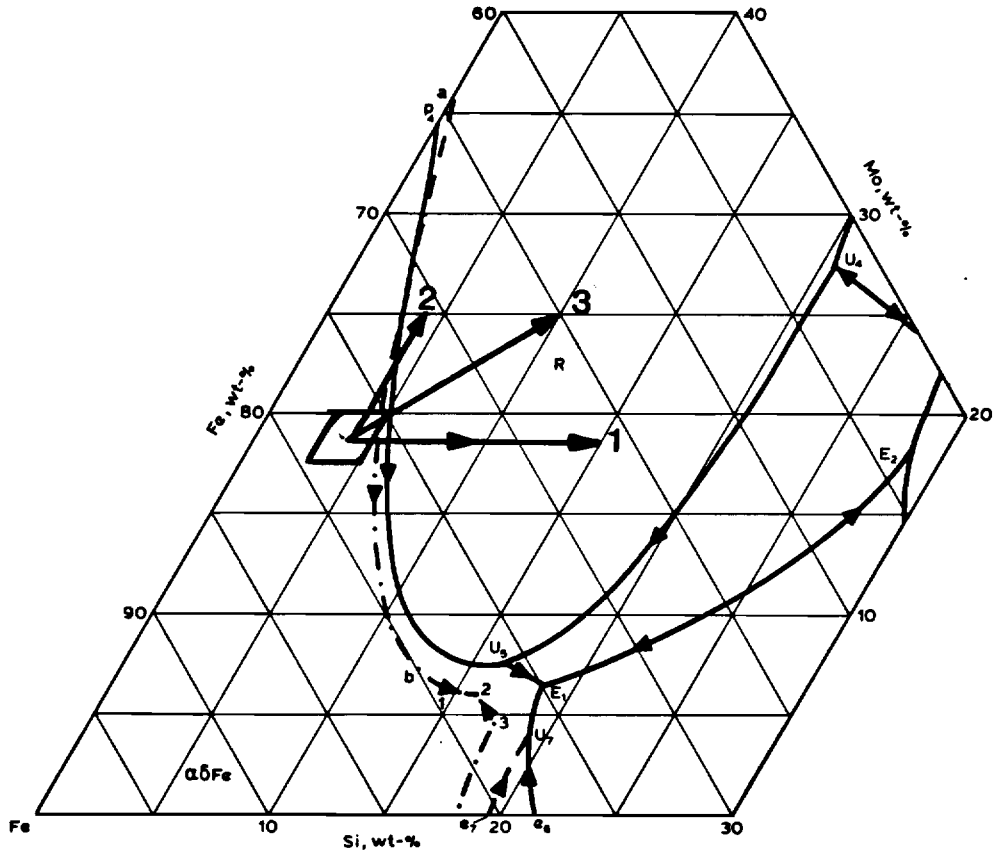

Figure 123. Projection of iron-rich primary surface, showing effect of composition changes.

5.0 Continued Research

The intent of this investigation was to indentify potentially useful hardfacing alloys and develop their wear resistance properties as far as time and means would allow. The focus was on intermetallic-hardened weld hardfacing alloys which did not contain strategic materials such as chromium and cobalt. The alloys developed were primarily based on Fe-Mo-Ni-Si compositions. In the course of the investigation a Fe-Mo-Ni-Si alloy, Fe-14Mo-10Ni-4.5Si, was found to have promising abrasive wear resistance. While the wear resistance as measured in the pin-on-drum test was only half that of commmercial high-chromium high-carbon weld metal alloys, it was better than that of common alloy steels. Alloy composition modifications to increase wear resistance have been discussed. These would be to increase the molybdenum content by 5 at.% and the silicon content by about 10 at.%. From phase diagram analysis this would increase the intermetallic volume fraction and also promote the formation of a harder intermetallic compound, Fe_2MoSi_2, rather than the Laves phase, $Fe_{(2-x)}MoSi_x$. Increased hard phase volume fraction and harder phases should increase abrasive wear resistance. Further research into wear behaviour of alloys with increased molybdenum and silicon content should prove valuable.

Along with continued wear research of higher molybdenum and nickel alloys, research should also explore hardening effects which accompany heat treatment of Fe-Mo-Ni-Si alloys. Heat treatment at 550-650°C increased the hardness of Fe-Mo-Ni-Si alloys, but the exact mechanism was not identified. It appears that a second phase precipitates in the matrix or the bcc_{Fe} s.s. dendrites of the solidification structure. The

matrix hardening itself should promote increased abrasive wear resistance.

An indication of weld alloy oxidation resistance was observed as a side effect of heat treating. At temperatures up to about 800°C little oxidation was observed on the weld metal surface. Only one set of oxidation resistance tests were performed, this at 1000°C and of a cyclic nature. Indications are that silicon promotes formation of a layer which inhibits the diffusion of oxygen into the weld metal and diffusion of molybdenum out of the weld metal. Additional oxidation testing would be worthwhile as would hot hardness testing and other tests of high temperature properties.

All wear tests performed on weld metal alloys were for determining abrasive wear resistance. Abrasive wear is only one of several wear processes seen in the real world. Another application for weld hardfacing alloys is for reducing metal-to-metal wear. Both self-mated and single sample tests for galling resistance and metal-to-metal wear resistance would be worthwhile to perform to further characterize the alloys.

During this investigation alloys based on a Fe-Mo-Ni-Si-C composition were examined along with intermetallic alloys. This offshoot came about through initial work examining effects of carbon pick-up from base metal on weld metal. At carbon contents of 1 wt.%, alloys with low silicon contents formed a 100% lamellar microstructure. At higher silicon contents other microstructures developed which included large carbides. Some of the latter alloys were found to have wear rates as low as 4.07 mg/m in the pin-on-drum test, which approaches wear rates seen in commercial high-chromium high-carbon hardfacing alloys, 2.5-3.5 mg/m. Experiments were also performed on inoculating the molten weld metal with

small amounts of titanium carbide, tungsten carbide, and hafnium carbide. This, however, appeared to have little influence on the wear rate. These alloys are essentially the same Fe-Mo-Ni-Si composition as the intermetallic-hardened alloy, but with a great amount of added carbon. The carbides formed in these alloys appear to be based on molybdenum and silicon. Most commercial hardfacing alloys are based on chromium and tungsten carbides. The Fe-Mo-Ni-Si-C alloys would be worth further investigation because of their favorable wear properties as a carbide--hardened hardfacing alloy without chromium-carbides.

6.0 Conclusions

The scope of this investigation was to identify potential abrasion resistant weld hardfacing alloys which have little or no strategic metal content, namely chromium and cobalt, and investigate some of thier properties. To that end the following conclusions have been reached:

1) Arc-melted alloys and weld metal alloys based on iron-rich Fe-Mo-Ni and Fe-Mo-Ni-Si compositions produced relatively close correlations with the phases predicted by the Fe-Mo-Ni and Fe-Mo-Si phase diagrams. Fe-Mo-Ni alloys had microstructures composed of $fcc_{(Fe,Ni)}$ solid solution dendrites with an $fcc_{(Fe,Ni)}$ plus Fe_7Mo_6 eutectic in interdendritic regions. Similar strutures were found in Fe-Mo-Ni-Si alloys except a bcc_{Fe} solid solution and an intermetallic compound identified as a $Fe_{(2-x)}MoSi_x$ Laves phase were present.

2) Through microstructural analysis of Fe-Mo-Ni-Si weld metal alloys and analysis of predicted solidification and solid state reaction paths, it was found that for practical purposes the Fe-Mo-Si phase diagram could be used to predict solidification structures and phases for iron-rich Fe-Mo-Ni-Si alloys. Additionally, at the nickel concentrations of up to 20%, the assumption of complete solubility of nickel atoms on iron sites was valid.

3) Pin-on-drum abrasive wear testing of the Fe-Mo-Ni-Si weld metals with an approximate composition of Fe-20Mo-15Ni-5Si produced the lowest wear rates, 6.3-6.5 mg/m, of the intermetallic-hardened materials

investigated.

4) Wear rate was found to be independent of bulk hardness and the concentrations of individual elements. Microstructure was found to have the greatest influence on the wear rate. It must be realized however, that there is a great deal of synergism between the effect of molybdenum and silicon contents and other elements present on the microstructure.

5) It was possible through heat treatment at 550-650°C to increase the hardness of a Fe-15Mo-10Ni-5Si alloy by almost 14 point HRC. The intermetallic phase, $Fe_{(2-x)}MoSi_x$, of the microstructure was unaffected by heat treatment. Precipitation of a second phase was observed at heat treatment temperatures over 750°C, where a hardness decrease was observed.

6) One possible avenue for further research would be to increase weld metal composition by 5 wt.% molybdenum and 10 wt.% silicon to a composition of Fe-20Mo-10Ni-15Si. Phase diagram data predicts that this composition should form a harder ternary intermetallic compound, Fe_2MoSi_2, with an overall greater volume fraction of hard phases. Another research direction would be further study of the Fe-15Mo-10Ni-5Si alloys containing over 1 wt.% carbon. Preliminary pin-on-drum wear tests on such an alloy yielded wear rates as low as 4.07 mg/m.

7.0 References

1. Huddle, F.P., "The Evolving National Policy for Materials", Science, 191 (1976) pp. 654-659.

2. Schwer, R.E., "Deficiencies of the U.S. Materials Stockpile", Journal of Metals, (1981) pp. 24-25, 32-33.

3. Piepgras, J.J. and Metz, H.J., "Managing Critical Materials in the 80's", Metals Progress, (1980) pp. 39-46.

4. Netschert, B.C., "The Future Availability of Raw Materials", Journal of Metals, (1978) pp. 11-15.

5. Cook, E., "Limits to Exploitation of Nonrenewable Resources", Science, 191 (1976) pp. 677-682.

6. Ford, J.A., "Get High Performance in New Alloys with Low Strategic Metal Levels", Industrial Research and Development, (1982) pp. 80-83.

7. Tien, J.K., Howson, T.E., Chen, G.L. and Xie, X.S., "Cobalt Availability and Superalloys", Journal of Metals, (1980) pp. 12-20.

8. Gray, A.G., "Substitution/Conservation Technology for Critical

Materials", Metals Progress, (1981) pp. 18-27.

9. Hartley, J.N., Chapter 4, "Is the Reserve Base Enough", World Mineral and Energy Resourse - Some Facts and Assessments, Battelle, 1974, pp. 43-66.

10. -----, U.S.B.M. Mineral Commodity Summary-1979, 1979.

11. Rabinowitz, Friction and Wear of Materials, Wiley and Sons, New York, 1965.

12. Kragelskii, I.V., Friction and Wear, Butterworth, London, 1965.

13. Vingsbo, O., "Wear and Wear Mechanisms", Wear of Materials, 1979, Proceedings of Conference, Dearborn, Mich., 16-18 April 1979, ASME, New York, 1979, pp. 620-635.

14. Misra, A. and Finnie, I., "Correlations between Two-body and Three-body Abrasion and Erosion of Metals", Wear, 68 (1981) pp. 33-39.

15. Beckmann, G. and Westermeier, G., "Sliding Wear of an Unlubricated Frictional Combination of Ductile Metal and Brittle Abrasive", Wear, 67 (1981) pp. 115-129.

16. Suh, N.P., "The Delamination Theory of Wear", Wear, 25 (1973)

pp. 111-124.

17. Murray, M.J., Mutton, P.J. and Watson, J.D., "Abrasive Wear Mechanisms in Steel", Wear of Materials, 1979, Proc. Conf. Dearborn, Mich., 16-18 April 1979, ASME, New York, 1979, pp. 257-265.

18. Bhansali, K., "Resistance of Pure Metals to Low Stress Abrasive Wear", Wear, 71 (1981) pp. 375-379.

19. Zum Gahr, K.-.H., "Relationship Between Abrasive Wear Rate and the Microstructure of Metals", Wear of Materials, 1979, Proc. Conf. Dearborn, Mich., 16-18 April 1979, ASME, New York, 1979, pp. 266-274.

20. Khruschov, M.M. and Babichev, M.A., "Resistance to Abrasive Wear of Structurally Inhomogeneous Materials", Friction and Wear in Machinery, 12 (1958) pp. 5-23.

21. Garrison, W.M., "Khruschov's Rule and the Abrasive Wear Resistance of Multiphase Steels", Wear, 82 (1982) pp. 213220.

22. Fulcher, J.K., Kosel, T.H. and Fiore, N.F., "The Effect of Carbide Volume Fraction on the Low-Stress Abrasion Resistance of High Cr-Mo White Cast Irons", Wear, 84 (1983) pp. 313-325.

23. Desai, V.M., Rao, C.M., Kosel, T.H. and Fiore, N.F., "Effect of Carbide Size on the Abrasion of Cobalt-Base Powder Metallurgical Alloys", Wear, 84 (1984) pp. 89-101.

24. Moore, M.A., "The Relationship Between the Abrasive Wear Resistance, Hardness, and Microstructure of Ferritic Materials", Wear, 28 (1974) pp. 59-68.

25. Richardson, R.C.D., "The Maximum Hardness of Strained Surfaces and the Abrasive Wear of Metals and Alloys", Wear, 10 (1976) pp. 353-382.

26. Larson-Badse, J. and Mathew, K.G., "Influence of Structure on the Abrasion Resistance of a 1040 Steel", Wear, 14 (1969) pp. 199-206.

27. Hurricks, P.L., "Some Metallurgical Factors Controlling the Adhesive and Abrasive Wear Resistance of Steels, A Review", Wear, 26 (1973) pp. 285-304.

28. Zum Gahr, K.-H. and Scholz, W.G., "Fracture Toughness of White Cast Irons", Journal of Metals, (1980) pp. 38-44.

29. Zum Gahr, K.-H., "Frature Analysis of White Cast Iron", Z. Metallkunde, 71 (1980) pp. 103-109.

30. De Gee, A.W.J., "Comments os "Resistance of Pure Metals to Low-Stress Abrasive Wear", Wear, 81 (1982) pp. 373-374.

31. Misra, A. and Finnie, I., "On the Size Effect in Abrasive and Erosive Wear", Wear, 65 (1981) pp. 359-373.

32. Kosel, T.H., Li, S.Z. and Rao, C.M., "The Size Effect in Abrasion of Dual-Phase Alloys", ASLE Transactions, 28 (1985) pp. 343-350.

33. Shetty, H.R., Kosel, T.H. and Fiore, N.F., "A Study of Abrasive Wear Mechanisms using Diamond and Alumina Scratch Tests", Wear, 80 (1982) pp. 347-376.

34. Prasad, S.V. and Kosel, T.H., "A Study of Carbide Removal Mechanisms During Quartz Abrasion. I: Insitu Scratch Test Studies", Wear, 92 (1983) pp. 253-268.

35. Misra, A. and Finnie, I., "Some Observations on Two-body Abrasive Wear", Wear, 68 (1981) pp. 41-56.

36. Ellis, D. and Squires, R.L., "Weld Deposition and "Properties of Nickel Based Hardfacing Alloys", Metal Construction, (1983) pp. 388-393.

37. Thomasson, H., "Hardfacing (Surfacing) Ferrous Alloys",

Canadian Welder and Fabrication, (1974) pp. 8-16.

38. Spencer, L.F., "Hardfacing - Preparation, Dilution, and other Problems", Welding Engineer, 56 (1971) pp. 40-45.

39. Spencer, L.F., "Hardfacing - Selection of Process and Procedures", Welding Engineer, 56 (1971) pp. 44-48.

40. -----, "Hardfacing by Arc Welding", The Procedure Handbook of Arc Welding, Lincoln Electric, 1973, pp. 13.7.1-13.7.20.

41. Bishnoi, Y.P.S., "Hardfacing Problems in Rajhara Mines and Iron Zone in Bhiliai Steel Plant", Journal of the Institution of Engineers, 52 (1971) pp. 4-8.

42. Verma, S.P., "Hardfacing with Cobalt-base Alloys", Tool and Alloy Steels, (1979) pp. 229-232.

43. Van Muysen, L., "Hardfacing with Co-Cr-X Alloys by Arc Welding Process", Cobalt, 55 (1972) pp. 67-78.

44. Nikolaenko, M.R. and Markushevich, I.S., "Hardfacing of the Rolls of Rolling Machines", Svar. Proiz., 10 (1981) pp. 29-30.

45. Jackson, C.E., Fluxes and Slags in Welding, WRC Bulletin 190,

Welding Research Council, New York, 1973.

46. Arnoldy, R.F. and Reynolds, G.H., "Iron-Chromium-Carbon Hardfacing with the Bulkweld Process", Metals Progress, (1977) pp. 31-35.

47. Kratz, J.A., "Hardfacing with the Bulkweld Process", Proc. 1968 Golden Gate Conf., 25-27 Sept. 1968, San Francisco, Cal., (1968).

48. Wilson, R.A., "New Hardfacing Technique has Numerous Applications", Iron Age Metalworking International, 9 (1970) pp. 35-38.

49. Paton, B.E., Electroslag Welding, 2nd ed., American Welding Society, New York, 1962.

50. Nakano, S., Nishiyama, N., Kamada, A. and Tsuboi, J., "MAGLAY - An Electroslag Technique for Overlay Welding", Metal Construction, (1982) pp. 610-614.

51. Van Bernst, A. and Dargent, P.h., "Electroslag Cladding using Nickel-Base Alloys", Metal Construction, (1983) pp. 730-733.

52. Bewley, J.G., "Plasma Hardfacing: Solving Today's Wear Problems", Materials Engineering, 92 (1980) pp. 71-73.

53. Bewley, J.G., "Plasma Hardfacing Extends Mill Roll Life", Iron and Steel Engineer, 57 (1980).

54. Matlock, W.M., Kocis, J.F. and Vitcha, E.T., "Plasma Arc Hardfacing Exhaust Valves with an Iron-Base Alloy", Metals Progress, (1978) pp. 38-43.

55. Swart, J.D., "Plasma-MIG Hardfacing Suited to Cladding Oil Delivery System", Welding and Metal Fabrication, (1982) pp. 477-480.

56. Glaeser, W.A., "Weld Failure Analysis", Wear of Materials 1979, Proc. Conf. Dearborn, Mich., 16-18 April 1979, ASME, New York, 1979, pp. 639-652.

57. Molian, P.A., Laser Surface Alloying of Chromium and Nickel on Iron and Carbon Steels, Phd thesis Oregon Graduate Center, 1982.

58. Mayer, C.A., "How to Select Hardsurfacing Materials", Welding Design and Fabrication, (1982) pp. 61-67.

59. Evans, C.J., "Selection of Hardfacing Alloys; a seminar report - London, October 1976", Welding and Metal Fabrication, 54 (1977) pp. 62-63.

60. Dawson, R.J., Shewchuk, S. and Pritchard, J.E., "Selection and Use of Hardfacing Alloys", Welding Journal, (1982) pp. 15-23.

61. Smart, M.D., "Hardfacing - An Engineering Tool", FWP Journal, 13 (1973) pp. 3-11.

62. Hickl, A.J., "An Alternative to Cobalt-Base Hardfacing Alloys", Journal of Metals, (1980) pp. 6-12.

63. Diesburg, D.E. and Borik, F., "Optimizing Abrasion Resistance and Toughness in Steels and Irons for the Mining Industry", Symposium: Materials for the Mining Industry; Vail, Col., 30-31 July, 1974, Climax Molybdenum, 1974, pp. 15-41.

64. Whelan, E.P., "Nickel-Base Wear Resistant Alloys", Report RP-57-78-03, Jan. 30, 1979; Climax Molybdenum, (1979).

65. Whelan, E.P., "Hardness and Abrasive-Wear Resistance of Ni-Cr-Mo-C Hardfacing Alloys", Journal of Metals, (1979) pp. 15-19.

66. Silence, W.L., "Effect of Structure on Wear Resistance of Co-, Fe-, and Ni- Base Alloys", W.A. Glaeser, K.C. Ludema, and S.K. Rhee (eds.), Wear of Materials 1977, Proc. Conf., ASME, New York, 1977, pp. 77-85.

67. Cameron, C.B. and Ferriss, D.P., "Tribaloy - Intermetallic Materials: New Wear- and Corrosion-Resistant Alloys", Cobalt, (1974) pp. 49-53.

68. Bhansali, K.J. and Silence, W.L., "Metallurgical Factors Affecting Wear Resistance of Metals", Metals Progress, (1977) pp. 39-43.

69. Drapier, J.M., Davin, A., Magnee, A., Coutsouradis, D. and Habraken, L., "Abrasion and Corrosion Resistant Cobalt Base Alloys for Hardfacing", Wear, 33 (1975) pp. 271-282.

70. Niset, M. and Daeman, D., "Recent Developments in High Temperature, Wear Resistant Co-Cr-C-X Alloys", Surfacing Journal, 16 (1985) pp. 40-44.

71. Shetty, H.R., Kosel, T.H. and Fiore, N.F., "A Study of Abrasive Wear Mechanisms in Cobalt-Base Alloys, Wear, 84 (1983) pp. 327-343.

72. Ferriss, D.P. and Cameron, C.B., "Wear Properties of Cast vs. Plasma- Sprayed Laves Intermetallic Alloys", Journal of Vacuum Science Technology, 12 (1975) pp. 795-799.

73. Halstead, A. and Rawlings, R.D., "Structure and Hardness of

Co-Mo-Cr-Si Wear Resistant Alloys (Tribaloys)", Metal Science, 18 (1984) pp. 491-500.

74. Allen, C., Ball, A. and Protheroe, B.E., "The AbrasiveCorrosive Wear of Stainless Steel", Wear, 74 (1981-82) pp. 287-305.

75. Salesky, W.J. and Thomas, G., "Medium Carbon Steel Alloy Design for Wear Applications", Wear, 75 (1982) pp. 21-40.

76. El-Koussy, R., El-Ragby, S.M. and El-Mehairy, A.E., "Effect of Heat Treatment Conditions and Composition on the Wear Resistance of Some Chromium Steels", Tribology, (1981) pp. 323-327.

77. Fabert, Jr, H.A., "Manganese Steels in Chrushing and Grinding Service", Symposium: Materials for the Mining Industry; Vail, Col., 30-31 July, 1974, 1974, pp. 163-168.

78. Gouin, C.E., "Manganese Steels that don't Require Heat Treatment", Molybdenum Mosaic, 1 (1975-76) pp. 10-14.

79. -----, "Austenitic Manganese Steel", Metals Handbook, Ninth Edition, Properties and Selection: Stainless Steels, Tool Materials, and Special Purpose Metals, American Society for Metals, Metals Park, 1980, pp. 568-588.

80. de Mello, J.D.B., Durand-Charre, M. and Hamar-Thibault, S.,

"Solidification and Solid State Transformations during Cooling of Chromium-Molybdenum White Cast Irons, Metallurgical Transactions A, 14A (1983) pp. 1793-1815.

81. Rivlin, V.G., "Phase Equilibria in Iron Ternary Alloys 14: Critical Review of Constitution of Carbon-Chromium-Iron and Carbon-Iron-Manganese Systems", International Metals Reviews, 26 (1984) pp. 299-327.

82. Norman, T.E., Soloman, A. and Doane, D.V., "Martensitic White Irons for Abrasion-Resistant Castings", Transactions of the American Foundary Society, 67 (1959) pp. 242-256.

83. Moestue, H., "Hardfacing Against Abrasive and Impact Types of Wear with Iron-Base Alloys", Philips Welding Reporter, 9 (1973) pp. 1-6.

84. Drzeniek, Dr.-Ing.H. and Lugscheider, Prof. Dr. E., "The Effect of the Cooling Rate on the Structure of Metal-Arc Welded Hardfacings Produced from Iron/Chromium/Carbon-based Cored-wire Electrodes", Schweissen und Schneiden, 35 (1983) pp. 366-369.

85. Pearce, J.T.H., "The Use of the Transmission Electron Microscope to Study the Effects of Abrasive Wear on the Matrix Structure of a High Chromium Iron, Wear, 89 (1983) pp. 333-344.

86. Gundlach, R.B. and Parks, J.L., "Influence of Abrasive Hardness and Particle Size on Wear Resistance of HighChromium Irons", W.A. Glaeser, K.C. Ludema, and S.K. Rhee (eds.), Wear of Materials 1977, Proc. Conf., ASME, New York, 1977, pp. 211-216.

87. Sare, I.R., "Abrasion Resistance and Fracture Toughness of White Cast Irons", Metals Technology, (1979) pp. 412-419.

88. Iwasaki, I., Riemer, S.C. and Orlich, J.N., "Corrosive and Abrasive Wear in Ore Grinding", Wear, 103 (1985) pp. 253-267.

89. Sare, I.R., "Repeated Impact-Abrasion of Ore-Crushing Hammers", Wear, 87 (1983) pp. 207-225.

90. Durman, R.W., "The Application of Alloyed White Cast Irons in Crushing, Grinding, and Material Handling Processes", British Foundaryman, 69 (1976) pp. 141-149.

91. Dodd, J. and Jackson, R.S., "High Chromium Cast Irons for Crushing and Grinding Machinery", Metallurgia, 76 (1967) pp. 107-110.

92. Hegmegee, Jr, P.E., "Utilization and Application of a Superior Abrasion Resistant Material for Severe Crushing Application", Symposium: Materials for the Mining Industry; Vail, Col., 30-31 July 1974, Climax Molybdenum, 1974, pp. 201-205.

93. Dodd, J. and Dunn, D.J., "High Chromium-Molybdenum Alloy Irons for the Mining Industry", Molybdenum Mosaic, 3 (1977-78) pp. 2-8.

94. Belikova, N.A., Grinberg, N.A. and Pruzhanskii, L. Yu, "Alloys for Hardfacing of Parts of Excavation Machines", Metal. Sci. and Heat Treatment, (1970) pp. 219-220.

95. Mason, V., Perrott, C.M. and Sare, I.R., "Wear Resistant Materials for Sugar Cane Shredder Hammers", Wear of Materials 1979, Proc. Conf. Dearborn, Mich., 16-18 April 1979, ASME, New York, 1979, pp. 343-350.

96. -----, "Amdry 754 (Nickel-base Hardfacing Alloy)", Alloy Digest, (1974).

97. -----, "Amdry 769 (Nickel-base Hardfacing Alloy)", Alloy Digest, (1974).

98. -----, "Amdry 850 (Cobalt-base Hardfacing Alloy)", Alloy Digest, (1974).

99. Bhat, M.S., Zackay, V.F. and Parker, E.R., "Alloy Design for Abrasive Wear", Wear of Materials 1979, Proc. Conf. Dearborn, Mich., 16-18 April 1979, ASME, New York, 1979, pp. 286-291.

100. Avery, H.S., "Work Hardening in Relation to Abrasion Resistance", Symposium: Materials for the Mining Industry; Vail, Col., 30-31 July 1974, Climax Molybdenum, 1974, pp. 43-77.

101. Ball, A., "On the Importance of Work Hardening in the Design of Wear Resistant Materials", Wear, 91 (1983) pp. 201-207.

102. Ohriner, E.K., "Galling Resistance of Intermetallic Strengthened Iron-Base Hardfacing Alloys", Report RP-50-8101, Feb. 2, 1982, Climax Molybdenum, (1982).

103. Ohriner, E.K. and Whelan, E.P., Wear of Materials 1985, Proc. Conf. Vancouver, B.C., Canada, (1985) pp. .

104. Koster, W., "Das System Eisen-Nickel-Molybdan", Archiv fuer das Eisenhuettenwesen, 8 (1934) pp. 169-171.

105. Das, D.K., Rideout, S.P. and Beck, P.A., "Intermediate Phases in the Mo-Fe-Co, Mo-Fe-Ni, and Mo-Ni-Co Ternary Systems", AIME Transactions, 194 (1952) pp. 1071-1075.

106. Van Loo, F.J.J., Bastin, G.F., Vrolijk, J.W.G.A. and Hendriks, J.J.M., "Phase Relations in the Systems Fe-Ni-Mo, Fe-Co-Mo, and Ni-Co-Mo at 1100° C", Journal of Less-Common Metals, 72 (1980) pp. 225-230.

107. Raynor, G.V. and Rivlin, V.G., "Phase Equilibria in Iron Ternary Alloys 15: Critical Evaluation of Ternary Alloys of Iron and Molybdenum with Cobalt, Chromium, Manganese, and Nickel", International Metals Review, 29 (1984) pp. 329-375.

108. Hoster, T., Entwicklung Kalorimetrisch Methoden zur Thermochemischen untersuchung Hochlegierter Stahle und Hochaffinen Doppel-Oxide, Dissertation, 1980, Rheinisch Westfalischen Technischen Hochschule, Aachen.

109. Wada, "Fe-Mo-Ni phase diagram", Metals Handbook, Eighth Edition, Metallography, Structures, and Phase Diagrams, American Society for Metals, Metals Park, (1973) p. 431.

110. Das, B.N. and Beck, P.A., "Relationship Between the Mu Phase and the Sigma Phase in the Mo-Mn-Co System", Transactions of the Metal Society, AIME, 218 (1960) p. 733.

111. Kardonskiy, V.M., "Ageing of Fe-Mo and Fe-Mo-Si Alloys", Physics of Metals and Metallography, 27 (1969) pp. 127-131.

112. Gupta, K.P., Rajan, N.S. and Beck, P.A., "Effect of Si and Al on the Stability of Certain Sigma Phases", Transactions of the Metal Society, AIME, 218 (1960) pp. 617-624.

113. Bardos, D.I., Gupta, K.P. and Beck, P.A., "Ternary Laves Phases with Transition Elements and Silicon", Transactions of the Metal Society, AIME, 221 (1961) pp. 1087-1088.

114. Bardos, A.M., Bardos, D.I. and Beck, P.A., "The Effective Atomic Radius of Silicon in Ternary Laves Phase Alloys", Transactions of the Metal Society, AIME, 227 (1963) pp. 991-993.

115. Vogel, V.R. and Gerhardt, R., "Das System Eisen-Molybdan--Silizium", Archiv fuer das Eisenhuettenwesen, 32 (1961) pp. 1-10.

116. Guard, R.W. and Smith, E.A., "Constitution of Nickel-base Ternary Alloys", Journal of the Institute of Metals, 88 (1959-60) pp. 285-287.

117. Virkar, A.N. and Raman, A., "Alloy Chemistry of Sigma (Beta-U)--related Phases II. The Characteristics of Sigma and Other Related Phases in Some Mo-NiX systems", Z. Metallkde, 60 (1969) pp. 594-600.

118. Raynor, G.V. and Rivlin, V.G., "Phase Equilibria in Iron Ternary Alloys 16: Critical Evaluation of Constitution of Iron-Molybdenum-Silicon Alloys", International Metal Reviews, 30 (1985) pp. 68-84.

119. Avery, H.S., "Classification and Precision of Abrasion Tests", W.A. Glaeser, K.C. Ludema, and S.K. Rhee (eds.), Wear of Materials 1977, Proc. Conf., ASME, New York, 1977, pp. 148-157.

120. Bardos, D.I., Gupta, K.P. and Beck, P.A., "New Ternary R-Phases Containing Silicon", Nature, 192 (1961) p. 744.

121. Kuo, K., "Ternary Laves and Sigma-Phases of Transition Metals", Acta Metallurgica, 1 (1953) pp. 720-724.

122. Nussler, H.D., Hoster, T. and Kubaschewski, o., "The Thermodynamical Properties of the System Iron-Molybdenum", Z. Metallkunde, 71 (1980) pp. 396-397.

123. Blickensderfer, R., Madsen, B.W. and Tylczak, J.H., "Comparison of Several Types of Wear Tests", Wear of Materials 1985, Proc. Conf. Vancouver, B.C., Canada, 1985, ASME, New York, 1985, pp. 313-323.

124. Berns, H. and Fischer, A., "Abrasive Wear Resistance and Microstructure of Fe-Cr-C-B Hard Surfacing Weld Deposits", Wear of Materials, 1985, Proc. Conf. Vancouver, B.C., Canada, 1985, ASME, New York, 1985, pp. 625-633.

125. Gladyshevskii, E.I. and Kuz'ma, Y.B., "The Molybdenum-Iron-Silicon

System", Zh. Strukt. Khim., 1 (1960) pp. 66-71.

126. Skolozdra, R.V. and Gladyshevskii, E.I., "The Crystal Structure of the Ternary Phases in Systems Mo(W)-Fe(Co,Ni)Si", Izv. Akad. Nauk SSSR Neorg. Mater., 2 (1966) pp. 1448-1453.

127. Rudy, E. and Progulski, G., "Ternary Phase Equilibria in Transition Metal-Boron-Carbon-Silicon Systems", AF 33(615)-1249, May 1967.

128. Blickensderfer, R. and J.H. Tylczak, Laboratory Tests of Spalling, Breaking, and Abrasion of Wear-Resistant Alloys Used in Mining and Mineral Processing, Report of Investigations 8988, U.S. Dept. of Interior.

129. Blickensderfer, R., J.H. Tzlczak, and B.W. Madsen, Laboratory Wear Testing Capabilities of the Bureau of Mines, Bureau of Mines Information Circular 9001, U.S. Dept. of Interior.

BIOGRAPHICAL NOTE

The author was raised in San Diego, California with a normal progression through the local schools before attending college at the California Polytechnic State University in San Luis Obispo. There he received his degree as a Bachelor of Science in Metallurgical and Welding Engineering, but not before acquiring a taste for antique engines and tractors, and for running.

From Cal Poly, he went on up the coast to the Oregon Graduate Center where he first completed a Masters Degree on the alloying of electroslag welded railroad rail, and subsequently completed his Doctorate, this dissertation being the culmination of that activity.